

RICE UNIVERSITY

**Solvothermal Synthesis and Supported Catalysis of Polyanion-derived
Metal Oxide Nanoparticles**

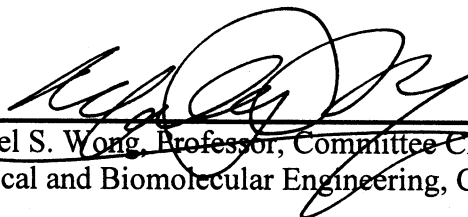
by

Nikolaos Soutanidis

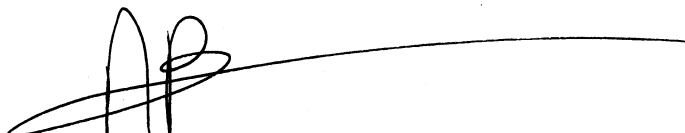
A THESIS SUBMITTED
IN PARTIAL FULFILLMENT OF THE
REQUIREMENTS FOR THE DEGREE

Doctor of Philosophy

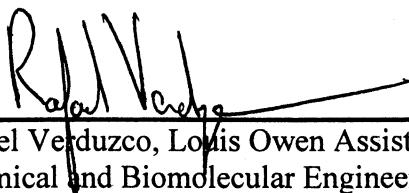
APPROVED, THESIS COMMITTEE:



Michael S. Wong, Professor, Committee Chair
Chemical and Biomolecular Engineering, Chemistry



Andrew R. Barron, Charles W. Duncan, Jr. - Welch Chair of
Chemistry and Professor of Materials Science



Rafael Verduzco, Louis Owen Assistant Professor
Chemical and Biomolecular Engineering

HOUSTON, TEXAS
NOVEMBER 2011

ABSTRACT

Solvothermal Synthesis and Supported Catalysis of Polyanion-derived Metal Oxide Nanoparticles

by

Nikolaos Soutanidis

Supported metal oxides (SMOs) are important catalytic materials that find numerous applications in important industrial processes. Improving the structural properties of SMOs is a challenging objective due to material synthesis and characterization limitations. Recent developments in the characterization of SMOs, specifically tungstated zirconia (WO_x/ZrO_2), have revealed structural information that renewed scientific interest in developing more sophisticated synthetic protocols for SMOs.

The current work aims to provide a robust characterization of WO_x/ZrO_2 by using different characterization techniques and probe reactions. Conventional and non-conventional synthetic methods are investigated to cover the whole spectrum of published methods in order to understand the properties and limitations of these techniques. In the second part of this work, a new synthetic approach is presented that successfully produces ultrasmall (smaller than 2 nm) tungsten oxide nanoparticles (WO_x NPs). By using conventional tungsten precursors and oleylamine, WO_x NPs are synthesized, characterized, and finally supported to test their propene metathesis activity.

Conventional WO_x/ZrO_2 catalysts were prepared and extensively studied by probing their *n*-pentane isomerization activity and methanol dehydration activity. WO_x/ZrO_2 prepared via incipient wetness impregnation shows maximum *n*-pentane isomerization turnover rates (*TOR*) at intermediate surface densities (ρ_{surf}). This method delivers the most active *n*-pentane isomerization WO_x/ZrO_2 catalysts since it maximizes the number density of the active sub-nm slightly distorted Zr- WO_x sites at ρ_{surf} between 5.2-6.2 W/nm^2 . By comparing the *n*-pentane isomerization activity with the methanol dehydration activity of WO_x/ZrO_2 , *n*-pentane isomerization is shown to be an excellent probe reaction for qualitatively identifying the relative (to the other species) population density of Zr- WO_x clusters. Bimolecular *n*-pentane isomerization is the prevailing mechanism and requires a higher population density of Zr- WO_x clusters than methanol dehydration.

In the second part of this work, a new solvothermal synthesis route for the preparation of ultrasmall tungsten oxide nanoparticles (WO_x NPs) is introduced. By using ammonium polyanionic salts and oleylamine, high yields ($92\pm 5\%$) of oleylamine-coated WO_x NPs were consistently synthesized. The co-addition of an organic oxidant during the synthesis led to smaller WO_x NPs thereby providing insight into the NP synthesis mechanism. Deposition and activation of the NPs on SiO_2 support by removal of oleylamine allows better control over the WO_x domain size than conventional methods. Oleylamine suppresses WO_x NP sintering during calcination and prevents the formation of larger polytungstates present in conventional catalysts. The supported WO_x NPs were found to be up to 3 times more selective for metathesis products than conventionally prepared tungstated silica likely due to their controlled structure.

Acknowledgements

I would like to thank my advisor, Prof. Michael S. Wong for giving me this unique opportunity to challenge and improve myself as a scientist during the last five years. His influence and guidance shaped my character and allowed me to develop a new perspective about research and life. I will never forget his support on my first “speed bump” with the Department’s qualifiers. His words of “take this moment as a speed bump and not an impassable obstacle” will remain branded in my memory, since they motivated me to overcome that moment and become a stronger and more focused individual.

I would also like to express my gratitude to and respect for Prof. Israel E. Wachs from Lehigh University for being extremely generous with sharing knowledge and resources during my PhD work. Exploring the Raman “world” even from a distance has been inspirational for me and it will continue to influence my future professional endeavors. I will always be indebted to Prof. Christopher J. Kiely and his student Dr. Wu Zhou for being my “eyes” in this journey. My PhD work would have never been the same without your scientific contribution and for that I am very thankful. My special thanks to Dr. William V. Knowles for sharing with me his technical experience at the beginning of my PhD. I have learned a lot, even without having the opportunity to work with you in person.

I would also like to thank my friends and co-authors Dr. Antonis C. Psarras and Dr. Eleni F. Iliopoulou for giving me the opportunity to work with them at the Chemical Process Engineering Research Institute. To my undergraduate advisors and mentors,

Prof. Iacovos A. Vasalos and Prof. Angeliki A. Lemonidou from Aristotle University, many thanks for showing me the door to the research world and for supporting me.

I want to thank DCG Partnership, especially Mr. Alejandro J. Gonzalez and Mr. Louis G. D'Agostaro for investing their resources and time into my projects. These memories of late hours working on the reactor are priceless and they will never be forgotten. Without both of you, I could never have completed any of my projects and for that I will always be grateful and indebted.

To Mr. Gautam Kini, Ms. Lori A. Pretzer, Dr. Hitesh Bagaria, Ms. Sravani Gullapalli, Mr. Juan Velazquez, Mr. Quang Nguyen, my lab-mates from the catalysis and nanomaterials laboratory, my brothers and sisters, many thanks for your scientific and personal help during this journey. To all these sleepless nights in the lab, sharing our frustrations and successes, I will always be there for all of you. Thank you for coping with me and thank you for not messing up my sample. I will miss you all, more than you can imagine.

I want to express my deepest gratitude to my family and friends for their support. To Dr. Kostas Bekris, Dr. Michail Stamatakis, Dr. Konstantinos Spetsieris and Ms. Venetia Rigou, I have no words to express my gratitude for having such wonderful friends. I would like to thank Mr. Christos Corovessis and the Corovessis family for being the most generous people I have met in my life. Thank you for everything you have done for me; I will always remember and I will always have you in my heart. Additionally, I would like to thank Mr. Larry Soward, Ms. Ashley K. Wadick, and Dr. Stephen Dowdall for their unconditional friendship and support these past five years. Thank you helping me survive in the "New World".

Finally, I would like to dedicate this work to my mother, Vasiliki Lagazali, for teaching me to fight for my dreams, for not compromising the quality of my education, and most importantly for being my mom and my best friend in the world.

Dedicated to my mother.

Vasiliki Lagazali

Nikolaos Soultanidis

November 2011

Table of Contents

Chapter 1. Background and research motivation

1.1	Nanoscience and nanotechnology.....	1
1.2	Nanotechnology and heterogeneous catalysis.....	2
1.3	Conventional supported metal oxide catalysts.....	6
1.4	Heterogeneous catalysis using metal oxide nanoparticles	7
1.4.1	Metal oxide nanoparticles us support.....	7
1.4.2	Metal oxide nanoparticles as supported/active phase.....	8
1.5	Tungstated zirconia.....	9
1.5.1	Iglesia and coworkers: polytungstate model.....	10
1.5.2	Knözinger and coworkers: Zr^{4+} heteropoly-tungstate model..	13
1.5.3	Santiesteban and coworkers: Brønsted and Lewis acidity.....	14
1.5.4	Wachs and coworkers: 3-D sub-nm Zr- WO_x clusters.....	14
1.6	Research motivation.....	16
1.7	References.....	18

Chapter 2. Relating *n*-pentane isomerization activity to the tungsten surface density of WO_x/ZrO_2

2.1	Introduction.....	29
2.2	Experimental methods.....	30
2.2.1	Chemicals.....	30
2.2.2	Catalyst preparation.....	31
2.3	Characterization.....	32
2.3.1	Nitrogen physisorption.....	32
2.3.2	X-ray diffraction.....	33

2.3.3	Electron microscopy.....	33
2.3.4	Pyridine FTIR.....	34
2.3.5	Thermogravimetric analysis	35
2.3.6	Catalytic studies.....	36
2.4	Results and discussion.....	37
2.4.1	Catalyst structure.....	37
2.4.2	Electron microscopy analysis.....	40
2.4.3	Surface acidity	49
2.4.4	<i>n</i> -pentane isomerization catalytic activity.....	53
2.5	Summary and conclusions.....	61
2.6	References.....	62

Chapter 3. Influence of synthesis on nature species in WO_x/ZrO₂

3.1	Introduction.....	67
3.2	Experimental methods.....	69
3.2.1	Chemicals.....	69
3.2.2	Incipient wetness impregnation.....	69
3.2.3	Co-precipitation method.....	71
3.2.4	Sol-gel.....	72
3.2.5	Surfactant templating synthesis.....	73
3.3	Characterization.....	73
3.3.1	Elemental analysis.....	73
3.3.2	Nitrogen physisorption.....	73
3.3.3	X-ray diffraction.....	74
3.3.4	<i>In Situ</i> Raman spectroscopy.....	75

3.3.5	Catalytic studies.....	76
3.4	Results.....	77
3.4.1	Nitrogen adsorption analysis of textural properties.....	77
3.4.2	X-ray diffraction analysis.....	81
3.4.3	<i>In Situ</i> Raman spectroscopy analysis of WO _x species.....	87
3.4.4	Reaction rate studies.....	91
3.5	Discussion.....	96
3.5.1	Comparison of XRD and <i>in situ</i> Raman spectroscopy.....	96
3.5.2	Influence of synthesis method on the WO _x structure.....	96
3.5.3	CH ₃ OH dehydration and nC ₅ isomerization.....	97
3.5.4	Hafnium doping effect on the formation of Zr-WO _x sites.....	99
3.6	Summary and conclusions.....	100
3.7	References.....	100

Chapter 4. Bimolecular *n*-pentane isomerization mechanism over WO_x/ZrO₂

4.1	Introduction.....	107
4.1.1	Paraffin isomerization studies.....	107
4.1.2	Paraffin isomerization mechanism.....	108
4.1.3	<i>n</i> -pentane isomerization mechanism.....	110
4.2	Experimental methods.....	111
4.2.1	Chemicals.....	111
4.2.2	Catalyst preparation.....	111
4.3	Characterization.....	112
4.4	Catalytic studies.....	112
4.5	Results and discussion.....	113

4.5.1	Olefin co-addition effect on <i>n</i> -pentane conversion.....	113
4.5.2	Olefin co-addition effect on product selectivity.....	115
4.7	Summary and conclusions.....	118
4.8	References.....	119

Chapter 5. *n*-Pentane isomerization activity of supported phosphotungstic acid

5.1	Introduction.....	124
5.2	Experimental methods and characterization.....	125
5.2.1	Chemicals.....	125
5.2.2	Catalyst preparation.....	126
5.2.3	Catalyst characterization.....	126
5.2.3	Catalytic studies.....	127
5.3	Results and discussion.....	127
5.3.1	Structure of supported phosphotungstic acid.....	127
5.3.2	Steady state <i>n</i> -pentane isomerization activity.....	129
5.3.3	Regeneration of silica supported phosphotungstic acid.....	131
5.3.4	Transient activity of silica supported phosphotungstic acid...	131
5.4	Summary and conclusions.....	134
5.5	References.....	134

Chapter 6. Solvothermal synthesis of ultrasmall metal oxide nanoparticles

6.1	Introduction.....	138
6.2	Synthesis of metal oxide nanoparticles.....	139
6.2.1	Hydrothermal methods.....	139
6.2.2	Solvothermal methods.....	140

6.2.3	Aqueous Sol-Gel methods.....	140
6.2.4	Non-aqueous Sol-Gel methods.....	142
6.3	Tungsten oxide nanoparticles.....	142
6.4	Experimental methods.....	143
6.4.1	Chemicals.....	143
6.4.2	Solvothermal synthesis of tungsten oxide nanoparticles.....	143
6.5	Characterization.....	145
6.5.1	Electron microscopy.....	145
6.5.2	Atomic force microscopy.....	146
6.5.3	Dynamic light scattering.....	147
6.5.4	Small-angle X-ray scattering.....	148
6.5.5	Thermogravimetric analysis.....	148
6.5.6	X-ray diffraction.....	149
6.6	Results and discussion.....	149
6.6.1	Tungsten oxide nanoparticle structure.....	149
6.6.2	Oxidant co-addition effect.....	152
6.6.3	Reductant co-addition effect.....	154
6.6.4	Tungsten oxide nanoparticle yield calculation.....	155
6.6.5	Pyridine ligand exchange of oleylamine.....	157
6.6.6	Tungsten oxide nanoparticle synthesis mechanism.....	158
6.6.7	Molybdenum and vanadium oxide nanoparticle synthesis....	161
6.7	Summary and conclusions.....	163
6.8	References.....	163

Chapter 7. Propene metathesis of silica supported tungsten oxide nanoparticles

7.1	Introduction.....	169
7.1.1	Olefin metathesis in industry.....	169
7.1.2	Propene metathesis using WO_x/SiO_2	170
7.1.3	Metal-carbene/metallacycle mechanism.....	172
7.2	Experimental methods.....	173
7.2.1	Chemicals.....	173
7.2.2	Synthesis of supported tungsten oxide nanoparticles.....	174
7.3	Characterization.....	176
7.4	Catalytic studies.....	177
7.5	Results and discussion.....	178
7.5.1	Structure of silica supported tungsten oxide nanoparticles....	178
7.3.2	<i>In Situ</i> Raman spectroscopy.....	181
7.3.3	Electron microscopy.....	183
7.3.4	Propene metathesis activity.....	185
7.4	Summary and conclusions.....	187
7.5	References.....	187

Chapter 8. Summary and recommendations for future research

8.1	Thesis summary.....	191
8.2	Recommendations for future research.....	193
8.2.1	Support/Supported phase interaction.....	193
8.2.2	Ligand modification/removal.....	195
8.2.3	Metal oxide nanoparticle doping.....	197

8.2.4	Encapsulation using SiO ₂ microcapsules.....	199
8.2.5	Sulfidation of metal oxide nanoparticles.....	201
8.3	References.....	201
Appendix A. Selection of catalytic particle size for gas-phase reactions		202
Appendix B. <i>n</i>-Pentane isomerization turnover rate calculations		203
Appendix C. Methanol dehydration turnover rate calculations		205
Appendix D. Mass balance and olefin consumption during <i>n</i>-pentane isomerization		207

Table of Figures

Figure 1.1	Particle size effect on CO oxidation using titania supported Au NPs. a) Scanning tunneling microscopy (STM) image, b) CO oxidation activity and c) Cluster growth model.....	4
Figure 1.2	STM images of MoS ₂ nanoparticles on Au (111). a) low coverage (0.06 nm ² MoS ₂ /nm ² _{geometric}), b) high coverage (0.23 nm ² MoS ₂ /nm ² _{geometric}). Exchange current density versus c) MoS ₂ area coverage and d) MoS ₂ edge length.....	5
Figure 1.3	Surface tungsten oxide species identified by the Iglesia group. A) Bare support, b) isolated monomeric species (monotungstates), c) polymerized species (polytungstates) and d) bulk crystalline species (Bulk WO ₃ crystals).....	11
Figure 1.4	Iglesia proposed model of <i>in situ</i> Brønsted acid site formation via partial reduction of W ⁶⁺ Lewis acid centers in polytungstate domains and subsequent stabilization of delocalized H ^{δ+}	13
Figure 1.5	Schematic of 3-dimensional sub-nm distorted Zr-WO _x cluster.....	15
Figure 2.1	Powder XRD patterns of WZrOH and Zr _x (OH) _{4-2x} calcined at 973 K, and bulk WO ₃ . Crystalline phases marked as (▼) m-WO ₃ , (●) m-ZrO ₂ and (■) t-ZrO ₂	39
Figure 2.2	Powder XRD patterns of WZrO ₂ (773) and WZrOH(773). Crystalline phases marked as (▼) m-WO ₃ , (●) m-ZrO ₂ and (■) t-ZrO ₂	40
Figure 2.3	Representative (a) TEM BF image, (b, c) HRTEM images and (d) HAADF-STEM image of the supported 2.5-WZrOH (7.0, 973) catalyst. Blue circles: surface monotungstate species; Green circles: surface polytungstate species; Red circles: sub-nm Zr-WO _x clusters.....	42
Figure 2.4	Representative (a) TEM BF image, (b) HRTEM image and (c, d) HAADF-STEM images of the supported 5.2-WZrOH (18.5, 973) catalyst. Blue circles: surface monotungstate species; Green circles: surface polytungstate species; Red circles: sub-nm Zr-WO _x clusters.....	44
Figure 2.5	Representative (a) SEM BSE images of 5.2-WZrOH (18.5, 973) and (b) 8.5-WZrOH (30.0, 973). Hundred-nm size WO ₃ crystals are circled.....	45

Figure 2.6	Representative (a) TEM BF image, (b) HRTEM image and (c, d) HAADF-STEM images of the supported 8.5–WZrOH (30.0, 973) catalyst. Blue circles: surface monotungstate species; Green circles: surface polytungstate species; Red circles: sub-nm Zr-WO _x clusters.....	46
Figure 2.7	Representative (a) TEM BF image, (b) HRTEM image and (c, d) HAADF-STEM images of the supported 4.4–WZrOH (21.7, 773) catalyst. Blue circles: surface monotungstate species; Green circles: surface polytungstate species; Red circles: sub-nm Zr-WO _x clusters.....	48
Figure 2.8	Brønsted acid site strength as a function of ρ_{surf} expressed as sites per W atom for (a) WZrOH (973) and (b) WZrOH (773) and Lewis acid site strength as a function of ρ_{surf} for (c) WZrOH (973) and (d) WZrOH (773). Acid strength quantified as pyridine desorbed up to 523 K (weak), 523-723 K (moderate) and pyridine undesorbed above 723 K (strong) ranges.....	50
Figure 2.9	(a) Steady-state nC ₅ consumption turnover rates (<i>TOR</i>) and (b) steady-state nC ₅ isomerization turnover rates as a function of tungsten surface density. Sample series include (◆) WZrOH(973), (■) WZrOH(773), and (×) WZrO ₂ (773). Reaction conditions: 523 K, 1.04 atm, 1% nC ₅ in He. Overall nC ₅ conversion < 3%.....	54
Figure 2.10	Steady-state product distribution of (a) WZrOH(973) and (b) WZrOH(773). Reaction conditions: 523 K, 1.04 atm, 1% nC ₅ in He. Overall nC ₅ conversion < 3%.....	55
Figure 2.11	Brønsted and Lewis acid sites of varying acid strengths for 5.2–WZrOH (18.5, 973) (a) before and (b) after the running nC ₅ isomerization reaction for 10 h.....	58
Figure 2.12	(a) nC ₅ transient turnover rates (<i>TOR</i>), (b) transient isomerization turnover rates (<i>TOR</i> _{iC₅}) and product distributions for (c) 5.2–WZrOH (18.5, 973), (d) 2.5–WZrOH (7.0, 973) and (e) 11.0–WZrOH (32.4, 973). Reaction conditions: 523 K, 1.04 atm, 1% nC ₅ in He. Overall nC ₅ conversion < 3%.....	60
Figure 3.1	Specific surface area and W surface density as functions of (a) calcination temperature and WO ₃ weight content of iwiWZr and (b) synthesis method for stsWZr (50.7,T), iwiWZr (19.5,T), coWZr (18.3,T) and sgWZr (11.9,T). Calcination temperature for each sample series increases (from left to right) from 773 to 1173 K.....	80

Figure 3.2	Powder XRD patterns of iwiWZr series calcined at a) 773 K, b) 873 K, c) 973 K, d) 1073 K, e) 1173 K, f) coWZr (18.3, T), g) stsWZr (50.7, T) and h) sgWZr (11.9, T). Crystalline phases marked as (▼) m-WO ₃ , (●) m-ZrO ₂ and (■) t-ZrO ₂	82
Figure 3.3	Powder XRD patterns of iwiWZr (15.0, 973) with different Hf-doping loadings, (●) m-ZrO ₂ and (■) t-ZrO ₂	84
Figure 3.4	a) m-ZrO ₂ and b) t-ZrO ₂ crystallite diameters in iwiWZr materials as estimated by the Scherrer equation applied to the (101) and (111) reflections of t-ZrO ₂ and m-ZrO ₂ , respectively, as a function of ρ_{surf}	85
Figure 3.5	Raman spectra of dehydrated iwiWZr samples with ρ_{surf} (a) below 4.5 W/nm ² , (b) between 5.2 and 7.0 W/nm ² , and (c) above 7.1 W/nm ² . ν_{as} of W-O-W of crystalline WO ₃ (dark gray), ν_{as} of W-O-W and ν_s of W-O-Zr bonds of slightly distorted Zr-stabilized WO _x clusters (blue), ν_{as} of W-O-W and ν_s of W-O-Zr bonds of highly distorted Zr-stabilized WO _x clusters (gray), ν_s of the terminal W=O bond from square-pyramidal surface monotungstate and polytungstate WO ₅ species (red). Dehydrated Raman spectra of iwiWZr collected at 298 K.....	89
Figure 3.6	Raman spectra of dehydrated (a) coWZr, (b) sgWZr and (c) stsWZr samples. The color scheme is the same as that used in Figure 3.5....	90
Figure 3.7	(a) Steady-state nC ₅ isomerization and CH ₃ OH dehydration activity of iwiWZr (973). (a) Steady-state nC ₅ isomerization activity comparison between iwiWZr (973), commercial iwiWZr (973) and crystalline iwiWZrO ₂ (773). (c) Steady-state nC ₅ isomerization turnover rates and (d) steady-state CH ₃ OH dehydration activity as a function of tungsten surface density for iwiWZr	91
Figure 3.8	Hf loading effect on nC ₅ isomerization activity of 6.2-iwiWZr (15.0, 973).....	95
Figure 4.1	a) Carbenium ion formation via hydride abstraction of alkanes on Lewis acid sites and b) carbonium ion formation via protonation of alkanes on Brønsted acid sites.....	109
Figure 4.2	a) Transient consumption <i>TOR</i> , b) percentage of nC ₅ reacted during reaction in the absence and presence of different olefins and c) transient isomerization turnover rates (<i>TOR</i>) of 5.2-WZrOH (18.5, 973) in the presence of olefins (1-C ₅ ⁼ and C ₃ ⁼) at different concentrations. Reaction conditions: 523 K, 1.04 atm, feed-gas reference composition: 1% nC ₅ in He. Olefin added blends included the composition shown here. No-olefin data were reported by Soultanidies <i>et al.</i>	114

Figure 4.3	Transient product distribution profiles of 1% nC ₅ and a) no olefin, b) 0.01% 1-C ₅ ⁼ , c) 0.1% 1-C ₅ ⁼ , d) 0.5% 1-C ₅ ⁼ , e) 0.8% C ₃ ⁼ , in He. No-olefin selectivities were reported by Soultanidies <i>et al.</i>	116
Figure 4.4	Steady-state product distribution profiles of results presented in Figure 4.3.....	117
Figure 5.1	3-D ball and spoke structure of tungstophosphoric acid. 12 edge- and corner-sharing WO ₆ octahedra (green planes) and one central PO ₄ tetrahedron (PO ₄) consist the Keggin structure. (Orange atom: Phosphorus, Red atom: oxygen).....	125
Figure 5.2	Representative STEM-HAADF images of PWA/ZrO ₂ (14, 553) showing high concentration of monotungstate species on both a) amorphous and b) crystalline ZrO ₂	128
Figure 5.3	Representative STEM-HAADF images of PWA/Al ₂ O ₃ (14, 553) showing a) high concentration of polytungstate species and lower of 3-D WO _x clusters and b) higher concentration of monotungstate species.....	128
Figure 5.4	Representative STEM-HAADF images of PWA/SiO ₂ (14, 553) showing concentrations of WO _x clusters.....	129
Figure 5.5	Steady-state nC ₅ isomerization rates as a function of tungsten oxide loading. Sample series include PWA/SiO ₂ , PWA/Al ₂ O ₃ , PWA/ZrO ₂ , iwiWZr and commercial iwiWZr from Chapter 3. Reaction conditions: 523 K, 1.04 atm, 1% nC ₅ in He. Overall nC ₅ conversion was < 3% for all samples except the PWA/SiO ₂	130
Figure 5.6	Steady-state nC ₅ isomerization rates as a function of tungsten oxide loading of PWA/SiO ₂ and commercial iwiWZr from Chapter 3, before and after regeneration. Regeneration took place at 823 K under air flow. Reaction conditions: 523 K, 1.04 atm, 1% nC ₅ in He. Overall nC ₅ conversion was < 3% for all samples except the PWA/SiO ₂	131
Figure 5.7	Transient nC ₅ isomerization rates as a function of tungsten oxide loading of a) PWA/SiO ₂ series and b) 5.2-WZrOH (18.5, 973) from chapter 2, PWA/ZrO ₂ (26,553) and PWA/Al ₂ O ₃ (26,553). Reaction conditions: 523 K, 1.04 atm, 1% nC ₅ in He.....	132
Figure 5.8	Transient product distributions for a) PWA/SiO ₂ (14,553), b) PWA/SiO ₂ (26,553), c) PWA/SiO ₂ (44,553) and d) PWA/SiO ₂ (63,553). iC ₅ transient selectivity profile of PWA/SiO ₂ (26.553) and 5.2-WZrOH(18.5, 973) (from Chapter 2).....	133

Figure 6.1	WO _x NP synthesis scheme.....	144
Figure 6.2	a) Atomic force microscopy image of high ordered pyrolytic graphite (HOPG), b) profile lines along different HOPG planes and c) Height profile along different flat surfaces.....	147
Figure 6.3	a) TEM , b) HR-TEM and c,d) HAADF STEM and e) AFM images of WO _x NPs, f) particle height distribution of image e. Inset: Toluene suspension of WO _x NPs.....	151
Figure 6.4	a) Powder x-ray diffraction pattern and b) electron diffraction pattern of WO _x NPs	152
Figure 6.5	a,b) HAADF STEM of WO _x sNPs and c) AFM images of WO _x sNPs, d) particle height distribution of image c.....	154
Figure 6.6	a) TEM and b) HAADF STEM of WO _x NRs, c) XRD of WO _x NRs and d) Uv-vis absorption spectra of WO _x NRs, NPs and sNPs normalized to same NP concentration. Inset: Toluene suspension of WO _x NRs.....	155
Figure 6.7	TGA of WO _x sNPs, NPs, NRs, oleylamine and AMT. Ramp rate of 3.0 K/min under flowing air (100cc/min).....	156
Figure 6.8	TGA/DSC of pyridine exchanged WO _x NPs. Py-1 represents ligand exchange was completed in 1-day and Py-3 in 3 days.....	158
Figure 6.9	TGA/FTIR of AMT and oleylamine. Ramp rate of 2.0 K/min under flowing argon (50cc/min).....	160
Figure 6.10	Proposed reaction mechanism of the WO _x NPS. The reaction steps are a) dehydration of the AMT core ,b) dissociation of amine groups from the AMT core and formation, c) reduction of the AMT core by oleylamine and NH ₃ , d) association between oleylamine and decomposed WO _x to initiate nucleation and e) composition between at least 12 WO _x units for the synthesis of WO _x NPs.....	161
Figure 6.11	a,b) HAADF STEM of MoO _x NPs and c) AFM images of MoO _x sNPs, d) particle height distribution of image c.....	162
Figure 6.12	a) HAADF STEM of a single VO _x NP and b) self assembly of VO _x NPs.....	163
Figure 7.1	Phillips triolefin process, productive (produces two different molecules) metathesis of propene to ethane and 2-butene and non-productive metathesis (reverse reaction).....	170

Figure 7.2	Propene metathesis via metal carbene/ metallacycle mechanism, where M is a metal atom. The mechanism precedes via 4 steps (also known as 2+2 reactions), (1,3) the formation of the metal carbene and (2,4) the formation of a metallacycle intermediate.....	173
Figure 7.3	Synthesis scheme of SiO ₂ supported WO _x NPs. The four steps include (1) mixing of support with toluene suspension of WO _x NPs, (2) slow evaporation of toluene at 313 K, (3) drying of the WO _x /SiO ₂ gel at 353 K and (4) calcination at the desired temperature. Residual oleylamine is detected up to 773 K.....	175
Figure 7.4	TGA plots of NP-WO _x /SiO ₂ show the different concentration of organic content for different loadings.....	175
Figure 7.5	Powder XRD patterns of a) NP-WO _x /SiO ₂ and b) WO _x /SiO ₂	180
Figure 7.6	Temperature programmed reduction profiles of a) NP-WO _x /SiO ₂ and b) WO _x /SiO ₂	181
Figure 7.7	Raman spectra of dehydrated a) WO _x /SiO ₂ , b) NP WO _x /SiO ₂ and c) sNP WO _x /SiO ₂	182
Figure 7.8	Representative HAADF-STEM images of a,b) 1.1-WO _x /SiO ₂ (9, 873), c,d) NP 1.0-WO _x /SiO ₂ (9, 873) and e,f) sNP 1.1-WO _x /SiO ₂ (9, 873). Blue (small) circles: surface monotungstate species; Green circles (medium): surface polytungstate species; Yellow circles (large): distorted WO _x clusters; Purple circles (larger): WO ₃ crystals.....	184
Figure 7.9	a) Steady state propene <i>TOR</i> as function of as a function of tungsten surface density, b) metathesis selectivity expressed as the ratio $C_2^-:C_4^-$ and c) steady state metathesis <i>TOR</i> of Lehigh WO _x /SiO ₂ , WO _x /SiO ₂ (873), NP WO _x /SiO ₂ (873) and SNP WO _x /SiO ₂ (873).....	186
Figure 8.1	STEM-HAADF images of NP-WO _x /MgO (14, 873) shows high dispersion of monotungstates and polytungstates on the MgO surface.....	194
Figure 8.2	Representative STEM-HAADF images of NP-WO _x /ZrO ₂ (11.2, 773) shows high dispersion of monotungstates (blue circles) and polytungstates (green circles) on the ZrO ₂ surface.....	194
Figure 8.3	STEM-HAADF images of NP-WO _x /Al ₂ O ₃ (14, 873) shows high dispersion of a) sub-nm WO _x clusters and b) monotungstates and polytungstates on the Al ₂ O ₃ surface.....	195

Figure 8.4	Steady state turnover rates (<i>TOR</i>) as a function of tungsten surface density. Sample series include WZrOH(z,973), WZrO ₂ (z,773), NP-ZrOH(z,973), NP-ZrOH(z,773) and Py-ZrOH(11.2,973). Steady state turnover rates for the WZrOH materials (taken from Chapter 2, Section 2.4.4, Figure 2.9).....	197
Figure 8.5	Schematic of a) WO _x sub-nm species on ZrO ₂ surface that are not expected to be very active acidic sites and b) desired super active sub-nm Zr-WO _x clusters. The addition of Zr-atoms increases the acidic strength of the cluster.....	199
Figure 8.6	Schematic of two NP assembly of silica-polymer microcapsules. Results published by Kadali <i>et al.</i>	200
Figure D.1	Percentage of olefin reacting as a function of time.....	209

Table of Tables

Table 1.1	Applications of supported metal oxide catalysts.....	7
Table 2.1	Coke content of selected spent WZrOH determined by TGA.....	36
Table 2.2	BET surface area, pore volume, and calculated tungsten surface density values of various supported WO_x/ZrO_2 catalyst.....	38
Table 2.3	Brønsted and Lewis acidity of supported WO_x/ZrO_2 catalysts determined by pyridine FTIR.....	49
Table 3.1	Nitrogen physisorption results and calculated tungsten surface density values of WO_x/ZrO_2 samples.....	78
Table 3.2	WO_3 crystallite diameters (nm) estimated from (002) XRD reflection of m- WO_3 and listed with W surface density values.....	86
Table 3.3	Reaction rate and product selectivity results of WO_x/ZrO_2 material..	92
Table 6.1	Size, composition and NP yield of WO_x NPs, sNPs and NRs.....	157
Table 7.1	N_2 -physisorption results and tungsten surface density of WO_x/SiO_2 samples calcined at 873 K.....	179
Table A.1	Selection of particle size range for 6.0-WZrOH (21.7, 973).....	202
Table D.1	Carbon mass balance during 10 hr run for 1% nC_5 in He.....	208
Table D.2	Carbon mass balance during 10 hr run for 0.01% $1-C_5^=$, 1% nC_5	208
Table D.3	Carbon mass balance during 10 hr run for 0.1% $1-C_5^=$, 1% nC_5	208
Table D.4	Carbon mass balance during 10 hr run for 0.5% $1-C_5^=$, 1% nC_5	208
Table D.5	Carbon mass balance during 10 hr run for 0.8% $C_3^=$, 1% nC_5	209

Chapter 1

Background and research motivation

1.1 Nanoscience and nanotechnology

Nanoscience and nanotechnology are two emerging fields that deal with the synthesis, characterization, and application of nanomaterials (substances with their dimensions ≤ 100 nm (1 nm = 10^{-9} m) [1]). Nanoscience is the investigation of the elemental properties of nanomaterials that appear to vary significantly from their corresponding bulk structures [2-6]. Among the different properties investigated, optical enhancement, ferromagnetic, and catalytic properties are only a few that have intrigued the academic and industrial communities in pursuing aggressively advanced applications of nanomaterials. Nanotechnology focuses on the applied side of nanomaterial research and is one of the few modern scientific fields that attract epic business investments.

Automobile emissions, water remediation (such as removal of arsenic or other cancerogenic compounds), and petrochemical refineries (hydrodesulfurization, catalytic cracking of light naphtha, etc.) are areas that have been revolutionized by catalytic nanomaterials in the last two decades. Even though significant progress has been made to understand the properties of such materials, important fundamental questions concerning their unique activity remain unanswered. The goal of this thesis is to provide answers to these fundamental questions, in regards to supported metal oxide nanocatalysts by rigorously analyzing the structure and activity of several representative catalysts.

1.2 Nanotechnology and heterogeneous catalysis

Heterogeneous catalysis has been significantly improved by the introduction of nanotechnology in the last two decades [7-9]. By heterogeneous catalysis, we describe the reaction between chemical reactant(s) (usually in the gas or liquid phase) on a catalytic surface (usually a solid or liquid) that is in a different state than the reactant(s). These interfacial reactions were investigated for years with a focus on the physical and chemical properties of the catalysts such as oxidation state, reducibility of the catalyst etc.; however, in many cases such studies were unable to explain the catalytic behavior of most materials. In recent years, catalytic research advanced to the point of studying the molecular or even atomic structure on the catalytic surface, which contributed significantly to the fundamental knowledge. This approach has brought about an improved understanding of reaction mechanisms but more importantly it identified surface properties that led to the synthesis of improved heterogeneous catalysts for numerous applications. New experimental techniques aim to control the size, shape, and the surrounding environment of the active sites (defined as an atom or cluster of atoms that are catalytically active) on a nanometer level [7,10] which differs from previous techniques that focused only on maintaining certain macroscale characteristics.

Before proceeding with this thesis, a short presentation of the three most important examples in modern catalysis, which capture the essence of this new era of the field, are presented here.

The best example that demonstrates the enormous impact of nanotechnology on heterogeneous catalysis and the global catalysis and materials market is the synthesis of zeolites [11-13]. Zeolites are crystalline aluminosilicate (Si-O-Al) materials that have a

well-defined molecular structure. They exhibit strong Lewis acidity (defined as electron acceptor active site) and Brønsted acidity (defined as a proton donating active site), are nanoporous (pore diameters < 2 nm), and have extremely high surface areas, which makes them ideal for a great number of applications [14]. Catalytic cracking, isomerization, metathesis, alkylation, aromatization, and polymerization are only a few of the most important reactions catalyzed by zeolites which have significant industrial application.

Another important discovery in nanocatalysis is that Au NPs catalyze olefin hydrogenation [15] and oxidize CO [16] (Figure 1.1). Many new catalytic applications for these Au NPs were subsequently developed, making Au nanoparticles one of the most applied nanomaterials. The nanoscale size of these NPs is undoubtedly important, since Au is only active when it is in the form of nanoparticles (usually less than 50 nm) [17-25] for every application tested. The importance of the Au particle size in CO oxidation by titania supported Au can be seen in Figure 1.1. Maximum activity is seen for Au clusters of ~ 3 nm in the range 2-6 nm, which indicates the strong correlation between particle size and catalytic activity. The discovery of this unknown property of nanogold initiated “chain reactions” in the field of catalysis with more than 800 manuscripts studying the effect and properties of Au NPs published solely in 2003 [26].

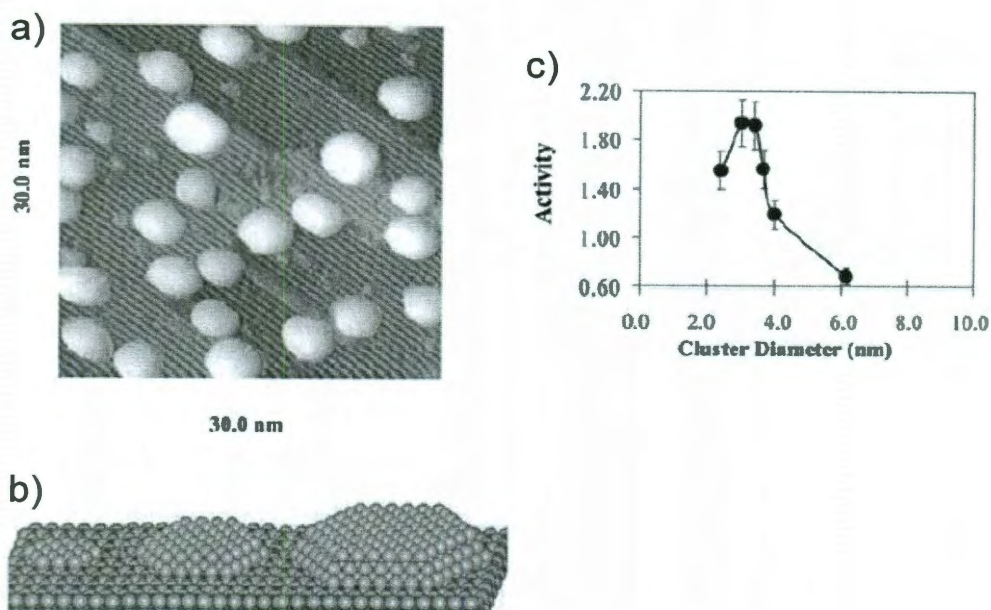


Figure 1.1. Particle size effect on CO oxidation using titania supported Au NPs. a) Scanning tunneling microscopy (STM) image, b) CO oxidation activity and c) Cluster growth model. Modified from [16]

Finally, the most important example that demonstrates the significance of studying the surface nanostructure is the identification of the active form of MoS₂ NPs [27]. Supported MoS₂ is an excellent hydrodesulfurization (HDS) catalyst that has been used in industry for decades [28,29]. Jaramillo *et al.* [27] discovered MoS₂ NPs are most active when they have a polygon-shape and their activity is proportional to the number of edge sites (Figure 1.2). As a result, a new approach for the synthesis of supported MoS₂ catalysts is applied today to form multifaceted particles that improve the overall efficiency and at the same time lower the cost of HDS catalysis.

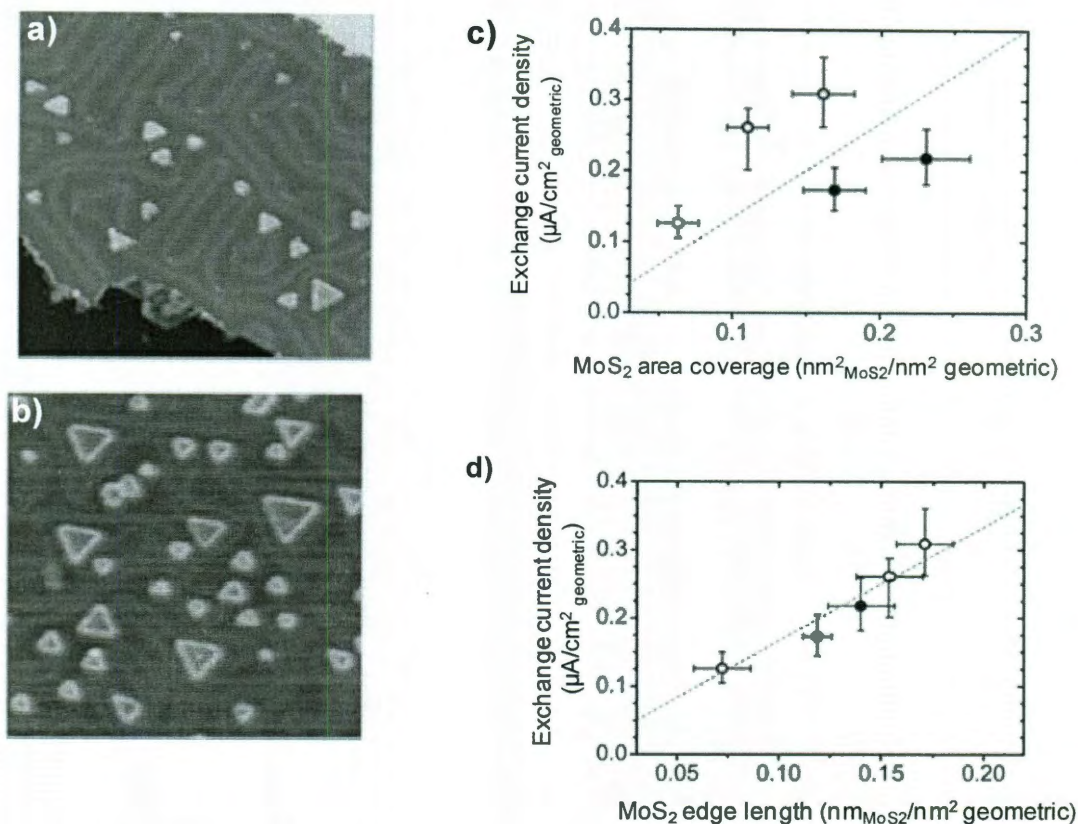


Figure 1.2. STM images of MoS₂ nanoparticles on Au (111). a) low coverage (0.06 nm² MoS₂/nm²_{geometric}), b) high coverage (0.23 nm² MoS₂/nm²_{geometric}). Exchange current density versus c) MoS₂ area coverage and d) MoS₂ edge length. Modified from [27].

From the different heterogeneous catalysts presented above, supported metal oxides (SMOs) comprise the most important class of catalytic materials. Understanding and controlling the size and shape of the supported metal oxide (MO_x) phase is a great challenge, since the size of the supported MO_x phase is usually in the nanometer or even sub-nanometer regime. This requires cutting-edge characterization and until recently such characterization was not available.

1.3 Conventional supported metal oxide catalysts

Conventional SMOs are extensively studied and used in academia and industry. Numerous methods have been developed to optimize properties such as: (1) dispersion of the active metal oxide phase (supported phase), (2) thermal stability of the catalyst, and (3) high surface area of the catalyst [30]. Incipient wetness impregnation (also known as dry impregnation), coprecipitation, sol-gel, deposition-precipitation, equilibrium absorption and chemical vapor deposition are well-established methods that have been employed for the synthesis of SMOs. Of these different techniques, dry impregnation is the most widespread method in both academia and industry due to its simplicity and hence low cost. Deposition-precipitation and coprecipitation methods are also used and in many cases are superior techniques, but the reproducibility of these techniques is questionable due to many more synthetic parameters (such as pH, type of precursor, solubility, extensive washes) that need to be taken into account using these methods. All the above synthesis techniques are used to make different SMOs for a range of applications summarized in table 1.1.

Many SMOs find application in environmental remediation technologies, such as (1) oxidation of harmful CO and other volatile organic compounds (VOCs) to CO₂ and (2) reduction of pollutants such as NO_x (NO₂, N₂O, NO) to N₂; and other SMOs find uses in important chemical production units such as (1) polymerization of ethylene to polyethylene and (2) catalytic cracking of naphtha to gasoline products.

Even though these technologies have been using conventional SMOs for decades, stringent environmental regulations and global competition raise the performance and purity requirements of SMOs. For this reason, the production of SMOs has evolved to

incorporate the techniques of nanotechnology and this new union gave “birth” to new synthetic approaches that attempt to resolve problems considered to be unsolvable by conventional synthetic methods.

Table 1.1. Applications of supported metal oxide catalysts [31]

Type of reaction	Example	Application
Oxidation ^a	CO and VOCs to CO ₂	Auto-catalytic converters
Reduction ^a	NO _x reduction to N ₂	Industrial emission control
Dehydrogenation ^a	Ethylbenzene to Styrene	Polystyrene synthesis
Oxidation ^a	Olefins to Maleic anhydride	Polyester resin synthesis
Polymerization ^a	Ethylene to Polyethylene	Polymer synthesis
Isomerization ^b	Paraffin isomerization	Fuel enrichment technology
Cracking ^b	Naphtha catalytic cracking	Gasoline synthesis
Oxidation ^b	Olefin to Acids & Aldehydes	Synthesis of chemicals
Dehydration ^b	Paraffin to olefin	Synthesis of chemicals
Dehydrogenation ^b	Alcohols to esters	Food additives
Metathesis ^b	Olefins to polymers	Polymer synthesis

^a classified as reduction-oxidation catalysis, ^b classified as acidic-basic catalysis

1.4 Heterogeneous catalysis using metal oxide nanoparticles

1.4.1 Metal oxide nanoparticles as support

Numerous MO_x have been used as supports for dispersing metal and metal oxide active phases, since increased surface coverage (metal atom/surface area) increases the number of available surface sites. Smaller clusters of metals or metal oxides of about 1 nm in diameter are required for achieving a complete 2-dimensional monatomic surface

coverage [32]; something that is almost impossible to achieve at higher loadings by conventional methods.

The use of MO_x NPs for the production of high surface area and thermostable supports has been investigated extensively. The general role of a metal oxide support is to: (1) provide high surface area and therefore improve the dispersion of the active sites, (2) maintain the structural and chemical integrity of the active sites at elevated temperatures, (3) participate directly or indirectly in the formation of the active sites, and (4) prevent catalytic poisoning of the active sites [32,33].

The most sophisticated approach for the synthesis of novel supports is called NP-surfactant templating synthesis (NPST) [34] and is derived from the traditional surfactant templating synthesis where molecular precursors are used to create well-defined structures [35-41]. In NPST the molecular precursors are replaced by MO_x NPs providing a solution to the previous difficulties of synthesizing similar structures [42-44]. By selecting the desired MO_x NP-precursor and the appropriate surfactant, a variety of MO_x mesoporous NP-supports can be synthesized with narrow and customized pore size distributions and exceptional thermomechanical stability.

1.4.2 Metal oxide nanoparticles as supported/active phase

When the supported phase is a metal oxide, high dispersion is theoretically achieved and complete surface coverage is defined as monolayer (ML) coverage. ML coverage is achieved at a specific number of metal atoms per nm^2 , which depends on both the supported phase and the support. By definition at ML coverage no crystalline species are expected and the surface is theoretically covered by polymeric MO_x species that are

considered to be the active sites. The deposition and activation of these species has been of great interest in previous years and limited improvements have been made towards successfully synthesizing samples that can adjust the size and properties of these species. This was, in most cases, of secondary importance since the only classes of species that were considered were monomers, oligomers, polymers, and crystals and the transition between those species was considered to occur almost linearly at a specific loading. The need for developing a method that controls the size of the supported MO_x phase was not an important task until recently when the complexity of the supported phase was discovered by studying tungstated zirconia (WO_x/ZrO_2) catalysts for methanol dehydration applications.

1.5 Tungstated zirconia

Tungstated zirconia (WO_x/ZrO_2) is a model solid acid catalyst that has been studied for over 20 years. The pioneers, Hino and Arata [45], discovered that WO_x/ZrO_2 is an active alkane isomerization catalyst at relatively low reaction temperatures, which is a characteristic of strong solid acid catalysts. Opposite to chlorinated platinum/alumina ($\text{Cl-Pt}/\text{Al}_2\text{O}_3$) [46-48] and sulfated zirconia (SO_4/ZrO_2) [49-62] that are susceptible to leaching (forming HCl and H_2S , respectively) [63], WO_x/ZrO_2 [58,64-70] catalysts are stable and can be regenerated easily. Massive interest in the catalytic properties of WO_x/ZrO_2 has been shown by manufacturing sectors that rushed to claim intellectual property [71-93] of this promising catalyst. Concomitantly academia [34,63,94-128] focused on identifying (1) the active species responsible for the catalytic activity and (2) the parameters that optimize the formation of these species.

Several distinguished groups have investigated the structure-activity correlations of WO_x/ZrO_2 for reactions such as methanol dehydration, 2-butanol dehydration, *o*-xylene isomerization, and *n*-pentane isomerization. Santiesteban and coworkers [101,114,119], Knözinger and coworkers [106,107,125], Iglesia and coworkers [104,111,115,126,129-132], and Wachs and coworkers [133-137], have all contributed significantly in identifying the structure and properties of the desired active sites.

A summary of the models developed by these groups that inspired the work presented in this thesis is presented here.

1.5.1 Iglesia and coworkers: polytungstate model

Iglesia and coworkers at the University of California-Berkeley have contributed significantly in characterizing the surface structure of dry-impregnated WO_x/ZrO_2 catalysts. Using numerous techniques such as X-ray absorption near-edge spectroscopy (XANES), UV-vis diffuse reflectance spectroscopy (DRS), and Raman spectroscopy [63,104,111,115,126,129-132], they identified the different tungsten oxide (WO_x) species that are schematically presented in Figure 1.3.

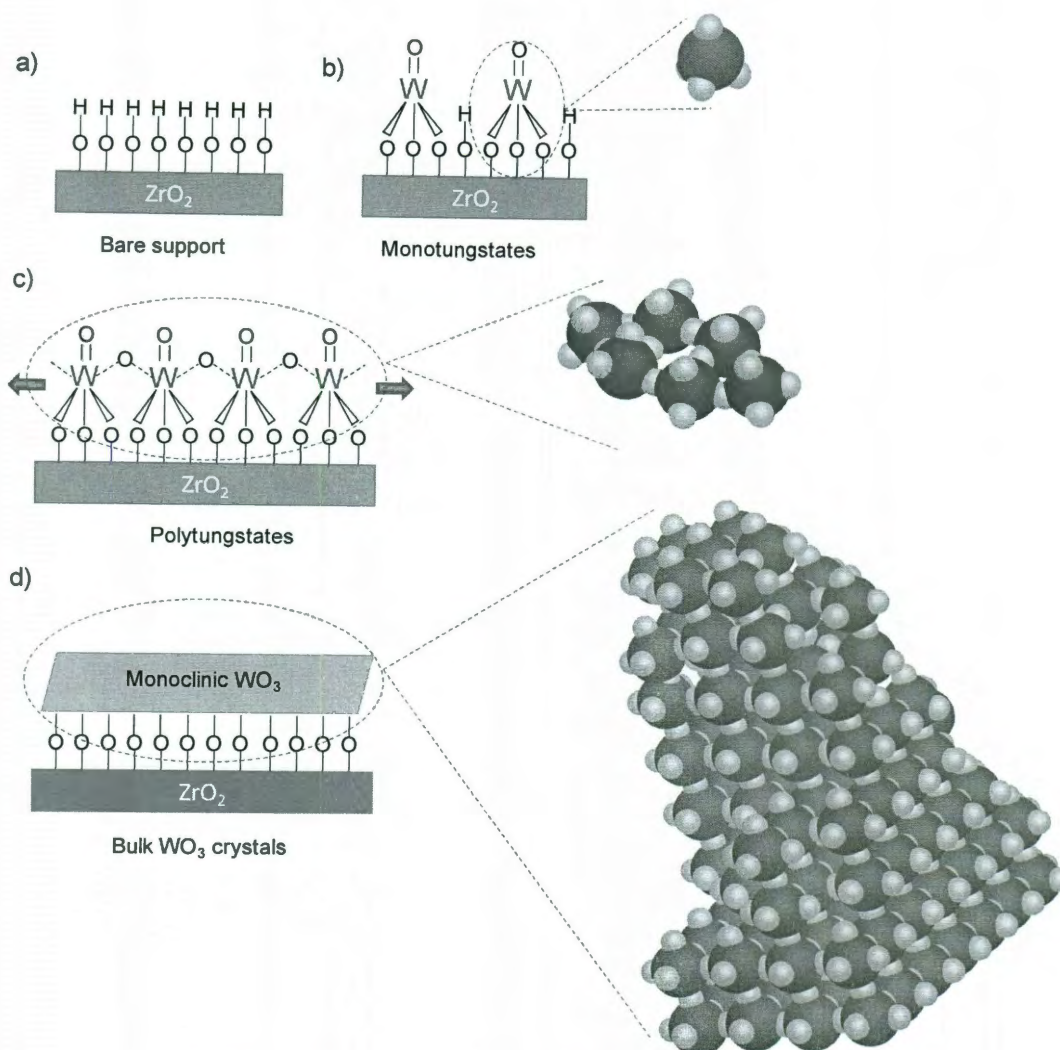


Figure 1.3. Surface tungsten oxide species identified by the Iglesia group [104,111,115,126,129-132]. A) Bare support, b) isolated monomeric species (monotungstates), c) polymerized species (polytungstates) and d) bulk crystalline species (Bulk WO₃ crystals).

The three different species identified by UV-vis DRS [111] were assigned to monotungstate species (Figure 1.3b) formed at high concentrations at surface densities (ρ_{surf}) less than 4 W atoms/nm², polytungstate species (Figure 1.3c) that have maximum concentration at 4-8 W atoms/nm², and WO₃ crystals (Figure 1.3d) that co-exist with polytungstates at >8 W atoms/nm².

The group proposed that polytungstates are the most active species after studying *o*-xylene isomerization [112] and 2-butanol dehydration [129], since maximum catalytic activity was observed at surface densities of $\sim 9.5 \text{ W/nm}^2$ and $\sim 7.5 \text{ W/nm}^2$ respectively. Irrespective of the calcination temperature the Iglesia group suggested that maximum activity is only a parameter of ρ_{surf} . Using *in situ* XANES it was shown that these polytungstate networks are octahedrally coordinated (WO_6) clusters [104]. It was proposed that polytungstates have the ability to delocalize protons (H^+) that are formed by (1) dissociation of H_2 or (2) as a dehydrogenation product by terminal C-H bonds of different reactants. The ability of these $(\text{W}^{6+}\text{O}_3)_n$ polytungstate species (Lewis sites) to partially reduce into $(\text{H}^+)(\text{W}^{6+})_{n-1}(\text{W}^{5+})\text{O}_{3n}$ [94] active Brønsted sites (Figure 1.4) defines the increased catalytic activity of these species over monotungstates and WO_3 crystals. It was suggested that an ideal size of the polytungstates ($\rho_{surf} \sim 7.0\text{-}10 \text{ W/nm}^2$) must exist, which promotes the proton stabilization mechanism and prevents its diffusion through the WO_x lattice to reduce the cluster ($\text{H}_y\text{WO}_{x-y}$). No further investigation or characterization was performed to support this argument. Moreover, the UV-vis DRS experiments suggested that H_2 did not reduce the WO_x surface at a $\rho_{surf} < 5 \text{ W/nm}^2$ and the role of Zr^{4+} atoms in the formation of these active polytungstates was not discussed.

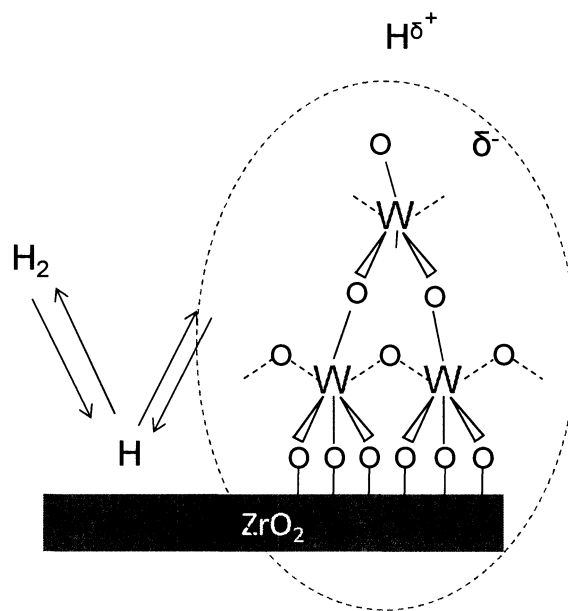


Figure 1.4. Iglesia proposed model of *in situ* Brønsted acid site formation via partial reduction of W⁶⁺ Lewis acid centers in polytungstate domains and subsequent stabilization of delocalized H^{δ+}. Modified from [63].

1.5.2 Knözinger and coworkers: Zr⁴⁺ heteropoly-tungstate model

Knözinger and coworkers at the University of Munich studied WO_x/ZrO₂ prepared by equilibrium adsorption [106,107,125] parallel to the Iglesia group. Using *in-situ* low temperature CO-FTIR spectroscopy, they identified that the active sites are 6-fold coordinated (WO₆) species with Brønsted acidity very similar to the Iglesia model. The group studied the *n*-pentane isomerization activity of WO_x/ZrO₂ and reported that catalysts with moderate metal loadings exhibited maximum catalytic activity. Even though they did not report ρ_{surf} values, using their published results, [138] it was estimated that their samples with $\rho_{surf} \sim 5 \text{ W/nm}^2$ exhibited maximum activity.

The major differences Knözinger and coworkers' work from the Iglesia model are that (1) they considered the role of Zr⁴⁺ in the formation of the active site (without proposing a specific mechanism); (2) they claimed that the partial reduction of the WO_x

polytungstates is not a requirement for the formation of Brønsted sites, (3) they reported that crystallization occurs at $\geq 5 \text{ W/nm}^2$ and (4) they reported that samples calcined at 923 K are more active than samples calcined at 1098 K, which suggests that calcination temperature has a secondary role in forming active sites, (5) they reported the presence of mono-oxo terminal W=O bonds at higher W loadings which suggested that monotungstates, polytungstates, and WO_3 bulk crystals may coexist.

1.5.3 Santiesteban and coworkers: Brønsted and Lewis acidity

Santiesteban and coworkers from Exxon Mobil focused on the chemical properties of WO_x/ZrO_2 prepared via impregnation and coprecipitation [65,70-74]. Using X-ray photoelectron spectroscopy (XPS) they performed a series of titration experiments using pyridine and the sterically-hindered 2,6-dimethylpyridine to identify the ratio between Lewis and Brønsted sites. The 1:1 ratio of strong Brønsted-to-Lewis acid sites was identified as the ideal combination for maximum *n*-pentane isomerization activity that was observed at ~16 wt% W (~20 wt% WO_3) [65]. No claim was made about the nature and properties of the active sites.

1.5.4 Wachs and coworkers: 3-D sub-nm Zr- WO_x clusters

Wachs and coworkers [133-137] from Lehigh University, Rice University, and the University of Virginia have investigated for the first time the actual surface structure and composition of all WO_x species. By using high-angle annular dark-field imaging in an aberration corrected scanning transmission electron microscopy (HAADF-STEM) and *in-situ* optical Raman spectroscopy, a new type of species was identified to be the

dominant species at moderate ρ_{surf} . Three-dimensional sub-nm distorted Zr-WO_x clusters (Zr-WO_x) (Figure 1.5) were for the first time identified as distinct species, different from 2-dimensional polymers (polytungstates).

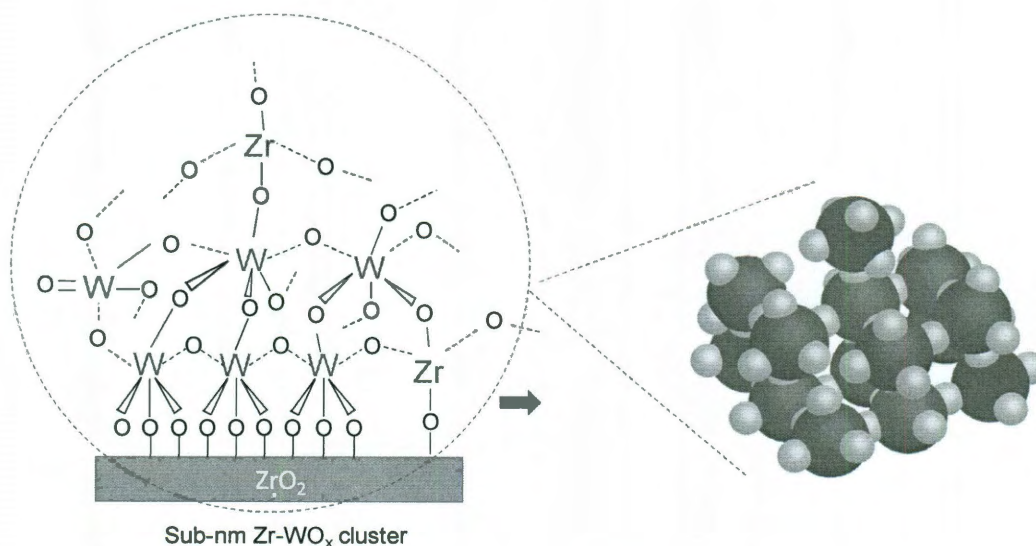


Figure 1.5. Schematic of 3-dimensional sub-nm distorted Zr-WO_x cluster.

The Wachs model identified that these distorted Zr-WO_x clusters are only formed via impregnation of a W-precursor into an amorphous ZrO₂ support followed by calcination [135] or by applying a post impregnation stage using both a W- and Zr-precursor [137]. For the first time it was demonstrated that below ML coverage all species coexist and above ML coverage the specie distribution shifts to larger aggregates, Zr-WO_x clusters, and eventually WO₃ bulk crystals. The incorporation of Zr- atoms within the WO_x cluster domain was directly seen by matching the atomic contrasts within a single cluster with simulated contrast profiles. By studying the methanol dehydration activity of WO_x/ZrO₂ it was noticed that maximum concentration of the Zr-WO_x clusters at $\rho_{surf} \sim 6.7 \text{ W/nm}^2$ corresponds to maximum catalytic activity.

The main differences from the Iglesia model are that this model (1) identifies the actual size and approximates the composition of the active site, (2) reports that maximum concentration of active sites is reached at $\rho_{surf} \sim 5-7 \text{ W/nm}^2$ (in close agreement with the Knözinger model) vs. $\rho_{surf} \sim 7-10 \text{ W/nm}^2$ that was proposed by Iglesia, (3) claims that WO_x species are not activated (reduced) by the presence of H_2 , which supports the Knözinger model and (4) shows for the first time that different species coexist at a wide range of ρ_{surf} .

Overall, the Wachs model could be considered as a more accurate model that completes the fundamental contributions of the previous models. Its major weaknesses derive (1) from using methanol dehydration as a probe reaction, a relatively weak acidic reaction and (2) from not being able to discriminate between the role of polytungstates and Zr- WO_x clusters, since at $\rho_{surf} \sim 5-7 \text{ W/nm}^2$ where the maximum activity is observed, both species coexist in significant quantities.

1.6 Research motivation

The overall goal of this thesis is to understand the formation of and control the surface species of SMOs, specifically WO_x/ZrO_2 , so that highly active catalysts may be synthesized. In the first part of this work, conventional synthesis techniques were investigated to establish an understanding of the limitations imposed by each method.

In the second part of this thesis, a new synthesis technique that successfully produces MO_x NPs such as WO_x is presented. The WO_x NPs were characterized, supported onto two different supports and were tested for their *n*-pentane isomerization

and propylene metathesis activity. An outline of what is presented in this thesis is given here.

In Chapter 2, WO_x/ZrO_2 was synthesized using amorphous and crystalline ZrO_2 . The *n*-pentane isomerization activity and selectivity as a function of tungsten surface density, catalyst support type, and calcination temperature was reported for each catalyst, providing structure-activity correlations that were not reported before. The results of this work were published as Soultanidis N., Zhou W., Psarras A.C., Gonzalez A.J., Iliopoulou E.F., Kiely C.J., Wachs I.E., and Wong M.S. "Relating *n*-Pentane Isomerization Activity to the Tungsten Surface Density of WO_x/ZrO_2 ". *J. Am. Chem. Soc.* 2010, 132, 13462-13471 [67].

In Chapter 3, four types of WO_x/ZrO_2 catalysts were synthesized (via incipient wetness impregnation, coprecipitation, sol-gel, and a surfactant templating synthesis) and extensively characterized after calcination through *in situ* Raman spectroscopy and x-ray diffraction. The ideal synthesis technique and parameters were identified for maximizing the concentrations of active Zr- WO_x clusters. This chapter is an extension of the work by Dr. Knowles' PhD thesis titled "New Insights Into Supported Metal Oxides for Heterogeneous Catalysis".

In Chapter 4, *n*-pentane isomerization in the presence of different olefins was investigated using WO_x/ZrO_2 . This study was performed to identify the conditions that promote the *n*-pentane bimolecular isomerization mechanism.

In Chapter 5, supported phosphotungstic acid (PWA) catalysts were investigated for their *n*-pentane isomerization activity. The effect of the support in the overall activity and the regeneration ability of WO_x/ZrO_2 vs. supported PWA are presented.

In Chapter 6, the solvothermal synthesis of ultra-small WO_x NPs is introduced. The method was optimized to produce high yields of NPs and the size of the particles was adjusted by controlling the nucleation-growth mechanism. This method was successfully applied for the synthesis of other metal oxides, namely molybdenum oxide and vanadium oxide. Results from this study were published in a provisional patent that is currently pending (Patent title: Synthesis of ultrasmall metal oxide nanoparticles).

In Chapter 7, the reactivity of ultrasmall WO_x NPs supported on silica support is compared with conventional and WO_x/SiO_2 . SiO_2 supported WO_x NPs were found to be 3 times more active than conventional WO_x/SiO_2 . Finally in chapter 8, a summary of the work presented in this thesis and future recommendations are discussed.

1.7 References

1. N. N. Initiative. 2006. <http://www.nano.gov>. National Science and Technology Council. National Nanotechnology Initiative.
2. R. Birringer and H. Gleiter, in: R. W. Cahn, (Ed.), Encyclopedia of Material Science and Engineering, Pergamon Press, Oxford. 339-349.
3. H. Gleiter, Progress in Materials Science 33 (1989) 223-315.
4. A. P. Alivisatos, Science 271 (1996) 933-937.
5. R. Kubo, A. Kawabata and S. Kobayashi, Annu. Rev. Mater. Sci. 14 (1984) 49-66.
6. J. Perenboom, P. Wyder and F. Meier, Phys. Rep.-Rev. Sec. Phys. Lett. 78 (1981) 173-292.
7. H. H. Kung and M. C. Kung, Catalysis Today 97 (2004) 219-224.

8. H. H. Kung and M. C. Kung, *Applied Catalysis A: General* 246 (2003) 193-196.
9. G. A. Somorjai and Y. G. Borodko, *Catalysis Letters* 76 (2001) 1.
10. T. Mizuki and I. Yasuhiro, *ChemInform* 37 (2006).
11. J. A. Rabo, P. E. Pickert, D. N. Stamiros and J. E. Boyle, *Actes Du Deuxieme Congr. Int. Catal.* 2 (1961) 2055-2074.
12. J. A. Rabo and M. W. Schoonover, *Applied Catalysis a-General* 222 (2001) 261-275.
13. J. A. Rabo, P. E. Pickert and J. E. Boyle. 1964. Decationized molecular sieve compositions. In Patent Office. Union Carbide Corporation, U.S.
14. H. F. Rase, *Handbook of commercial catalysts: heterogeneous catalysts*. CRC Press, Boca Raton, 2000.
15. G. C. Bond, P. A. Sermon, G. Webb, D. A. Buchanan and P. B. Wells, *J. Chem. Soc. Chem. Commun.* (1973) 444-445.
16. A. T. Bell, *Science* 299 (2003) 1688-1691.
17. M. Haruta, *Nature* 437 (2005) 1098-1099.
18. G. J. Hutchings, *Catalysis Today* 100 (2005) 55-61.
19. T. Hayashi, K. Tanaka and M. Haruta, *Journal of Catalysis* 178 (1998) 566-575.
20. L. Prati and M. Rossi, *Journal of Catalysis* 176 (1998) 552-560.
21. S. Carrettin, P. McMorn, P. Johnston, K. Griffin and G. J. Hutchings, *Chem. Commun.* (2002) 696-698.
22. S. Carrettin, P. McMorn, P. Johnston, K. Griffin, C. J. Kiely and G. J. Hutchings, *Phys. Chem. Chem. Phys.* 5 (2003).

23. D. Andreeva, V. Idakiev, T. Tabakova and A. Andreev, *Journal of Catalysis* 158 (1996) 354-355.
24. F. Boccuzzi, A. Chiorino, M. Manzoli, D. Andreeva and T. Tabakova, *Journal of Catalysis* 188 (1999) 176-185.
25. F. Boccuzzi, A. Chiorino, M. Manzoli, D. Andreeva, T. Tabakova, L. Ilieva and V. Iadakiev, *Catalysis Today* 75 (2002) 169-175.
26. A. S. K. Hashmi and J. H. Graham, *Angewandte Chemie International Edition* 45 (2006) 7896-7936.
27. T. F. Jaramillo, K. P. Jorgensen, J. Bonde, J. H. Nielsen, S. Horch and I. Chorkendorff, *Science* 317 (2007) 100-102.
28. H. Topsøe, B. S. Clausen and F. E. Massoth, *Catalysis Science and Technology*. Springer-Verlag, New York, 1996.
29. R. R. Chianelli, M. H. Siadati, M. P. De la Rosa, G. Berhault, J. P. Wilcoxon, R. Bearden and B. L. Abrams, *Catalysis Reviews: Science and Engineering* 48 (2006) 1 - 41.
30. W. V. Knowles, M. O. Nutt and M. S. Wong, *Supported Metal Oxides and Surface Density Metric*. Taylor and Francis: Boca Raton, 2006.
31. H. G. Lintz, *Berichte der Bunsengesellschaft für physikalische Chemie* 94 (1990) 895-895.
32. J. R. Regalbuto, *Catalyst Preparation: Science and Engineering*. Taylor and Francis Group, LLC, 2007.
33. W. Peukert, H.-C. Schwarzer, M. Götzinger, L. Günther and F. Stenger, *Advanced Powder Technology* 14 (2003) 411-426.
34. M. S. Wong, in: J. L. G. Fierro, (Ed.), *Metal oxides: Chemistry and applications*, Taylor & Francis Group, LLC, Boca Raton. 31-54.

35. J. S. Beck, J. C. Vartuli, G. J. Kennedy, C. T. Kresge, W. J. Roth and S. E. Schramm, *Chem. Mat.* 6 (1994) 1816-1821.
36. J. S. Beck, J. C. Vartuli, W. J. Roth, M. E. Leonowicz, C. T. Kresge, K. D. Schmitt, C. T.-W. Chu, D. H. Olson, E. W. Sheppard, S. B. McCullen, J. B. Higgins and J. L. Schlenker, *J. Am. Chem. Soc.* 114 (1992) 10834-10843.
37. C. T. Kresge, M. E. Leonowicz, W. J. Roth and J. C. Vartuli. 1990. Synthetic mesoporous crystalline material. Mobil Oil Corp., U.S.
38. C. T. Kresge, M. E. Leonowicz, W. J. Roth, J. C. Vartuli and J. S. Beck, *Nature* 359 (1992) 710-712.
39. J. C. Vartuli, C. T. Kresge, M. E. Leonowicz, A. S. Chu, S. B. McCullen, I. D. Johnson and E. W. Sheppard, *Chem. Mat.* 6 (1994) 2070-2077.
40. J. C. Vartuli, K. D. Schmitt, C. T. Kresge, W. J. Roth, M. E. Leonowicz, S. B. McCullen, S. D. Hellring, J. S. Beck, J. L. Schlenker, D. H. Olson and E. W. Sheppard, *Chem. Mat.* 6 (1994) 2317-2326.
41. S. Inagaki, Y. Fukushima and K. Kuroda, *J. Chem. Soc.-Chem. Commun.* (1993) 680-682.
42. A. Sayari and P. Liu, *Microporous Materials* 12 (1997) 149-177.
43. F. Schüth, *Chemistry of Materials* 13 (2001) 3184-3195.
44. J. Y. Ying, C. P. Mehnert and M. S. Wong, *Angewandte Chemie-International Edition* 38 (1999) 56-77.
45. M. Hino and K. Arata, *Journal of the Chemical Society-Chemical Communications* (1988) 1259-1260.
46. P. G. Menon, R. P. De Pauw and G. F. Froment, *Industrial & Engineering Chemistry Product Research and Development* 18 (1979) 110-116.
47. B. Ducourty, G. Szabo, J. P. Dath, J. P. Gilson, J. M. Goupil and D. Cornet, *Applied Catalysis A: General* 269 (2004) 203-214.

48. R. Zhang, X. Meng, Z. Liu, J. Meng and C. Xu, *Industrial & Engineering Chemistry Research* 47 (2008) 8205-8210.
49. V. Adeeva, H.-Y. Liu, B.-Q. Xu and W. Sachtler, *Topics in Catalysis* 6 (1998) 61-76.
50. K. B. Fogash, Z. Hong, J. M. Kobe and J. A. Dumesic, *Applied Catalysis A: General* 172 (1998) 107-116.
51. M. A. Coelho, W. E. Alvarez, E. C. Sikabwe, R. L. White and D. E. Resasco, *Catalysis Today* 28 (1996) 415-429.
52. N. Lohitharn, J. G. Goodwin Jr and E. Lotero, *Journal of Catalysis* 234 (2005) 199-205.
53. M. V. Luzgin, S. S. Arzumanov, V. P. Shmachkova, N. S. Kotsarenko, V. A. Rogov and A. G. Stepanov, *J. Catal.* 220 (2003) 233-239.
54. S. Hammache and J. G. Goodwin, *Journal of Catalysis* 218 (2003) 258-266.
55. M. Pérez-Luna, A. Cosultchi, J. Toledo-Antonio and M. Cortés-Jácome, *Catalysis Letters* 131 (2009) 285-293.
56. H. Matsushashi, H. Shibata, H. Nakamura and K. Arata, *Applied Catalysis A: General* 187 (1999) 99-106.
57. C. Y. Hsu, C. R. Heimbuch, C. T. Armes and B. C. Gates, *Journal of the Chemical Society, Chemical Communications* (1992) 1645-1646.
58. E. Iglesia, D. G. Barton, S. L. Soled, S. Miseo, J. E. Baumgartner, W. E. Gates, G. A. Fuentes, G. D. Meitzner, W. N. D. E. I. Joe W. Hightower and T. B. Alexis, *Studies in Surface Science and Catalysis*, Elsevier. 533-542.
59. B. Li and R. D. Gonzalez, *Applied Catalysis A: General* 174 (1998) 109-119.
60. R. Ahmad, J. Melsheimer, F. C. Jentoft and R. Schlögl, *Journal of Catalysis* 218 (2003) 365-374.

61. V. Adeeva, G. D. Lei and W. M. H. Sachtler, *Applied Catalysis A: General* 118 (1994) L11-L15.
62. F. Garin, L. Seyfried, P. Girard, G. Maire, A. Abdulsamad and J. Sommer, *Journal of Catalysis* 151 (1995) 26-32.
63. C. D. Baertsch, S. L. Soled and E. Iglesia, *Journal of Physical Chemistry B* 105 (2001) 1320-1330.
64. M. Scheithauer, T. K. Cheung, R. E. Jentoft, R. K. Grasselli, B. C. Gates and H. Knözinger, *Journal of Catalysis* 180 (1998) 1-13.
65. M. Scheithauer, R. E. Jentoft, B. C. Gates and H. Knözinger, *Journal of Catalysis* 191 (2000) 271-274.
66. J. G. Santiesteban, J. C. Vartuli, S. Han, R. D. Bastian and C. D. Chang, *Journal of Catalysis* 168 (1997) 431-441.
67. N. Soultanidis, W. Zhou, A. C. Psarras, A. J. Gonzalez, E. F. Iliopoulou, C. J. Kiely, I. E. Wachs and M. S. Wong, *Journal of the American Chemical Society* 132 13462-13471.
68. N. Essayem, Y. Ben Taârit, C. Feche, P. Y. Gayraud, G. Sapaly and C. Naccache, *Journal of Catalysis* 219 (2003) 97-106.
69. B.-Q. Xu and W. M. H. Sachtler, *Journal of Catalysis* 167 (1997) 224-233.
70. S. Kuba, P. Lukinskas, R. Ahmad, F. C. Jentoft, R. K. Grasselli, B. C. Gates and H. Knözinger, *Journal of Catalysis* 219 (2003) 376-388.
71. C. D. Chang, R. D. Bastian, S. Han and J. G. Santiesteban. 1995. U.S. Patent No. 5,382,731.
72. C. D. Chang, S. Han, J. D. Lutner and J. G. Santiesteban. 1995. U.S. Patent No. 5,449,847.
73. C. D. Chang, S. Han, J. G. Santiesteban, M. M. Wu and Y. Xiong. 1995. U.S. Patent No. 5,453,556.

74. C. D. Chang, J. G. Santiesteban, D. S. Shihabi and S. A. Stevenson. 1995. U.S. Patent No. 5,401,478.
75. C. D. Chang, J. C. Cheng, S. Han, J. G. Santiesteban and D. E. Walsh. 1996. U.S. Patent No. 5,563,311.
76. C. D. Chang, F. T. DiGuseppi and S. Han. 1996. U.S. Patent No. 5,563,310.
77. C. D. Chang, S. Han, D. J. Martenak, J. G. Santiesteban and D. E. Walsh. 1996. U.S. Patent No. 5,543,036.
78. C. D. Chang, S. Han, J. G. Santiesteban, M. M. Wu and Y. Xiong. 1996. U.S. Patent No. 5,516,954.
79. C. D. Chang, C. T. Kresge, J. G. Santiesteban and J. C. Vartuli. 1996. U.S. Patent No. 5,510,309.
80. C. D. Chang, J. G. Santiesteban, D. S. Shihabi, D. L. Stern and J. C. Vartuli. 1996. U.S. Patent No. 5,552,128.
81. C. D. Chang, T. J. Huang, J. G. Santiesteban and J. C. Vartuli. 1997. U.S. Patent No. 5,608,133.
82. C. D. Chang, F. T. DiGuseppi, S. Han, J. G. Santiesteban and D. L. Stern. 1998. U.S. Patent No. 5,854,170.
83. C. D. Chang, F. T. DiGuseppi and J. G. Santiesteban. 1998. U.S. Patent No. 5,780,382.
84. C. D. Chang, S. D. Hellring, D. O. Marler, J. G. Santiesteban and J. C. Vartuli. 1998. U.S. Patent No. 5,780,703.
85. C. D. Chang, J. G. Santiesteban and D. L. Stern. 1998. U.S. Patent No. 5,719,097.
86. C. D. Chang, S. Han, R. A. Morrison and J. G. Santiesteban. 1999. U.S. Patent No. 5,993,643.

87. C. D. Chang, J. G. Santiesteban and D. L. Stern. 2000. U.S. Patent No. 6,080,904.
88. K. Murata, T. Hayakawa and S. Hamakawa. 2000. U.S. Patent No. 6,071,849.
89. C. D. Chang, S. Han, D. J. Martenak, J. G. Santiesteban and D. E. Walsh. 2001. U.S.
90. R. D. Gillespie. 2004. U.S. Patent No. 6,818,589 B1.
91. J. Y. Ying and J. Xu. 2004. U.S. Patent No. 6,767,859 B2.
92. R. D. Gillespie. 2005. U.S. Patent No. 6,977,322 B2.
93. Y.-N. Kim. 2005. U.S. Patent No. 6,855,661 B2.
94. E. Iglesia, D. G. Barton, S. L. Soled, S. Miseo, J. E. Baumgartner, W. E. Gates, G. A. Fuentes and G. D. Meitzner, *Studies in Surface Science and Catalysis* 101 (1996) 533-542.
95. D. S. Kim, M. Ostromecki and I. E. Wachs, *Journal of Molecular Catalysis a-Chemical* 106 (1996) 93-102.
96. G. Larsen, S. Raghavan, M. Marquez and E. Lotero, *Catalysis Letters* 37 (1996) 57-62.
97. B. Zhao, X. Xu, J. Gao, Q. Fu and Y. Tang, *Journal of Raman Spectroscopy* 27 (1996) 549-554.
98. R. A. Boyse and E. I. Ko, *Journal of Catalysis* 171 (1997) 191-207.
99. D. Gazzoli, M. Valigi, R. Dragone, A. Marucci and G. Mattei, *Journal of Physical Chemistry B* 101 (1997) 11129-11135.
100. G. Larsen, E. Lotero, L. M. Petkovic and D. S. Shobe, *Journal of Catalysis* 169 (1997) 67-75.

101. J. G. Santiesteban, J. C. Vartuli, S. Han, R. D. Bastian and C. D. Chang, *Journal of Catalysis* 168 (1997) 431-441.
102. S. R. Vaudagna, R. A. Comelli and N. S. Figoli, *Applied Catalysis a-General* 164 (1997) 265-280.
103. J. C. Yori, C. R. Vera and J. M. Parera, *Applied Catalysis a-General* 163 (1997) 165-175.
104. D. G. Barton, S. L. Soled and E. Iglesia, *Topics in Catalysis* 6 (1998) 87-99.
105. L. M. Petkovic, J. R. Bielenberg and G. Larsen, *Journal of Catalysis* 178 (1998) 533-539.
106. M. Scheithauer, T. K. Cheung, R. E. Jentoft, R. K. Grasselli, B. C. Gates and H. Knozinger, *Journal of Catalysis* 180 (1998) 1-13.
107. M. Scheithauer, R. K. Grasselli and H. Knozinger, *Langmuir* 14 (1998) 3019-3029.
108. J. R. Sohn and M. Y. Park, *Langmuir* 14 (1998) 6140-6145.
109. J. R. Sohn and M. Y. Park, *Journal of Industrial and Engineering Chemistry* 4 (1998) 84-93.
110. N. Vaidyanathan, M. Houalla and D. M. Hercules, *Surface and Interface Analysis* 26 (1998) 415-419.
111. D. G. Barton, M. Shtein, R. D. Wilson, S. L. Soled and E. Iglesia, *Journal of Physical Chemistry B* 103 (1999) 630-640.
112. D. G. Barton, S. L. Soled, G. D. Meitzner, G. A. Fuentes and E. Iglesia, *Journal of Catalysis* 181 (1999) 57-72.
113. N. Naito, N. Katada and M. Niwa, *Journal of Physical Chemistry B* 103 (1999) 7206-7213.

114. J. C. Vartuli, J. G. Santiesteban, P. Traverso, N. Cardona-Martinez, C. D. Chang and S. A. Stevenson, *Journal of Catalysis* 187 (1999) 131-138.
115. C. D. Baertsch, R. D. Wilson, D. G. Barton, S. L. Soled and E. Iglesia, *Studies in Surface Science and Catalysis* 130D (2000) 3225-3230.
116. R. D. Wilson, D. G. Barton, C. D. Baertsch and E. Iglesia, *Journal of Catalysis* 194 (2000) 175-187.
117. G. S. Wong, D. D. Kragten and J. M. Vohs, *Journal of Physical Chemistry B* 105 (2001) 1366-1373.
118. C. D. Baertsch, K. T. Komala, Y. H. Chua and E. Iglesia, *Journal of Catalysis* 205 (2002) 44-57.
119. D. C. Calabro, J. C. Vartuli and J. G. Santiesteban, *Topics in Catalysis* 18 (2002) 231-242.
120. S. De Rossi, G. Ferraris, M. Valigi and D. Gazzoli, *Applied Catalysis a-General* 231 (2002) 173-184.
121. N. Vaidyanathan, D. M. Hercules and M. Houalla, *Analytical and Bioanalytical Chemistry* 373 (2002) 547-554.
122. M. Valigi, D. Gazzoli, I. Pettiti, G. Mattei, S. Colonna, S. De Rossi and G. Ferraris, *Applied Catalysis a-General* 231 (2002) 159-172.
123. G. Ferraris, S. De Rossi, D. Gazzoli, I. Pettiti, M. Valigi, G. Magnacca and C. Morterra, *Applied Catalysis A-General* 240 (2003) 119-128.
124. S. Kuba, P. Lukinskas, R. Ahmad, F. C. Jentoft, R. K. Grasselli, B. C. Gates and H. Knozinger, *Journal of Catalysis* 219 (2003) 376-388.
125. S. Kuba, P. Lukinskas, R. K. Grasselli, B. C. Gates and H. Knozinger, *Journal of Catalysis* 216 (2003) 353-361.
126. J. Macht, C. D. Baertsch, M. May-Lozano, S. L. Soled, Y. Wang and E. Iglesia, *Journal of Catalysis* 227 (2004) 479-491.

127. V. M. Benitez, J. C. Yori, C. R. Vera, C. L. Pieck, J. M. Grau and J. M. Parera, *Industrial & Engineering Chemistry Research* 44 (2005) 1716-1721.
128. I. E. Wachs, J. M. Jehng and W. Ueda, *Journal of Physical Chemistry B* 109 (2005) 2275-2284.
129. C. D. Baertsch, K. T. Komala, Y.-H. Chua and E. Iglesia, *Journal of Catalysis* 205 (2002) 44-57.
130. C. D. Baertsch, S. L. Soled and E. Iglesia, *The Journal of Physical Chemistry B* 105 (2001) 1320-1330.
131. A. Barron. 2009. Oxide Nanoparticles. In *Connexions Web*
132. J. Macht and E. Iglesia, *Phys. Chem. Chem. Phys.* 10 (2008) 5331-5343.
133. I. E. Wachs, T. Kim and E. I. Ross, *Catalysis Today* 116 (2006) 162-168.
134. T. Kim, A. Burrows, C. J. Kiely and I. E. Wachs, *Journal of Catalysis* 246 (2007) 370-381.
135. E. I. Ross-Medgaarden, W. V. Knowles, T. Kim, M. S. Wong, W. Zhou, C. J. Kiely and I. E. Wachs, *Journal of Catalysis* 256 (2008) 108-125.
136. E. I. Ross-Medgaarden and I. E. Wachs, *The Journal of Physical Chemistry C* 111 (2007) 15089-15099.
137. W. Zhou, E. I. Ross-Medgaarden, W. V. Knowles, M. S. Wong, I. E. Wachs and C. J. Kiely, *Nat Chem* 1 (2009) 722-728.
138. M. Scheithauer, R. K. Grasselli and H. Knozinger, *Langmuir* 14 (1998) 3019-3029.

Chapter 2

Relating *n*-pentane isomerization activity to the tungsten surface density of WO_x/ZrO₂

2.1 Introduction

Supported metal oxide catalysts comprise an important class of industrial catalytic materials, with tungstated zirconia (WO_x/ZrO₂) representing an important model for an acid catalytic material [1-5]. It is strongly acidic and structurally more stable than sulfated zirconia and chlorided Pt/Al₂O₃, which can release H₂S and HCl during reaction and regeneration conditions [5-7].

Structure-activity correlations for WO_x/ZrO₂ have been studied actively by several research groups. Santiesteban and coworkers attributed the balance between *in situ* strong Brønsted and Lewis sites to the high *n*-pentane isomerization activity observed at intermediate tungsten oxide loadings [8-10]. Knözinger and coworkers proposed that Zr⁴⁺-exposed WO_x polytungstates generated strong Brønsted acidity for structures similar to that of heteropolyacids [11-13]. *o*-xylene isomerization and 2-butanol dehydration activity was investigated by Iglesia and coworkers, who proposed that the slight reduction of surface polytungstate species formed *in situ* Brønsted acid sites, of which maximum activity was found at ~7-8 W/nm² [5,14-18]. Most recently, Ross-Medgaarden *et al.* proposed a model in which maximum methanol dehydration activity observed at surface densities between of 6-7 W/nm² was attributed to high concentrations of 0.8-1.0 nm Zr-containing WO_x 3-dimensional ("Zr-WO_x") clusters [4], which was later confirmed by Zhou *et al.* via direct imaging of all the surface WO_x species using aberration-corrected STEM high-angle annular dark-field (HAADF) imaging [19]. The surface acid sites active for this reaction are presumably weaker than those required for

more acid-demanding reactions like alkane isomerization and cracking [20,21]. However, systematic investigation of WO_x/ZrO_2 catalysts for *n*-pentane isomerization, a more acid-demanding reaction, as a function of WO_x surface density has not been reported before.

In this work (published as Soultanidis N., Zhou W., Psarras A.C., Gonzalez A.J., Iliopoulou E.F., Kiely C.J., Wachs I.E., Wong M.S. “Relating *n*-Pentane Isomerization Activity to the Tungsten Surface Density of WO_x/ZrO_2 ”. *J. Am. Chem. Soc.* 2010, 132, 13462-13471 [22]), we report the catalytic properties as a function of tungsten surface density and deduce the structure-activity relationship in supported WO_x/ZrO_2 solid acid catalysts for *n*-pentane isomerization. Amorphous and crystalline zirconia materials were used as support to prepare the WO_x/ZrO_2 catalysts through incipient wetness impregnation, which allowed us to investigate the effect of the support material on the nature of the active sites. The atomic structure of various surface WO_x species was characterized by aberration-corrected STEM-HAADF imaging. We assessed surface acidity through pyridine adsorption FTIR studies. The purpose of this chapter is to test the *n*-pentane isomerization activity of the Zr- WO_x clusters formed on WO_x/ZrO_2 , and to identify the conditions that maximize the concentration of these species.

2.2 Experimental methods

2.2.1 Chemicals

Ammonium metatungstate ($(\text{NH}_4)_{10}\text{W}_{12}\text{O}_{41}\cdot 5\text{H}_2\text{O}$, AMT) was purchased by Sigma-Aldrich, zirconium oxyhydroxide ($\text{ZrO}_x(\text{OH})_{4-2x}$, MEI XZO 880/01) was provided

by MEI and model crystalline zirconium oxide (ZrO_2 , Degussa) was provided by Degussa. All chemicals were used without further purification.

2.2.2 Catalyst preparation

All catalysts were synthesized by incipient wetness impregnation of an aqueous solution of AMT into (1) $\text{ZrO}_x(\text{OH})_{4-2x}$ and (2) ZrO_2 support. These two supports were initially sieved (-170 mesh) and mixed overnight using an automated VWR rocking platform. The amorphous $\text{ZrO}_x(\text{OH})_{4-2x}$ was found to have a specific surface area (SSA) of $330 \text{ m}^2/\text{g}$ and pore volume of $0.33 \text{ cm}^3/\text{g}$; while the crystalline ZrO_2 support was found to have a specific surface area of $58 \text{ m}^2/\text{g}$ and pore volume of $0.15 \text{ cm}^3/\text{g}$, as determined from nitrogen physisorption analysis of three different batches of each support type.

Prior to impregnation, the support was degassed in a vacuum oven overnight at a moderate temperature (343 K) in order to remove the excess moisture without causing any significant structural changes. Aqueous solutions of AMT (Aldrich), with different tungsten oxide loadings were impregnated up to 95% of the pore volume of the support. A correction to the calculated aqueous AMT solution volume was applied prior to impregnation according to previously reported observations [23] to assure accuracy. After impregnation, all samples were hand mixed and dried at 343 K overnight in static air. Samples were then crushed, sieved and finally heated up at a ramp rate of $3.0 \text{ K}/\text{min}$ under flowing air ($100 \text{ cc}/\text{min}$) and calcined at the desired calcination temperature for 3 hr. Crushing and sieving were repeated once more to acquire a fine powder with a catalyst particle size of $150 \mu\text{m}$ or less (-170 mesh).

The following sample notations are employed in this paper. ρ_{surf} -WZrOH(z,T) refers to AMT-impregnated amorphous $ZrO_x(OH)_{4-2x}$, where ρ_{surf} is the surface density calculated using the surface area of the catalyst after calcination (W-atoms/nm² [4,23,24]), z is the tungsten oxide weight loading (wt% of WO₃) and T the calcination temperature (K). For the samples supported on model crystalline ZrO₂ the nomenclature used was ρ_{surf} -WZrO₂(z,T). A simplified notation is used when referring to specific series of samples, namely WZrOH(T) and WZrO₂(T). Bulk WO₃ powder (Sigma) was used without further purification as a control sample. To determine the proper catalyst particle sizes to avoid diffusion limitations [25,26], three different particle size ranges were studied. More information about the procedure can be found in Appendix A.

2.3 Characterization

2.3.1 Nitrogen physisorption

Nitrogen physisorption studies were performed on Micromeritics ASAP 2010 using Matheson ultra high purity (UHP) nitrogen. All synthesized samples with the exception of the amorphous support were evacuated for more than 4 hours at 523 K until the degas rate was less than 4×10^{-3} mmHg/min. For $Zr_x(OH)_{4-2x}$ the temperature was kept at 343 K for about 2 days. The instrument was calibrated weekly by using a SiO₂/Al₂O₃ reference standard provided by Micromeritics. Instrument accuracy is approximately ± 1.5 % (relative standard deviation, $n=60$) of measured value.

N₂ adsorption-desorption isotherms were obtained for representative samples (not presented) by a 91-point analysis [27]. The isotherms in all cases were of type IV, which was indicative of a mesoporous structure. The t-plot analysis of the isotherms indicated

the absence of micropores. For the rest of the samples, the specific surface area (SSA) was calculated using a 5-point BET analysis ($P/P_0 = 0.06, 0.08, 0.12, 0.16, 0.20$) and the pore volume (V_p) was measured at relative pressure $P/P_0 = 0.985$. BET C values were in the range 50 – 150, which verified the validity of the results and also the absence of micropores for all samples [24,28].

2.3.2 X-ray diffraction

X-ray diffraction (XRD) patterns were acquired on a Rigaku D/Max-2100PC using a continuous scanning mode with 0.02° step size and a scan rate of 2.5 s/step [4, 22]. The instrument is configured with a vertical theta/theta goniometer and uses a graphite monochromator instead of conventional filters. The diffractometer works at 40 kV and 40mA using monochromatic Cu K_α radiation ($\lambda = 1.5406 \text{ \AA}$). The XRD patterns were compared to tetragonal ZrO_2 (JCPDS 79-1769), monoclinic ZrO_2 (JCPDS 37-1484) and monoclinic WO_3 (JCPDS 72-0677).

2.3.3 Electron microscopy

The microstructure of a subset of the WZrOH catalysts was studied by various electron microscopy techniques. Samples suitable for transmission electron microscopy (TEM) and scanning transmission electron microscopy (STEM) analysis were prepared by dipping a 300 mesh copper TEM grid, coated with a lacy carbon film, into the dry catalyst powder and then shaking off any loosely bound residue. Bright field (BF) images and selective area diffraction (SAD) of the samples were obtained using a JEOL 2000FX TEM operating at 200kV. Chemical analyses by X-ray energy dispersive

spectroscopy (XEDS) were also carried out on the same instrument. High resolution TEM (HRTEM) imaging and high-angle annular dark field (HAADF) imaging [29] were performed on a 200 kV JEOL 2200FS (S)TEM equipped with a CEOS probe C_s-corrector at Lehigh University. The HAADF images presented have been low-pass filtered to reduce background noise. The catalyst samples were also characterized by secondary electron (SE) imaging and backscattered electron (BSE) imaging on a Hitachi 4300LV scanning electron microscope (SEM). Samples suitable for SEM analysis were made by directly dispersing the catalyst powder onto carbon tape and coated with iridium (Ir) to mitigate charging effects.

2.3.4 Pyridine FTIR

Qualitative and quantitative acid site measurements were performed on a Nicolet 5700 FTIR spectrometer using a MCT-A detector and a homemade stainless steel, vacuum cell, with CaF₂ windows [30]. Lewis (L) and Brønsted (B) site concentrations were calculated according to the Beer-Lambert law corrected with the normalized weight of the wafers, with a radius of 0.405 cm and thickness of ~ 1 mm. The molar extinction coefficients of 1.67 and 2.22 cm/μmol for the L and B sites, respectively, were used [31].

Sample preparation consisted of forming fine self-supporting wafers that were pretreated *in situ* at 723 K under high vacuum (10⁻⁶ mbar) for 1 hr in order to remove any moisture and impurities from the pores of the catalysts. After cooling down to 423 K, pyridine was introduced to the system periodically in pulses within 1 hr to assure complete surface titration. Transmission spectra collection occurred systematically until

no intensity difference was observed and were transformed to absorption spectra as reported in literature [32].

The weak and moderate acid sites were quantified by the amount of pyridine desorbed in the ranges of 423-523 K and 523-723 K; the amount of un-desorbed pyridine quantified the amount of strong acid sites. For each temperature, the sample was cooled down and spectra were collected at 423 K to avoid inconsistencies caused by band broadening and intensity amplification at elevated temperatures.

The following band assignments were considered for the different interactions of pyridine with L/B acid sites: 1445 cm^{-1} and 1610 cm^{-1} for pyridine coordinated to Lewis sites; 1545 cm^{-1} and 1640 cm^{-1} for pyridinium cations formed on Brønsted sites; 1575 cm^{-1} for hydrogen bonded and physisorbed pyridine; and 1488 cm^{-1} as an overlapping band for both L-bound and B-bound pyridine. Among these, the L-bound pyridine band at $\sim 1445 \text{ cm}^{-1}$ and the B-bound pyridine band at $\sim 1545 \text{ cm}^{-1}$ were used for quantification purposes [30,31]. L and B acid site concentrations were expressed in two ways: (1) in μmol chemisorbed Py per gram-catalyst and (2) in sites per W atom [9, 14, 29, 31].

2.3.5 Thermogravimetric analysis

Thermogravimetric analysis (TGA) was used to evaluate the post-reaction (after 10 hours) coke content for three selected samples (2.5-WZrOH (7.0, 973), 5.2-WZrOH (18.5, 973) and 11.0-WZrOH (32.4, 973)) on a SDT 2960 Simultaneous DSC-TGA TA instrument. The samples were initially degassed at 473 K for 45 min under continuous N_2 flow (100cc/min) and further heated at a rate of 20 K/min up to 873 K. At this temperature they were heated isothermally for 45 min before switching to air

(100cc/min). Total coke content ranged between 1.2 and 1.9% of the catalyst weight (W_{cat}) (Table 2.1).

Table 2.1. Coke content of selected spent WZrOH determined by TGA

Catalyst Sample	Coke content [% W_{cat}]
2.5-WZrOH (7.0, 973)	1.2
5.2-WZrOH (18.5, 973)	1.9
11.0-WZrOH (32.4, 973)	1.4

2.3.6 Catalytic studies

The catalytic studies were performed on an isothermal downflow reactor at 523 K, with internal diameter (ID) of 6.26 mm, packed with ~0.33 g of catalyst. The catalyst bed length was fixed to be 2.22 cm long by adjusting the catalyst loading ± 0.02 g in order to assure a constant gas-hourly space velocity (GHSV = 68). GHSV is equal to u_0/V , where $u_0 = 0.78$ mL/min is the volumetric flow rate measured at standard temperature and pressure (STP) and $V = 0.68$ mL is the volume of the catalytic bed. The temperature was measured with two thermocouples, an internal and an external one, and the system was insulated to minimize heat losses. The temperature along the catalytic bed was successfully controlled with minor temperature fluctuations ± 1 K using Labview. The preheating zone was selected to be 15 cm long at 523 K and the downflow line leading to the GC was kept at 343 K to prevent any condensation of heavier hydrocarbon fractions ($>C_6$). Two pressure transducers placed at the entrance and exit of the quartz reactor indicated that the reaction took place at 1.04 atm, almost atmospheric conditions, with no pressure drop observed along the catalytic bed.

A flame ionization detector with a capillary column (ResTek #19703) and a thermal conductivity detector with a packed column (ResTek PC 3533) were used simultaneously to quantify the hydrocarbon and non-hydrocarbon (argon internal standard) concentrations of the reactor effluent stream. Prior to each reaction run, samples were pre-treated *in situ* at 673 K under continuous flow (100cc/min) of ultra high purity (UHP) air for 1 hr. Then, the reactor was cooled down to 523 K under flowing UHP He (100cc/min) in order to remove any physisorbed oxygen. The reactor feed gas was a blend of 1% *n*-pentane and 1% argon in helium (prepared by gravimetric blending).

Before the start of a reaction, the bypass line was purged with the feed gas and gas chromatograms were collected until minor changes in the *n*-pentane concentration were observed (± 3 ppm). The reaction was initiated by switching the feed gas to the reactor zone and the first chromatogram was collected at $t = 5$ min. The duration of all runs presented in this paper was 10 hr, during which a chromatogram was collected every 23 minutes. For calculating the partial *n*-pentane conversion to the various products, a carbon mass balance approach was used and detailed information can be found in appendix B.

2.4 Results and discussion

2.4.1 Catalyst structure

The SSA and V_p for the catalyst samples are summarized in Table 2.2. Surface tungsten oxide density values were calculated in two ways: (1) using the measured SSA of the catalysts after calcination, to give units of W/nm^2 and (2) using the SSA of the support materials ($ZrO_x(OH)_{4-2x}$ or ZrO_2) after calcination, to give units of W/nm_{supp}^2

(Table 2.2). These calculations gave similar values for low tungsten oxide content, and differed significantly at high tungsten oxide content [4,23].

Table 2.2. BET surface area, pore volume, and calculated tungsten surface density values of various supported WO_x/ZrO_2 catalyst.

Catalyst sample (WO_3 wt%, calcination temperature K)	BET S.S.A. [m^2/g]	Pore volume [cm^3/g]	Surface density ρ_{surf}	
			[W/nm^2]	[$\text{W}/\text{nm}_{\text{supp}}^2$]
2.5–WZrOH (7.0, 973)	72.0	0.185	2.5	2.8
3.6–WZrOH (13.2, 973)	92.3	0.183	3.6	5.2
5.2–WZrOH (18.5, 973)	93.0	0.199	5.2	7.6
6.0–WZrOH (21.7, 973)	95.5	0.210	6.0	8.8
8.5–WZrOH (30.0, 973)	92.0	0.204	8.5	12.0
11.0–WZrOH (32.4, 973)	76.0	0.168	11.0	13.0
2.2–WZrOH (9.2, 773)	109.0	0.230	2.2	2.9
3.5–WZrOH (18.5, 773)	138.0	0.218	3.5	6.0
4.4–WZrOH (21.7, 773)	128.0	0.206	4.4	7.1
8.0–WZrOH (30.0, 773)	98	0.185	8.0	9.5
2.2–WZrO ₂ (4.8, 773)	56.0	0.195	2.2	2.2
3.5–WZrO ₂ (7.0, 773)	53.0	0.165	3.5	3.2
4.4–WZrO ₂ (8.8, 773)	52.0	0.163	4.4	4.0
6.1–WZrO ₂ (12.2, 773)	52.0	0.147	6.1	5.5

The SSA of WZrOH samples increased to a maximum before decreasing with tungsten oxide loading, which is consistent with the reported thermal stabilizing role of WO_x on the amorphous $\text{ZrO}_x(\text{OH})_{4-2x}$ support during calcination [13,16,24]. The SSA of the model WZrO₂ materials, however, was not affected much by the calcination.

The XRD patterns for the WZrOH(973) material are presented in Figure 2.1. All samples calcined at 973 K were crystalline with both tetragonal ("t-ZrO₂") and monoclinic ("m-ZrO₂") zirconia phases. Monoclinic WO_3 ("m-WO₃") crystals were also detected at higher ρ_{surf} . The observed trends were in agreement with published reports that indicated the ability of WO_x to retard the phase transformation of t-ZrO₂ to the thermodynamically more stable m-ZrO₂ phase [4,5,13]. XRD peaks for m-WO₃ crystal

phase was seen to emerge at a surface density between 3.6 and 5.2 W/nm², which was lower than 7-8 W/nm² observed by others [4,18]. Bulk WO₃ formed at a lower surface density than expected, perhaps due to incomplete spreading of the metatungstate salt solution over the ZrO_x(OH)_{4-2x} support during the impregnation process [24].

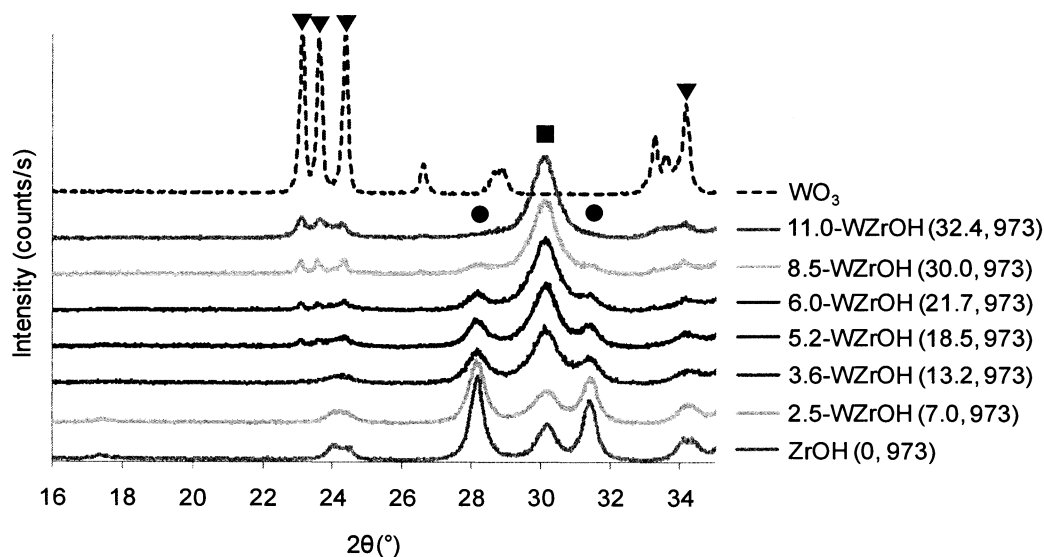


Figure 2.1. Powder XRD patterns of WZrOH and Zr_x(OH)_{4-2x} calcined at 973 K, and bulk WO₃. Crystalline phases marked as (▼) m-WO₃, (●) m-ZrO₂ and (■) t-ZrO₂.

In contrast to the observations made for the WZrOH samples calcined at 973 K, the WZrOH samples calcined at 773 K appeared to be mostly amorphous at low ρ_{surf} , and no m-ZrO₂ was formed in samples with W surface densities below 8.0 W/nm²; WO₃ crystals were not detected in any of the WZrOH(773) catalysts (Figure 2.2). The WO_x species in these samples were therefore expected to be monotungstates and polytungstates species [24,33-35].

The crystal structure of the ZrO₂ support in the WZrO₂ catalysts remained similar at all the investigated WO_x surface densities, and a small fraction of WO₃ crystals were observed in the 6.1 WZrO₂ (12.2, 773) catalyst.

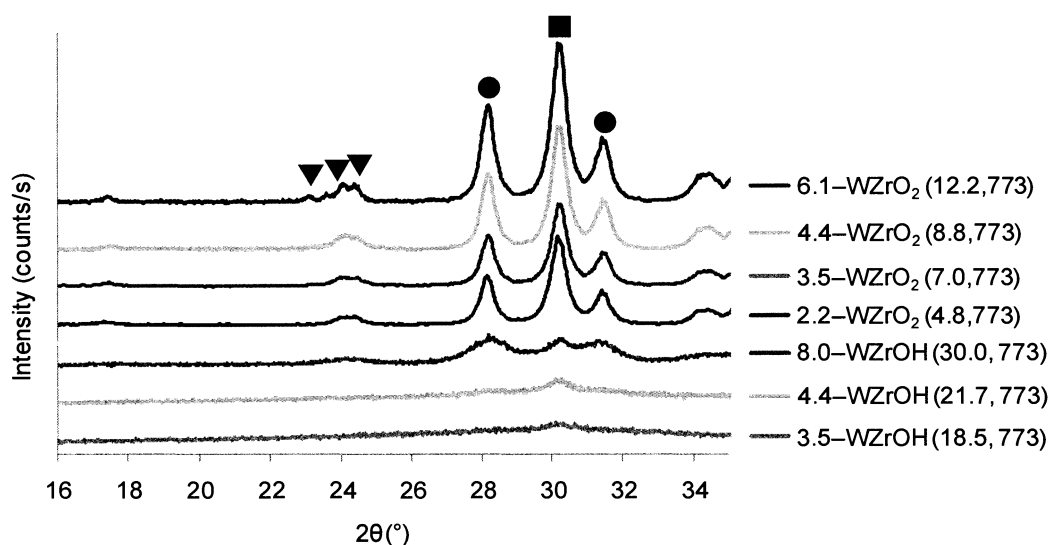


Figure 2.2. Powder XRD patterns of WZrO₂(773) and WZrOH(773). Crystalline phases marked as (▼) m-WO₃, (●) m-ZrO₂ and (■) t-ZrO₂.

2.4.2 Electron microscopy analysis

Catalyst with low WO_x loading below monolayer coverage. Bright field (BF) TEM imaging was used to characterize the morphology of the catalyst samples. As shown in Figure 2.3a, two distinct morphologies were observed in the 2.5-WZrOH (7.0, 973) catalyst: agglomerates of smaller (5-12nm) ZrO₂ particles (labeled X), and agglomerates of larger (15-40nm) ZrO₂ particles (labeled Y). The HRTEM image of a typical larger ZrO₂ particle (Figure 2.3b) shows clear lattice fringes extending right out to the surface of the grain, indicating a loading below surface WO_x monolayer coverage. In contrast, some dark speckles can be seen (Figure 2.3c) at the boundaries and surface of the aggregates of the smaller ZrO₂ particles, which can either be caused by amorphous interfacial films or clusters on the surface.

The structure and distribution of WO_x surface species were investigated using HAADF-STEM imaging, which provides z-contrast information. In Figure 2.3d, the

heavier W atoms show up as very bright spots while the ZrO_2 crystals show fainter lattice fringe contrast. Features corresponding to surface mono-tungstate (*i.e.* isolated W atoms as circled in blue), and surface polytungstate (*i.e.*, interconnected two-dimensional WO_x species with W atoms linked by oxygen bridging bonds as circled in green) are visible on both ZrO_2 morphologies. The surface W atoms were found to sit preferentially above the Zr atom columns; this phenomenon becomes clearer when the ZrO_2 crystal is oriented along a major zone axis as in the upper right hand side particle in Figure 2.3d. This preferential location of W atoms has been proposed [19] to be a consequence of the strong interaction between WO_x species and surface defect sites on the ZrO_2 support. Although the nominal WO_x surface coverage of this catalyst was below the ML, occasional sub-nm clusters were still found (circled in red in Figure 2.3d) especially at the intersections of adjacent small ZrO_2 support particles and at the edge of surface pits. The formation of such WO_x clusters at particle boundaries is presumably due to capillary effects; while the edge of surface pits provides lots of step edge sites for trapping WO_x species. It is important to note that these sub-nm clusters were exclusively found to be associated with the agglomerates of smaller ZrO_2 particles (*i.e.*, X morphology) with very low number density. Thus, the larger particles (*i.e.*, Y morphology) were possibly formed as a consequence of local inhomogeneities in the WO_x distribution and calcination conditions.

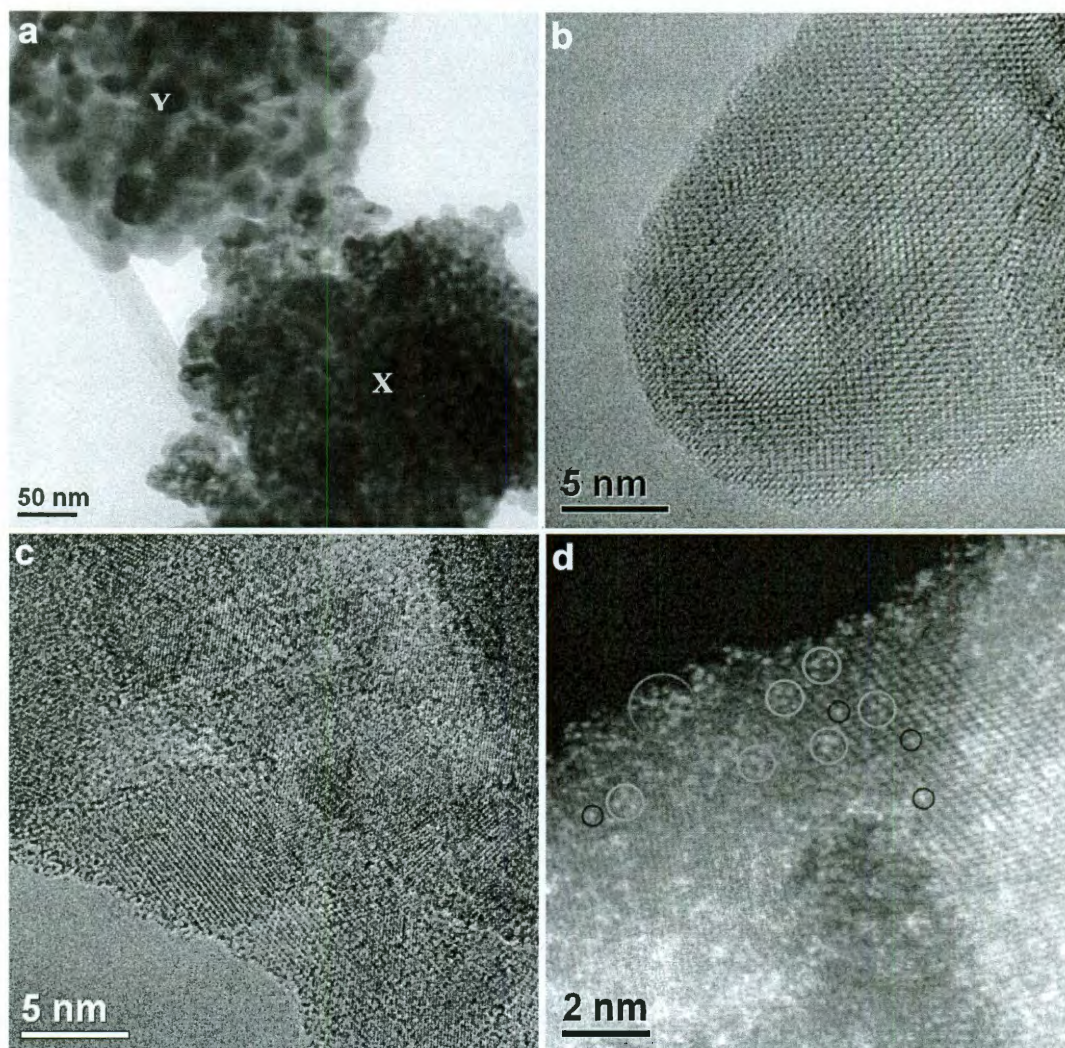


Figure 2.3. Representative (a) TEM BF image, (b, c) HRTEM images and (d) HAADF-STEM image of the supported 2.5-WZrOH (7.0, 973) catalyst. Blue circles: surface monotungstate species; Green circles: surface polytungstate species; Red circles: sub-nm Zr-WO_x clusters.

Catalyst with WO_x loading close to monolayer coverage. Three different morphologies were found in 5.2-WZrOH (18.5, 973) (Figure 2.4a). The first morphology (labeled X) consists of agglomerates of small (5-12 nm) ZrO₂ support particles; the second morphology (labeled Y) consists of clumps of larger (15-50 nm) ZrO₂ support particles; the third distinct morphology (labeled Z) is comprised large isolated single crystalline particles up to a few hundred nm in size. The X and Y

morphologies are similar to those found in the low loading catalyst, but with a smaller volume fraction of morphology Y, which is consistent with the slight peak broadening noted in the corresponding XRD spectrum. Evidence of internal voids and/or surface pits due to the loss of water from the $\text{ZrO}_x(\text{OH})_{4-2x}$ precursor material during calcination of the support could be seen in both ZrO_2 morphologies, which again serve as preferential sites for WO_x cluster nucleation.

Sub-nm dark flecks can be seen in both ZrO_2 morphologies in HRTEM images (Figure 2.4b). However, an accurate evaluation of the size and number density of these clusters is only possible from lower magnification HAADF-STEM images (Figure 2.4c) which shows a high number density of 0.8-1 nm clusters. The high resolution HAADF image (Figure 2.4d) shows the WO_x clusters having a considerably higher image contrast as compared with the monotungstate and polytungstate species, confirming their three-dimensional nature. A rough estimate, based on the size of the clusters, suggests that each cluster should contain between 10 and 15 WO_x units. Subtle contrast variations in a single cluster are noticeable in such images, and Zhou *et al.* [19] recently showed that these were Zr- WO_x clusters, which were the most active for methanol dehydration. The grain boundary grooves between intersecting ZrO_2 particles again served as preferential sites for WO_x clustering, but the overall increase in WO_x loading saturated the ZrO_2 surface and formed a high number density of these Zr- WO_x clusters. The Zr- WO_x clusters found in this more highly loaded sample had a larger average domain size (Figure 2.4d) compared to those found in the lower loaded 2.5-WZrOH (7.0, 973) sample.

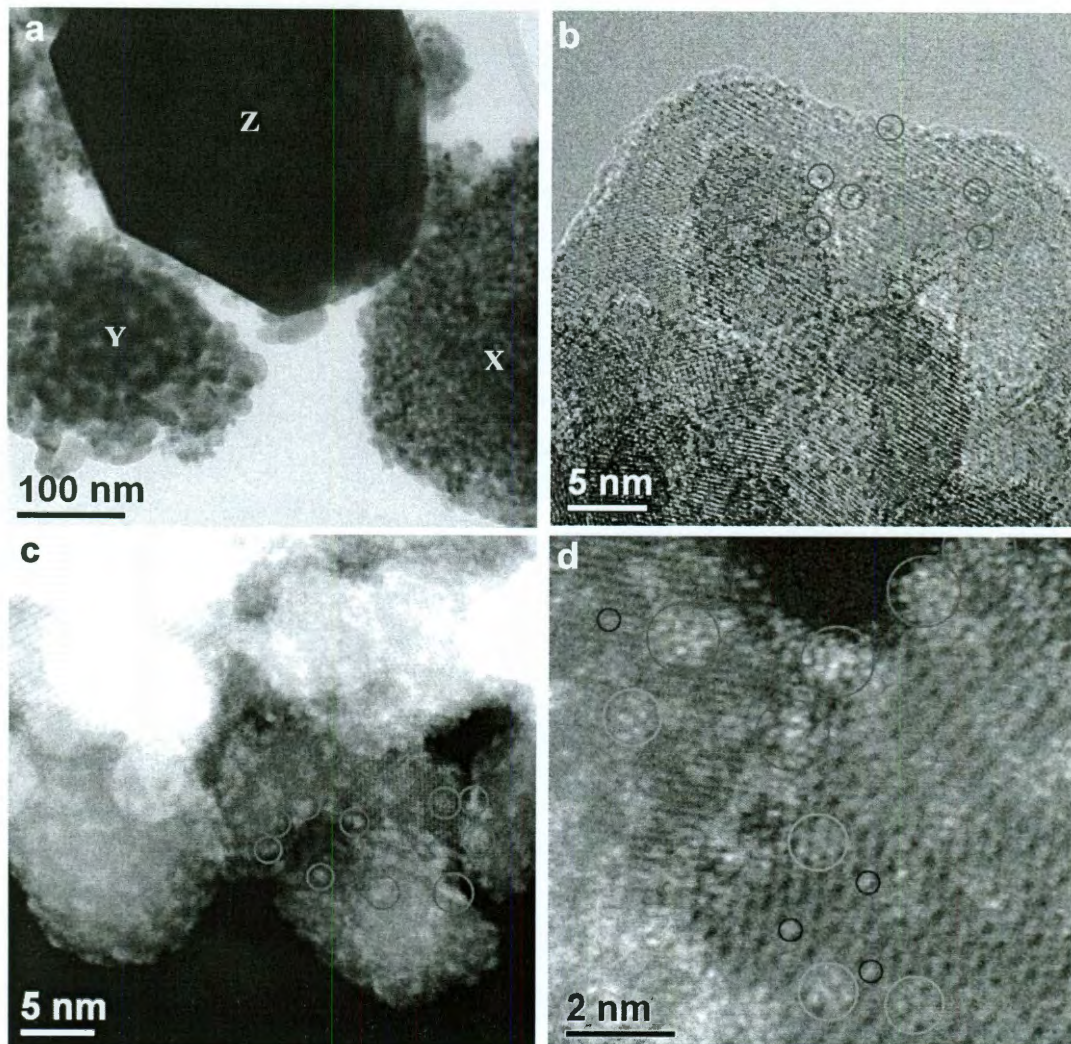


Figure 2.4. Representative (a) TEM BF image, (b) HRTEM image and (c, d) HAADF-STEM images of the supported 5.2-WZrOH (18.5, 973) catalyst. Blue circles: surface monotungstate species; Green circles: surface polytungstate species; Red circles: sub-nm Zr-WO_x clusters.

The much larger particles (labeled Z in Figure 2.4a) were identified using EDS and electron diffraction techniques to be WO₃ crystals, which were identified to be the monoclinic phase via XRD (Figure 2.1). Backscattered electron (BSE) imaging in SEM also contains z-contrast information, and can be used to locate the WO₃ crystals in the WO₃/ZrO₂ catalysts due to their higher atomic number. SEM BSE images from the 5.2-WZrOH (18.5, 973) catalyst sample (Figure 2.5a) clearly reveal the distribution of 200-

600 nm WO_3 crystals in the sample. These bulk WO_3 crystals are known to possess very low activity for methanol dehydration [4,36].

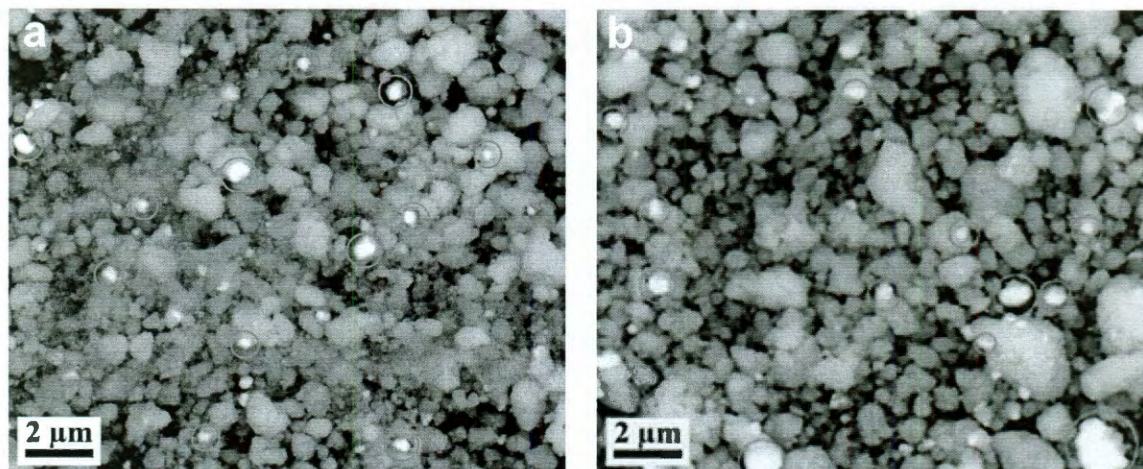


Figure 2.5. Representative (a) SEM BSE images of 5.2-WZrOH (18.5, 973) and (b) 8.5-WZrOH (30.0, 973). Hundred-nm size WO_3 crystals are circled.

Catalyst with WO_x loading above monolayer coverage. Similar to the 5.2-WZrOH (18.5, 973) sample, the three distinct morphologies (X, Y and Z) were also observed in the 8.5-WZrOH (30.0, 973) catalyst. The two ZrO_2 morphologies (X and Y) are shown in Figure 2.6a. The larger Y-type ZrO_2 particles appeared even less frequently when compared with the two samples discussed previously. The increase in WO_x loading tended to inhibit the sintering of the ZrO_2 support particles, and stabilized the smaller metastable tetragonal ZrO_2 polymorphs, as indicated by the peak broadening and increase in signals for the tetragonal ZrO_2 phase in the XRD spectrum.

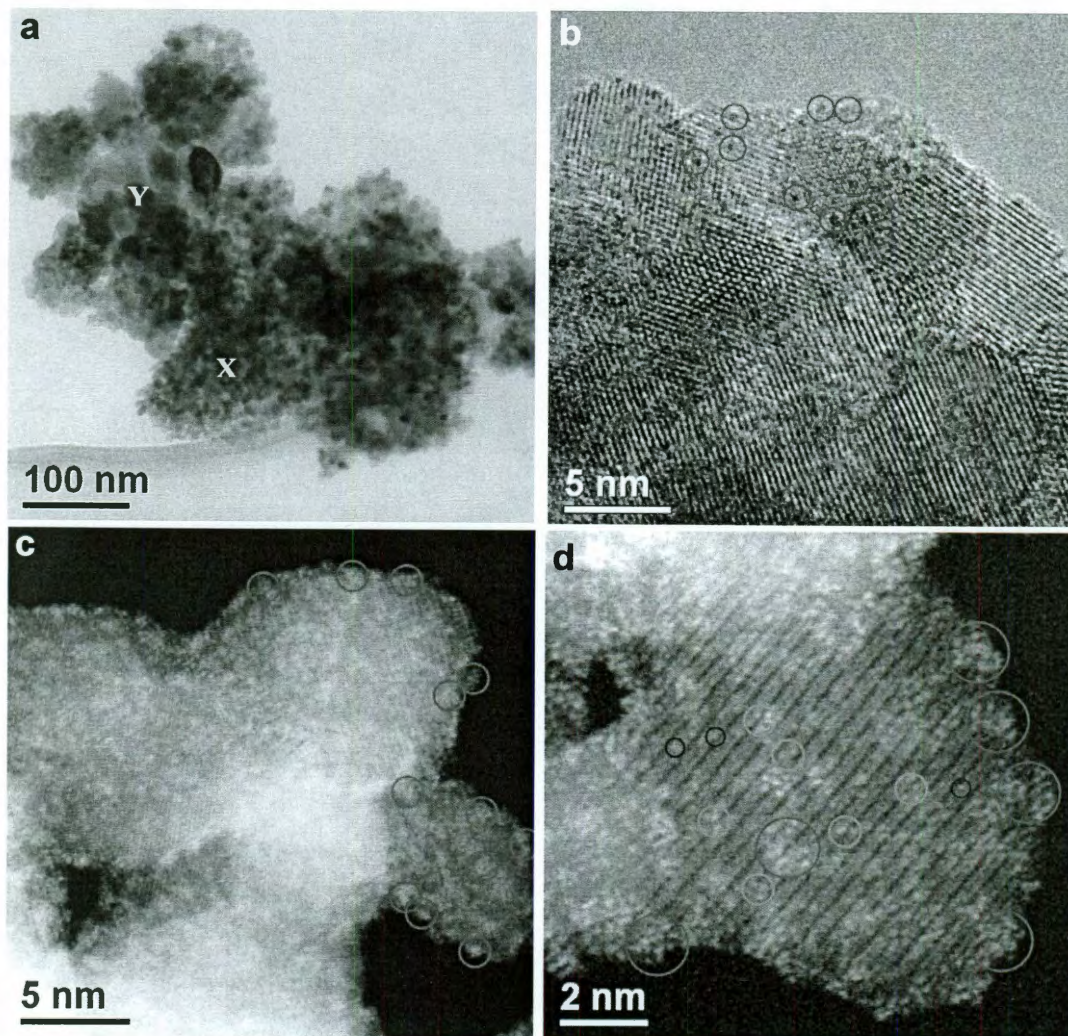


Figure 2.6. Representative (a) TEM BF image, (b) HRTEM image and (c, d) HAADF-STEM images of the supported 8.5-WZrOH (30.0, 973) catalyst. Blue circles: surface monotungstate species; Green circles: surface polytungstate species; Red circles: sub-nm Zr-WO_x clusters.

A high number density of sub-nm Zr-WO_x clusters were also observed in this sample using both HRTEM and HAADF-STEM imaging (Figure 2.6b, c and d). The BSE-SEM image (Figure 2.5b) shows a higher volume fraction of bulk WO₃ crystals in this catalyst sample as compared with 5.2-WZrOH (18.5, 973) catalyst. The average size of the WO₃ particles also increased as the nominal tungsten surface density increased

from 5.2 to 8.5 W/nm². The significant intensity increase of the m-WO₃ XRD peaks indicated an increased amount of WO₃ crystals.

Catalyst calcined at lower temperature with WO_x loading close to monolayer coverage. One of the WO_x/ZrO₂ catalysts calcined at a lower temperature of 773K was also characterized for comparative purposes. The major morphology found in the 4.4-WZrOH (21.7, 773) catalyst were aggregates of small (5-15 nm) ZrO₂ particles. However, they differed from the catalysts calcined at 973K, in that the ZrO₂ was largely amorphous, according to electron diffraction (Figure 2.7a) and x-ray diffraction (Figure 2.2). The ZrO₂ support structure is more clearly shown in the HRTEM image in Figure 2.7b, where only a very small fraction of the ZrO₂ particles are crystalline in nature as revealed by the occasional localized lattice fringes. HAADF-STEM images were taken from both the amorphous (Figure 2.7c) and crystalline (Figure 2.7d) regions of the ZrO₂ support, respectively. Although the speckle contrast from the amorphous ZrO₂ made it slightly more difficult to definitively locate the W atom positions, the WO_x species were seen in Figure 2.7c to be highly dispersed on the amorphous ZrO₂ support surface as isolated WO_x units and probably as some polytungstate species. In contrast, surface polytungstate was the dominant species found on the crystalline portion of ZrO₂ (Figure 2.7d), with occasional sub-nm Zr-WO_x clusters also found.

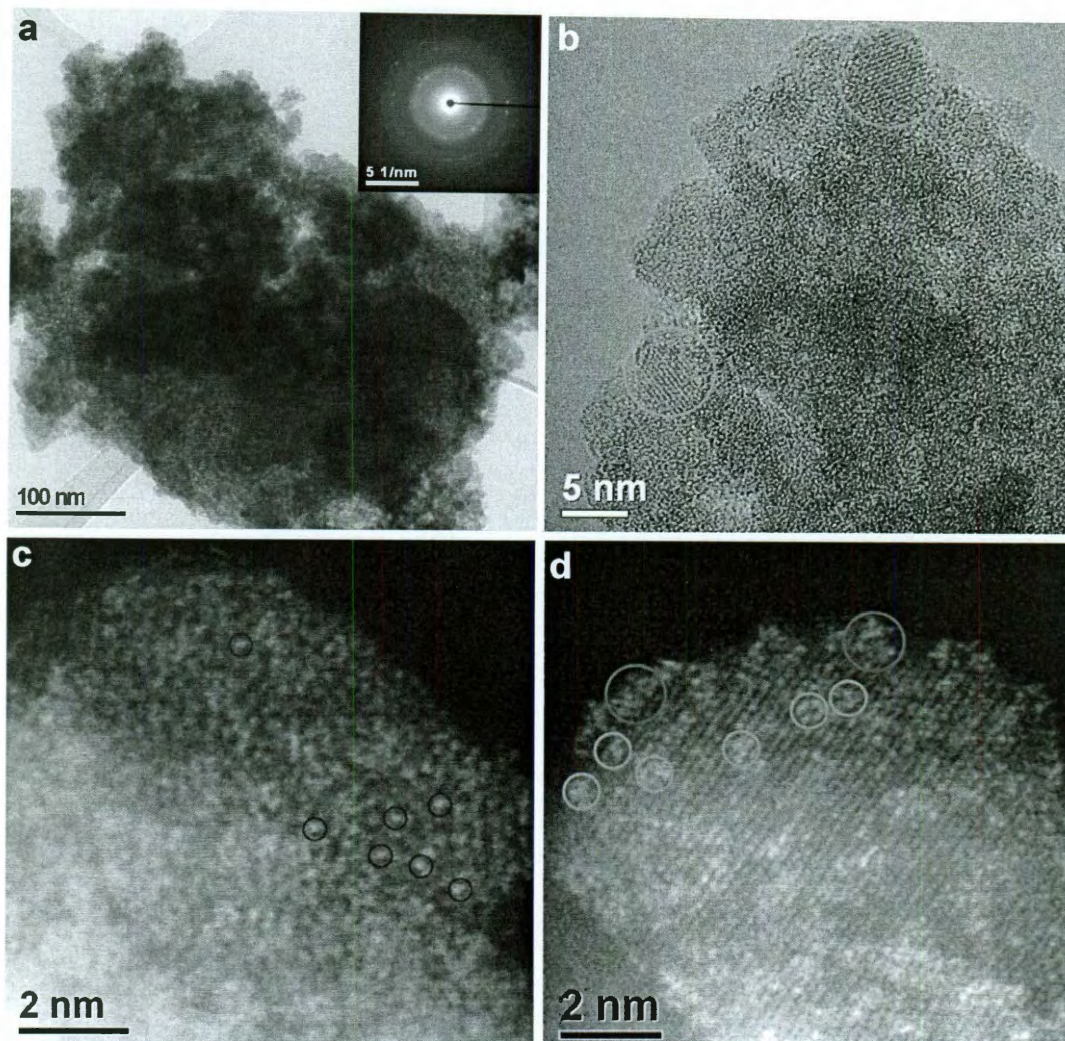


Figure 2.7. Representative (a) TEM BF image, (b) HRTEM image and (c, d) HAADF-STEM images of the supported 4.4-WZrOH (21.7, 773) catalyst. Blue circles: surface monotungstate species; Green circles: surface polytungstate species; Red circles: sub-nm Zr-WO_x clusters.

As noted previously [19,37] and also in the present study, the W atoms have a tendency to sit directly above Zr sites on the ZrO₂ surface. Thus, the lack of structural order in the amorphous ZrO₂ support reduced the ability of adjacent W atoms to form a polytungstate network or Zr-WO_x clusters. Previous reports [4,19,37] have suggested that Zr-WO_x clusters and polytungstate species are much more catalytically active than

monotungstate species. Therefore, the predominance of the highly dispersed monotungstate WO_x species on the amorphous ZrO_2 surface could be the underlying reason for the extremely low catalytic activity exhibited by this sample. A more crystallized sample with a similar W surface density was found to be more active as a result of the formation of Zr- WO_x clusters and/or polytungstates.

2.4.3 Surface acidity

Pyridine FTIR experiments were performed under ultrahigh vacuum conditions and the acquired results represented surface acidity, *i.e.*, the acidic state of the catalyst assessed under non-reaction conditions. The total acidity of the WZrOH(773) and WZrOH(973) series are presented in Table 2.3.

Table 2.3. Brønsted and Lewis acidity of supported WO_x/ZrO_2 catalysts determined by pyridine FTIR

Catalyst Sample	Brønsted	Lewis	Brønsted	Lewis	<i>B:L</i> ratio
	[$\mu\text{mol/g}_{\text{cat}}$]		[sites/ W_{atom}]		
ZrOH (0, 973)	–	29.4	–	–	–
2.5–WZrOH (7.0, 973)	10.3	54.7	0.035	0.183	0.19
3.6–WZrOH (13.2, 973)	20.1	68.0	0.035	0.117	0.29
5.2–WZrOH (18.5, 973)	23.7	64.2	0.027	0.080	0.34
6.0–WZrOH (21.7, 973)	23.7	69.5	0.025	0.073	0.34
8.5–WZrOH (30.0, 973)	24.7	72.9	0.019	0.056	0.34
11.0–WZrOH (32.4, 973)	28.8	52.2	0.019	0.033	0.58
Spent 5.2–WZrOH (18.5, 973) ^a	12.3	61.0	0.016	0.080	0.20
4.4–WZrOH (21.7, 773)	29.5	168.3	0.031	0.175	0.18
8.0–WZrOH (30.0, 773)	30.3	147.7	0.023	0.113	0.21

^a Post-reaction sample collected after 10 hr. Reaction conditions: 523 K, 1.04 atm, 1% $n\text{C}_5$ in He. Overall $n\text{C}_5$ conversion < 3%.

Surface Brønsted acidity of the WZrOH(973) catalysts, on a per-gram-catalyst basis, increased with ρ_{surf} , correlating to the increasing WO_x content (Figure 2.8).

However, on a per-W-atom basis, the number of B sites was constant at ~ 0.035 sites/ W_{atom} below ML coverage ($\rho_{\text{surf}} \sim 4.5$ W/nm² [4,8,18,38]), and decreased gradually above ML coverage; this apparent decrease in acidity resulted from the presence of WO₃ crystals above ML coverage. The B sites to which the pyridine molecule chemisorbed were likely hydroxyl groups (W-O-W-OH or Zr-O-W-OH) associated with W⁶⁺ and W⁵⁺ atoms [39,40] depending on the individual cluster size [41]. In fact, the formation of B sites has been directly correlated to the existence of surface polytungstate species [5,8,12-18]. Calcination at a lower temperature (773K) slightly increased the number of B acid sites for comparable surface densities in the WZrOH catalysts.

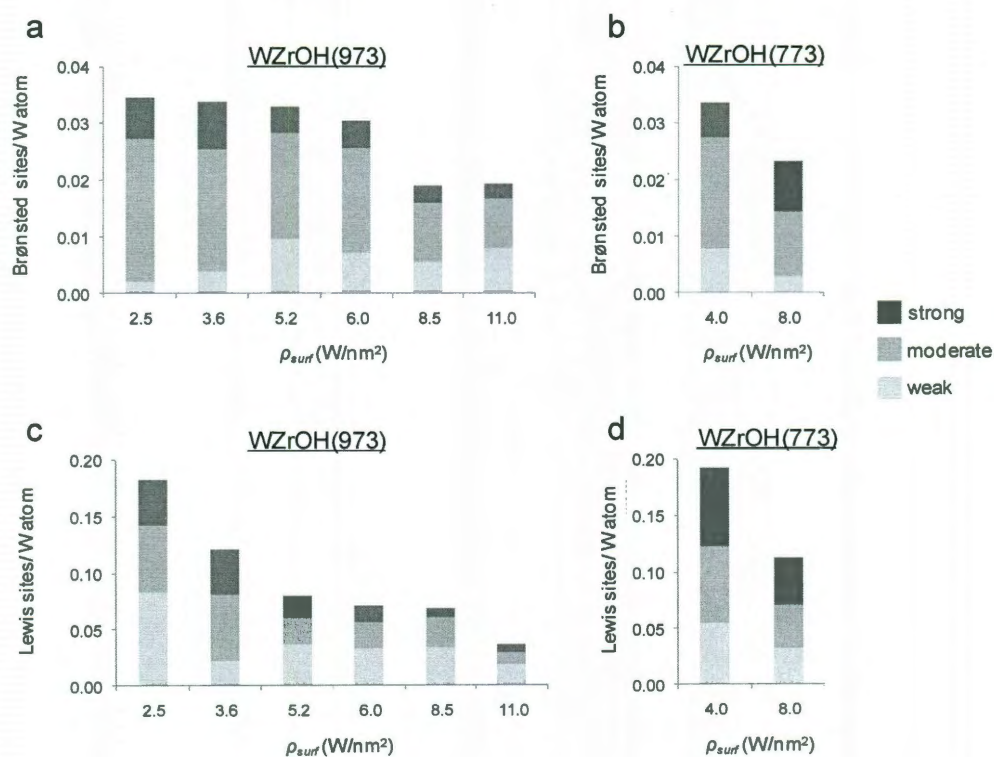


Figure 2.8. Brønsted acid site strength as a function of ρ_{surf} expressed as sites per W atom for (a) WZrOH (973) and (b) WZrOH (773) and Lewis acid site strength as a function of ρ_{surf} for (c) WZrOH (973) and (d) WZrOH (773). Acid strength quantified as pyridine desorbed up to 523 K (weak), 523-723 K (moderate) and pyridine undesorbed above 723 K (strong) ranges.

Our observations of B site density compared favorably with results reported by others. Scheithauer *et al.* [12,13] studied the B acid site amount and strength using low-temperature CO-IR spectroscopy. Based on the carbonyl stretching frequency, B site density reached maximum above $\sim 6.0 \text{ W/nm}^2$ (which we calculated using the SSA and the WO_3 loading values reported for each sample), and remained unchanged by further increasing ρ_{surf} . Baertsch *et al.* [16] studied the acidity of WO_x/ZrO_2 catalysts using NH_3 -IR spectroscopy combined with temperature-programmed desorption TPD measurements, and concluded that the maximum B site density per W atom was found at an intermediate ρ_{surf} of $\sim 5.5 \text{ W/nm}^2$, which differs from the maximum *o*-xylene isomerization activity observed at $\rho_{surf} \sim 10.0 \text{ W/nm}^2$. The same group [15] also investigated the *in situ* acidity of WO_x/ZrO_2 by studying its kinetics during 2-butanol dehydration at reaction temperature of 373 K in the presence of pyridine (Py) or 2,6-di-*tert*-butyl-Py. The maximum site density was estimated $\sim 0.04 \text{ B sites/W}_{atom}$ and $\sim 0.04 \text{ L sites/W}_{atom}$ at $\rho_{surf} \sim 6.0 \text{ W/nm}^2$. These results agreed well with the *in situ* B site density ($\sim 0.033 \text{ sites/W}_{atom}$) measured by Santiesteban *et al.* during $n\text{C}_5$ isomerization in the presence of Py or 2,6-di-*tert*-butyl-Py [8], but were much lower than those reported by Baertsch *et al.* using NH_3 -IR, *i.e.*, $0.2 \text{ B sites/W}_{atom}$ and $\sim 0.08 \text{ L sites/W}_{atom}$ at 5.5 W/nm^2 [16]. The maximum 2-butanol dehydration rate was similarly observed at $\rho_{surf} \sim 9.0 \text{ W} \cdot \text{nm}^{-2}$, which again did not correspond to maximum B site density.

Lewis acidity of $\text{WZrOH}(973)$, normalized per gram catalyst, increased significantly with ρ_{surf} up to 8.5 W/nm^2 and dropped by 37% at 11.0 W/nm^2 . This follows a similar pattern as the specific surface area of the catalysts (Table 2.2). This can be well explained by the fact that the sintering of the parent $\text{ZrO}_x(\text{OH})_{4-2x}$ support

structure was hindered by a high WO_3 content, yielding more coordinatively unsaturated Zr^{4+} cations that are accessible as L acid surface sites. A lower calcination temperature also led to higher L acid content due to reduced sintering of the support [5,38].

When normalized to the WO_x surface density, L acid content decreased with increasing ρ_{surf} , which is consistent with previous reports [12,13,15,16]. Whereas B site content decreased slowly with increasing W surface density above 3.6 W/nm^2 , L site content decreased more rapidly. Considered in a different way, per W atom, the number of acidic hydroxyl groups decreases more than the number of open Zr sites does, as W content increases.

The B:L ratios were measured to be less than 1 for all samples with the ratio remaining identical between $5.2\text{-}8.5 \text{ W/nm}^2$. For comparison, Santiesteban *et al.* [8] reported a “strong” B:L ratio of 1:1 for co-precipitated WO_x/ZrO_2 catalysts and Baertsch *et al.* [15] reported an *in situ* B:L ratio of 1.75:1 for impregnated WO_x/ZrO_2 materials. The difference in B:L ratio could be due (1) to the difference in catalyst surface environments under reaction or non-reaction conditions; (2) to the difference in material preparation, in which coprecipitated samples have a higher B site density than impregnated ones [8]; (3) to the stronger basicity of 2,6-di-*tert*-butyl-Py than Py in the gas phase [42,43]; and (4) to the *in situ* transformation of L to B sites as shown by Baertsch *et al.* for WO_x/ZrO_2 [16]. In addition, during *in situ* characterization the reactant molecule is co-fed with the probe molecule, which leads to a competitive chemisorption mechanism that may underestimate the exact number of B and/or L sites.

2.4.4. *n*-pentane isomerization catalytic activity

Dependence on surface density. Steady-state turnover rates (TOR) for all materials are presented in Figure 2.9. All the WZrOH catalysts demonstrated cracking, isomerization and oligomerization activity with a TOR maxima at $\rho_{surf} \sim 5.2 \text{ W/nm}^2$. In contrast, even though the WZrO₂ samples calcined at 773 K were reported to possess mild activity for methanol dehydration [4], they were found to be almost inactive for nC₅ isomerization due to the more demanding acid nature of the nC₅ isomerization reaction. Similarly, bulk WO₃ crystals that are active for methanol dehydration [4] were also found to be inactive for nC₅ isomerization.

For the WZrOH(973) series, both the overall activity (Figure 2.9a) and isomerization activity (Figure 2.9b) reached a maximum at 5.2 W/nm^2 , correlating well to the large population of Zr-WO_x clusters in this sample as discussed in previous sections. The stronger dependence of isomerization rates on surface density suggested that these clusters favored the isomerization of *n*-pentane over other acid-catalyzed pathways.

The WZrOH catalysts calcined at 773 K were found to be less active (Figure 2.9a) and less selective for isopentane (iC₅) formation (Figure 2.9b). While calcination temperature was not found to impact the activity of WO_x/ZrO₂ for methanol dehydration [4], 2-butanol dehydration [15] and *o*-xylene isomerization [5], it affected WO_x/ZrO₂ catalytic activity for other reactions. For example, Scheithauer *et al.* reported that WO_x/ZrO₂ calcined at 923 K was ~5 times more active for nC₅ isomerization than those calcined at 1098 K [12]. López *et al.* reported up to ~5 times higher acetic acid esterification activity for samples calcined at 1073 K in the range 673 – 1173 K [44]. With our results, such observations show a clear calcination temperature effect, for which

the optimum temperature promotes the formation of highly active Zr-WO_x clusters [4,19].

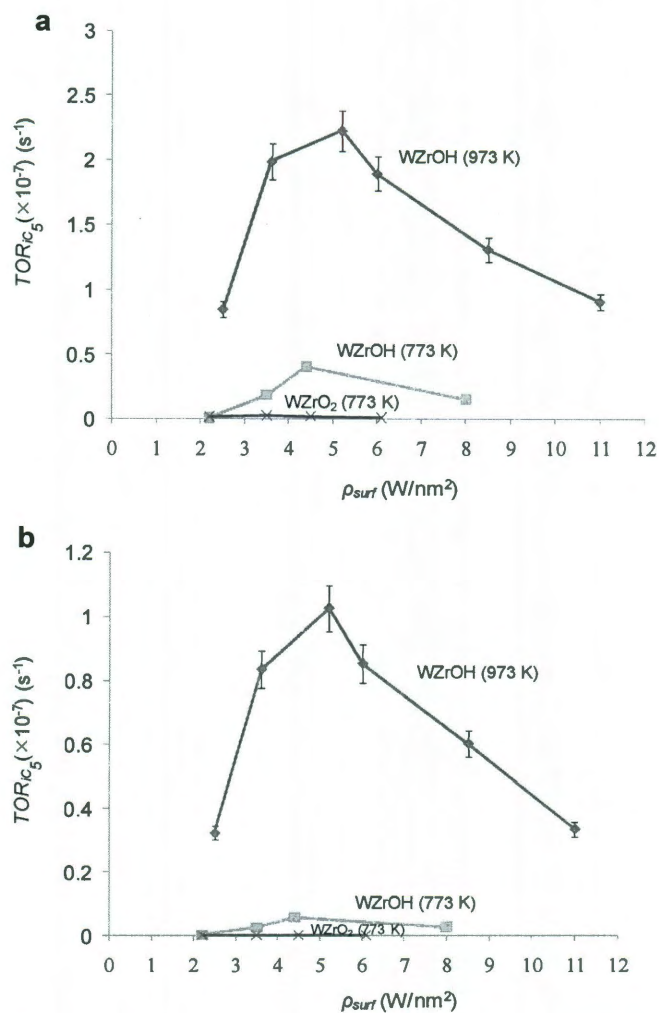


Figure 2.9. (a) Steady-state nC₅ consumption turnover rates (*TOR*) and (b) steady-state nC₅ isomerization turnover rates as a function of tungsten surface density. Sample series include (◆) WZrOH(973), (■) WZrOH(773), and (×) WZrO₂(773). Reaction conditions: 523 K, 1.04 atm, 1% nC₅ in He. Overall nC₅ conversion < 3%.

The selectivity profiles at different surface densities indicate cracking (C₁-C₄), isomerization (iC₅) and oligomerization (>C₆) hydrocarbon products (Figure 2.10). Carbon mass balances closed at 95-98%, with the remaining carbon mass in the forms of

coke precursor (which are more volatile and therefore more easily removable) and hard coke (which are harder to remove, after formed from further dehydrogenation of the coke precursors) [45]. No H_2 was detected, indicating that any H_2 released from cracking reactions was consumed *in situ*.

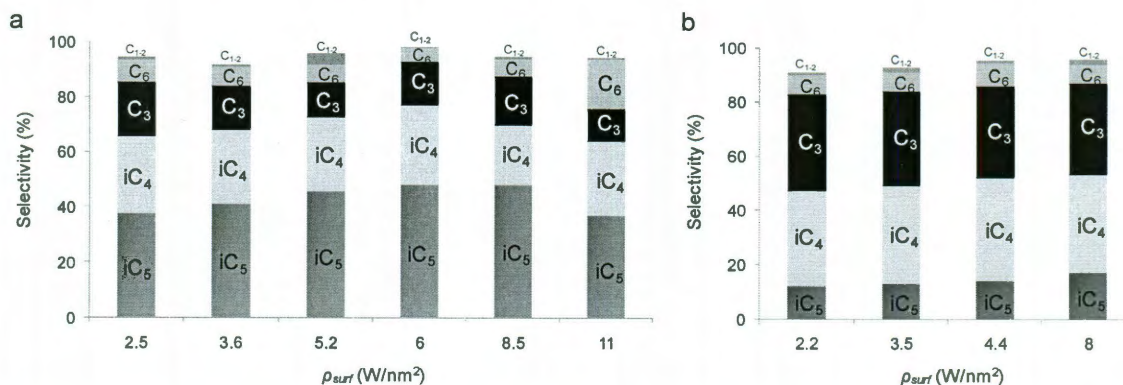


Figure 2.10. Steady-state product distribution of (a) WZrOH(973) and (b) WZrOH(773). Reaction conditions: 523 K, 1.04 atm, 1% nC_5 in He. Overall nC_5 conversion < 3%.

A monomolecular mechanism was previously proposed for nC_5 isomerization over WO_x/ZrO_2 catalysts under similar reaction conditions [11]. The reaction is initiated via the formation of a carbenium (C_5^+) cation [46] followed by its skeletal isomerization or β -scission [47] to produce iC_5 or C_1 - C_4 respectively, similar to what has been reported for zeolite catalysts. The detection of ethane and ethylene (C_2) and traces of methane (C_1) in this study was evidence for a monomolecular cracking mechanism [48].

Hexane and hexenes (C_6) and traces of higher molecular-weight hydrocarbons were detected in this study also, in accordance with similar studies performed on paraffin cracking over zeolites [47-51], WO_x/ZrO_2 [9] and sulfated zirconia (SO_4/ZrO_2) [52,53]. The detection of species larger than pentane indicates intermolecular transformations were occurring, suggesting that nC_5 isomerization could also occur through a bimolecular reaction pathway. C_6 can be produced from the combination of methyl cation (CH_3^+ ,

generated from D3 β -scission of nC_5 [47]) with nC_5 . It can also come from a C_{10} surface intermediate formed from the coupling of pentane and pentene molecules, which then cracks into C_6 's and C_4 's, similar to what has been proposed for SO_4/ZrO_2 [52-55]. The same C_{10} intermediate could undergo skeletal isomerization and cracking to generate iC_5 . nC_5 isomerization is likely to occur via a bimolecular reaction mechanism for WO_x/ZrO_2 but this point has not been established in literature yet. We are currently studying this in more detail by analyzing the effect of adding alkenes as co-feed.

Selectivity to iC_5 increased from 38% for $\rho_{surf} = 2.5 \text{ W/nm}^2$ to a maximum of 46-48% for ρ_{surf} between 5.2 and 8.5 W/nm^2 for the WZrOH catalysts calcined at 973 K (Figure 2.10a), where the number density of Zr- WO_x clusters also reached a maximum. The isobutane (iC_4) percentage remained constant (~27%) at the surface densities studied. Propane/propylene (C_3) percentages were relatively low at all surface densities except at 2.5 and 3.6 W/nm^2 , where their relative concentration increased to 14-20%. C_6 were detected in low amounts at all surface densities except at 11.0 W/nm^2 , where its percentage increased to 14%. Small amounts of C_1 and C_2 were detected, with n -butane (nC_4) detected in trace amounts (not shown).

The WZrOH samples calcined at 773 K were found to greatly favor cracking over isomerization of nC_5 , with iC_5 selectivities remaining below 20% between 2.2 and 8.0 W/nm^2 (Figure 2.10b). iC_4 and C_3 were the main cracking byproducts with their relative concentrations remaining unchanged (~30% and ~25% respectively) at all surface densities. C_6 products were also detected at all surface densities.

WZrOH samples calcined at 973 K were at least twice as good as samples calcined at 773 K as nC_5 isomerization catalysts. We suggest that surface monotungstate

species – found in large amounts in the 773 K-calcined WZrOH samples (Figure 2.7) but only in small amounts in the 973 K-calcined samples near or above WO_x monolayer coverage (Figures 2.4 and 2.6) – promotes monomolecular cracking reaction. We further suggest that the 0.8-1 nm Zr- WO_x clusters found in the 973 K-calcined samples, with the highest presence near W monolayer coverage, are responsible for bimolecular isomerization activity.

Correlation to surface acidity. The concentrations of weak, moderate and strong B sites were comparable for the WZrOH(973) series up to 5.2 W/nm^2 (Figure 2.8). A minor increase in weak B acidity and a small decrease in strong B acidity were noticed in this range, with moderate sites remaining unchanged. High ρ_{surf} decreased moderate and strong B acidity, which corresponded to higher molecular-weight reaction products (Figure 2.10a). The total B site content of WZrOH(773) material was in line with that of WZrOH(973), on a W surface density basis. No pattern could be discerned from the different B acid strength concentrations (Figure 2.8a and b) to explain how WZrOH(773) were at least two times less active. As noted earlier, the 773 K-calcined samples contained more L sites per W than 973 K samples (Table 2, cf. 3.6 and 4.0 W/nm^2 , and 8.5 and 8.0 W/nm^2). No pattern could be discerned from the different L acid strength concentrations either to explain the differences in catalytic activity (Figure 2.8c and d).

Recognizing that coke deposition occurred during the reaction that could impact the acid site amount and strengths, we assessed the surface acidity of 5.2-WZrOH (18.5, 973) after 10 hr under reaction conditions. Pyridine adsorption FTIR results indicated that the total B acidity decreased from 0.028 to 0.016 sites/ W_{atom} , the amounts of strong,

medium, and weak acid sites proportionally decreased, and total L acidity remained the same at 0.08 sites/ W_{atom} (Figure 2.11). These observation pointed to the direct participation of B sites during nC_5 isomerization reaction, in agreement with previous reports [8,15] and suggested that L sites did not participate as active sites.

That the measured B and L site concentrations did not correlate with the observed catalytic activity trends suggested that the catalytically active sites are most likely to form *in situ*, and that the surface tungstate species sites likely generate these active sites during the reaction. This latter point has been considered by several research groups in the context of an observed induction period during flow reactor studies. For WO_x/ZrO_2 , the induction period was proposed to result from the *in situ* generation of B sites from L sites [5,14-16]. For the related material SO_4/ZrO_2 , the induction period found in *n*-butane skeletal isomerization was attributed to the formation of an oligomeric intermediate via a bimolecular reaction pathway [52-55].

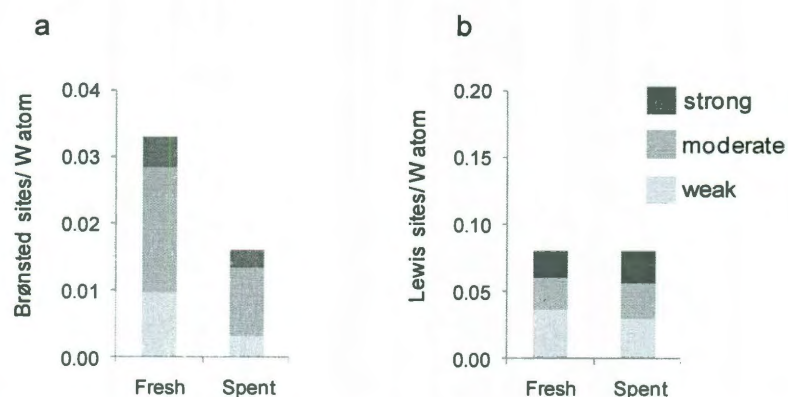


Figure 2.11. Brønsted and Lewis acid sites of varying acid strengths for 5.2-WZrOH (18.5, 973) (a) before and (b) after the running nC_5 isomerization reaction for 10 h.

Time-dependent catalytic behavior. Reaction rates and product concentrations were quantified and monitored over 10 hr for WO_x/ZrO_2 samples at different surface densities (2.5-WZrOH (7.0, 973), 5.2-WZrOH (18.5, 973) and 11.0-WZrOH (32.4, 973)). In

agreement with other reports [12,55-57], an induction period was observed in all cases, during which the *TOR* reached a maximum (Figure 2.12a,b). 5.2-WZrOH (18.5, 973) showed the highest *TOR* at $\sim 5.5 \times 10^{-7} \text{ s}^{-1}$ at 1 hr, which decreased to a stable value of $\sim 2.0 \times 10^{-7} \text{ s}^{-1}$ after 7 hr. The rapid drop in *TOR* corresponded with the rapid decrease in *iC*₄ and C₃ formation (Figure 2.12c), presumably due to the deactivation of the most active acid sites which favored cracking [57]. C₃ is exclusively produced via a monomolecular mechanism as indicates the absence of C₇ in the product stream. On the other hand *iC*₄ can be formed both via a monomolecular and a bimolecular mechanism. The initial high concentration of *iC*₄ that declines similar to C₃ suggests they share a common monomolecular cracking pathway. The fact that the C₃ concentration drops to the minimum faster (within ~ 1 hr) opposite to *iC*₄ that gradually decreases within ~ 5 hr implies a secondary reaction pathway contributing to the formation of *iC*₄. This bimolecular mechanism generates among other *iC*₄ that reaches a steady state concentration within the same time the concentration of C₆ maximizes.

During the 10-hr period, TOR_{iC_5} dropped to $\sim 1.0 \times 10^{-7} \text{ s}^{-1}$ (Figure 2.12b) but the *iC*₅ selectivity increased from 14% to 46% for the most active 5.2-WZrOH(18.5, 973) catalyst (Figure 2.12c), indicating that the acid sites responsible for isomerization were deactivated to a lesser extent. C₆ followed the same trend as *iC*₅ (Figure 2.12c), supporting the idea of a common reaction pathway (via a C₁₀ intermediate) for these two products and, more specifically, the bimolecular mechanism model for C₅ isomerization.

We speculate that the 5.2-WZrOH(18.5, 973) catalyst, which contains comparable amounts of polytungstate and Zr-WO_x clusters, catalyze the cracking and isomerization of *nC*₅. Whereas the polytungstates deactivate immediately with time on

stream, the clusters undergo an activation process (through partial reduction [54,58]) to form the iC_5 -forming B sites.

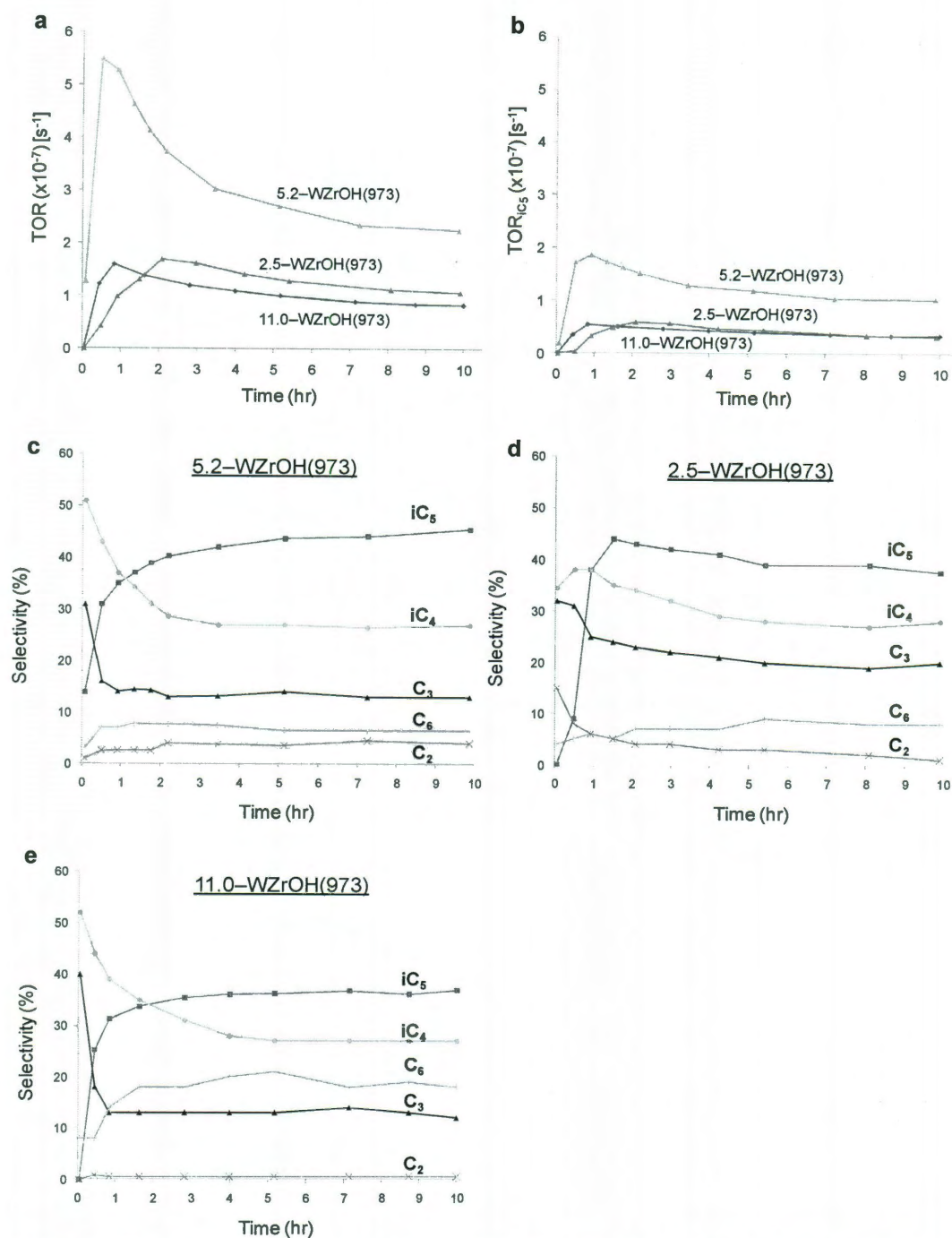


Figure 2.12. (a) nC_5 transient turnover rates (TOR), (b) transient isomerization turnover rates (TOR_{iC_5}) and product distributions for (c) 5.2-WZrOH (18.5, 973), (d) 2.5-WZrOH (7.0, 973) and (e) 11.0-WZrOH (32.4, 973). Reaction conditions: 523 K, 1.04 atm, 1% nC_5 in He. Overall nC_5 conversion < 3%.

These sites catalyze the bimolecular pathway, leading to the co-formation of the observed C_6 's, and deactivate with time as the result of C_{10} deposition or oligomerization.

For 2.5–WZrOH and 11.0–WZrOH, the TOR did not increase to the same extent, almost reaching a maximum of $2.0 \times 10^{-7} \text{ s}^{-1}$. This may be due to the smaller populations of polytungstates and Zr- WO_x clusters compared to that of 5.2–WZrOH; the 2.5–WZrOH sample had relatively more monotungstates, and the 11.0–WZrOH had more WO_3 crystals. Whereas the 11.0–WZrOH reached maximum TOR in the same time as 5.2–WZrOH, the lower surface density sample took twice as long to reach maximum TOR (Figure 2.12a). This observation suggested that the Zr- WO_x clusters took longer to become activated, perhaps due to their being located at the interstices of adjacent small ZrO_2 particles and defect sites. (Figure 2.3d).

2.5 Summary and conclusions

Pentane isomerization activity of WO_x/ZrO_2 is strongly affected by the nature of the support, calcination temperature and tungsten oxide surface density. WZrOH samples demonstrated a volcano-shape dependence on tungsten surface density with maximum activity at 5.2 W/nm^2 , above ML coverage and at the onset of the WO_3 crystallization, in contrast to model WZrO₂ that were inactive. The calcination temperature of 973 K, not 773 K, favored the formation of sub-nm Zr- WO_x clusters and in the overall activity of WZrOH, without promoting their surface acidic properties. The induction period which is critical for the activation of the highly selective Zr- WO_x clusters is responsible for the increased catalytic activity and selectivity seen at intermediate ρ_{surf} . The reducible nature of the Zr- WO_x clusters results to the formation

of very active and selective sites *in situ*. The bimolecular isomerization mechanism, which plays a significant role and requires further investigation, appears to be promoted by the *in situ* activated Zr-WO_x sites.

2.6 References

1. M. Hino and K. Arata, J. Chem. Soc. Chem. Commun. 18 (1988) 1259.
2. M. Hino and K. Arata, Chem. Lett. 6 (1989) 971.
3. D. G. Barton, S. L. Soled and E. Iglesia, Topics in Catalysis 6 (1998) 87-99.
4. E. I. Ross-Medgaarden, W. V. Knowles, T. Kim, M. S. Wong, W. Zhou, C. J. Kiely and I. E. Wachs, Journal of Catalysis 256 (2008) 108-125.
5. D. G. Barton, S. L. Soled, G. D. Meitzner, G. A. Fuentes and E. Iglesia, Journal of Catalysis 181 (1999) 57-72.
6. J. M. Thomas, Scientific American 266 (1992) 112-118.
7. A. Corma, Catalysis Letters 22 (1993) 33-52.
8. J. G. Santiesteban, J. C. Vartuli, S. Han, R. D. Bastian and C. D. Chang, Journal of Catalysis 168 (1997) 431-441.
9. J. C. Vartuli, J. G. Santiesteban, P. Traverso, N. Cardona-Martínez, C. D. Chang and S. A. Stevenson, Journal of Catalysis 187 (1999) 131-138.
10. D. C. Calabro, J. C. Vartuli and J. G. Santiesteban, Topics in Catalysis 18 (2002) 231-242.
11. S. Kuba, P. Lukinskas, R. Ahmad, F. C. Jentoft, R. K. Grasselli, B. C. Gates and H. Knözinger, Journal of Catalysis 219 (2003) 376-388.

12. M. Scheithauer, T. K. Cheung, R. E. Jentoft, R. K. Grasselli, B. C. Gates and H. Knözinger, *Journal of Catalysis* 180 (1998) 1-13.
13. M. Scheithauer, R. K. Grasselli and H. Knozinger, *Langmuir* 14 (1998) 3019-3029.
14. R. D. Wilson, D. G. Barton, C. D. Baertsch and E. Iglesia, *Journal of Catalysis* 194 (2000) 175-187.
15. C. D. Baertsch, K. T. Komala, Y.-H. Chua and E. Iglesia, *Journal of Catalysis* 205 (2002) 44-57.
16. C. D. Baertsch, S. L. Soled and E. Iglesia, *The Journal of Physical Chemistry B* 105 (2001) 1320-1330.
17. C. D. Baertsch, R. D. Wilson, D. G. Barton, S. L. Soled and E. Iglesia, *Studies in Surface Science and Catalysis* 130D (2000) 3225-3230.
18. D. G. Barton, M. Shtein, R. D. Wilson, S. L. Soled and E. Iglesia, *J. Phys. Chem. B* 103 (1999) 630-640.
19. W. Zhou, E. I. Ross-Medgaarden, W. V. Knowles, M. S. Wong, I. E. Wachs and C. J. Kiely, *Nat Chem* 1 (2009) 722-728.
20. A. Corma, *Chemical Reviews* 95 (1995) 559-614.
21. A. Corma, *Current Opinion in Solid State and Materials Science* 2 (1997) 63-75.
22. N. Soultanidis, W. Zhou, A. C. Psarras, A. J. Gonzalez, E. F. Iliopoulou, C. J. Kiely, I. E. Wachs and M. S. Wong, *Journal of the American Chemical Society* 132 13462-13471.
23. W. V. Knowles, M. O. Nutt and M. S. Wong, *Supported Metal Oxides and Surface Density Metric*. Taylor and Francis: Boca Raton, 2006.
24. N. Soultanidis, W. V. Knowles, E. I. Ross-Medgaarden, I. E. Wachs and M. S. Wong, in preparation (2009).

25. P. B. Weisz, C. D. Prater, V. I. K. W.G. Frankenburg and E. K. Rideal, *Advances in Catalysis*, Academic Press. 143-196.
26. H. S. Fogler, *Elements of Chemical Reaction Engineering*. Prentice Hall PTR, New York, 2005.
27. S. Kadali, N. Soultanidis and M. Wong, *Topics in Catalysis* 49 (2008) 251-258.
28. P. A. Webb and C. Orr, *Analytical methods in fine particle technology*. Micromeritics Instrument Corporation, Norcross, GA, 1997.
29. P. D. Nellist and S. J. Pennycook, *Science* 274 (1996) 413-415.
30. A. C. Psarras, E. F. Iliopoulou, K. Kostaras, A. A. Lappas and C. Pouwels, *Microporous and Mesoporous Materials* 120 (2009) 141-146.
31. C. A. Emeis, *Journal of Catalysis* 141 (1993) 347-354.
32. J. A. Lercher and A. Jentys, *Stud. Surf. Sci. Catal.* 168 (2007) 435-476.
33. I. E. Wachs, T. Kim and E. I. Ross, *Catalysis Today* 116 (2006) 162-168.
34. E. I. Ross-Medgaarden and I. E. Wachs, *The Journal of Physical Chemistry C* 111 (2007) 15089-15099.
35. D. S. Kim, M. Ostromecki and I. E. Wachs, *Journal of Molecular Catalysis A: Chemical* 106 (1996) 93-102.
36. T. Kim, A. Burrows, C. J. Kiely and I. E. Wachs, *Journal of Catalysis* 246 (2007) 370-381.
37. W. Zhou, E. Ross-Medgaarden, I. E. Wachs and C. J. Kiely, *Microscopy and Microanalysis* 14 (2008) 1350-1351.
38. J. Macht, C. D. Baertsch, M. May-Lozano, S. L. Soled, Y. Wang and E. Iglesia, *Journal of Catalysis* 227 (2004) 479-491.

39. F. Di Gregorio and V. Keller, *Journal of Catalysis* 225 (2004) 45-55.
40. S. Kuba, P. C. Heydorn, R. K. Grasselli, B. C. Gates, M. Che and H. Knözinger, *Phys. Chem. Chem. Phys.* 3 (2001) 146.
41. M. A. Cortés-Jácome, C. Angeles-Chavez, E. López-Salinas, J. Navarrete, P. Toribio and J. A. Toledo, *Applied Catalysis A: General* 318 (2007) 178-189.
42. R. Hosmane and J. Liebman, *Structural Chemistry* 20 (2009) 693-697.
43. E. P. L. Hunter and S. G. Lias, *Journal of Physical and Chemical Reference Data* 27 (1998) 413-656.
44. D. E. López, K. Suwannakarn, D. A. Bruce and J. G. Goodwin Jr, *Journal of Catalysis* 247 (2007) 43-50.
45. B. Wang and G. Manos, *Journal of Catalysis* 250 (2007) 121-127.
46. M. Boronat, P. Viruela and A. Corma, *The Journal of Physical Chemistry* 100 (1996) 16514-16521.
47. J. S. Buchanan, J. G. Santiesteban and W. O. Haag, *Journal of Catalysis* 158 (1996) 279-287.
48. F. C. Jentoft and B. C. Gates, *Topics in Catalysis* 4 (1997) 1-13.
49. S. Jolly, J. Saussey, M. M. Bettahar, J. C. Lavalley and E. Benazzi, *Applied Catalysis A: General* 156 (1997) 71-96.
50. H. Y. Chu, M. P. Rosynek and J. H. Lunsford, *Journal of Catalysis* 178 (1998) 352-362.
51. A. Corma, P. J. Miguel and A. V. Orchilles, *Journal of Catalysis* 145 (1994) 58-64.
52. N. Lohitharn, E. Lotero and J. G. Goodwin Jr, *Journal of Catalysis* 241 (2006) 328-341.

53. J. E. Tabora and R. J. Davis, *Journal of the American Chemical Society* 118 (1996) 12240-12241.
54. S. Kuba, P. C. Heydorn, R. K. Grasselli, B. C. Gates, M. Che and H. Knözinger, *Phys. Chem. Chem. Phys.* (2001) 146-154.
55. S. Kuba, P. Lukinskas, R. K. Grasselli, B. C. Gates and H. Knözinger, *Journal of Catalysis* 216 (2003) 353-361.
56. S. De Rossi, G. Ferraris, M. Valigi and D. Gazzoli, *Applied Catalysis A: General* 231 (2002) 173-184.
57. S. Kuba and H. Knözinger, *Journal of Raman Spectroscopy* 33 (2002) 325-332.
58. F. Di Gregorio, N. Keller and V. Keller, *Journal of Catalysis* 256 (2008) 159-171.

Chapter 3

Influence of synthesis on nature of WO_x species in WO_x/ZrO_2

3.1 Introduction

Acidic solid catalysts comprised of highly dispersed oxyanions of tungsten on a zirconia support have received enormous interest from both manufacturing [1-23] and academic sectors [24-60] since the first report of its low temperature activity for light alkane isomerization twenty years ago [61]. Fuel enrichment applications such as *n*-paraffin isomerization for increasing the gasoline octane number [5,12,13,15,17,20,22], the catalytic reduction of NO_x pollutants to N_2 [2,8] and the removal of sulfur- and nitrogen- contaminants from gasoline and diesel streams on Pt supported on WO_x/ZrO_2 [7] attracted significant industrial interest.

Recent studies into zirconium oxide-supported tungsten oxide acid catalysts have illuminated the nature of the catalytic active sites that are present in the WO_x/ZrO_2 mixed oxide system. Consensus is gathering that the catalytic active site(s) responsible for the high acidic activity for multiple reactions forms concomitantly with a maximum in polytungstate (“ WO_x ” amorphous, polymerized species adjoined by metal-oxygen-metal-linkages) surface concentration. Santiesteban *et al.* [31] and Scheithauer *et al.* [36] both discovered activity maxima for *n*-pentane isomerization in the intermediate region of WO_3 loading of 10-20 wt%, corresponding a tungsten surface density (ρ_{surf}) of 5-6 W/nm^2 [62], Based on UV-vis and Raman spectroscopies and steady-state reaction results [34,42,45,47], Iglesia and co-workers correlated maximum reactivity to intermediate ρ_{surf} values ($\sim 7\text{-}10 \text{ W}/\text{nm}^2$) at which the population of WO_x surface polytungstates was at a

maximum with respect to isolated amorphous monomeric species and crystalline WO_3 domains [41].

Recent molecular level characterization and catalytic findings allowed for distinguishing between amorphous WO_x (monotungstates and polytungstates surface species), sub-nm Zr-containing WO_x 3-dimensional clusters ("Zr- WO_x ") and crystalline WO_3 nanoparticles [63-65]. Based on the more recent *in situ* UV-vis spectroscopy, *in situ* Raman spectroscopy and aberration-corrected STEM high-angle annular dark-field (HAADF) imaging findings, a new fundamental structure-property model was developed that attributes the maxima in solid acid catalyzed reaction to the presence of Zr- WO_x clusters (methanol dehydration activity maximum in the region of 6-7 W/nm^2 [63] and *n*-pentane isomerization activity maximum in the region of 5-6 W/nm^2 [64]). These ~ 1 nm Zr- WO_x clusters were only formed when using an amorphous support [63-65] and their concentration maximizes just above monolayer (ML) coverage, with monolayer coverage corresponding to $\rho_{surf} \sim 4.5 \text{ W}/\text{nm}^2$ [31,57,63,66].

In this chapter, we extend this understanding of WO_x/ZrO_2 synthesized via incipient wetness impregnation ("iwiWZr") to materials prepared through coprecipitation ("coWZr"), sol-gel synthesis ("sgWZr"), and a surfactant templating synthesis ("stsWZr") that generates samples with high concentrations of amorphous WO_x polytungstate surface species and Zr- WO_x clusters. Detailed analysis through *in situ* Raman spectroscopy studies led to clearer identification of transitions between the various molecular surface tungstate structures (*i.e.*, surface monotungstate, surface polytungstate, Zr- WO_x clusters, WO_3 crystals) as a function of tungsten surface density on the zirconia support and their relationships to the activity of acid catalyzed reactions.

The samples presented in this chapter have been synthesized characterized by Dr. Knowles in his PhD Thesis “New insights into supported metal oxides for heterogeneous catalysis”. Analysis of the data and additional characterization and catalytic testing studies were performed that concluded this work and the results are presented here. The purpose of this chapter is to test the efficiency in forming Zr-WO_x clusters on WO_x/ZrO₂ via each synthesis method.

3.2 Experimental methods

3.2.1 Chemicals

Ammonium metatungstate ((NH₄)₁₀W₁₂O₄₁·5H₂O, AMT), ZrOCl₂·8H₂O (98%), silver nitrate (AgNO₃), propanol, ascorbic acid and hafnium chloride were purchased by Sigma-Aldrich, ammonium hydroxide (NH₄OH) and potassium chromate indicator (K₂CrO₄) by Fisher, nonionic triblock copolymer (ethylene oxide)₂₀(propylene oxide)₇₀(ethylene oxide)₂₀ (Pluronic P123) was purchase by BASF and zirconia NPs (Zr10/20) by Nyacol Nanotechnologies. The commercial supports were the same reported in the previous chapter: zirconium oxyhydroxide (ZrO_x(OH)_{4-2x}, MEI XZO 880/01) was provided by MEI and crystalline ZrO₂ by Degussa. All chemicals were used without further purification.

3.2.2 Incipient wetness impregnation method

Amorphous zirconium oxyhydroxide (ZrO_x(OH)_{4-2x}) support was prepared at room temperature (RT) by completely dissolving 313.3 g ZrOCl₂·8H₂O into 0.7 L deionized water, solution pH ~1 [63]. The solution was added dropwise into 600 mL

deionized water with 15.8 M NH_4OH causing the pH to increase ~ 10 and resulting in immediate precipitation of white powder. The precipitate was dried at 343 K and was crushed, sieved (<170 mesh) and washed until supernatant chloride ion concentration was minimized as verified by AgNO_3 , titration with K_2CrO_4 (Mohr method [67,68]). A description of the Mohr method is presented here:

Mohr method for calculating the Cl⁻ concentration

The procedure for verifying that the samples were free of $[\text{Cl}^-]$ is as follows:

- 1) The sample was initially repeatedly washed (5 times) to remove any $[\text{Cl}^-]$
- 2) 5 ml of the supernatant (last wash) was acquired and an indicator solution of 0.25 M K_2CrO_4 was added to the solution
- 3) 0.01 M AgNO_3 was added drop-wise until a color change was observed
- 4) Color of the final solution was compared to 5 ml of deionized water
- 5) The procedure was repeated until the supernatant was free of $[\text{Cl}^-]$ as indicated by comparing with deionized water

The powder was finally dried at 398 K followed by crushing and sieving (<170 mesh) [63]. This "lab-made" support was found to have a specific surface area (SSA) of $253 \text{ m}^2/\text{g}$ and pore volume (V_p) of $0.17 \text{ cm}^3/\text{gr}$. The iwiWZr samples were prepared via incipient wetness impregnation of aqueous solutions of AMT and were hand-mixed, dried and calcined as described in Chapter 2.

The following nomenclature is used for the impregnated samples. " ρ_{surf} -iwiWZr(z,T)" refers to AMT-impregnated $\text{ZrO}_x(\text{OH})_{4-2x}$, where ρ_{surf} is the surface

density normalized to the surface area of the catalyst after calcination (with units of W-atoms/nm² [63]), z is the tungsten weight loading calculated in the form of WO₃ (wt%-WO₃), and T is the calcination temperature (K). Two commercial sources of support were used for comparison, ZrO_x(OH)_{4-2x} and crystalline ZrO₂, yielding WO_x/ZrO₂ materials with notations "commercial ρ_{surf} -iwiWZr(z,T)", which was denoted as ρ_{surf} -WZrOH(z,T) and "crystalline ρ_{surf} -iwiWZrO₂(z,T)", which was denoted as ρ_{surf} -WZrO₂(z,T) in chapter 2 . Both those sample series were presented in Chapter 2. The relative error for calculating ρ_{surf} was primarily due to the mass balance and N₂-physisorption instrument limitations and was estimated to be $\leq 5\%$.

Hafnium doped samples were also synthesized by the following procedure. An aqueous solution of HFCl₄ was impregnated into the "lab-made" ZrO_x(OH)_{4-2x}. The support dried at RT and was washed with H₂O until it was free of [Cl⁻] as described above. After drying at 343 K overnight, the samples were impregnated with an aqueous solution of AMT (15.0 wt%-WO₃). All Hf-doped samples were calcined at 973 K and they are denoted as % Hf- ρ_{surf} -iwiWZr(15.0,973).

3.2.3 Co-precipitation method

An aqueous (0.05 L deionized water) solution of 5.4 g AMT and 26.3 g NH₄OH at pH ~11 was added drop-wise over 45 minutes to a stirring solution of 50.1 g ZrOCl₂·8H₂O in 0.7 L water at RT and pH ~1; addition was stopped after final solution pH ~10. The precipitate formed, was repeatedly washed to remove chloride ions and the supernatant titrated with 0.01 M AgNO₃ until the [Cl⁻] leveled near that of the background deionized water; an indicator solution of 0.25 M K₂CrO₄ was used to help

identify the titration point (Mohr method [67,68] described above). The aqueous solution was refluxed for 72 hr at atmospheric pressure, decanted, and the filter cake dried overnight in static air at 398 K before crashing, sieving and calcining. The nomenclature used for these samples was " $\rho_{surf-coWZr(z,T)}$."

3.2.4 Sol-gel synthesis

The sol-gel synthesis method is initiated by preparation of ZrO_2 nanoparticles (NPs) [69,70]. 105 g of zirconium *n*-propoxide was transferred to a beaker quickly and under argon purge to prevent quick oxidation. 74.7 g propanol and 31.0 g nitric acid (Fisher, 70 wt% in H_2O) was added to the alkoxide and was quickly stirred for 1.5 minutes at room temperature. 74.7 g propanol was added along with 6.2 g deionized water and the solution stirred for another ~11 minutes at constant rate until the gelation point in a 600 mL beaker. The gel acquired had a transparent golden yellow color. The gel was aged for 1 hr followed by pulverization with a spatula and the master batch was divided into multiple sub-batches. The AMT aqueous solution (2.17 g of 0.137 g/mL) was stirred into an 18.2 g of the original gel for 5 min and an ascorbic acid solution (2.72 g of 26.5 wt% aqueous solution) was added and stirred into the mixture for 5 min. Finally, the mixture was dried at 343 K in static air for 20 hours and the acquired powder was treated similar to the supports used for impregnation. The nomenclature used for these samples was " $\rho_{surf-sgWZr(z,T)}$."

3.2.5 Surfactant templating synthesis

As a modification to a synthesis method published previously [71], 20 g ammonium metatungstate and 200 g of a 10 wt% solution of Pluronic P123 were mixed at RT until dissolution. The pH of this mixture was measured to be ~ 6 . To this mixture the ~ 5 nm zirconia NPs were added (200 g of a 20 wt% colloidal sol) along with 10 wt% nitric acid, which resulted to pH drop to ~ 0.5 . At final solution pH ~ 2 a white precipitate was formed and the mixture was aged for 1 day at RT after stirring for 1 hr. Triple filtration and centrifugation followed and the final residue was dried at RT followed by grinding and calcination as reported for the impregnated samples. The nomenclature used for these samples was " ρ_{surf} -stsWZr(z,T)."

3.3 Characterization

3.3.1 Elemental analysis

Elemental analysis was performed at Lehigh Testing Laboratories, Inc. (New Castle, DE) [63] to confirm the mass balance methodology for calculating wt%-WO₃ loadings. All measured values matched within 3% of the expected content. The thermal decomposition of the Pluronic P123 surfactant resulted in no detectible carbon on the stsWZr samples. For the iwiWZr samples, Hf impurities were detected in all cases at a concentration of < 2 wt %.

3.3.2 Nitrogen physisorption

Nitrogen physisorption studies were performed on a Micromeritics ASAP 2010 [63,64,72,73]. The procedure is described in detail in Chapter 2.

3.3.3 X-ray diffraction

X-ray diffraction (XRD) patterns were collected using a Rigaku D/Max-2100PC diffractometer [64] as reported in Chapter 2. For estimating the relative volume fractions of the two crystalline forms of ZrO₂, monoclinic and tetragonal, an empirical relationship was used [63,74,75] by comparing the integrated areas of the ($\bar{1}11$) and (111) reflections for m-ZrO₂ and the (101) reflection for t-ZrO₂ [63].

Crystallite diameters were estimated from the Scherrer equation [76] corrected for instrumental peak broadening according to equation (3.1):

$$D = \frac{K\lambda}{B \cos(\theta)} \quad (3.1)$$

Where $K=0.9$ is the shape factor of the average crystallite, θ is the peak position, and B is the full-width, half-max (FWHM) of the peak after correcting for instrument broadening according to equation (3.2)

$$B^2 = B_{obs}^2 - B_{inst}^2 \quad (3.2)$$

B_{obs} is the FWHM of the measured peak and B_{inst} is calculated from the FWHM instrument broadening curve as based on a LaB₆ powder standard (NIST 660a). The accuracy of the Scherrer equation for calculating crystallite size is limited by the accuracy of the instrument; a crystallite size of ~100 nm leads to broadening equal to the instrumental broadening on our instrument ($B_{inst} = 0.085^\circ$ at $2\theta = 20^\circ$), thereby representing the upper limit of meaningful estimates. Peaks were profile-fitted with the

Pearson-VII model on Jade v6.1.3 software after subtraction of the $K_{\alpha 2}$ contribution. Crystallite sizes were estimated from the (002) reflection of m-WO₃, (101) reflection of t-ZrO₂, and (111) reflection of m-ZrO₂.

3.3.4 *In Situ* Raman spectroscopy

Raman spectra were collected on a UV-vis Raman spectrometer (Jobin Yvon-Horiba LabRam HR). The laser excitation source employed was 532 nm from a He-Ne laser (Kimmon). The *in situ* Raman spectra of all dehydrated samples, in loose powder form, were recorded at 298 K after O₂ oxidation at 873 K for 1 hr in an environmental reactor cell (Linkam Scientific Instruments T1500) [63]. The y-axis was enhanced for this study to investigate the different WO_x species present in the WO₃/ZrO₂ catalysts.

The Raman bands of the amorphous WO_x phases supported on ZrO₂ are dominated by the much stronger Raman bands of the ZrO₂ support below 650 cm⁻¹ [25,37,63]. The ZrO₂ crystalline phases (t- and m-ZrO₂), however, do not exhibit Raman-active bands above 700 cm⁻¹, thereby, making this range of the vibrational spectrum available for characterization of the amorphous WO_x and crystalline WO₃ phases present in the WO_x/ZrO₂ samples. The areas under the Raman bands were not deconvoluted to its components in this study due to significant overlap and broadness of the individual bands. The following ranges were used for Raman band assignments:

805, 715 and 270 cm⁻¹: well-ordered, crystalline WO₃ NPs (ν_{as} of W-O-W) [63,66].

810-885 cm⁻¹: slightly distorted Zr-WO_x clusters (ν_{as} of W-O-W and possibly ν_s of W-O-Zr bonds) [63,77] with higher ZrO_x content.

885-975 cm⁻¹: highly distorted Zr-WO_x clusters with relatively lower ZrO_x content (ν_{as} of W-O-W and possibly ν_s of W-O-Zr bonds) [63,77]. A distinct band seen at ~ 760 cm⁻¹ corresponds also to the Zr-WO_x clusters, but it was not considered for this study due to possible overlap with the well-ordered WO₃ NP band at 715cm⁻¹ [63].

1000-1025 cm⁻¹: mono-oxo surface WO₅ species (ν_s of the terminal W=O bond from square-pyramidal surface monotungstate and polytungstate WO₅ species – band shifts to higher wavenumber with extent of surface WO₅ polymerization [66,77].

Isolated dioxo surface WO₄ species are not seen in this study [78]. Monotungstates coexist with other species at all surface densities [63-65] but their relative concentration is much lower than other WO_x species for $\rho_{surf} > 2.0$ W/nm².

3.3.5 Catalytic studies

Steady-state CH₃OH dehydration experiments were conducted in an ambient pressure reactor consisting of a single-pass downflow reactor at 573 K and 1 atm. Pretreatment consisted of calcining each catalyst at 623 K in 86 sccm dry flowing gas for 30 min. The gas mixture consisted of ultra-high purity (UHP) oxygen and UHP helium controlled at a molar O₂:He ratio of 13:73 by two independent Coriolis mass flow controllers. The reactor was then cooled to 573 K and the feed gases were bubbled through a liquid methanol saturator (Alfa Aesar, ACS grade). The gas phase methanol concentration was controlled by the temperature of an overhead condenser, operated at 290 K for these experiments. The final composition of the reactor feed stream was 6% CH₃OH, 12% O₂ in He at 97 sccm total flow (STP = 273.15 K, 1 atm). Reactor effluent gases were analyzed by an online GC, operated in split mode with a 10-port valve

diverting two samples in parallel as a capillary column to the FID and a packed column to the TCD. Steady-state CH_3OH dehydration performance was expressed in CH_3OH dehydration turnover rate TOR_i [s^{-1}] [63] (CH_3OH converted to DME per W-atom per unit time) (calculation details in Appendix C) and was determined by averaging 3-4 gas chromatograph (GC) cycles. No time-on-stream (TOS) deactivation studies were performed, but inspection of the GC data suggested no observable die-off after ~ 2 h time-on-stream. No systematic deactivation as a function of TOS was observed for CH_3OH dehydration, unlike *n*-pentane [36,55,64] and *n*-butane [51,79] isomerization.

The *n*-pentane isomerization activity and selectivity of WO_x/ZrO_2 catalysts was tested on an isothermal downflow reactor at 523 K and 1.04 atm. During nC_5 isomerization, a preliminary induction period was necessary to reach highest activities in accordance with previous observations [36,55,64]. The steady state catalytic activity and selectivity was expressed in terms of nC_5 isomerization turnover rate TOR_{iC5} [s^{-1}] (nC_5 molecules isomerized per W-atom per unit time) and was collected at $t = 10$ hr, as described in Chapter 2.

3.4 Results

3.4.1 Nitrogen adsorption analysis of textural properties

Figure 3.1a shows the BET SSA as a function of ρ_{surf} and calcination temperature for the *iwiWZr* samples. The positive effect of amorphous WO_x polytungstates in preventing structural collapse upon calcination was clearly seen for the samples calcined at 773-973 K. Increasing ρ_{surf} at constant calcination temperature led initially to an increase and then to a decrease in SSA. The maximum SSA for each sample series

increased with calcination temperature in the range 773-973 K from $\sim 4\text{-}7$ W/nm^2 . In general, the surface areas for samples calcined at the same temperature shifted to lower values and higher surface densities with increasing calcination temperatures. The shifting of maximum SSA was (1) due to the variations in the tungsten oxide species population and (2) due to structural collapse of the zirconia tungsten oxide phases, both influenced by increasing calcination temperature. At temperatures >1073 K, no significant changes in the SSA were seen due to the sintering of the underlying amorphous support and formation of bulk WO_3 [37,47,53,63]. Detailed nitrogen physisorption results for all materials are presented in Table 3.1.

Table 3.1. Nitrogen physisorption results and calculated tungsten surface density values of WO_x/ZrO_2 samples.

Catalyst Sample	BET S.S.A. (m^2/g)	BET C value	Pore volume (cm^3/g)	ρ_{surf}	
				W/nm^2	$\text{W}/\text{nm}^2_{su}$ _p
1.7- <i>iwi</i> WZr (5.1, 773) ^a	76	85	0.107	1.7	2.8
2.9- <i>iwi</i> WZr (10.1, 773)	89	79	0.100	2.9	5.5
4.1- <i>iwi</i> WZr (15.0, 773)	96	80	0.091	4.1	8.4
4.1- <i>iwi</i> WZr (19.5, 773)	123	90	0.103	4.1	10.7
5.4- <i>iwi</i> WZr (23.3, 773)	113	89	0.095	5.4	12.9
7.1- <i>iwi</i> WZr (26.6, 773)	98	83	0.085	7.1	14.8
2.6- <i>iwi</i> WZr (5.1, 873)	51	102	0.099	2.6	4.5
3.9- <i>iwi</i> WZr (10.1, 873)	66	78	0.094	3.9	8.6
4.9- <i>iwi</i> WZr (15.0, 873)	80	72	0.090	4.9	13.1
5.5- <i>iwi</i> WZr (19.5, 873)	91	70	0.096	5.5	16.7
7.1- <i>iwi</i> WZr (23.3, 873)	86	70	0.089	7.1	20.3
9.0- <i>iwi</i> WZr (26.6, 873)	77	70	0.081	9.0	23.0
3.5- <i>iwi</i> WZr (5.1, 973)	37	104	0.098	3.5	8.2
5.2- <i>iwi</i> WZr (10.1, 973)	50	87	0.087	5.2	16.4
6.2- <i>iwi</i> WZr (15.0, 973)	63	73	0.095	6.2	24.4
6.7- <i>iwi</i> WZr (19.5, 973)	75	68	0.094	6.7	31.4
9.5- <i>iwi</i> WZr (23.3, 973)	64	75	0.093	9.5	37.7
12.0- <i>iwi</i> WZr (26.6, 973)	57	76	0.089	12.0	43.1
4.3- <i>iwi</i> WZr (5.1, 1073)	31	99	0.100	4.3	12.0
6.2- <i>iwi</i> WZr (10.1, 1073)	42	88	0.100	6.2	23.8

Table 3.1. (continued)

Catalyst Sample	BET S.S.A. (m ² /g)	BET C value	Pore volume (cm ³ /g)	ρ_{surf} W/nm ²	W/nm^2_{su} _p
8.4-iwiWZr (15.0, 1073)	46	88	0.100	8.4	35.4
10.6-iwiWZr (19.5, 1073)	48	86	0.104	10.6	46.0
14.0-iwiWZr (23.3, 1073)	43	89	0.095	14.0	54.8
17.1-iwiWZr (26.6, 1073)	40	88	0.090	17.1	62.9
5.9-iwiWZr (5.1, 1173)	23	111	0.097	5.9	22.3
9.8-iwiWZr (10.1, 1173)	27	101	0.096	9.8	43.7
15.8-iwiWZr (15.0, 1173)	25	123	0.090	15.8	65.0
20.2-iwiWZr (19.5, 1173)	25	116	0.090	20.2	84.4
24.1-iwiWZr (23.3, 1173)	25	111	0.098	24.1	101
29.4-iwiWZr (26.6, 1173)	23	104	0.089	29.4	115
8.6-coWZr (18.3, 873)	55	77	0.060	8.6	10.6
15.2-coWZr (18.3, 973)	31	101	0.090	15.2	15.2
15.4-coWZr (18.3, 1073)	31	101	0.080	15.4	18.9
22.0-coWZr (18.3, 1173)	22	99	0.080	22.0	27.0
3.9-sgWZr (11.9, 873)	80	86	0.100	3.9	4.4
5.5-sgWZr (11.9, 973)	56	94	0.090	5.5	6.3
9.5-sgWZr (11.9, 1073)	33	87	0.080	9.5	10.7
15.9-sgWZr (11.9, 1173)	20	121	0.060	15.9	18.1
9.4-stsWZr (50.7, 773)	140	98	0.150	9.4	19.0
12.1-stsWZr (50.7, 873)	109	104	0.138	12.1	24.6
42.5-stsWZr (50.7, 973)	31	123	0.130	42.5	86.0
52.7-stsWZr (50.7, 1073)	25	113	0.130	52.7	107
6 % Hf-6.7-iwiWZr(15.0, 973)	58	82	0.082	6.2	26.0
10 % Hf-7.1-iwiWZr(15.0, 973)	55	91	0.076	7.1	28.2
20 % Hf-7.8-iwiWZr(15.0, 973)	50	85	0.072	7.8	29.9

iwiWZr *et al.* [63].

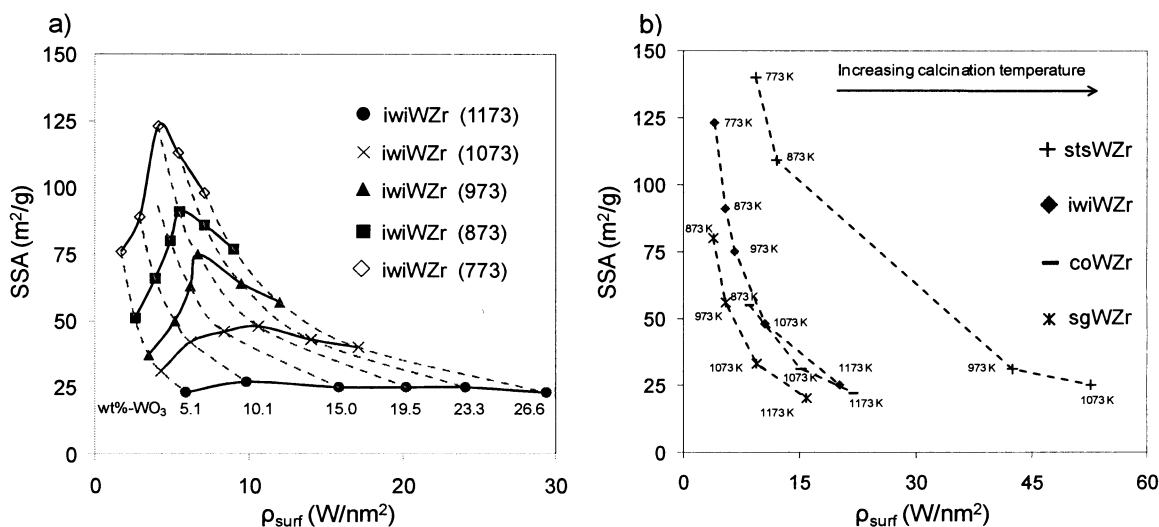


Figure 3.1. Specific surface area and W surface density as functions of (a) calcination temperature and WO₃ weight content of iwiWZr and (b) synthesis method for stsWZr (50.7,T), iwiWZr (19.5,T), coWZr (18.3,T) and sgWZr (11.9,T). Calcination temperature for each sample series increases (from left to right) from 773 to 1173 K.

Samples with different WO_x loadings and calcination temperatures can have similar ρ_{surf} values, *e.g.*, 6.2-iwiWZr(15.0,973) with a SSA of 63 m²/g and 6.2-iwiWZr(10.1,1073) with a SSA of 42 m²/g. Further, two samples with different WO_x loadings calcined at the same temperature can have similar ρ_{surf} values, *e.g.*, 4.1-iwiWZr(15.0,773) with a SSA of 96 m²/g and 4.1-iwiWZr(19.5,773) with a SSA of 123 m²/g. This phenomenon can be explained by considering that at low WO_x loadings, exposed zirconia is not directly titrated by tungstate anions, allowing sintering to occur to a greater extent. At higher WO_x loadings the decrease in SSA is generally associated with pore blockage primarily due to WO_x crystallization.

Hf-doping reduces the SSA of WO_x/ZrO₂; even a 2% doping reduces the SSA from 63 to 58 m²/g. This indicates that Hf interacts differently with W atoms during calcination. At the highest loading the SSA drops from 63 to 50 m²/g causing the WO_x ρ_{surf} to increase from 6.3 to 7.8 W/nm².

The surface area as a function of ρ_{surf} at constant WO_x loadings and different calcination temperatures for materials prepared via different synthesis methods is shown in Figure 3.1b. The surfactant-templated materials had the highest SSA of all materials, even at very high WO_x loadings, which was unusual for WO_x/ZrO_2 catalysts and significantly exceeded those of *iwiWZr*, *coWZr* or *sgWZr* materials.

3.4.2 X-ray diffraction analysis

The XRD patterns for all material are presented in Figure 3.2 and the observed trends are generally consistent with published results [37,42,43]. The commercial *iwiWZr* and crystalline *iwiWZrO₂* material [63] can be found in Chapter 2, and their trends are similar to the *iwiWZr* samples presented here.

Every *iwiWZr* sample possessed some fraction of *t-ZrO₂* and at least a trace of *m-ZrO₂*. Higher calcination temperatures and WO_x surface loading promote the formation of *m-ZrO₂* similar to what has been previously reported [63]. Just as WO_x delays the loss of SSA with calcination temperature, it also delays the phase transformation of metastable *t-ZrO₂* to the thermodynamically stable phase of *m-ZrO₂*. The volume fraction of *m-ZrO₂* was observed to increase with decreasing WO_x loading at constant calcination temperature. The *iwiWZr* (773 K) and (873 K) samples that have high SSA had high concentrations of XRD-amorphous WO_x at all ρ_{surf} (Figure 3.2a,b) [63]. At higher calcination temperatures (> 873 K), the formation of crystalline WO_3 was unavoidable at $\rho_{surf} \geq 8.0$ W/nm² (Figure 3.2c-e).

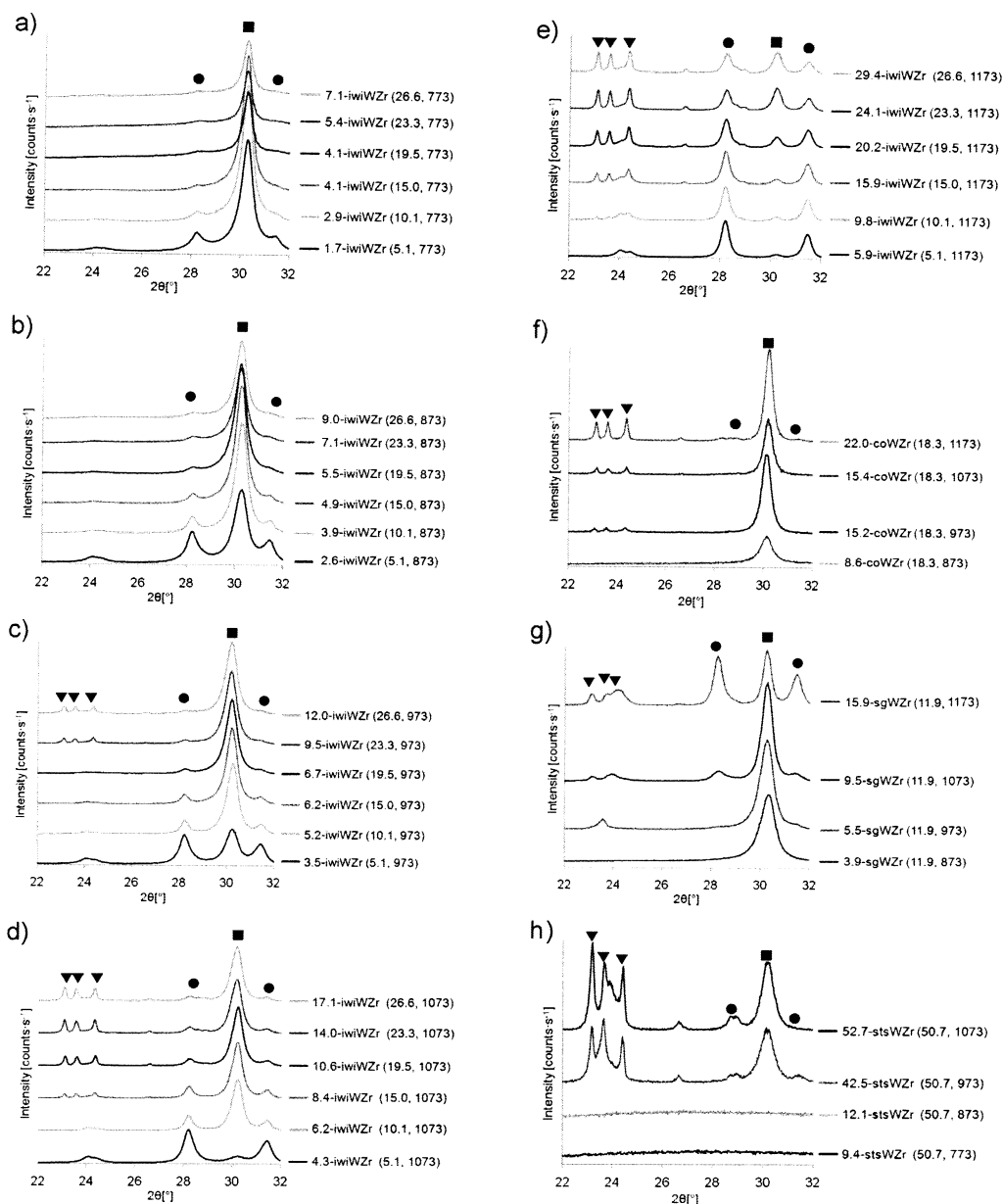


Figure 3.2. Powder XRD patterns of iwiWZr series calcined at a) 773 K, b) 873 K, c) 973 K, d) 1073 K, e) 1173 K, f) coWZr (18.3, T), g) stsWZr (50.7, T) and h) sgWZr (11.9, T). Crystalline phases marked as (▼) m- WO_3 , (●) m- ZrO_2 and (■) t- ZrO_2 .

Coprecipitated samples (Figure 3.f) had similar XRD patterns to the iwiWZr series [31]. 8.6-coWZr(18.3,873) was free of WO_3 crystals, similar to 9.0-iwiWZr(26.6,873). sgWZr materials were free of WO_3 crystals at calcination

temperatures up to 973 K, with t-ZrO₂ phase being observed at all calcination temperatures. In contrast to all the other WO_x/ZrO₂ catalysts examined, the stsWZr samples (Figure 3.2g) remained completely XRD amorphous up to calcination temperatures of at least 873 K [71]. This observation was consistent with investigations showing that zirconia supports exhibit greater stability against sintering with increasing WO_x surface density [36,38,42,53], but the absence of t-ZrO₂ was nevertheless unusual for WO_x/ZrO₂ materials calcined at 873 K. The 12.1-stsWZr(50.7,873) sample had the highest ρ_{surf} of the samples calcined at 873 K for this study, and to the best of our knowledge, there are no published examples of WO_x/ZrO₂ materials at comparable ρ_{surf} in which both zirconia and tungsten oxide phases remain XRD-amorphous at 873 K.

The presence of Hf has a drastic effect on the crystal structure of ZrO₂ (Figure 3.3). A significant decrease in the metastable t-ZrO₂ phase is noticed even at the lowest Hf loading. m-ZrO₂ is the dominant phase at Hf loadings ≥ 10 % and the formation of WO₃ nanocrystals is promoted (smaller crystals are formed) due to (1) the reduction in SSA and (2) the poor interaction between WO_x-ZrO₂ that stabilizes the t-ZrO₂ phase and prevents the crystallization of WO_x species.

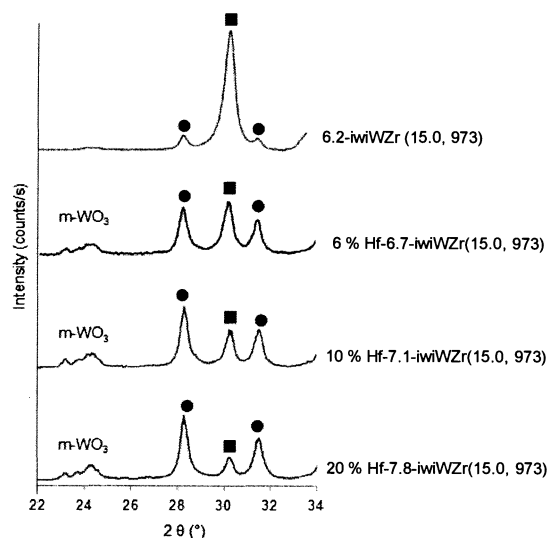


Figure 3.3. Powder XRD patterns of iwiWZr (15.0, 973) with different Hf-doping loadings, (●) m-ZrO₂ and (■) t-ZrO₂.

The crystallite diameters of all crystalline phases were estimated from the Scherrer equation. The m- and t-ZrO₂ crystallite diameters varied from ~13-23 nm with W surface density and calcination temperature. Calcination temperature does not have a significant effect on the t-ZrO₂ diameter but have an effect on the size of the m-ZrO₂. The size of the m-ZrO₂ crystals reaches a maximum at moderate ρ_{surf} and then decreases similar to the activity plots reported [42,49,63]. That effect is not seen with t-ZrO₂ crystals.

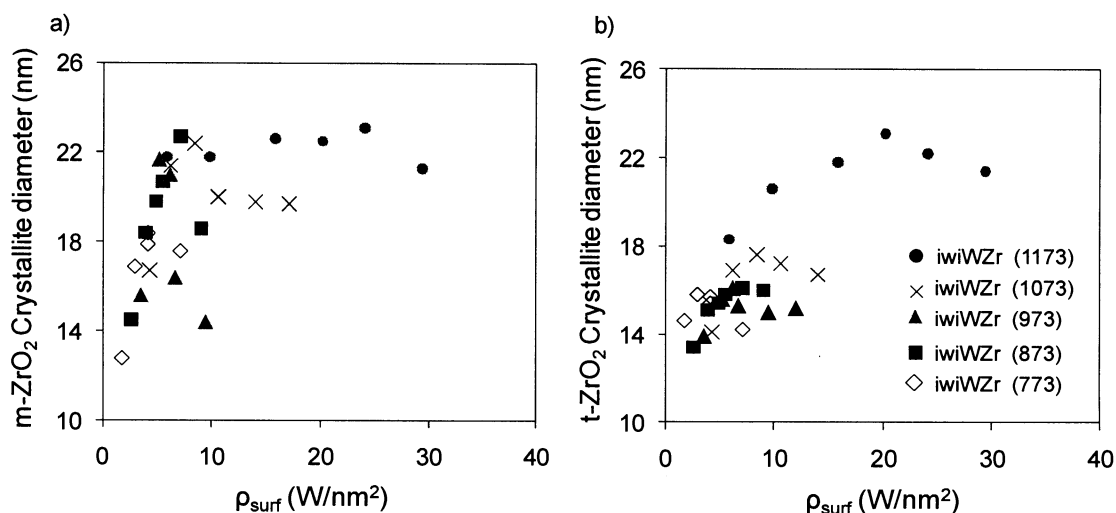


Figure 3.4. a) m-ZrO₂ and b) t-ZrO₂ crystallite diameters in iwiWZr materials as estimated by the Scherrer equation applied to the (101) and (111) reflections of t-ZrO₂ and m-ZrO₂, respectively, as a function of ρ_{surf} .

Estimates for XRD-detectable WO₃ (monoclinic phase) crystallite diameters are listed in Table 3.2. The combination of low temperature and low WO_x concentration yielded only XRD-undetectable amorphous tungsta species. Consistent with the literature, high calcination temperature led to the formation of XRD-detectable crystalline WO₃ nanoparticles. The onset of XRD-detectable WO₃ nanocrystallites was observed at a calcination temperature of 873 K with diameters > 5 nm. Much larger WO₃ crystallites (size \geq 50 nm) were formed at calcination temperatures \geq 973 K. Compared to the iwiWZr at similar W surface densities, the co-precipitated samples had comparable WO₃ crystal sizes and the sol-gel samples had smaller WO₃ crystal sizes. StsWZr had no detectible WO₃ crystals at similar W surface densities. Only at high enough calcination temperatures to significantly sinter the material (which gave W surface densities > 40 W/nm²) were WO₃ crystals observed, and even these crystals were smaller than those of incipient wetness impregnated samples of 20-30 W/nm² surface density.

Table 3.2. WO₃ crystallite diameters (nm) estimated from (002) XRD reflection of m-WO₃ and listed with W surface density values.

T _{calc.}	iwiWZr						coWZr	sgWZr	stsWZr	
	5.1 wt% ^a	10.1 wt%	15.0 wt%	19.5 wt%	23.3 wt%	26.6 wt%	18.3 wt%	11.9 wt%	50.7 wt%	
1173 K	–	>52 nm	>100 nm ^b	>100 nm	>100 nm	>100 nm	100 nm	34 nm	n/a ^e	
	(5.9 W/nm ²)	(9.8 W/nm ²)	(15.8 W/nm ²)	(20.2 W/nm ²)	(24.1 W/nm ²)	(29.4 W/nm ²)	(22.0 W/nm ²)	(15.9 W/nm ²)		
1073 K	–	–	50 nm	97 nm	99 nm	86 nm	97 nm	32 nm	52 nm	
	(4.3 W/nm ²)	(6.2 W/nm ²)	(8.4 W/nm ²)	(10.6 W/nm ²)	(14.0 W/nm ²)	(17.1 W/nm ²)	(15.4 W/nm ²)	(9.5 W/nm ²)	(52.7 W/nm ²)	
973 K	–	–	–	–	100 nm	84 nm	n/a ^d	–	50 nm	
	(3.5 W/nm ²)	(5.2 W/nm ²)	(6.2 W/nm ²)	(6.7 W/nm ²)	(9.5 W/nm ²)	(12.0 W/nm ²)	(15.2 W/nm ²)	(5.5 W/nm ²)	(42.5 W/nm ²)	
873 K	–	–	–	–	n/a ^c	n/a ^d	–	–	–	
	(2.6 W/nm ²)	(3.9 W/nm ²)	(4.9 W/nm ²)	(5.5 W/nm ²)	(7.1 W/nm ²)	(9.0 W/nm ²)	(8.6 W/nm ²)	(3.9 W/nm ²)	(12.1 W/nm ²)	
773 K	–	–	–	–	–	n/a ^d	n/a ^e	n/a ^e	–	
	(1.7 W/nm ²)	(2.9 W/nm ²)	(4.1 W/nm ²)	(4.1 W/nm ²)	(5.4 W/nm ²)	(7.1 W/nm ²)			(9.4 W/nm ²)	

^a WO₃-equivalent WO_x loading (wt%)

^b Limited by the accuracy of the instrument to ≤100 nm.

^c WO₃ crystallites not detectable by XRD. 7.1-iwiWZr (23.3, 873)) were the only one in the study with Raman-detectable WO₃ crystallites which were below the XRD detection limit. This indicates WO₃ grain sizes were in the 1-4 nm range.

^d WO₃ crystallites were observed, but were too small to reproducibly estimate their diameter using the Scherrer equation

^e Sample not calcined at this temperature.

3.4.3 *In situ* Raman spectroscopy analysis of WO_x species

Analysis of the samples under dehydrated conditions with *in situ* Raman spectroscopy corroborated the XRD results and provided additional molecular structural information about the XRD-undetectable phases. The Raman spectra of dehydrated WO_x/ZrO₂ samples prepared using the different methods are grouped and analyzed together based on similar surface density values, and presented with Raman regions colored for particular WO_x species (Figure 3.5 and 3.6). The Raman bands characteristic of crystalline ternary ZrW₂O₈ phases or heteropolyacids (H₄ZrW₁₂O₄₀) are not present, indicating all samples consisted of only WO_x overlayers on the ZrO₂ support.

At $\rho_{surf} \sim 4.0$ W/nm², all spectra shared similar features (Figure 3.5a) with high concentrations of polytungstates, slightly and highly distorted Zr-WO_x clusters. The band assigned to the slightly distorted Zr-WO_x clusters (~ 815 - 860 cm⁻¹) appeared to shift to lower wavenumber with increasing calcination temperature. At the same time the band attributed to the slightly distorted Zr-WO_x clusters at ~ 760 cm⁻¹ appears only for the samples calcined at higher temperatures > 773 K. The highly distorted Zr-WO_x band (~ 890 - 975 cm⁻¹) appears to split into two by increasing the calcination temperature, i.e. from ~ 900 cm⁻¹ at 773 K to 880 cm⁻¹ and 975 cm⁻¹ to 873 K. Differences were seen with 4.3-iwiWZr (5.1, 1073), which has two additional unidentified bands between 815-975 cm⁻¹.

The lowest ρ_{surf} samples (1.7-2.6 W/nm²) [63] showed mono-oxo W=O bands at ~ 1006 cm⁻¹ and shifts to ~ 1012 cm⁻¹ ($\rho_{surf} \sim 4.0$ W/nm²) due to vibrational coupling of adjacent terminal W=O bonds in surface WO_x polytungstates reflecting the polymerization of surface WO_x species with W surface density in the sub-monolayer

region [77]. For samples with $5.2 \text{ W/nm}^2 < \rho_{surf} < 7.0 \text{ W/nm}^2$, the mono-oxo W=O band for the polytungstate surface species and the W-O-W band of two different types of Zr- WO_x clusters are observed in all the Raman spectra. Similar features with the samples with $\rho_{surf} \sim 4.0 \text{ W/nm}^2$ are noticed in this case also. At 973 K, the WO_x amorphous species aggregate to form slightly distorted Zr- WO_x clusters and at 1073 K multiple unknown bands are detected possibly due to the stronger interaction of WO_x with the support. At 773 K (Figure 3.5b), a broad band is detected between 745-945 cm^{-1} that is characteristic of catalysts with high concentration of highly distorted Zr- WO_x .

For samples with $\rho_{surf} > 7.1 \text{ W/nm}^2$, the Raman spectra exhibit similar features (Figure 3.5c). The terminal mono-oxo W=O bands shifts to slightly higher wavenumbers (1018-1020 cm^{-1}) because of further polymerization of the surface WO_x species, consistent with larger polytungstate domains. Evidence of only highly distorted Zr- WO_x nanoclusters was seen from the band $\sim 900 \text{ cm}^{-1}$ for 9.5-iwiWZr(23.3,973), with the samples calcined $< 873 \text{ K}$ having a broad band in the region 910-980 cm^{-1} due to high concentrations of highly distorted Zr- WO_x nanoclusters. No evidence of slightly distorted Zr- WO_x nanoclusters is seen due to substantial formation of WO_3 crystals seen by the band at $\sim 807 \text{ cm}^{-1}$. Highly distorted Zr- WO_x species and polytungstates were only detected in coWZr, stsWZr and sgWZr catalysts at all calcination temperatures (Figure 3.6a). Slightly distorted Zr- WO_x nanoclusters are not detected for the samples prepared here and WO_3 nanocrystals are formed at higher calcination temperatures ($\geq 973 \text{ K}$).

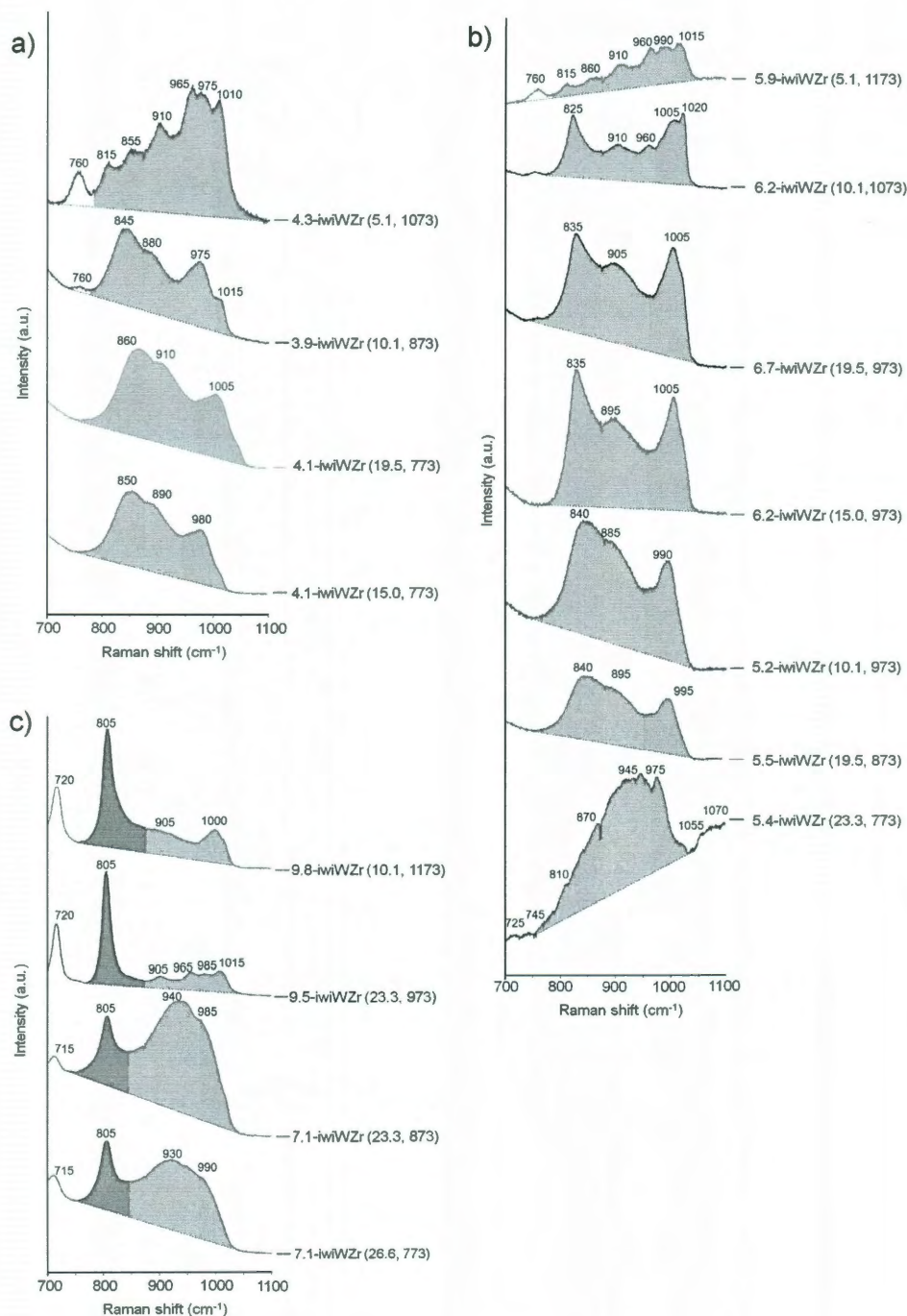


Figure 3.5. Raman spectra of dehydrated iwiWZr samples with ρ_{surf} (a) below 4.5 W/nm^2 , (b) between 5.2 and 7.0 W/nm^2 , and (c) above 7.1 W/nm^2 . ν_{as} of W-O-W of crystalline WO_3 (dark gray), ν_{as} of W-O-W and ν_s of W-O-Zr bonds of slightly distorted Zr-stabilized WO_x clusters (blue), ν_{as} of W-O-W and ν_s of W-O-Zr bonds of highly distorted Zr-stabilized WO_x clusters (gray), ν_s of the terminal W=O bond from square-pyramidal surface monotungstate and polytungstate WO_5 species (red). Dehydrated Raman spectra of iwiWZr collected at 298 K, adapted from *et al.* [63].

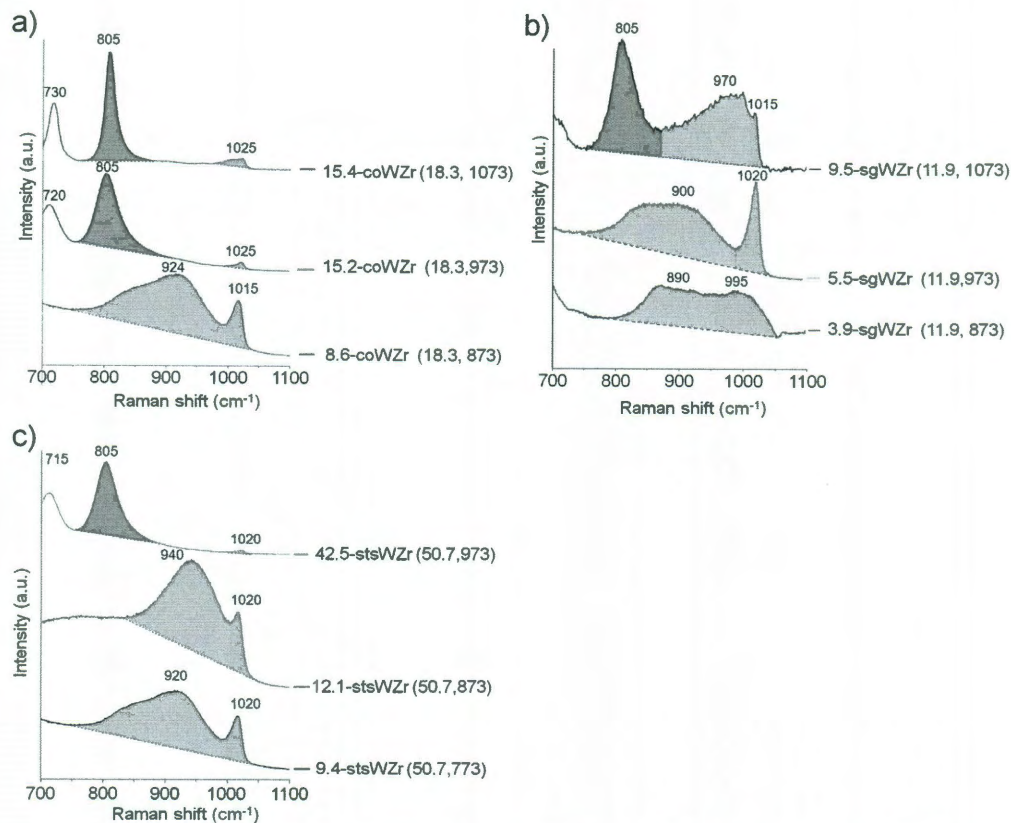


Figure 3.6. Raman spectra of dehydrated (a) coWZr, (b) sgWZr and (c) stsWZr samples. The color scheme is the same as that used in Figure 3.5.

Since highly distorted Zr-WO_x nanoclusters comprise surface WO_5 species, their domain size could be assessed very qualitatively by the band area for internal W-O stretches. A WO_x/ZrO_2 with small domain of highly distorted Zr-WO_x nanocluster would have a relatively small gray band, whereas one with large domains would have a relatively large gray band. Thus, the co-precipitated sample calcined at 873 K at a 8.6 W/nm^2 , the sol-gel-derived sample calcined at 973 K at 5.5 W/nm^2 and the surfactant-templated samples calcined at 773 and 873 K at 9.4 and 12.1 W/nm^2 respectively had "large" domains (Figure 3.6).

3.4.4 Reaction rate studies

An overlay of the nC_5 isomerization and CH_3OH dehydration activity curves for the *iwiWZr*(973) catalyst is presented in Figure 3.7a. The two curves exhibit maxima at ρ_{surf} of 6.2 and 6.7 W/nm^2 for nC_5 isomerization and CH_3OH dehydration, respectively, similar to previous reports [42,49]. This small difference in surface density values for maxima activities for different reactions has previously not been pointed out or discussed.

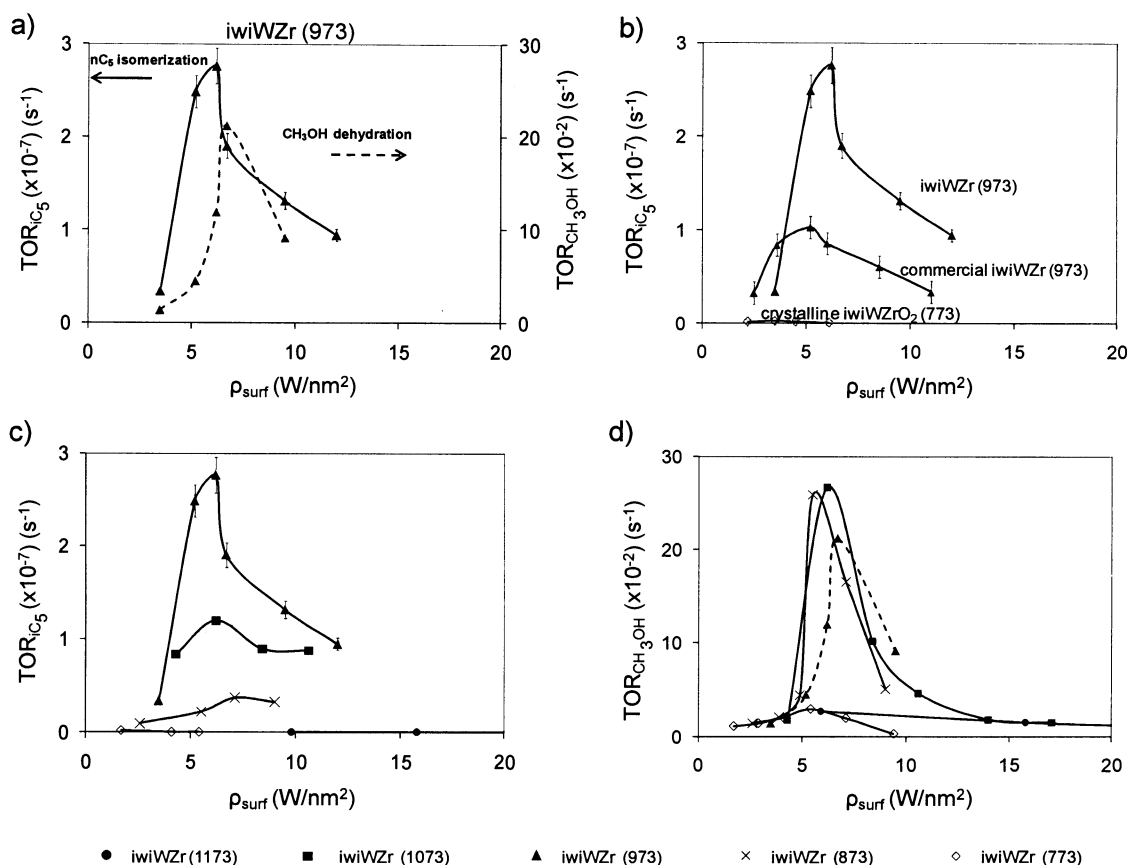


Figure 3.7. (a) Steady-state nC_5 isomerization and CH_3OH dehydration activity of *iwiWZr* (973). (a) Steady-state nC_5 isomerization activity comparison between *iwiWZr* (973), commercial *iwiWZr* (973) and crystalline *iwiWZrO_2* (773) (results adapted from Soutanidis *et al.*[64]). (c) Steady-state nC_5 isomerization turnover rates and (d) steady-state CH_3OH dehydration activity as a function of tungsten surface density for *iwiWZr* calcined at different temperatures (adapted from Ross *et al.* [63]). Steady-state nC_5 isomerization reaction conditions: 523 K, 1.04 atm, 1% nC_5 in He. Overall nC_5 conversion < 3%. Steady-state CH_3OH dehydration reaction conditions: 573 K, 1 atm, 6% CH_3OH , 12% O_2 in He and overall CH_3OH conversion < 10%.

The nC_5 isomerization activity for the iwiWZr(973 K), "commercial iwiWZr(973 K)" and "crystalline iwiWZrO₂(773 K)" series [64] are compared in Figure 3.7b. The "commercial iwiWZr(973 K)" catalyst reached its maximum isomerization activity at 5.2 W/nm² and the iwiWZr(973 K) catalyst reached its maximum activity at 6.2 W/nm². Compared to the latter, the commercial samples were ~ 3 times less active and ~15% less selective to isopentane (cf. ~48% [64] vs. 55%, Table 3.3). Thus, using a commercial source of zirconium oxyhydroxide in place of the lab-made source led to a less active isomerization catalyst at a given surface density, which is consistent with the formation of less-active WO₃ nanocrystals at lower surface densities, as previously reported [62]. That the onset of WO₃ crystallization did not occur at the same surface density is attributed to some subtle difference in the zirconium oxyhydroxide nanostructures present in the home and commercial starting materials. The "crystalline iwiWZrO₂" catalysts were nearly inactive for nC_5 isomerization [64], though they are active for CH₃OH dehydration [63], indicating the formed active sites did not satisfy the surface acidity requirements for these two reactions.

Table 3.3. Reaction rate and product selectivity results of WO_x/ZrO₂ materials

Sample	Steady-state CH ₃ OH dehydration ^a		Steady-state nC_5 isomerization ^b	
	Selectivity DME (%)	TOR ($\times 10^{-2} \text{ s}^{-1}$)	Selectivity iC_5 (%)	TOR_{iC_5} ($\times 10^{-7} \text{ s}^{-1}$)
1.7-iwiWZr (5.1, 773)	100	1.07	10	0.02
2.9-iwiWZr (10.1, 773)	100	1.37	–	–
4.1-iwiWZr (15.0, 773)	100	1.91	11	0.01
4.1-iwiWZr (19.5, 773)	100	2.00	–	–
5.4-iwiWZr (23.3, 773)	100	2.90	12	0.02
7.1-iwiWZr (26.6, 773)	100	1.93	–	–
2.6-iwiWZr (5.1, 873)	100	1.38	29	0.09
3.9-iwiWZr (10.1, 873)	100	2.03	–	–
4.9-iwiWZr (15.0, 873)	100	4.38	–	–

Table 3.3. (continued)

Sample	Steady-state CH ₃ OH dehydration ^a		Steady-state nC ₅ isomerization ^b	
	Selectivity DME (%)	TOR ($\times 10^{-2} \text{ s}^{-1}$)	Selectivity iC ₅ (%)	TOR _{iC₅} ($\times 10^{-7} \text{ s}^{-1}$)
5.5-iwiWZr (19.5, 873)	100	25.90	26	0.22
7.1-iwiWZr (23.3, 873)	100	16.50	32	0.37
9.0-iwiWZr (26.6, 873)	100	5.00	34	0.32
3.5-iwiWZr (5.1, 973)	100	1.36	51	0.34
5.2-iwiWZr (10.1, 973)	100	4.42	55	2.67
6.2-iwiWZr (15.0, 973)	100	11.90	54	2.76
6.7-iwiWZr (19.5, 973)	100	21.20	47	1.63
9.5-iwiWZr (23.3, 973)	100	9.10	48	1.31
12.0-iwiWZr (26.6, 973)	100	12.80	49	0.94
4.3-iwiWZr (5.1, 1073)	100	1.72	43	0.83
6.2-iwiWZr (10.1, 1073)	100	26.70	42	1.19
8.4-iwiWZr (15.0, 1073)	100	10.10	43	0.89
10.6-iwiWZr (19.5, 1073)	100	4.58	45	0.87
14.0-iwiWZr (23.3, 1073)	100	1.76	–	–
17.1-iwiWZr (26.6, 1073)	100	1.45	–	–
5.9-iwiWZr (5.1, 1173)	100	2.67	~0	~0
9.8-iwiWZr (10.1, 1173)	–	–	~0	~0
15.8-iwiWZr (15.0, 1173)	100	1.48	~0	~0
20.2-iwiWZr (19.5, 1173)	100	1.18	~0	~0
24.1-iwiWZr (23.3, 1173)	100	1.12	~0	~0
29.4-iwiWZr (26.6, 1173)	100	1.07	~0	~0
8.6-coWZr (18.3, 873)	100	0.56	–	–
15.2-coWZr (18.3, 973)	100	0.43	–	–
15.4-coWZr (18.3, 1073)	98 ^d	0.86	~0	~0
22.0-coWZr (18.3, 1173)	100	0.37	–	–
3.9-sgWZr (11.9, 873)	100	0.12	~0	~0
5.5-sgWZr (11.9, 973)	100	0.70	~0	~0
9.5-sgWZr (11.9, 1073)	100	2.02	–	–
15.9-sgWZr (11.9, 1173)	100	1.84	–	–
9.4-stsWZr (50.7, 873)	100	0.27	~0	~0
12.1-stsWZr (50.7, 873)	73 ^e	0.29	~0	~0
42.5-stsWZr (50.7, 973)	–	–	–	–
52.7-stsWZr (50.7, 1073)	100	0.35	–	–

^aSteady-state CH₃OH dehydration reaction conditions: 573 K, 1 atm, 6% CH₃OH, 12% O₂ in He. Overall CH₃OH conversion < 10%.

^bSteady-state nC₅ isomerization reaction conditions: 523 K, 1.04 atm, 1% nC₅ in He. Overall nC₅ conversion < 3%.

^cLow activity samples, results within the error range

^dDimethoxy methane trace was detected

^eCO₂ was detected.

The iwiWZr catalyst series calcined from 873-1073 K possess both nC₅ isomerization (Figure 3.7c) and CH₃OH dehydration activity (Figure 3.7d) with *TOR* maxima at $\rho_{surf} \sim 6 \text{ W/nm}^2$ and $\sim 7 \text{ W/nm}^2$ respectively, consistent with activity dependences of *o*-xylene [42] at $\rho_{surf} \sim 10 \text{ W/nm}^2$ and 2-butanol dehydration [49] at $\rho_{surf} \sim 7\text{-}8 \text{ W/nm}^2$. For nC₅ isomerization, catalysts calcined at 973 K are ~ 2 times more active than catalysts calcined at 1073 K and ~ 10 times more active than catalysts calcined at 873 K. The nC₅ isomerization rate-surface density curves for these samples does not fall onto a common curve, unlike the CH₃OH dehydration-surface curves for the same samples. Both the iwiWZr(773 K) and iwiWZr(1173 K) catalyst series are slightly active for CH₃OH dehydration and only iwiWZr(773 K) shows low activity for nC₅ isomerization.

The coWZr, sgWZr, and stsWZr catalysts have no nC₅ isomerization activity and exhibited low CH₃OH dehydration activity (Table 3.3). The coWZr catalysts studied here, possessed low methanol dehydration activity and no nC₅ isomerization activity, though it was reported to be active for nC₅ isomerization carried out at 350 psig and 210 °C under H₂ co-feed [31]. The sol-gel-derived catalysts shared similar structural features to the stsWZr catalysts and consisted only of polytungstates and highly distorted Zr-WO_x clusters at moderate ρ_{surf} . These material possessed low methanol dehydration activity and no nC₅ isomerization activity, similar to iwiWZr calcined at 773 K and 1173 K.

Every catalyst was 100% selective for CH₃OH conversion to dimethyl ether (DME) (Table 3.3). The 15.4-coWZr (18.3,1073) and 12.1-stsWZr(50.7,873) catalysts surprisingly produced small amounts of dimethoxymethane (2%) and CO₂ (27%) suggesting the presence of some redox and basic sites, respectively [80]. For nC₅

isomerization to isopentane (iC_5), the most selective catalysts, 45-55% selectivity, associated with the $iwiWZr$ series calcined at 973 K. The next most selective catalysts were the $iwiWZr$ (1073 K) and $iwiWZr$ (873 K) catalyst series with 43-45% and 26-34%, respectively. The $iwiWZr$ (773 K) catalysts exhibited lowest isomerization selectivity ($\sim 10\%$), favoring the formation of cracking products C_2-C_4 as previously observed [64]. The $iwiWZr$ (1173 K) catalysts were inactive at all ρ_{surf} for n-pentane isomerization.

In Figure 3.8 the effect of Hf in the nC_5 isomerization activity of $iwiWZr$ is presented. It is noticed that Hf-doping has a drastic negative effect on nC_5 isomerization. An addition of 6% Hf drops activity to less than $10^{-7} s^{-1}$, similar to the commercial $iwiWZr$ samples. 10 % Hf is enough to complete deactivate the catalyst with activities remaining below $10^{-8} s^{-1}$ similar to the $WZrO_2$ presented in Chapter 2.

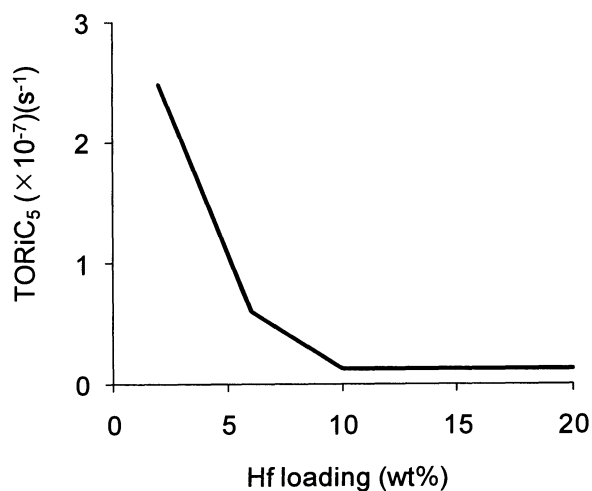


Figure 3.8. Hf loading effect on nC_5 isomerization activity of 6.2- $iwiWZr$ (15.0, 973)

3.5 Discussion

3.5.1 Comparison of XRD and *in situ* Raman spectroscopy

The intensity of both the XRD peaks and Raman bands generally increase with the dimension of the structure (e.g., larger WO_3 crystallites > smaller crystallites) [63]. XRD can only detect crystalline domains with long-range order at least as long as the coherent scattering length of the x-ray source, which is typically 4-5 nm [81]. The volume averaging aspect of XRD means that larger crystals disproportionately contribute to the overall XRD signal. Thus, XRD cannot detect structures with small domain size and favors large crystalline domains (WO_3 nanocrystals in the 34-100nm range and ZrO_2 nanocrystals in the ~13-23nm range). Raman spectroscopy, however, can detect both nanocrystal domains smaller than 4-5 nm and amorphous phases (surface species and clusters). Polytungstates, Zr- WO_x clusters, and WO_3 crystals are identified in agreement with recent optical microscopy studies [63-65]. High resolution analysis of the Raman spectra allows the identification of two distinct Zr- WO_x clusters (slightly and highly distorted). A combination of XRD and Raman spectroscopy allows mapping of all the different species from amorphous WO_x species to larger WO_3 crystals.

3.5.2 Influence of synthesis methods on the WO_x structure

The synthesis method and the different parameters (calcination temperature and ρ_{surf}) play a significant role in WO_x species distribution. The most diverse iwiWZr catalysts show high concentrations of polytungstates, two types of distorted Zr- WO_x clusters and WO_3 crystals at moderate and higher ρ_{surf} . Slightly and highly distorted Zr- WO_x clusters are detected at $\rho_{surf} \geq 3.9 \text{ W/nm}^2$ and their concentration reaches maximum

at $\sim 6\text{-}7$ W/nm². By increasing the calcination temperature at a constant ρ_{surf} , high order within the domain of the slightly and highly distorted Zr-WO_x cluster is achieved as captured by the Raman band shift to lower wavenumbers. Overall, higher calcination temperatures (higher than the WO₃ Tammann temperature (~ 873 K) [82]) allow thermodynamic forces to erase the structural advantages engineered at lower temperatures, ultimately reorganizing all frameworks toward a thermodynamically equivalent structure. The samples calcined between 873-1173 K have qualitatively similar Raman features. At 773K, polytungstates and highly distorted Zr-WO_x clusters are the dominant species. Activated diffusion along grain boundaries, dislocations, pinholes and voids [83] does not take place to great extent at the lower calcination temperatures, resulting to lower concentration of slightly distorted Zr-WO_x. At 1173 K two new unidentified bands appear, possibly due to two distinct Zr-WO_x species.

coWZr, stsWZr and sgWZr share similar surface properties. High concentrations of polytungstates and highly distorted Zr-WO_x clusters at moderate and higher ρ_{surf} are detected, with the absence of slightly distorted Zr-WO_x clusters indicating a strong interaction between the ZrO₂ support and the WO_x species. For these materials, WO₃ crystals are formed at much higher ρ_{surf} . The stsWZr catalysts possess the largest amount of highly distorted Zr-WO_x clusters in this study and no WO₃ crystals are detected up to 12.1 W/nm².

3.5.3 CH₃OH dehydration and nC₅ isomerization

Two different probe molecules were used to study the structure-activity relationship of WO_x/ZrO₂. iwiWZr catalysts calcined from 873-1173 K display similar

features; very high concentrations of slightly distorted Zr-WO_x clusters, high concentrations of highly distorted Zr-WO_x clusters and lower concentrations of polytungstates. At a specific ρ_{surf} the distribution of the species shifts from the amorphous polytungstates to the slightly distorted Zr-WO_x clusters by increasing calcination temperature. At lower calcination temperatures (773 K), the sample surface is covered by polytungstates and highly distorted Zr-WO_x clusters.

iwiWZr are very active CH₃OH dehydration and nC₅ isomerization catalysts only when calcined from 873-1073 K, with the catalytic activity strongly correlated to the concentration of the slightly distorted Zr-WO_x clusters. At 1173 K, the significant decrease in SSA suggests that even though the samples have high concentrations of the slightly distorted Zr-WO_x clusters, they are probably inaccessible to the CH₃OH and nC₅ molecules. iwiWZr calcined at 973K possess high activity for nC₅ isomerization, and are much more active than the catalysts calcined at 873 K and 1073 K (Figure 3.7c, Table 3.3). Similar observations about WO_x/ZrO₂ were reported for nC₅ isomerization by Scheithauer *et al.*[36] and for acetic acid esterification by López *et al.*[84]. This effect is strongly correlated to a bimolecular mechanism where the formation of an intermediate surface species (C₁₀ for nC₅ isomerization) is critical. Between 973-1073 K the slightly distorted Zr-WO_x cluster density (defined as the number of slightly distorted Zr-WO_x cluster sites per nm²) possibly promotes the formation of such an intermediate. This is not a requirement for CH₃OH dehydration[63], 2-butanol dehydration [49] and *o*-xylene isomerization[42], which explains sole activity dependence to ρ_{surf} .

The iwi catalysts calcined at 773 K were slightly active for dehydration and non-active for isomerization, indicating that the dehydration reaction was catalyzed by the

acidic active sites associated with slightly distorted Zr-WO_x clusters and other WO_x surface species [63]. The curve relating surface density to methanol dehydration activity was similar in shape but different in maximum position. This is consistent with CH₃OH dehydration being a less acid demanding reaction compared to *n*C₅ isomerization, allowing a larger population of WO_x surface species (possibly highly distorted Zr-WO_x clusters) to catalyze this reaction. Beyond this conclusion, it was difficult to be more definitive about structural differences as there were not enough data points collected between 6 and 7 W/nm² for the samples calcined at 873 K and 1073 K.

3.5.4 Hafnium doping effect on the formation of Zr-WO_x sites

Maximizing the concentration of the sub-nm Zr-WO_x clusters is achieved by controlling the WO_x loading and calcination temperature and by selecting the appropriate support. Low concentrations of Hf-impurities in the amorphous supports are desired to increase the catalytic activity of WO_x/ZrO₂. The hafnium concentration had an adverse impact on the metastable tetragonal ZrO₂ (t-ZrO₂) crystal phase accompanied with an exponential decrease of the *n*-pentane isomerization activity of WO_x/ZrO₂. Even though the t-ZrO₂ is not directly correlated to the catalytic activity of WO_x/ZrO₂ it appears to be the preferred nucleation phase of the sub-nm Zr-WO_x species. Hafnium impurities prevent the WO_x-precursor to form sub-nm Zr-WO_x clusters and promote the growth of monoclinic ZrO₂ that appears to promote aggregation of the amorphous WO_x species to XRD-detectable WO₃ crystals. The difference in Hf concentrations could be a reason why the commercial and “lab-made” amorphous support generated samples with different catalytic activity.

3.6 Summary and conclusions

WO_x/ZrO_2 catalysts were synthesized in four different manners. Coprecipitation, sol-gel, and surfactant-templating methods led to WO_x/ZrO_2 materials that, after calcination, had only highly distorted Zr- WO_x nanoclusters and polytungstates. In comparison, incipient wetness impregnation led to WO_x/ZrO_2 materials with populations of polytungstates, slightly and highly distorted Zr- WO_x clusters that were adjustable by WO_3 weight content, calcination temperature, and support precursor. The appearance of WO_3 nanocrystallites (which were detectible through x-ray diffraction and Raman spectroscopy) in these samples coincided with the maximum concentration of slightly distorted Zr- WO_x clusters (which are Raman detectible but not XRD detectible). Essentially all WO_x/ZrO_2 types were catalytically active for methanol dehydration. As the only type to be active for *n*-pentane isomerization, the impregnated WO_x/ZrO_2 material had volcano-shape catalytic activity for both reactions as a function of W surface density. *n*-pentane isomerization activity is more sensitive than methanol dehydration to the presence and relative density of slightly distorted Zr- WO_x clusters. Hf-doping has negative effect on the formation of slightly distorted Zr- WO_x clusters that possibly emerge on metastable *t*- ZrO_2 .

3.7 References

1. C. D. Chang, R. D. Bastian, S. Han and J. G. Santiesteban. 1995. U.S. Patent No. 5,382,731.
2. C. D. Chang, S. Han, J. D. Lutner and J. G. Santiesteban. 1995. U.S. Patent No. 5,449,847.

3. C. D. Chang, S. Han, J. G. Santiesteban, M. M. Wu and Y. Xiong. 1995. U.S. Patent No. 5,453,556.
4. C. D. Chang, J. G. Santiesteban, D. S. Shihabi and S. A. Stevenson. 1995. U.S. Patent No. 5,401,478.
5. C. D. Chang, J. C. Cheng, S. Han, J. G. Santiesteban and D. E. Walsh. 1996. U.S. Patent No. 5,563,311.
6. C. D. Chang, F. T. DiGuseppi and S. Han. 1996. U.S. Patent No. 5,563,310.
7. C. D. Chang, S. Han, D. J. Martenak, J. G. Santiesteban and D. E. Walsh. 1996. U.S. Patent No. 5,543,036.
8. C. D. Chang, S. Han, J. G. Santiesteban, M. M. Wu and Y. Xiong. 1996. U.S. Patent No. 5,516,954.
9. C. D. Chang, C. T. Kresge, J. G. Santiesteban and J. C. Vartuli. 1996. U.S. Patent No. 5,510,309.
10. C. D. Chang, J. G. Santiesteban, D. S. Shihabi, D. L. Stern and J. C. Vartuli. 1996. U.S. Patent No. 5,552,128.
11. C. D. Chang, T. J. Huang, J. G. Santiesteban and J. C. Vartuli. 1997. U.S. Patent No. 5,608,133.
12. C. D. Chang, F. T. DiGuseppi, S. Han, J. G. Santiesteban and D. L. Stern. 1998. U.S. Patent No. 5,854,170.
13. C. D. Chang, F. T. DiGuseppi and J. G. Santiesteban. 1998. U.S. Patent No. 5,780,382.
14. C. D. Chang, S. D. Hellring, D. O. Marler, J. G. Santiesteban and J. C. Vartuli. 1998. U.S. Patent No. 5,780,703.
15. C. D. Chang, J. G. Santiesteban and D. L. Stern. 1998. U.S. Patent No. 5,719,097.

16. C. D. Chang, S. Han, R. A. Morrison and J. G. Santiesteban. 1999. U.S. Patent No. 5,993,643.
17. C. D. Chang, J. G. Santiesteban and D. L. Stern. 2000. U.S. Patent No. 6,080,904.
18. K. Murata, T. Hayakawa and S. Hamakawa. 2000. U.S. Patent No. 6,071,849.
19. C. D. Chang, S. Han, D. J. Martenak, J. G. Santiesteban and D. E. Walsh. 2001. U.S. Patent No. 6,217,747 B1.
20. R. D. Gillespie. 2004. U.S. Patent No. 6,818,589 B1.
21. J. Y. Ying and J. Xu. 2004. U.S. Patent No. 6,767,859 B2.
22. R. D. Gillespie. 2005. U.S. Patent No. 6,977,322 B2.
23. Y.-N. Kim. 2005. U.S. Patent No. 6,855,661 B2.
24. E. Iglesia, D. G. Barton, S. L. Soled, S. Miseo, J. E. Baumgartner, W. E. Gates, G. A. Fuentes and G. D. Meitzner, *Studies in Surface Science and Catalysis* 101 (1996) 533-542.
25. D. S. Kim, M. Ostromecki and I. E. Wachs, *J. Mol. Catal. A-Chem.* 106 (1996) 93-102.
26. G. Larsen, S. Raghavan, M. Marquez and E. Lotero, *Catal. Lett.* 37 (1996) 57-62.
27. B. Zhao, X. Xu, J. Gao, Q. Fu and Y. Tang, *Journal of Raman Spectroscopy* 27 (1996) 549-554.
28. R. A. Boyse and E. I. Ko, *J. Catal.* 171 (1997) 191-207.
29. D. Gazzoli, M. Valigi, R. Dragone, A. Marucci and G. Mattei, *J. Phys. Chem. B* 101 (1997) 11129-11135.
30. G. Larsen, E. Lotero, L. M. Petkovic and D. S. Shobe, *J. Catal.* 169 (1997) 67-75.

31. J. G. Santiesteban, J. C. Vartuli, S. Han, R. D. Bastian and C. D. Chang, *J. Catal.* 168 (1997) 431-441.
32. S. R. Vaudagna, R. A. Comelli and N. S. Figoli, *Appl. Catal. A-Gen.* 164 (1997) 265-280.
33. J. C. Yori, C. R. Vera and J. M. Parera, *Appl. Catal. A-Gen.* 163 (1997) 165-175.
34. D. G. Barton, S. L. Soled and E. Iglesia, *Topics in Catalysis* 6 (1998) 87-99.
35. L. M. Petkovic, J. R. Bielenberg and G. Larsen, *J. Catal.* 178 (1998) 533-539.
36. M. Scheithauer, T. K. Cheung, R. E. Jentoft, R. K. Grasselli, B. C. Gates and H. Knozinger, *J. Catal.* 180 (1998) 1-13.
37. M. Scheithauer, R. K. Grasselli and H. Knozinger, *Langmuir* 14 (1998) 3019-3029.
38. J. R. Sohn and M. Y. Park, *Langmuir* 14 (1998) 6140-6145.
39. J. R. Sohn and M. Y. Park, *Journal of Industrial and Engineering Chemistry* 4 (1998) 84-93.
40. N. Vaidyanathan, M. Houalla and D. M. Hercules, *Surface and Interface Analysis* 26 (1998) 415-419.
41. D. G. Barton, M. Shtein, R. D. Wilson, S. L. Soled and E. Iglesia, *J. Phys. Chem. B* 103 (1999) 630-640.
42. D. G. Barton, S. L. Soled, G. D. Meitzner, G. A. Fuentes and E. Iglesia, *J. Catal.* 181 (1999) 57-72.
43. N. Naito, N. Katada and M. Niwa, *J. Phys. Chem. B* 103 (1999) 7206-7213.
44. J. C. Vartuli, J. G. Santiesteban, P. Traverso, N. Cardona-Martinez, C. D. Chang and S. A. Stevenson, *J. Catal.* 187 (1999) 131-138.

45. C. D. Baertsch, R. D. Wilson, D. G. Barton, S. L. Soled and E. Iglesia, *Studies in Surface Science and Catalysis 130D* (2000) 3225-3230.
46. R. D. Wilson, D. G. Barton, C. D. Baertsch and E. Iglesia, *J. Catal.* 194 (2000) 175-187.
47. C. D. Baertsch, S. L. Soled and E. Iglesia, *J. Phys. Chem. B* 105 (2001) 1320-1330.
48. G. S. Wong, D. D. Kragten and J. M. Vohs, *J. Phys. Chem. B* 105 (2001) 1366-1373.
49. C. D. Baertsch, K. T. Komala, Y. H. Chua and E. Iglesia, *J. Catal.* 205 (2002) 44-57.
50. D. C. Calabro, J. C. Vartuli and J. G. Santiesteban, *Topics in Catalysis* 18 (2002) 231-242.
51. S. De Rossi, G. Ferraris, M. Valigi and D. Gazzoli, *Appl. Catal. A-Gen.* 231 (2002) 173-184.
52. N. Vaidyanathan, D. M. Hercules and M. Houalla, *Analytical and Bioanalytical Chemistry* 373 (2002) 547-554.
53. M. Valigi, D. Gazzoli, I. Pettiti, G. Mattei, S. Colonna, S. De Rossi and G. Ferraris, *Appl. Catal. A-Gen.* 231 (2002) 159-172.
54. G. Ferraris, S. De Rossi, D. Gazzoli, I. Pettiti, M. Valigi, G. Magnacca and C. Morterra, *Appl. Catal. A-Gen.* 240 (2003) 119-128.
55. S. Kuba, P. Lukinskas, R. Ahmad, F. C. Jentoft, R. K. Grasselli, B. C. Gates and H. Knozinger, *J. Catal.* 219 (2003) 376-388.
56. S. Kuba, P. Lukinskas, R. K. Grasselli, B. C. Gates and H. Knozinger, *J. Catal.* 216 (2003) 353-361.
57. J. Macht, C. D. Baertsch, M. May-Lozano, S. L. Soled, Y. Wang and E. Iglesia, *J. Catal.* 227 (2004) 479-491.

58. V. M. Benitez, J. C. Yori, C. R. Vera, C. L. Pieck, J. M. Grau and J. M. Parera, *Industrial & Engineering Chemistry Research* 44 (2005) 1716-1721.
59. I. E. Wachs, J. M. Jehng and W. Ueda, *J. Phys. Chem. B* 109 (2005) 2275-2284.
60. M. S. Wong, in: J. L. G. Fierro, (Ed.), *Metal oxides: Chemistry and applications*, Taylor & Francis Group, LLC, Boca Raton. 31-54.
61. M. Hino and K. Arata, *Journal of the Chemical Society-Chemical Communications* (1988) 1259-1260.
62. W. V. Knowles, M. O. Nutt and M. S. Wong, *Supported Metal Oxides and Surface Density Metric*. Taylor and Francis: Boca Raton, 2006.
63. E. I. Ross, W. V. Knowles, T. Kim, M. S. Wong, W. Zhou, C. J. Kiely and I. E. Wachs, *J. Catal.* 256 (2008) 108-125.
64. N. Soulntanidis, W. Zhou, A. C. Psarras, A. J. Gonzalez, E. F. Iliopoulou, C. J. Kiely, I. E. Wachs and M. S. Wong, *J. Am. Chem. Soc.* 132 (2010) 13462-13471.
65. W. Zhou, E. I. Ross-Medgaarden, W. V. Knowles, M. S. Wong, I. E. Wachs and C. J. Kiely, *Nat Chem* 1 (2009) 722-728.
66. T. Kim, A. Burrows, C. J. Kiely and I. E. Wachs, *J. Catal.* 246 (2007) 370-381.
67. H. W. Doughty, *J. Am. Chem. Soc.* 46 (1924) 2707-2709.
68. D. A. Skoog, D. M. West, F. J. Holler and S. R. Crouch, *Fundamentals of Analytical Chemistry*. Saunders College Pub, 2003.
69. D. A. Ward and E. I. Ko, *Chem. Mat.* 5 (1993) 956-969.
70. D. A. Ward and E. I. Ko, *J. Catal.* 157 (1995) 321-333.
71. M. S. Wong, E. S. Jeng and J. Y. Ying, *Nano Letters* 1 (2001) 637-642.

72. P. A. Webb and C. Orr, Analytical methods in fine particle technology. Micromeritics Instrument Corporation, Norcross, GA, 1997, 172.
73. C. T. Kresge, M. E. Leonowicz, W. J. Roth, J. C. Vartuli and J. S. Beck, Nature 359 (1992) 710-712.
74. R. C. Garvie and P. S. Nicholson, J. Am. Ceram. Soc. 55 (1972) 303-305.
75. H. Toraya, M. Yoshimura and S. Sōmiya, J. Am. Ceram. Soc. 67 (1984) C119-C121.
76. P. Scherrer, Nachrichten von der Gesellschaft der Wissenschaften zu Göttingen, Mathematisch-Physikalische Klasse 2 (1918) 98-100.
77. L. Nakka, J. E. Molinari and I. E. Wachs, J. Am. Chem. Soc. 131 (2009) 15544-15554.
78. E. L. Lee and I. E. Wachs, The Journal of Physical Chemistry C 111 (2007) 14410-14425.
79. N. Lohitharn, E. Lotero and J. G. Goodwin Jr, J. Catal. 241 (2006) 328-341.
80. M. Badlani and I. E. Wachs, Catal. Lett. 75 (2001) 137-149.
81. V. G. Keramidas and W. B. White, J. Am. Ceram. Soc. 57 (1974) 22-24.
82. G. Tammann, Fristallisieren und Schmelzen. Johann Ambrosius Barth, Leipzig, 1903, 26-46.
83. M.-A. Nicolet, Thin Solid Films 52 (1978) 415-443.
84. D. E. López, K. Suwannakarn, D. A. Bruce and J. G. Goodwin Jr, J. Catal. 247 (2007) 43-50.

Chapter 4

Bimolecular *n*-pentane isomerization mechanism over WO_x/ZrO_2

4.1 Introduction

4.1.1 Paraffin isomerization studies

Paraffin isomerization is an important catalytic reaction that requires very strong acid catalytic material. Super acid catalysts, such as chlorinated $\text{Pt}/\text{Al}_2\text{O}_3$ [1-3] and heteropoly acids (HPAs) [4-9], have the ability to isomerize light alkanes such as *n*-butane (nC_4) and *n*-pentane (nC_5), and heavier ones such as *n*-hexane (nC_6) and *n*-heptane (nC_7) via a monomolecular reaction pathway. SO_4/ZrO_2 [10-23], WO_x/ZrO_2 [5,19,24-29], and zeolites [3,5,30-34], even though less acidic [35-37] than the former, have been also classified as super acid catalysts [23,37-40] and isomerize lighter alkanes primarily via a bimolecular mechanism.

A monomolecular mechanism is highly desired [5,28], since very few byproducts are formed, which means isomerization selectivities are usually very high (usually > 80%). Super acids achieve high activities and selectivities but are in many cases chemically and thermally unstable, meaning that continuous regeneration or even complete replacement of the catalyst is required. Chlorinated $\text{Pt}/\text{Al}_2\text{O}_3$ has been successfully used in petroleum industry but fails to meet the chemical stability standards (continuous chlorination is required [8,41] due to losses of Cl^- that forms of HCl). HCl is corrosive [8] and harmful and therefore imposes a further purification step that increases the overall production cost. HPAs are very active but thermally unstable since they decompose at low temperatures (usually lower than 773 K), which makes their regeneration virtually impossible in industrial applications. SO_4/ZrO_2 has been studied

extensively [10-18,20,22,23,28,42-48] for replacing current catalysts, especially for the isomerization of nC_4 . Even though they are more stable than Pt/ Al_2O_3 and HPAs, severe deactivation caused by coke deposition [20] and the formation of the undesired H_2S [47,49] in the presence of H_2O [49,50] are two important problems. Zeolites are stable material [41] but less selective [31,51], since they require higher reaction temperatures [5,8,26,30,41], which promote cracking over isomerization.

WO_x/ZrO_2 [19,24-27,29,52-55] catalysts have been proposed as a promising catalyst that satisfies the industrial requirements in terms of chemical and thermal stability. To our knowledge, no studies have identified the prevailing nC_5 isomerization mechanism over unpromoted WO_x/ZrO_2 catalysts. In this study, we report the nC_5 isomerization activity and selectivity of a WO_x/ZrO_2 catalyst calcined at 973 K with moderate surface density (5.2 W/nm^2). Two different olefin molecules were co-fed (propylene (C_3^-) and 1-pentene ($1-C_5^-$)) separately along with nC_5 to investigate if the reaction proceeds via a monomolecular or a bimolecular mechanism. The optimum concentration of $1-C_5^-$, which is the best isomerization promoter, was studied by adjusting the concentration of $1-C_5^-$ in the nC_5 stream. The purpose of this chapter is to verify if n -pentane isomerization proceeds on WO_x/ZrO_2 via a bimolecular mechanism on Zr- WO_x sites.

4.1.2 Paraffin isomerization mechanism

The isomerization mechanism of alkanes is generally accepted to be initiated via their transformation to a carbocation [5,10-29]. This model was established by Whitmore [56] in 1932 for the dehydration of alcohols and later for hydrocarbon cracking [57,58]

using liquid acids. Using various spectroscopic techniques the existence and stability of carbocations was studied on solid acid catalysts that were able to stabilize the formation of cations on their catalytic surface [17,19,24,29,52,53,55,59-63]. Carbocations are classified as carbenium and carbonium ions depending on the coordination of the positively charged carbon atom. Carbenium ions contain a three-coordinated carbon atom that is formed upon hydride abstraction (Figure 4.1a) on Lewis acid sites and carbonium ion intermediates contain a five-coordinated carbon atom that is formed upon protonation of the carbon atom (Figure 4.1b) by a Brønsted acid at elevated temperatures, low pressures and low conversions. Carbonium intermediates cannot be detected. They decompose readily to carbenium ions giving a trivalent carbenium ion and H₂.

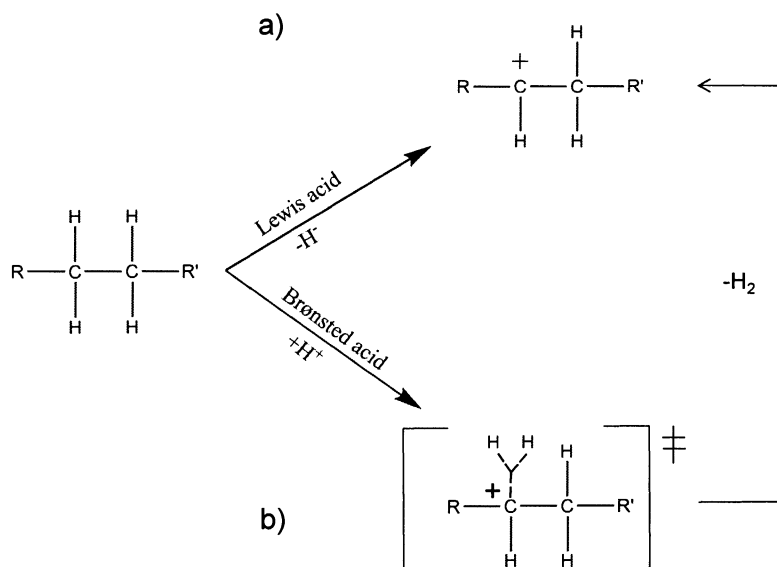


Figure 4.1. a) Carbenium ion formation via hydride abstraction of alkanes on Lewis acid sites and b) carbonium ion formation via protonation of alkanes on Brønsted acid sites

The stable carbenium ion can undergo cracking, alkylation or isomerization via different mechanisms. Two possible isomerization mechanisms are considered in

literature: a monomolecular isomerization mechanism that proceeds via cyclization of the carbenium ion followed by ring opening and a bimolecular isomerization mechanism that proceeds via the formation of higher molecular weight intermediate (usually composed by a carbenium ion and another molecule. Finally, cracking generates isomerization or other byproducts.

4.1.3 *n*-pentane isomerization mechanism

SO₄/ZrO₂ has been the model catalyst for studying monomolecular and the bimolecular alkane isomerization. nC₅ isomerization was found to proceed via both mechanisms on SO₄/ZrO₂ [21,61], with the latter being activated by the *in situ* formation of unsaturated surface species. Pt-promoted SO₄/ZrO₂ [17,59-61] studies revealed that nC₅ isomerization proceeds via a monomolecular (intra-molecular) mechanism on Lewis acid sites and a bimolecular mechanism (inter-molecular) mechanism on Brønsted acid sites, only after a substantial amount of surface alkene-species are formed.

Using UV-vis spectroscopy, Kuba *et al.* [29] detected unsaturated intermediates forming during the induction period over WO_x/ZrO₂. Scheithauer *et al.* [24] verified the existence of the species using in-situ Raman and UV-vis spectroscopy, and suggested they are of alkenic or possibly aromatic nature of higher molecular weight ≥C₁₀. Both authors concluded that the intermediate species crack on acid sites to generate the products (C₃-C₅). No C₂ and C₆ were detected, opposite to other studies [26,27], which led the authors to propose that the reaction does not proceed via a classic monomolecular or bimolecular mechanism. Alkane isomerization over Pt-WO_x/ZrO₂, has been extensively studied [19,29,52,53,55,62,63] because of their increased isomerization activity. By using ¹³C-labeled nC₅ NMR, Knözinger and coworkers [29,62] proposed

that nC_5 isomerization proceeds via a monomolecular mechanism at the beginning of the reaction followed by a bimolecular mechanism. The improved isomerization activity of Pt-promoted WO_x/ZrO_2 was suggested to be either due to a possible *in situ* formation of Brønsted acid sites or to the dehydrogenation activity of Pt, also supported by others [55]. Bifunctional Pt- WO_x/ZrO_2 converts alkanes to alkenes that isomerize on Brønsted acid sites via a monomolecular or bimolecular mechanism. A discrimination between the two mechanisms is not trivial on bifunctional catalysts, since it is complicated to determine if the increased isomerization activity is due to promoting the monomolecular isomerization mechanism.

4.2 Experimental methods

4.2.1 Chemicals

Ammonium metatungstate ($(NH_4)_{10}W_{12}O_{41} \cdot 5H_2O$, AMT) was purchased by Sigma-Aldrich, zirconium oxyhydroxide ($ZrO_x(OH)_{4-2x}$, MEI XZO 880/01) was provided by MEI and model crystalline zirconium oxide (ZrO_2 , Degussa) was provided by Degussa. All chemicals were used without further purification.

4.2.2 Catalyst preparation

The catalyst was synthesized by incipient wetness impregnation of an aqueous solution of AMT into amorphous zirconium oxyhydroxide $ZrO_x(OH)_{4-2x}$, as described in previous chapters. Calcination was performed by heating at a rate of 3.0 K/min up to 973 K, followed by isothermal heating for 3 hr under flowing air (100cc/min). Crushing, sieving and mixing were performed to acquire a fine powder. The tungsten oxide weight

loading (wt% of WO_3) was 18.5 % and the surface density (ρ_{surf}) calculated using the surface area of the catalyst after calcination (W-atoms/nm^2) was 5.2 W/nm^2 . The nomenclature for the sample studied here is 5.2-WZrOH (18.5, 973) and it is the same sample that was presented in Chapter 2.

4.3 Characterization

Nitrogen physisorption studies were performed on Micromeritics ASAP 2010 using Matheson ultra high purity (UHP) nitrogen. The specific surface area (SSA) of the catalyst and the pore volume (V_p) were found to be $93 \text{ m}^2/\text{g}$ and $0.199 \text{ cm}^3/\text{g}$ [27]. X-ray diffraction (XRD) patterns were acquired on a Rigaku D/Max-2100PC and the results were presented previously [27]. The support was completely crystalline with both tetragonal (JCPDS 79-1769) and monoclinic ZrO_2 (JCPDS 37-1484). Monoclinic WO_3 (JCPDS 72-0677) was also detected but the crystals were too small to estimate from the Scherrer equation. High resolution TEM imaging and high-angle annular dark field (HAADF) imaging was performed on a 200 kV JEOL 2200FS (S)TEM equipped with a CEOS probe C_s -corrector at Lehigh University. Monotungstates, polytungstates, Zr- WO_x clusters and WO_3 crystals were detected on the catalytic surface of the catalyst. At the ρ_{surf} and calcination temperature tested here, 1 nm Zr- WO_x clusters were found at a very high number density relative to the other species [27].

4.4 Catalytic studies

The n-pentane isomerization studies were performed on a downflow packed-bed reactor [27] at 523 K and atmospheric pressure. The feed-gas reference composition

contained 1% n-pentane (nC_5) and 1% argon (helium balance) prepared by gravimetric blending. The four olefin-added feeds studied here contained the reference composition and additional 0.01% 1-pentene ($1-C_5^=$), 0.1% $1-C_5^=$, 0.5% $1-C_5^=$, or 0.08% propylene ($C_3^=$). The equations used to calculate the conversion, selectivity and turnover rate were adjusted from Soultanidis *et al.* [27] to include the total C_{5in} , where C_{5in} is the moles of nC_5 and $1-C_5^=$ or $C_3^=$ fed to the reactor. Both the transient consumption turnover rate (TOR) and the isomerization TOR are reported in this study.

4.5 Results and discussion

4.5.1 Olefin co-addition effect on *n*-pentane conversion

The transient TOR in the absence and presence of olefin co-feeds are presented in Figure 4.2a. When 1% nC_5 is co-fed with 0.08% $C_3^=$, the TOR increases over 10 times in the first 1 h followed by fast deactivation (TOR drops 65%). With 0.5% $1-C_5^=$ co-fed, no induction period is noticed and the TOR remains high (over 5 times higher than without olefin) in the 10 h period. In this case, the TOR drops 20 % after 7 h. A lower concentration of 0.1% $1-C_5^=$ increases the transient TOR over 2 times and no change is seen in 10 h. Lower concentration of 0.01% $1-C_5^=$ has no effect on the overall catalytic activity. In all cases, $1-C_5^=$ was consumed completely during the reaction and $C_3^=$ was only consumed completely in the first 2 h (Appendix D, Figure D.1). It is important to notice that only in the presence of 0.1% or 0.5% of $1-C_5^=$, nC_5 is at least 7-8 times more reactive at all times as seen in Figure 4.2b.

The transient isomerization TOR in the absence and presence of olefin co-feeds (Figure 4.2c) show significant differences from the TOR . With only exception the 0.01%

$1-C_5^-$, catalytic activity increased in the 10 hour period in the presence of $1-C_5^-$ or C_3^- . In the presence of the 0.1% $1-C_5^-$ isomerization activity increases up to 10 hr opposite to what is noticed in all other cases. This seems to be the optimum concentration in our study at which severe deactivation does not take place. When 1% nC_5 is co-fed with 0.5% $1-C_5^-$, isomerization activity increases up to 8 times within the first 4 h and then drops $\sim 20\%$. This effect is seen more severely in the presence of 0.08% C_3^- , isomerization TOR increases by 5 fold within 2 h followed by a 70% deactivation.

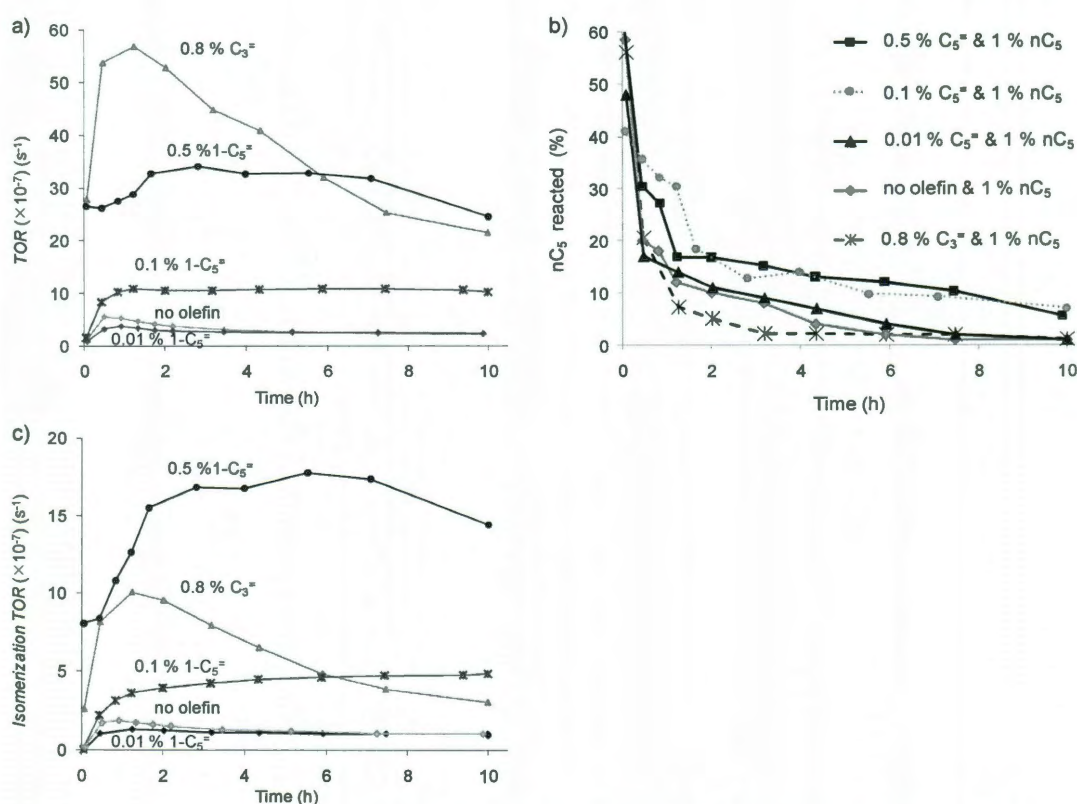


Figure 4.2. a) Transient consumption TOR , b) percentage of nC_5 reacted during reaction in the absence and presence of different olefins and c) transient isomerization turnover rates (TOR) of 5.2-WZrOH (18.5, 973) in the presence of olefins ($1-C_5^-$ and C_3^-) at different concentrations. Reaction conditions: 523 K, 1.04 atm, feed-gas reference composition: 1% nC_5 in He. Olefin added blends included the composition shown here. No-olefin data were reported by Soutanidies *et al.* [27]

The effect of olefin “impurities” during paraffin isomerization has been reported for nC_4 isomerization over SO_4/ZrO_2 catalysts [11-13,15,64-66]. Lohitharn *et al.* [13] reported that the addition of $C_3^=$, 1-butene ($1-C_4^=$) and $1-C_5^=$ had a non-specific positive effect on the maximum nC_4 isomerization activity of SO_4/ZrO_2 catalysts and also reduced the activation period time to almost half. nC_5 isomerization appears to be a more demanding acidic reaction over WO_x/ZrO_2 because the type of olefin modifies the product selectivity. Both $1-C_5^=$ and $C_3^=$ react readily due to lower required activation energies associated with carbenium and carbonium ion formation.

4.5.2 Olefin co-addition effect on product selectivity

The product distribution profiles are presented in Figure 4.3. The selectivity to isopentane (iC_5) increases during the reaction due to activation of the Zr- WO_x clusters. At the same time the concentrations of isobutene (iC_4), propane and propylene (C_3) follows an opposite trend as a result of the deactivation of the more acidic sites[27] (Figure 4.3a). The byproduct concentrations remain low with hexane and C_6 olefins (C_6) increasing with time similar to what is noticed for iC_5 .

The addition of $1-C_5^=$ has a positive effect and increases the iC_5 selectivity, from 48% to 59% when 0.5% $1-C_5^=$ is co-fed. At the same time there is a significant increase of the initial iC_4 concentration that seems to be stable for 0.1 % $1-C_5^=$ (from 40% at $t=0$ hr to 35% at $t=10$ hr) but not for 0.5 % $1-C_5^=$ (from 52% at $t=0$ hr to 12% at $t=10$ hr). The presence of $1-C_5^=$ also reduces the formation of C_3 , with selectivities remaining below 10% at the highest 0.5% $1-C_5^=$. The exact opposite effect is noticed for C_6 , with their concentration increasing significantly in the presence of $1-C_5^=$, from 5 % without

any olefin to 9% and 19% with 0.1% and 0.5% 1-C₅⁼ respectively. When 0.8 % C₃⁼ is co-fed the product distribution profiles change radically with iC₄ being the main product (selectivity of 52% at t= 0 hr to 31% at t= 10 hr) and only 20% iC₅ detected all times. C₆ concentration increase in the product stream as the reaction progresses to reach from 0 to 30% within 10 hr.

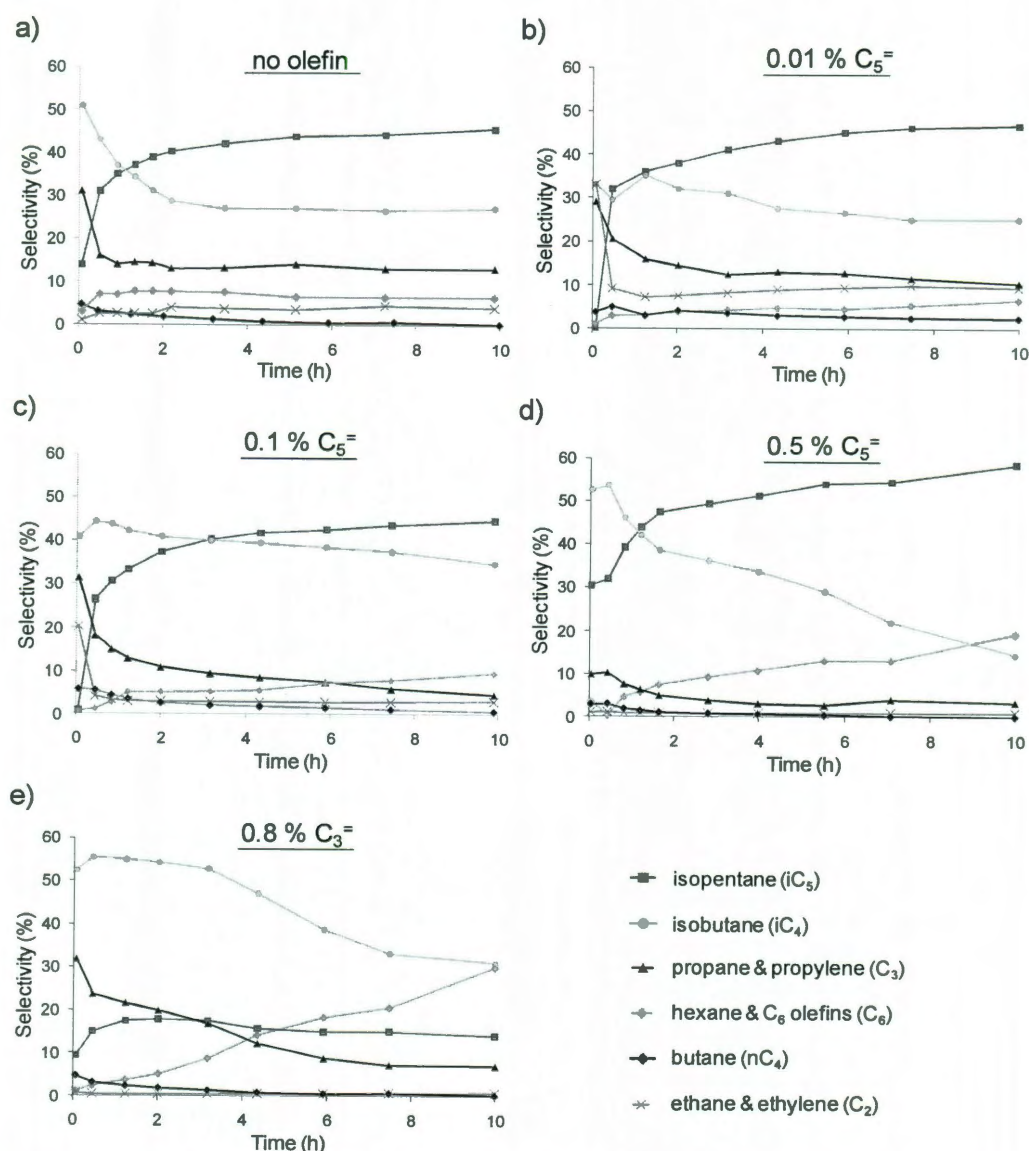


Figure 4.3. Transient product distribution profiles of 1% nC₅ and a) no olefin, b) 0.01% 1-C₅⁼, c) 0.1% 1-C₅⁼, d) 0.5% 1-C₅⁼, e) 0.8% C₃⁼, in He. No-olefin selectivities were reported by Sultandies *et al.* [27]

The steady-state (after 10 hr) concentration profiles are summarized in Figure 4.4. The lower concentrations of $1-C_5^=$ do not have as significant effect on the isomerization selectivity. At 0.5 % $1-C_5^=$, $nC_5:1-C_5^=$ molar ratio of 2:1, selectivity to iC_5 increases from 48% (no olefin) to 59%. iC_4 and C_3 concentrations were low and a noticeable increase on C_6 is observed. When 0.8 % $C_3^=$ is used, the steady-state profile shows significant concentrations of C_6 and iC_4 , with only 14 % iC_5 being formed. The mass-balance did not close in this case due (Appendix D) because (1) the high concentrations of C_7-C_9 that were not accounted but were detected in the product stream and (2) significant condensation noticed in the down-flow line before the GC.

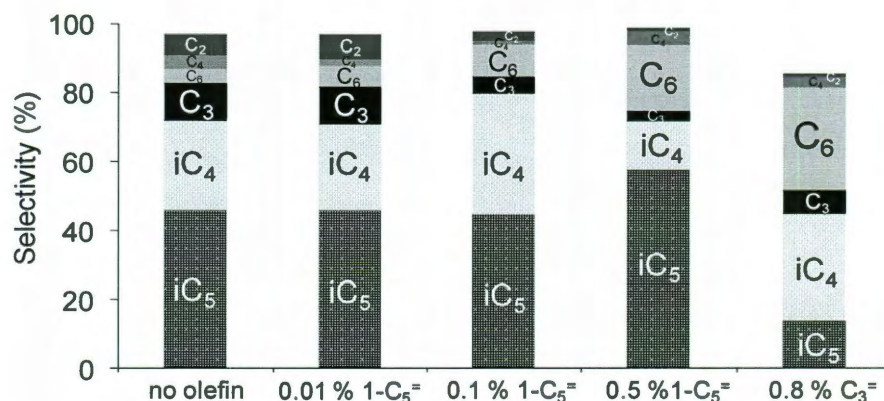


Figure 4.4: Steady-state product distribution profiles of results presented in Figure 4.2.

It was demonstrated that $1-C_5^=$ activates the isomerization mechanism when a minimum of 10:1 $nC_5:1-C_5^=$ ratio is used. The formation of both iC_5 and C_6 is promoted in the presence of $1-C_5^=$, which suggests a common reaction pathway for the two products. A C_{10} intermediate is expected to generate nC_5 and iC_5 or C_6 and iC_4 among other byproducts and explains the observed distributions. In the case of 0.5% $1-C_5^=$,

drastic disappearance of iC_4 is possibly due to a reaction between the protonated iC_4^+ species and $1-C_5^-$ to form intermediate long chain species that further crack to give C_6 and C_3^+ that easily form C_6 .

Cracking products dominate in the presence of C_3^- with the iC_5 selectivity remaining very low while C_6 and $> C_6$ (not shown here) species are formed in high yields. The high concentration of iC_4 strongly supports the model of a bimolecular disproportionation mechanism similar to SO_4/ZrO_2 [61]. The high concentrations of iC_4 and not nC_4 suggest that the reaction proceeds via a carbenium ion formation, carbenium ion rearrangement (isomerization) and chain propagation to form the C_8 intermediate that cracks to iC_4 and C_6 . The severe coking noticed is due to the strong chemisorptions between C_3^- and the Brønsted acid sites (Lewis sites are not directly associated to nC_5 isomerization over WO_x/ZrO_2 [27]). C_3^- easily dimerizes on weaker Brønsted sites to form C_6 , which explains the high concentration of these species later in the reaction when the most acidic cracking and isomerization sites are deactivated.

4.6 Summary and conclusions

n-Pentane isomerization is a demanding acidic reaction that proceeds primarily via a bimolecular mechanism on tungstated zirconia. When 1-pentene is co-fed with *n*-pentane, higher isomerization activity is achieved and *n*-pentane conversion increases by a sevenfold due to activation of the bimolecular pathway. An opposite effect is noticed when propylene is used as the olefin source, with isobutene being the main reaction product suggesting a prevailing bimolecular disproportionation mechanism.

4.7 References

1. P. G. Menon, R. P. De Pauw and G. F. Froment, *Industrial & Engineering Chemistry Product Research and Development* 18 (1979) 110-116.
2. B. Ducourty, G. Szabo, J. P. Dath, J. P. Gilson, J. M. Goupil and D. Cornet, *Applied Catalysis A: General* 269 (2004) 203-214.
3. R. Zhang, X. Meng, Z. Liu, J. Meng and C. Xu, *Industrial & Engineering Chemistry Research* 47 (2008) 8205-8210.
4. W. Kuang, A. Rives, M. Fournier and R. Hubaut, *Applied Catalysis A: General* 250 (2003) 221-229.
5. N. Essayem, Y. Ben Taârit, C. Feche, P. Y. Gayraud, G. Sapaly and C. Naccache, *Journal of Catalysis* 219 (2003) 97-106.
6. Z. Ma, W. Hua, Y. Ren, H. He and Z. Gao, *Applied Catalysis A: General* 256 (2003) 243-250.
7. A. V. Ivanov, T. V. Vasina, V. D. Nissenbaum, L. M. Kustov, M. N. Timofeeva and J. I. Houzvicka, *Applied Catalysis A: General* 259 (2004) 65-72.
8. Y. Ono, *Catalysis Today* 81 (2003) 3-16.
9. T. Okuhara, N. Mizuno, M. Misono, W. O. H. D.D. Eley and G. Bruce, *Advances in Catalysis*, Academic Press. 113-252.
10. V. Adeeva, H.-Y. Liu, B.-Q. Xu and W. Sachtler, *Topics in Catalysis* 6 (1998) 61-76.
11. K. B. Fogash, Z. Hong, J. M. Kobe and J. A. Dumesic, *Applied Catalysis A: General* 172 (1998) 107-116.
12. M. A. Coelho, W. E. Alvarez, E. C. Sikabwe, R. L. White and D. E. Resasco, *Catalysis Today* 28 (1996) 415-429.

13. N. Lohitharn, J. G. Goodwin Jr and E. Lotero, *Journal of Catalysis* 234 (2005) 199-205.
14. M. V. Luzgin, S. S. Arzumanov, V. P. Shmachkova, N. S. Kotsarenko, V. A. Rogov and A. G. Stepanov, *J. Catal.* 220 (2003) 233-239.
15. S. Hammache and J. G. Goodwin, *Journal of Catalysis* 218 (2003) 258-266.
16. M. Pérez-Luna, A. Cosultchi, J. Toledo-Antonio and M. Cortés-Jácome, *Catalysis Letters* 131 (2009) 285-293.
17. H. Matsubishi, H. Shibata, H. Nakamura and K. Arata, *Applied Catalysis A: General* 187 (1999) 99-106.
18. C. Y. Hsu, C. R. Heimbuch, C. T. Armes and B. C. Gates, *Journal of the Chemical Society, Chemical Communications* (1992) 1645-1646.
19. E. Iglesia, D. G. Barton, S. L. Soled, S. Miseo, J. E. Baumgartner, W. E. Gates, G. A. Fuentes, G. D. Meitzner, W. N. D. E. I. Joe W. Hightower and T. B. Alexis, *Studies in Surface Science and Catalysis*, Elsevier. 533-542.
20. B. Li and R. D. Gonzalez, *Applied Catalysis A: General* 174 (1998) 109-119.
21. R. Ahmad, J. Melsheimer, F. C. Jentoft and R. Schlögl, *Journal of Catalysis* 218 (2003) 365-374.
22. V. Adeeva, G. D. Lei and W. M. H. Sachtler, *Applied Catalysis A: General* 118 (1994) L11-L15.
23. F. Garin, L. Seyfried, P. Girard, G. Maire, A. Abdulsamad and J. Sommer, *Journal of Catalysis* 151 (1995) 26-32.
24. M. Scheithauer, T. K. Cheung, R. E. Jentoft, R. K. Grasselli, B. C. Gates and H. Knözinger, *Journal of Catalysis* 180 (1998) 1-13.
25. M. Scheithauer, R. E. Jentoft, B. C. Gates and H. Knözinger, *Journal of Catalysis* 191 (2000) 271-274.

26. J. G. Santiesteban, J. C. Vartuli, S. Han, R. D. Bastian and C. D. Chang, *Journal of Catalysis* 168 (1997) 431-441.
27. N. Soultanidis, W. Zhou, A. C. Psarras, A. J. Gonzalez, E. F. Iliopoulou, C. J. Kiely, I. E. Wachs and M. S. Wong, *Journal of the American Chemical Society* 132 13462-13471.
28. B.-Q. Xu and W. M. H. Sachtler, *Journal of Catalysis* 167 (1997) 224-233.
29. S. Kuba, P. Lukinskas, R. Ahmad, F. C. Jentoft, R. K. Grasselli, B. C. Gates and H. Knözinger, *Journal of Catalysis* 219 (2003) 376-388.
30. J. A. Gray and J. T. Cobb, *Journal of Catalysis* 36 (1975) 125-141.
31. A. Chica and A. Corma, *Journal of Catalysis* 187 (1999) 167-176.
32. R. A. Asuquo, G. Edermirth and J. A. Lercher, *Journal of Catalysis* 155 (1995) 376-382.
33. V. Nieminen, M. Kangas, T. Salmi and D. Y. Murzin, *Industrial & Engineering Chemistry Research* 44 (2004) 471-484.
34. A. Zhang, I. Nakamura, K. Aimoto and K. Fujimoto, *Industrial & Engineering Chemistry Research* 34 (1995) 1074-1080.
35. D. Farcasiu, A. Ghenciu and J. Q. Li, *Journal of Catalysis* 158 (1996) 116-127.
36. B. Umansky, J. Engelhardt and W. K. Hall, *Journal of Catalysis* 127 (1991) 128-140.
37. J. Sommer, R. Jost and M. Hachoumy, *Catalysis Today* 38 (1997) 309-319.
38. K. Arata, *Applied Catalysis A: General* 146 (1996) 3-32.
39. M. Hino and K. Arata, *Journal of the Chemical Society, Chemical Communications* (1979) 1148-1149.

40. M. Hino and K. Arata, *Chemistry Letters* 8 (1979) 1259-1260.
41. H. Weyda and E. Köhler, *Catalysis Today* 81 (2003) 51-55.
42. C. Morterra, G. Cerrato, F. Pinna, M. Signoretto and G. Strukul, *Journal of Catalysis* 149 (1994) 181-188.
43. G. D. Yadav and J. J. Nair, *Microporous and Mesoporous Materials* 33 (1999) 1-48.
44. G. Yaluris, R. B. Larson, J. M. Kobe, M. R. González, K. B. Fogash and J. A. Dumesic, *Journal of Catalysis* 158 (1996) 336-342.
45. C. Morterra, G. Cerrato, F. Pinna and M. Signoretto, *The Journal of Physical Chemistry* 98 (1994) 12373-12381.
46. M. R. González, J. M. Kobe, K. B. Fogash and J. A. Dumesic, *Journal of Catalysis* 160 (1996) 290-298.
47. M. T. Tran, N. S. Gnep, G. Szabo and M. Guisnet, *Applied Catalysis A: General* 171 (1998) 207-217.
48. H. Knözinger, *Topics in Catalysis* 6 (1998) 107-110.
49. M. R. González, K. B. Fogash, J. M. Kobe and J. A. Dumesic, *Catalysis Today* 33 (1997) 303-312.
50. S. X. Song and R. A. Kydd, *Journal of the Chemical Society, Faraday Transactions* 94 (1998) 1333-1338.
51. P. Mériaudeau, V. A. Tuan, V. T. Nghiem, S. Y. Lai, L. N. Hung and C. Naccache, *Journal of Catalysis* 169 (1997) 55-66.
52. G. Larsen, E. Lotero, R. D. Parra, W. N. D. E. I. Joe W. Hightower and T. B. Alexis, *Studies in Surface Science and Catalysis*, Elsevier. 543-551.

53. S. R. Vaudagna, R. A. Comelli and N. S. Fígoli, *Applied Catalysis A: General* 164 (1997) 265-280.
54. S. R. Vaudagna, S. A. Canavese, R. A. Comelli and N. S. Fígoli, *Applied Catalysis A: General* 168 (1998) 93-111.
55. J. C. Yori, C. L. Pieck and J. M. Parera, *Applied Catalysis A: General* 181 (1999) 5-14.
56. F. C. Whitmore, *The Journal of the American Chemical Society* 54 (1932) 3274-3283.
57. H. Voge Hervey, *Heterogeneous Catalysis*, American Chemical Society. 235-240.
58. B. S. Greensfelder, H. H. Voge and G. M. Good, *Industrial & Engineering Chemistry* 41 (1949) 2573-2584.
59. M. Risch and E. E. Wolf, *Catalysis Today* 62 (2000) 255-268.
60. Y. Liu, K. Na and M. Misono, *Journal of Molecular Catalysis A: Chemical* 141 (1999) 145-153.
61. S. Rezgui, R. Jentoft and B. Gates, *Catalysis Letters* 51 (1998) 229-234.
62. S. V. Filimonova, A. V. Nosov, M. Scheithauer and H. Knözinger, *Journal of Catalysis* 198 (2001) 89-96.
63. G. Larsen and L. M. Petkovic, *Applied Catalysis A: General* 148 (1996) 155-166.
64. N. Lohitharn, E. Lotero and J. G. Goodwin Jr, *Journal of Catalysis* 241 (2006) 328-341.
65. S. Y. Kim, J. G. Goodwin, S. Hammache, A. Auroux and D. Galloway, *Journal of Catalysis* 201 (2001) 1-12.
66. J. E. Tabora and R. J. Davis, *Journal of the American Chemical Society* 118 (1996) 12240-12241.

Chapter 5

n-Pentane isomerization activity of supported phosphotungstic acid

5.1 Introduction

Heteropolyacids (HPAs) such as phosphotungstic acid (PWA) are polyanionic compounds with useful properties in the field of acidic and reduction-oxidation (redox) catalysis [1-10]. The PWA molecule ($\text{H}_3\text{PW}_{12}\text{O}_{40}$) has a Keggin structure [8,11,12] named after J.F. Keggin who discovered the morphology of this structure [13]. It is composed of a central tetrahedron (PO_4) surrounded by 12 edge- and corner-sharing WO_6 octahedra (Figure 5.1). The structural and electronic configuration of this anionic Keggin core allows it to stabilize one or more counter-cations (such as H^+ , H_3O^+ and H_5O_2^+) in a way that they remain very mobile opposite to what is seen in zeolites [4,14,15]. As a result PWA is a strong Brønsted acid with an acidity similar to H-modernite [16,17], but is characterized as a pseudoliquid [18,19] due to its high cation mobility similar to what real liquid acids. This property can find many applications in heterogeneous catalysis [1-3,6,9,12,18-23] such as methacrolein oxidation and olefin hydration [4,6] and light alkane isomerization [24-30]. The low specific surface area (SSA) [8,11,12] and the relative low thermal stability of HPAs [4,31] compile the two most important challenges that prevent their use in many heterogeneous catalysis applications.

The properties of supported PWA are investigated in this chapter. In order to increase the dispersion of PWA, which has extremely low surface area (less than $5 \text{ m}^2/\text{g}$ [4,18]), metal oxide supports such as Al_2O_3 , SiO_2 , ZrO_2 were used. SiO_2 is reported [32,33] to be the best support because it enhances good dispersion of PWA up to 20 wt % by retaining its acidity at all loadings opposite to Al_2O_3 . Among the different supports

used, SiO_2 has strong Brønsted acidity and very weak Lewis acidity (usually counter-balanced by basic sites on the support) [4,16,17] opposite to WO_x/ZrO_2 and it can therefore be used as model catalyst to identify Brønsted activated reactions. The thermal stability of PWA/SiO_2 was investigated by regenerating the spent catalyst (calcination under air flow at 873 K).

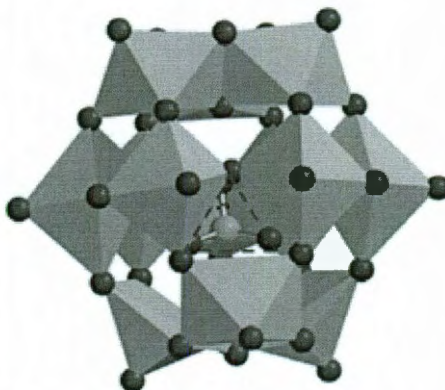


Figure 5.1. 3-D ball and spoke structure of tungstophosphoric acid. 12 edge- and corner-sharing WO_6 octahedra (green planes) and one central PO_4 tetrahedron (PO_4) consist the Keggin structure. (Orange atom: Phosphorus, Red atom: oxygen)

The purpose of this chapter is to explore an alternative strong acid catalyst such as PWA/SiO_2 and to compare it to WO_x/ZrO_2 in terms of activity and stability.

5.2 Experimental methods and characterization

5.2.1 Chemicals

Phosphotungstic acid (PWA) hydrate was purchased by Sigma-Aldrich, colloidal SiO_2 (VP Aeroperl ® Pharma) was provided by Degussa, Al_2O_3 was purchased by Engelhard-BASF and amorphous zirconium oxyhydroxide ($\text{ZrO}_x(\text{OH})_{4-2x}$ XZO 880/01)) by MEI. All chemicals were used without further purification.

5.2.2 Catalyst preparation

The catalyst was synthesized by incipient wetness impregnation of an aqueous solution of PWA into (1) amorphous zirconium oxyhydroxide $\text{ZrO}_x(\text{OH})_{4-2x}$ (specific surface area (SSA) of $330 \text{ m}^2/\text{g}$ and pore volume (V_p) of $0.33 \text{ cm}^3/\text{gr}$), (2) colloidal SiO_2 (SSA of $270 \text{ m}^2/\text{g}$ and V_p of $1.44 \text{ cm}^3/\text{g}$) and (3) Al_2O_3 (SSA of $171 \text{ m}^2/\text{g}$ and V_p of $0.74 \text{ cm}^3/\text{g}$). Calcination was performed by heating at a rate of $3.0 \text{ K}/\text{min}$ up to 553 K , followed by isothermal heating for 3 hr under flowing air ($100 \text{ cc}/\text{min}$). This temperature is lower than what is presented in the previous chapters because HPA decomposes at higher calcination temperatures. Crushing, sieving and mixing were performed similar to previous chapters and the nomenclature used is PWA/Support (z, 553), where z is the tungsten oxide weight loading (wt% of WO_3).

5.2.3 Catalyst characterization

Nitrogen physisorption studies were performed on Micromeritics ASAP 2010 using Matheson ultra high purity (UHP) nitrogen only for the supports prior to impregnation. High resolution TEM (HRTEM) imaging and high-angle annular dark field (HAADF) imaging was performed on a 200 kV JEOL 2200FS (S)TEM equipped with a CEOS probe C_s -corrector at Lehigh University. The TEM results presented here were discussed in detail by Dr. Wu Zhou in his thesis “Nanostructural and Chemical Characterization of Supported Metal Oxide Catalysts by Aberration Corrected Analytical Electron Microscopy” and a brief presentation of these results is included in this chapter.

5.2.4 Catalytic studies

The *n*-pentane isomerization activity and selectivity of supported PWA catalysts was tested on an isothermal downflow reactor at 523 K similar to what was reported in previous chapters. Prior to each reaction run, samples were pre-treated *in situ* at 553 K under continuous flow (100cc/min) of ultra high purity (UHP) air for 1 hr. The pretreatment temperature was selected to 553 K vs. 673 K that was chosen for WO_x/ZrO_2 to avoid any possible decomposition of PWA. The activity reported in this chapter is expressed as $n\text{C}_5$ isomerization rate opposite to turnover rate in the previous chapters. The $n\text{C}_5$ isomerization rates for iwiWZr (973) and commercial iwiWZr (973) from Chapter 3 are reported here for comparison.

5.3 Results and discussion

5.3.1 Structure of supported phosphotungstic acid

The surface structure of PWA/ ZrO_2 (14, 553) is presented in Figure 5.2. Both amorphous and crystalline ZrO_2 is noticed in agreement with what was reported in Chapter 2 for WO_x/ZrO_2 at similar calcination temperatures. Highly dispersed monotungstate and polytungstate species are the only species observed. This indicates that the PWA molecules decompose upon calcination at 553 K on ZrO_2 surface.

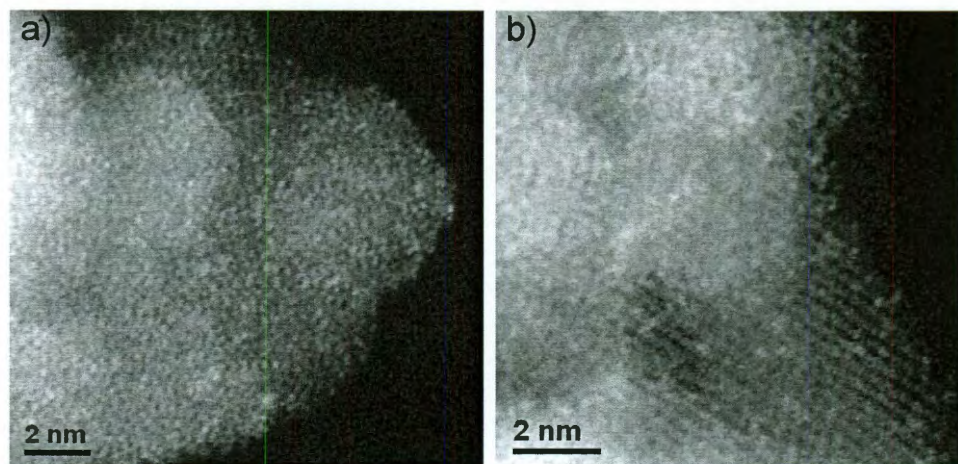


Figure 5.2. Representative STEM-HAADF images of PWA/ZrO₂ (14, 553) showing high concentration of monotungstate species on both a) amorphous and b) crystalline ZrO₂

The surface structure of PWA/Al₂O₃ (14, 553) is presented in Figure 5.3, showing variety of species, monotungstate, polytungstate and sub-num WO_x cluster species. Al₂O₃ is a weak Lewis acid support, opposite to ZrO₂, which means that a weak attraction between the PWA and the Al₂O₃ Lewis acid sites results to formation of larger aggregates. Similar to ZrO₂ the PWA Keggin structure is not retained as indicated by the presence of the monotungstates and smaller polytungstates.

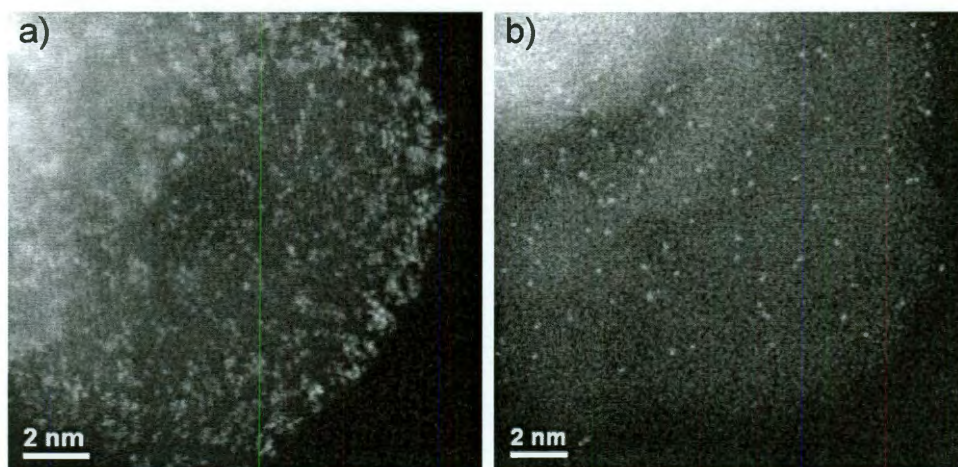


Figure 5.3. Representative STEM-HAADF images of PWA/Al₂O₃ (14, 553) showing a) high concentration of polytungstate species and lower of 3-D WO_x clusters and b) higher concentration of monotungstate species

Opposite to PWA/ZrO₂ (14, 553) and PWA/Al₂O₃ (14, 553) the surface structure of PWA/SiO₂ (14, 553) demonstrates significantly different features (Figure 5.4). High number density of 0.8-2 nm WO_x clusters is observed on the amorphous SiO₂ surface along with some larger agglomerates. SiO₂ appears to be an excellent candidate for possibly sustaining the PWA Keggin molecule [34,35] due to its amphoteric surface. Both weak acid and basic sites on the catalytic surface facilitate a weak interaction between WO_x and SiO₂ as it was demonstrated by others [36,37]. Two types of species are expected to be found on the catalytic : (type A) intact Keggin H₃PW₁₂O₄₀ molecules and (type B) structures with a chemical formula of H₆P₂W₁₈O₆₂ or H₆P₂W₂₁O₇ [36-38] that are usually detected at lower PWA loadings.

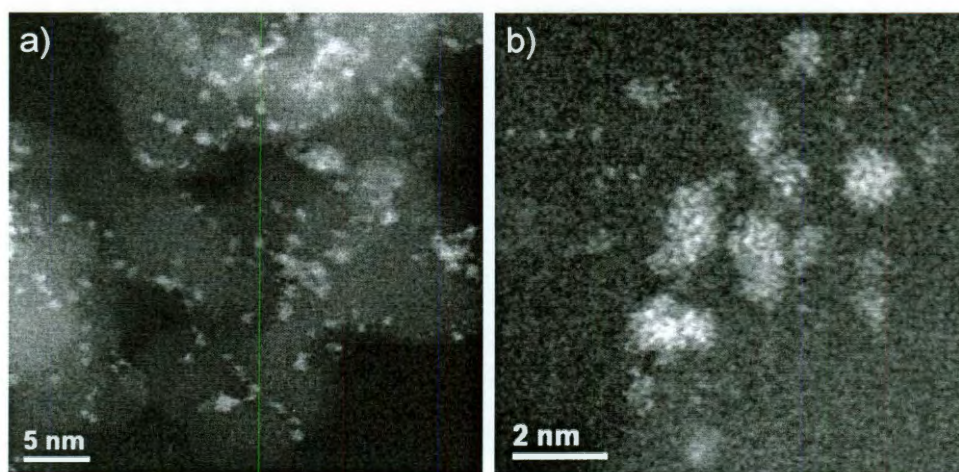


Figure 5.4. Representative STEM-HAADF images of PWA/SiO₂ (14, 553) showing concentrations of WO_x clusters

5.3.2 Steady state *n*-pentane isomerization activity

The steady-state nC₅ isomerization rates of the supported PWA samples are presented in Figure 5.5. PWA/SiO₂ samples are at least 9 times more active than iwiWZr and commercial iwiWZr opposite to PWA/ZrO₂ and PWA/Al₂O₃ that are at least 10

times less active than iwiWZr and commercial iwiWZr. The low activity of PWA/ZrO₂ and PWA/Al₂O₃ suggests that the PWA Keggin structure on the ZrO₂ and Al₂O₃ surface was destroyed upon calcination as verified by STEM-HAADF. The enhanced catalytic activity of PWA/SiO₂ over WO_x/ZrO₂ suggests that SiO₂ prevents the complete decomposition of the PWA Keggin structure [36,37]. Activity reaches a maximum for PWA/SiO₂ at a PWA loading of 26 wt%, which is possibly due to the change in the species distribution (from type B to type A). Further investigations would provide more information about the species concentrations and how it correlates to their nC₅ isomerization activity.

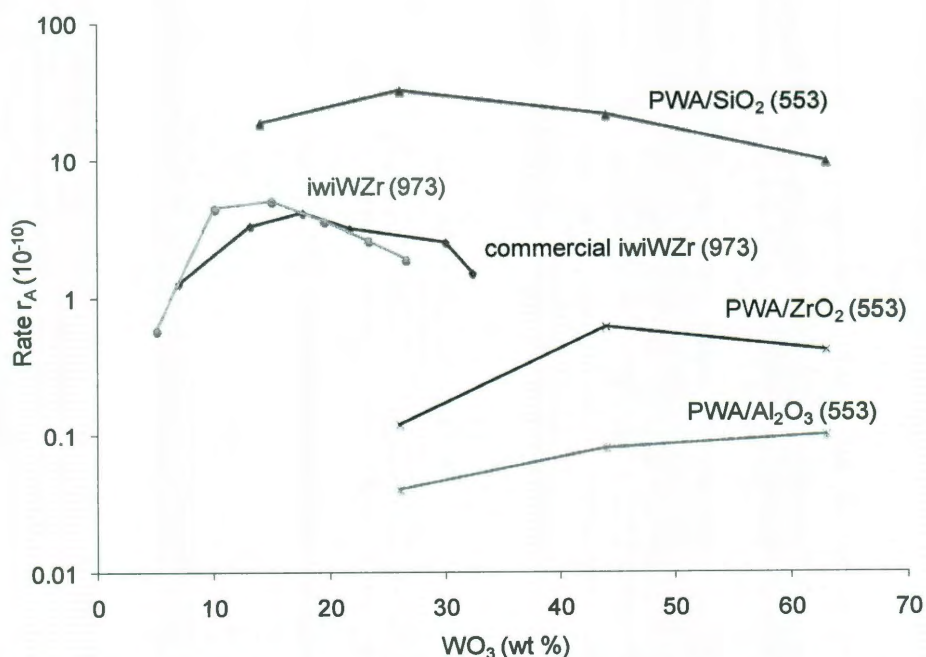


Figure 5.5. Steady-state nC₅ isomerization rates as a function of tungsten oxide loading. Sample series include PWA/SiO₂, PWA/Al₂O₃, PWA/ZrO₂, iwiWZr and commercial iwiWZr from Chapter 3. Reaction conditions: 523 K, 1.04 atm, 1% nC₅ in He. Overall nC₅ conversion was < 3% for all samples except the PWA/SiO₂.

5.3.3 Regeneration of silica supported phosphotungstic acid

After regeneration, the isomerization activity of PWA/SiO₂ drops by ~100 times opposite to what is noticed for WO_x/ZrO₂ (Figure 5.6). Regeneration by calcination at > 823 K (which is the minimum temperature required for burning off coke) destroys the PWA Keggin structure and generates regular WO_x species, similar to WO_x/ZrO₂. It is expected that such an effect would decrease the overall Brønsted acidity as proven by the low nC₅ isomerization activity. The catalytic activity of regenerated PWA/SiO₂ is similar to the crystalline WZrO₂ samples presented in Chapter 2.

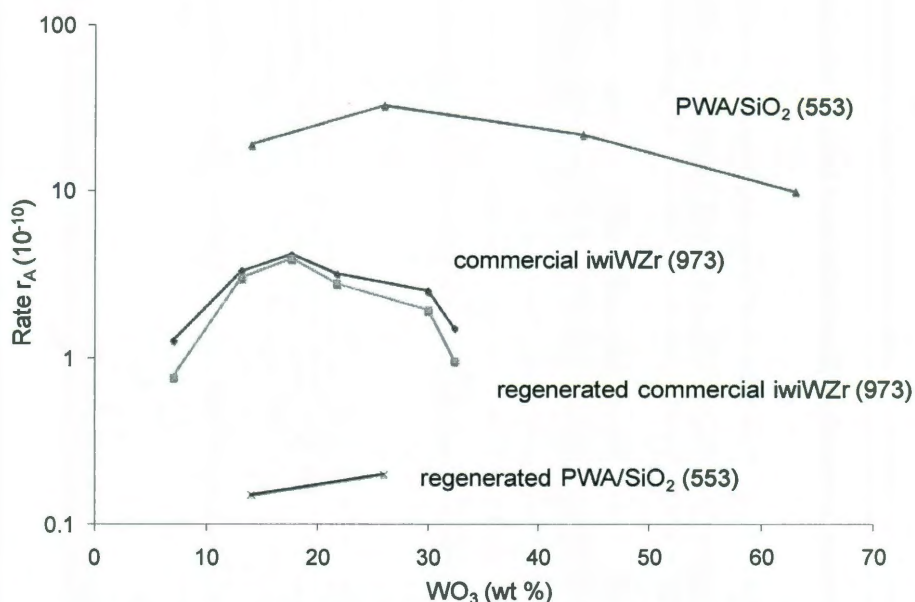


Figure 5.6. Steady-state nC₅ isomerization rates as a function of tungsten oxide loading of PWA/SiO₂ and commercial iwiWZr from Chapter 3, before and after regeneration. Regeneration took place at 823 K under air flow. Reaction conditions: 523 K, 1.04 atm, 1% nC₅ in He. Overall nC₅ conversion was < 3% for all samples except the PWA/SiO₂.

5.3.4 Transient activity of silica supported phosphotungstic acid

No activation period is noticed over PWA/SiO₂ (Figure 5.7a) opposite to WO_x/ZrO₂ and PWA/Al₂O₃ (Figure 5.7b). Independent to the PWA loading, activity

starts at a maximum and declines with time due to coking for PWA/SiO₂. PWA/SiO₂ (26, 553) is the most active sample, followed by PWA/SiO₂ (44, 553), PWA/SiO₂ (14, 553) and finally PWA/SiO₂ (63, 553). All samples are resistant to coking as seen by the slope ($\leq 20\%$ deactivation) with a single exception PWA/SiO₂ (14, 553) that appears to lose $\sim 80\%$ of its initial isomerization activity within 10 h. It is possible that this effect is associated with the low coverage of the SiO₂ support which is not promoting the bimolecular mechanism based on the model presented in Chapter 3. Strongly chemisorbed species that cannot further react tend to block the active sites and eventually get dehydrogenated to form coke precursors on the catalytic surface.

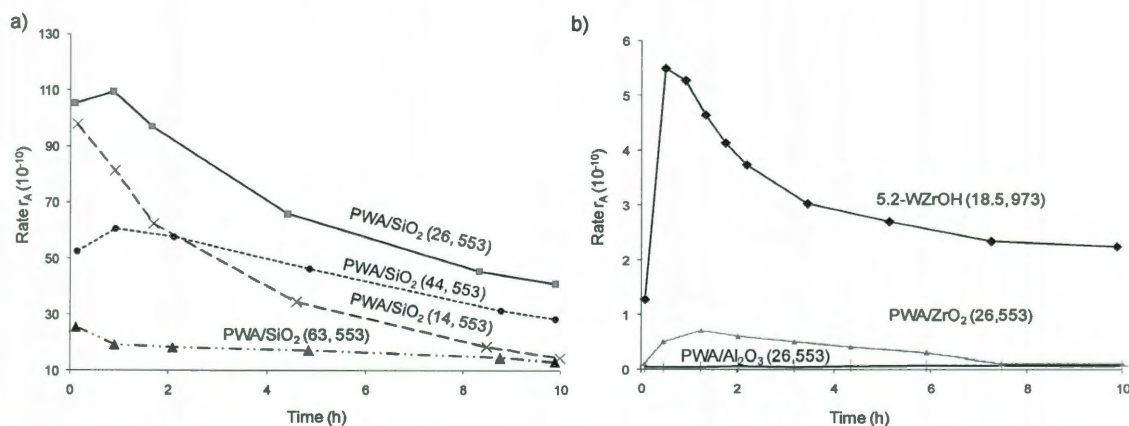


Figure 5.7. Transient nC₅ isomerization rates as a function of tungsten oxide loading of a) PWA/SiO₂ series and b) 5.2-WZrOH (18.5, 973) from chapter 2, PWA/ZrO₂ (26,553) and PWA/Al₂O₃ (26,553). Reaction conditions: 523 K, 1.04 atm, 1% nC₅ in He.

A completely different behavior is seen for the 5.2-WZrOH (18.5, 973) where the activation of Zr-WO_x sites requires ~ 1 h to reach maximum activity. PWA/ZrO₂ (26,553) shows a small activation period similar to the low activity samples presented in chapter 2. This is an indication that Zr-WO_x sites may have been formed upon decomposition of the PWA molecule. PWA/Al₂O₃ (26,553) has very low activity and no activation period is

noticed, which supports the mechanism proposed in Chapter 2. Same trends are noticed for all PWA/ZrO₂ and PWA/Al₂O₃ (only representative samples shown here).

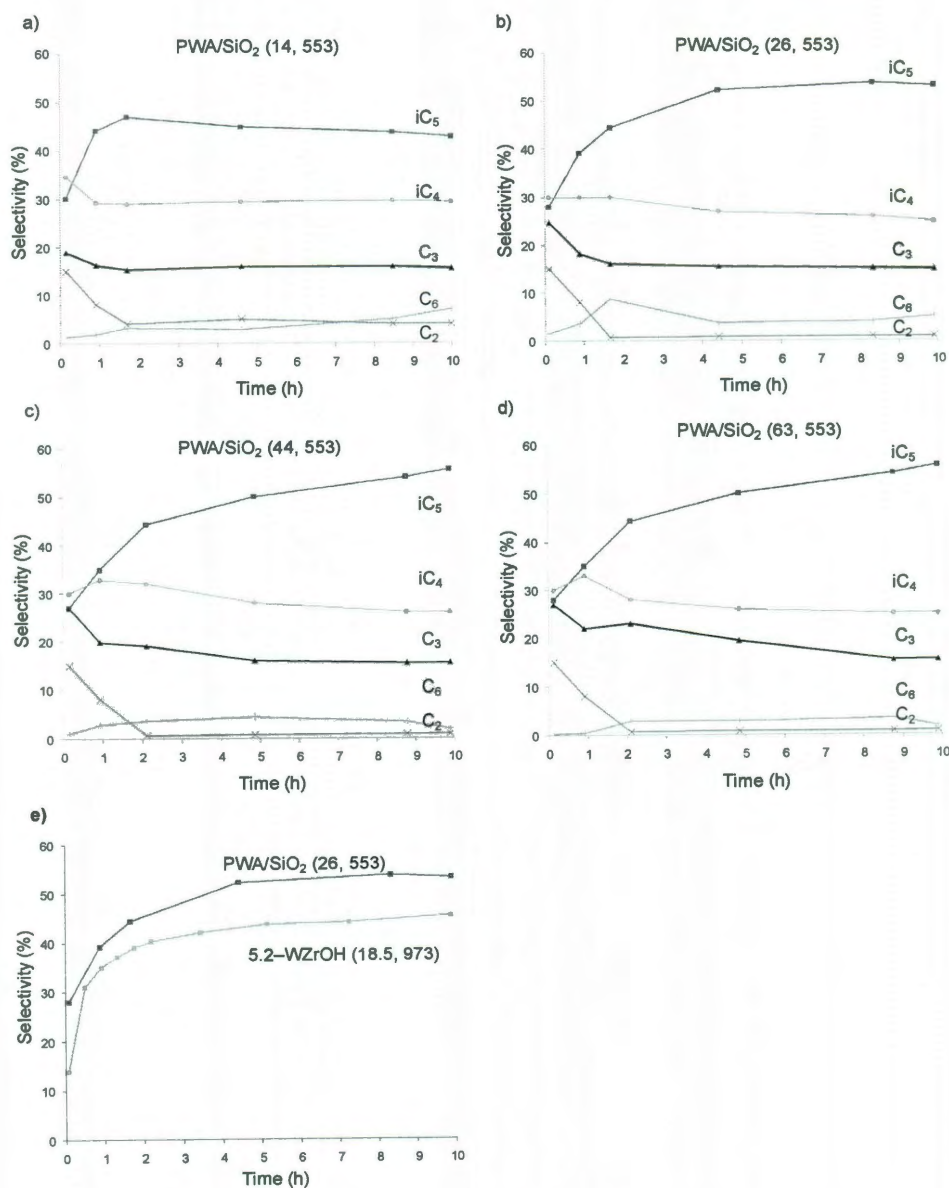


Figure 5.8. Transient product distributions for a) PWA/SiO₂ (14,553), b) PWA/SiO₂ (26,553), c) PWA/SiO₂ (44,553) and d) PWA/SiO₂ (63,553). iC₅ transient selectivity profile of PWA/SiO₂ (26.553) and 5.2-WZrOH (18.5, 973) (from Chapter 2).

To identify the dominant reaction mechanism, the transient nC₅ isomerization product distribution profiles of PWA/SiO₂ are presented in Figure 5.8. No significant

difference is noticed between PWA/SiO₂ and WO_x/ZrO₂ (Chapter 2). The presence of C₆ suggests that a bimolecular mechanism via a C₁₀ intermediate is an important reaction mechanism. This excludes the possibility of a monomolecular mechanisms and suggests that the lack of an activation period (Figure 5.7) is due to (1) the super strong Brønsted sites of PWA/SiO₂ [39,40] that are already protonated and to (2) the strong acidity of PWA/SiO₂ vs. WO_x/ZrO₂ that promotes more easily the formation of the C₁₀ intermediate.

5.4 Summary and conclusions

Silica supported PWA catalysts exhibit superior *n*-pentane isomerization activity. The PWA Keggin acid sites have the ability to promote the bimolecular mechanism similar to WO_x/ZrO₂ without an active site activation required. SiO₂ is the best support for retaining the PWA Keggin acid sites (Brønsted sites) opposite to Al₂O₃ and ZrO₂. A critical problem is the poor thermal stability of PWA/SiO₂, which results to destruction of the PWA Keggin structure after regeneration of the catalyst. Similar to WO_x/ZrO₂ there is an optimum concentration of PWA for synthesizing an active catalyst PWA/SiO₂, which corresponds to the presence of two types of species, an intact type A HPA Keggin structure and a modified type B acidic structure that retains the enhanced acidity of HPA. Further investigation would provide a more specific surface species-activity correlation.

5.5 References

1. K. I. Matveev, Kinet. Katal. 18 (1977) 862.
2. I. V. Kozhevnikov and O. A. Kholdeeva, Izv. Akad. Nauk SSSR, Ser. Khim. null (1983) 2663.

3. I. V. Kozhevnikov, *Stud. Surf. Sci. Catal.* 90 (1994) 21.
4. I. V. Kozhevnikov, *Chemical Reviews* 98 (1998) 171-198.
5. J. B. Moffat, *J. Mol. Catal.* 52 (1989) 169.
6. M. Misono and N. Nojiri, *Appl. Catal.* 64 (1990) 1.
7. Y. Izumi, M. Ogawa, W. Nohara and K. Urabe, *Chem. Lett.* null (1992) 1987.
8. M. T. Pope, *Heteropoly and Isopoly Oxometalates*. Springer Verlag, New York, 1983.
9. A. Corma, *Chem. Rev.* 95 (1995) 559.
10. D. E. Katsoulis, *Chemical Reviews* 98 (1998) 359-388.
11. G. A. Tsigdinos, *Top. Curr. Chem.* 76 (1978) 1.
12. M. T. Pope and A. Muller, *Angew. Chem., Int. Ed. Engl.* 30 (1991) 34.
13. J. F. Keggin, *Proceedings of the Royal Society of London. Series A* 144 (1934) 75-100.
14. N. Mizuno and M. Misono, *Chemical Reviews* 98 (1998) 199-217.
15. Kozhevnikov. I.V, *Journal of Molecular Catalysis A: Chemical* 305 (2009) 104-111.
16. M. Misono, N. Mizuno, K. Katamura, A. Kasai, Y. Konishi, K. Sakata, T. Okuhara and Y. Yoneda, *Bull. Chem. Soc. Jpn.* 55 (1982) 400.
17. M. Furuta, K. Sakata, M. Misono and Y. Yoneda, *Chem. Lett.* null (1979) 31.
18. M. Misono, *Catal. Rev. Sci. Eng.* 29 (1987) 269.

19. T. Okuhara, N. Mizuno and M. Misono, *Adv. Catal.* 41 (1996) 113.
20. I. V. Kozhevnikov, *Catal. Rev. Sci. Eng.* 37 (1995) 311.
21. I. V. Kozhevnikov and O. A. Kholdeeva, *Izv. Akad. Nauk SSSR, Ser. Khim.* null (1987) 528.
22. J. B. Moffat, *Rev. Chem. Intermed.* 8 (1987) 1.
23. R. J. Jansen, H. M. van Veldhuizen, M. A. Schwegler and H. van Bekkum, *Recl. Trav. Chim. Pays-Bas* 113 (1994) 115.
24. G. A. Olah, G. K. S. Prakash and J. Sommer, *Superacids*. Wiley, New York, 1985.
25. W. Kuang, A. Rives, M. Fournier and R. Hubaut, *Applied Catalysis A: General* 250 (2003) 221-229.
26. N. Essayem, Y. Ben TaËcrit, C. Feche, P. Y. Gayraud, G. Sapaly and C. Naccache, *Journal of Catalysis* 219 (2003) 97-106.
27. Z. Ma, W. Hua, Y. Ren, H. He and Z. Gao, *Applied Catalysis A: General* 256 (2003) 243-250.
28. O. Yoshio, *Catalysis Today* 81 (2003) 3-16.
29. P.-Y. Gayraud, N. Essayem and J. Vdrine, *Catalysis Letters* 56 (1998) 35-41.
30. M. Guisnet, P. Bichon, N. S. Gnep and N. Essayem, *Topics in Catalysis* 11-12 (2000) 247-254.
31. C. Rocchiccioli-Deltcheff, M. Amirouche, G. Herve, M. Fournier, M. Che and J. M. Tatibouet, *J. Catal.* 126 (1990) 591.
32. G. I. Kapustin, T. R. Brueva, A. L. Klyachko, M. N. Timofeeva, S. M. Kulikov and I. V. Kozhevnikov, *Kinet. Katal.* 31 (1990) 1017.

33. F. Lefebvre and n. Jouquet, *React. Kinet. Catal. Lett.* 53 (1994) 297.
34. Y. Izumi, K. Matsuo and K. Urabe, *J. Mol. Catal.* 84 (1983) 299.
35. S. M. Kulikov, M. N. Timofeeva, I. V. Kozhevnikov, V. I. Zaikovskii, L. M. Plyasova and I. A. Ovsyannikova, *Izv. Akad. Nauk SSSR, Ser. Khim.* null (1989) 763.
36. F. Lefebvre, *J. Chem. Soc., Chem. Commun.* null (1992) 756.
37. I. V. Kozhevnikov, K. R. Kloetstra, A. Sinnema, H. W. Zandbergen and H. van Bekkum, *J. Mol. Catal. A* 114 (1996) 287.
38. V. M. Mastikhin, S. M. Kulikov, A. V. Nosov, I. V. Kozhevnikov, I. L. Mudrakovsky and M. N. Timofeeva, *J. Mol. Catal.* 60 (1990) 65.
39. K. Nowinska, R. Fiedorow and J. Adamiec, *J. Chem. Soc., Faraday Trans.* 87 (1991) 749.
40. T. Okuhara, T. Nishimura, H. Watanabe and M. Misono, *J. Mol. Catal.* 74 (1992) 247.

Chapter 6

Solvothermal synthesis of ultrasmall metal oxide nanoparticles

6.1 Introduction

Efficient structural control in the low limits of the nanometer scale (< 10 nm) is of increasing interest in the synthesis of MO_x NPs that have exceptional physical and chemical properties with applications in the field of energy storage [1-4] and conversion [1,5], gas sensing [6-10], and catalysis [11-13]. Thermodynamic as well as experimental limitations pose significant difficulties towards the controlled synthesis of ultra-small MO_x NPs. With the majority of the transition metal atoms having Van der Waals atomic radii in the range of 0.15-0.20 nm, it is realized that a MO_x cluster of ≤ 2 nm would comprise 10-20 metal atoms, depending on its oxidation state and conformation. The synthesis of and deposition of such clusters onto supports are expected to contribute significantly to the fundamental study of supported heterogeneous catalysts.

Especially for early transition metals, such as W [14-18], Mo [19-23], and V [24-29], the synthesis of small NPs is a difficult procedure and usually results in the formation rod- or wire- shaped nanoparticles. Tungsten oxide (WO_x) nanowires [14,16] and nanorods [15,17,18] have been successfully synthesized by a wide range of methods from electrochemical etching [17] to organometallic synthetic methods using various surfactants [18]. Similar to WO_x , the synthesis of vanadium oxide (VO_x) nanowires [24,25] and nanotubes [26-29] and molybdenum oxide (MoO_x) nanowires [19-21,23] have been reported with dimensions above 20 nm.

There are several methods that can be used to synthesize a variety of MO_x materials with 0-D to 3-D complex structures. Before proceeding with presenting and

explaining the method chosen, a synoptic presentation of the most critical synthetic approaches is presented here. The purpose of this chapter is to investigate a novel synthesis technique of WO_x NPs that can be used for the preparation of supported tungsten oxide catalysts.

6.2 Synthesis of metal oxide nanoparticles

6.2.1 Hydrothermal methods

Hydrothermal synthesis is the most extensively studied technique in MO_x synthesis. As the name implies, the formation of metal oxide or mixed oxides takes place in aqueous solutions at high temperatures and pressures that benefit the hydrolysis, precipitation, and, finally, crystal growth rate. The whole process takes place usually in sealed vessels, called bombs or autoclaves that can withstand high temperatures and pressures. Under supercritical conditions that usually far exceed the boiling point of water, highly insoluble to water MO_x precursors dissolve to form a wide range of MO_x nanomaterials. Major advantages of the method include not only the low cost of the material and instrumentation required, but also the simplistic synthetic procedures that allow excellent reproducibility. On the other hand, the limited available precursors and the high-pressure procedure requirements impose significant obstacles.

The most common MO_x precursors used are metal nitrates ($\text{M}(\text{NO}_3)_x$), hydroxides ($\text{M}(\text{OH})_x$), and chlorides ($\text{M}(\text{Cl})_x$). Different modes as isothermal, non-isothermal can be used for synthesizing a variety of pure or mixed MO_x NPs.

6.2.2 Solvothermal methods

Similar to hydrothermal methods, solvothermal methods involve the heating of solvents and metal coordination compounds in the presence of an organic capping agent at high temperatures. A major difference from the hydrothermal methods is that due to the higher boiling point of the solvent, solvothermal synthesis takes place usually in a regular stainless steel or glass reactor under atmospheric pressure. The solvothermal method is comprised of three stages: (1) heating of the solution or slurry suspension at which dissociation of the metal-precursor occurs (usually above 523 K); (2) aging of the solution at the desired temperature for further particle nucleation and growth that finalizes the size and surface properties of the particles; and (3) particle acquisition and separation from the un-reacted material and the solvent. The most important advantage of this method is that it can be used to synthesize a wide range of materials; however related to the multiple steps can lead to poor reproducibility. The most important MO_x precursors used include metal-acetylacetonates ($\text{M}(\text{C}_5\text{H}_8\text{O}_2)_x$) also known as $\text{M}(\text{acac})_x$, metal carbonyls ($\text{M}(\text{CO})_x$), and metal chlorides $\text{M}(\text{Cl})_x$. Various organic ligands have been used in such processes with the most popular ones being oleic acid and oleylamine. Oxidizing or reducing agents can also be used for synthesizing the desired metal oxide or zero-valent metallic NPs.

6.2.3 Aqueous Sol-Gel methods

Gels are cross-linked networks of polymers and/or particles held together by physical or chemical bonding and can be classified as aquagels, alcogels (discussed in following section), xerogels, and aerogels, depending on the medium contained within

the gel's network of particles. The synthesis of gels proceeds via a polymerization step between the precursor and the ligands to create the 3-D network of particles. These particles operate as nuclei for further growth until depletion of the available precursor.

Further aging of the gel contributes to more polycondensation and solvent extraction from the gel pores. Ostwald ripening and phase transformations are two mechanisms occurring during the polymerization step which constitute the particle growth mechanism. During the growth stages, smaller and highly soluble particles are consumed by larger ones until no difference between the particle solubility exists. The final dried gel contains no solvent within its pores and is classified as a xerogel when the solvent is removed by drying at moderate temperatures or as an aerogel when the drying process takes place under supercritical conditions.

In aqueous sol-gel synthesis, the precursor consists of a metal salt; in other words, a metal or metalloid element chemically bound to inorganic ligands, which serve as cross-linking agents. Sol-gel methods are efficient and cost-effective since they can be done at low temperatures and pressures. This method has been used to generate a wide number of MO_x cross-linked networks of NPs with good thermomechanical stability and structural homogeneity. The main drawback of the sol-gel technique is that variation in particle morphology, specifically size, can occur due to pH variations during the synthesis procedure. Due to the final cross-linked structure, sol-gel methods are often used for the synthesis of catalytic supports and not for the synthesis and deposition of MO_x NPs using conventional techniques.

6.2.4 Non-aqueous Sol-Gel methods

Non-aqueous sol-gel methods are similar to aqueous sol-gel techniques with the notable exception that organic solvents are used for the purpose of enhancing particle homogeneity. Akin to aqueous sol-gel methods, non-aqueous sol-gel methods use metal precursors, typically alkoxides ($M(OR)_x$) in combination with a linking agent, usually an alcohol, to form MO_x cross-linked particles. Basic advantages of the non-aqueous sol-gel method include (1) synthesis of a broader range of metal oxide materials and (2) higher reproducibility due to lower pH sensitivity.

6.3 Tungsten oxide nanoparticles

WO_x NPs have been successfully synthesized via chemical vapor deposition [30,31], sonochemical [32], combustion [33], and solvothermal techniques with a focus on 1-dimensional WO_x nanorods [4,15,18,34-36] or nanowires [10,14,30,37] and 2-dimensional films [31,38-41] due to their interesting optical [15,31,39,40], semiconducting [33,38], and photocatalytic [41] properties. Ultrasmall WO_x nanoparticles with diameters < 2 nm are considered to have interesting catalytic properties [42-45] and have not been synthesized or proposed for catalytic applications.

In this chapter, the novel synthesis of 1.6 ± 0.3 nm WO_x NPs using a polyanionic salt (ammonium metatungstate hydrate) and a cationic organic amine (oleylamine) is presented. Ultrasmall WO_x NPs (WO_x NPs) (1.0 ± 0.35 nm) were successfully prepared by using an oxidation agent (trimethylamine N-oxide (TANO)). Larger rod-shaped WO_x nanorods (WO_x NRs) were successfully produced by replacing TANO with 1,12-

dodecandiol. The method was further applied for the synthesis of molybdenum oxide (MoO_x) and vanadium oxide (VO_x) nanoparticles.

6.4 Experimental methods

6.4.1 Chemicals

Ammonium metatungstate hydrate (AMT, $(\text{NH}_3)_8\text{W}_{12}\text{O}_{40} \cdot x\text{H}_2\text{O}$), ammonium metamolybdate tetrahydrate (AMM, $(\text{NH}_4)_6\text{Mo}_7\text{O}_{24} \cdot 4\text{H}_2\text{O}$), ammonium metavanadate (AMV, NH_4VO_3), oleylamine, pyridine, acetone, toluene, trimethyl-amine n-oxide, and 1,2-dodecanediol were purchased by Sigma-Aldrich. All chemicals were used without further purification.

6.4.2 Solvothermal synthesis of tungsten oxide nanoparticles

The synthesis of WO_x NPs consists of 3 steps (synthesis, nanoparticle separation, and redispersion in organic solvent). A slurry solution of the ammonium salt (0.1 mmol) and 20 ml of oleylamine is introduced into a 4-neck batch reactor, which is slowly heated up to 523 K at a controlled rate of 2.0 K/min under continuous flowing argon (10cc/min). A reflux condenser was used to prevent any oleylamine losses due to evaporation. The solution is left to soak for 2 h at 523 K and then cooled down to room temperature. Particle collection consists of washing with acetone (20 ml) and centrifuging at 4000 rpm for 2 h. After removing the supernatant (oleylamine and acetone), the acquired WO_x NPs are dried at room temperature and are finally redispersed in toluene. Before any further characterization the toluene suspension of the WO_x NPs is centrifuged to remove any large aggregates.

Another series of synthesis experiments was performed by adding 5 mmol of trimethyl aminie N-oxide (TANO) or 5 mmol of 1,12-dodecanediol to the initial slurry solution. MoO_x and VO_x NPs were synthesized by replacing AMT with AMM and AMV, respectively.

Pyridine ligand-exchange experiments were performed to replace oleylamine. 5 ml of pyridine was mixed with a 40 ml toluene suspension of WO_x NPs and they were rigorously stirred in a fumehood under argon flow (10 cc/min) at (1) 323 K resulting in complete evaporation of toluene in 1 day (with the resulting sample labeled "Py-1") and (2) at room temperature resulting in complete evaporation of toluene in 3 days (with the resulting sample labeled "Py-3").

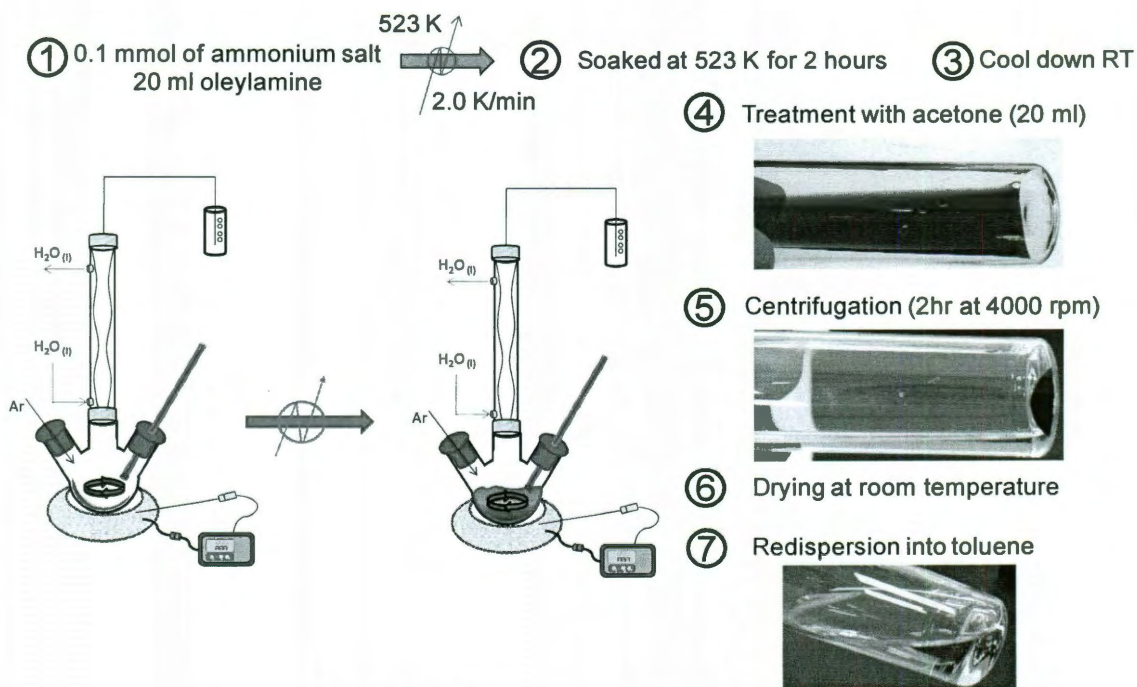


Figure 6.1. WO_x NP synthesis scheme.

6.5 Characterization

6.5.1 Electron microscopy

TEM samples of the as-synthesized WO_x NPs were prepared by pipetting a drop of the suspension of the WO_x NPs onto a continuous ultra-thin carbon film supported on a copper mesh TEM grid. The TEM samples were left under ambient conditions until the solvent had completely evaporated. Bright field (BF) and high resolution TEM (HRTEM) images of the samples were obtained using a JEOL 2100FX TEM operating at 200kV. Aberration-corrected high-angle annular dark field (HAADF) Z-contrast imaging were performed on a 200 kV JEOL 2200FS (S)TEM equipped with a CEOS probe C_s -corrector located at Lehigh University.

For STEM-HAADF imaging, typically a $\sim 1\text{\AA}$ (FWHM) coherent electron beam with $\sim 30\text{pA}$ probe current was used. Dwell times between 48-62 μs per pixel were typically employed. The TEM samples for the as-synthesized WO_x NPs were pre-treated with an “electron beam shower” in order to reduce the carbon contamination during high magnification STEM-HAADF imaging. This “electron beam shower” treatment entailed by allowing a broad intense electron probe to illuminate a large area of the sample for a short time, which can in principle reduce the mobility of any surface hydrocarbon molecules. The HAADF images presented have been low-pass filtered to reduce background noise. The particle size was estimated using *Image J* software [46].

Using a standard Au NP sample as a reference, an estimation of the d spacing was made using the following equation [47]:

$$Rd = \lambda L \quad (6.1)$$

where λ is the wavelength of the electron beam, L is the camera length, and R is the distance between the incident beam and the diffracted beam (diffracted rings). Under the same magnification a direct relationship between the tested sample and the standard Au NP can be made using equation 2.2 [47].

$$d_{NP} = \frac{R_{Au}}{R_{NP}} d_{Au} \quad (6.2)$$

The first diffraction ring of a Au NP corresponds to the (111) plane of a cubic conformation ($d_{Au} = 0.236$ nm). An estimation of the d spacing for the synthesized NPs can be made by measuring R_{Au} and R_{NP} .

6.5.2 Atomic force microscopy

Atomic force microscopy (AFM) measurements were performed on a digital instrument (Nanoscope IIIA). Toluene dispersed NPs were deposited and spin-coated onto high ordered pyrolytic graphite (HOPG) for optimal dispersion properties. The HOPG surface was completely flat with variations < 1 nm along the vertical z-axis (Figure 6.2). All scans were performed on a tapping-mode using gold coated AFM-tips. Image analysis was performed using the WSXM software [48] and the particle size distribution was calculated using Origin (OriginLab, Northampton, MA).

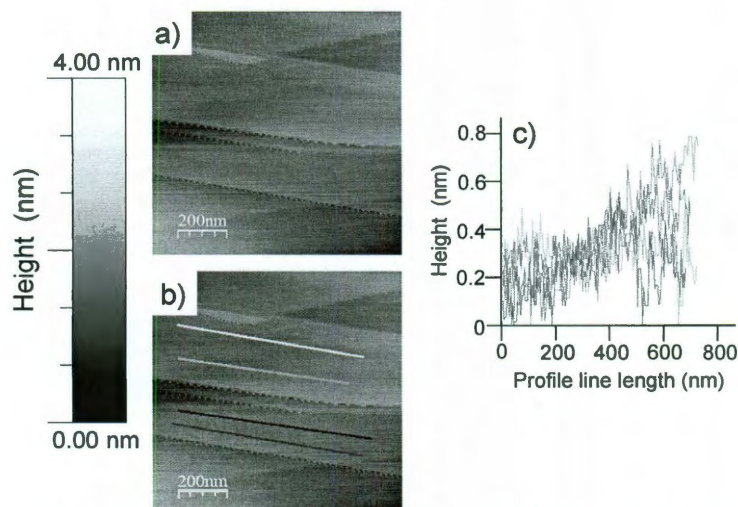


Figure 6.2. a) Atomic force microscopy image of high ordered pyrolytic graphite (HOPG), b) profile lines along different HOPG planes and c) Height profile along different planes.

6.5.3 Dynamic light scattering

Dynamic light scattering studies were used to identify the WO_x NP size when dissolved in toluene using a ZetaPALS (Brookhaven Instruments Corporation) instrument equipped with a He-Ne laser ($\lambda=656$ nm), a detector set at 90° and a BI-9000AT digital autocorrelator that records scattered light. The toluene suspension of the WO_x NPs was transferred into 4 mL quartz cuvettes at room temperature and analyzed in triplicates over intervals of 3 minutes to ensure reproducibility. The laser was stabilized for 15 min prior to each measurement and the instrument was calibrated using a colloidal polystyrene standard (diameter: 92 ± 3 nm). The diffusion coefficient of toluene was estimated using a built-in routine and the particle diameter was calculated using the Stokes-Einstein relationship. Nonlinear least square (NNLS) and CONTIN fitting routines were used to size the particle diameters by the instrument software (9KDLSW) [49].

6.5.4 Small-angle X-ray scattering

Small-angle X-ray scattering studies were performed on a Rigaku SmartLab X-ray diffractometer using a Cu K α radiation source ($\lambda=1.54 \text{ \AA}$). A toluene suspension of WO_x NPs was sealed in borosilicate glass capillaries and analyzed in transmission mode at 40 kV and 44 mA. Average particle size distributions were determined by simulating the profile from 2θ values of 0.2-4.0° using Nanosolver (Rigaku software) [50]. A core/shell model was applied for all calculations and the shell (oleylamine) thickness was set to 2 nm. Experimental and simulated data (fitted data) matched completely for $2\theta > 0.04^\circ$ (R-factor < 2 %).

6.5.5 Thermogravimetric analysis

Thermogravimetric analysis was performed on a Q600 TA instrument that so that the organic content of the particles could be calculated. All samples were dried prior to analysis at room temperature overnight and were heated to 1073 K at a ramp rate of 3.0 K/min under flowing air (100cc/min). Combined TGA-FTIR analysis was performed to study the decomposition of AMT in the presence of oleylamine. Similar to the synthesis conditions, the sample was heated under continuous flowing argon and the outgas line was passed to a Nicolet FTIR. The downstream gas exhaust-line between the TGA and the FTIR was heated at (393 K) to prevent any condensation. In this case, the sample was prepared by drying at room temperature overnight and heating to 523 K at a ramp rate of 2.0 K/min under flowing argon (50cc/min). It is noted that the system is not operated under vacuum conditions; hence, CO₂ is observed in the obtained IR-spectra.

Since no reflux condenser is used in this case, partial decomposition and incomplete combustion of oleylamine was unavoidable.

6.5.6 X-ray diffraction

X-ray diffraction (XRD) patterns were acquired on a Rigaku D/Max-2100PC using a continuous scanning mode with 0.02° step size [45] and a scan rate of 2.5 s/step. The XRD pattern of WO_x NRs was matched to $\text{W}_{18}\text{O}_{49}$ (PDF 00-005-0392).

6.6 Results and discussion

6.6.1 Tungsten oxide nanoparticle structure

DLS analysis verified the formation of WO_x NPs; both NNLS and CONTIN routines fitted a number weighted average diameter of 1.1 ± 0.2 nm, which demonstrates that the particles were very small for acquiring accurate hydrodynamic diameter measurements. SAXS estimated the size of the NP core to be ~ 1.7 nm by considering a core-shell model where the size of the shell was set to 2 nm (full length of oleylamine molecule).

Representative BF-TEM and HRTEM images of the as-synthesized WO_x NPs are shown in Figures 6.3a and 6.3b. These WO_x NPs were found to have very small average diameter (1.6 nm) and a rather narrow relative size distribution (relative size distribution; $\text{RSD} = \text{standard deviation} \div \text{mean}$ of $\sim 12.5\%$) (Figure 6.3A). The HRTEM image presented in Figure 6.3b suggests that these WO_x NPs have irregular spherical shapes, and some of them (highlighted in red) are crystalline in nature as revealed by the presence of lattice fringes.

Structural deformation of the WO_x NPs could in principle occur as the oleylamine molecules were disrupted or modified on the NP surface during the “electron beam shower” procedure, although no significant particle size distribution change is noticed by comparing the DLS and SAXS results with the HAADF images. This observation suggests that when WO_x NPs are supported on a carbon film they do not agglomerate under intense electron beam shower to form larger particles.

STEM-HAADF imaging provided Z-contrast information and was also applied in order to directly image the WO_x structures present and estimate the number of WO_x structural units within each WO_x NP. Each atomic column can be clearly resolved in Figures 6.3c and 6.3d, and the intensity variations between different atomic columns are directly related to the number of W atoms in the columns along the z direction. By directly counting the number of W atoms of each bright spot associated with a cluster, it is found that most of the WO_x NPs found in this sample contain between 20 and 36 W atoms (or WO_x structural units) and about 80% of the W atoms are on the surface.

STEM-HAADF imaging revealed that that the WO_x NPs were not highly crystalline (Fig. 6.3c), which could be due to either an inherent semi-crystalline nature of the WO_x NPs or slight structural damage induced by the “electron beam shower” pre-treatment. The presence of single W atoms (highlighted by yellow circles in Figure 6.3c), presumably in the form of isolated WO_x structural units, could be partially due to a severe reduction of the polyoxometalate core during synthesis or partially by structural damage induced by the electron beam.

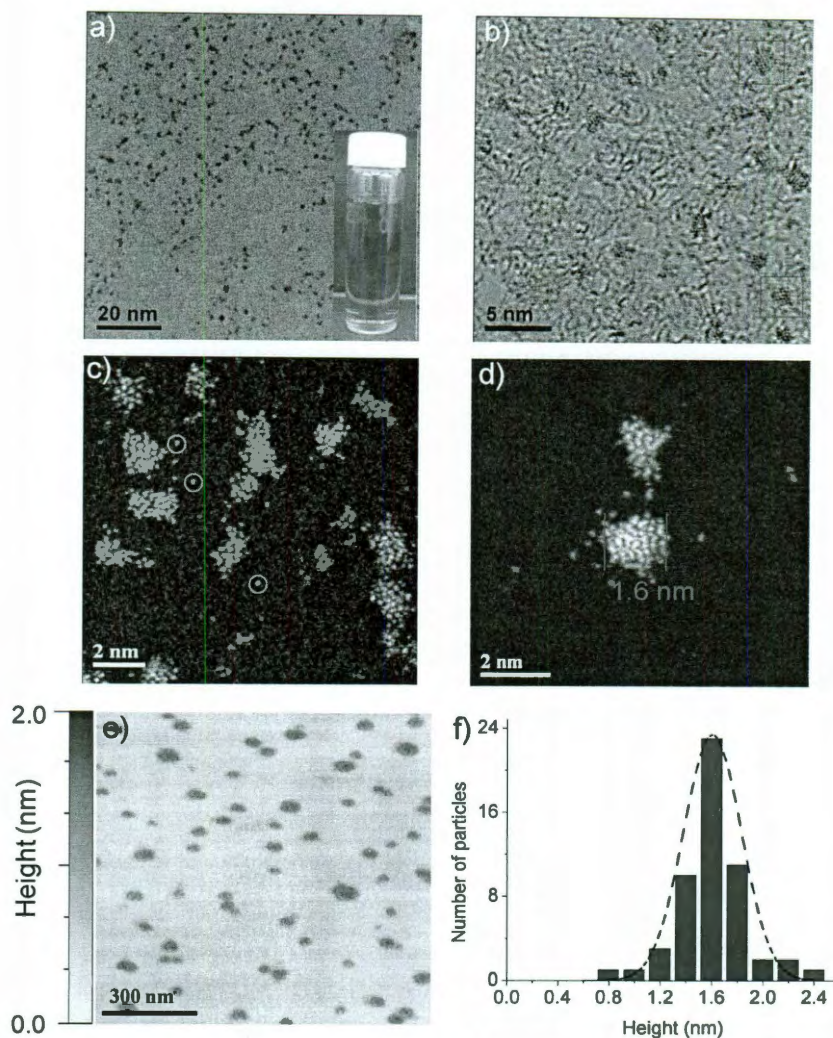


Figure 6.3: a) TEM , b) HR-TEM and c,d) HAADF STEM and e) AFM images of WO_x NPs, f) AFM particle height distribution . Inset: Toluene suspension of WO_x NPs.

The average WO_x NP height and associated distribution was accurately estimated using AFM. In Figure 6.3 e and f, we observed that the HOPG surface is covered by WO_x NPs with a narrow particle size distribution of 1.6 nm and a standard deviation of 0.3 nm (Figure 6.3f) or a relative standard deviation (RSD) of 19 %.

Studying the crystallinity of the synthesized NPs is challenging due to the small particle diameter. The XRD patterns presented were acquired after drying the NPs at room temperature for 4 days (Figure 6.4a). Two broad XRD peaks are noticed at $2\theta \sim$

27° and 50° (Figure 6.4a) that do not match with any crystal plane of WO_3 . Even though the results were reproducible (~ 2 nm estimated diameter), an accurate estimation of the grain size cannot be considered using this approach due to method limitations. Scherrer's formula (discussed in chapter 3, section 3.3.3, equation 3.1) does not provide an accurate measurement since the particles are < 4 nm, which is the lowest XRD detection limit. Low signal to noise ratio and limitations concerning Scherrer's formula make it difficult to estimate grain sizes outside the range of 4 – 100 nm.

From the electron diffraction image presented in Figure 6.4b, no clear assignment can be made since the diffraction rings are rather diffused, a characteristic of very small NPs. Nevertheless using equation 6.1, the d-spacing for the first diffused ring was estimated to be ~ 0.25 nm.

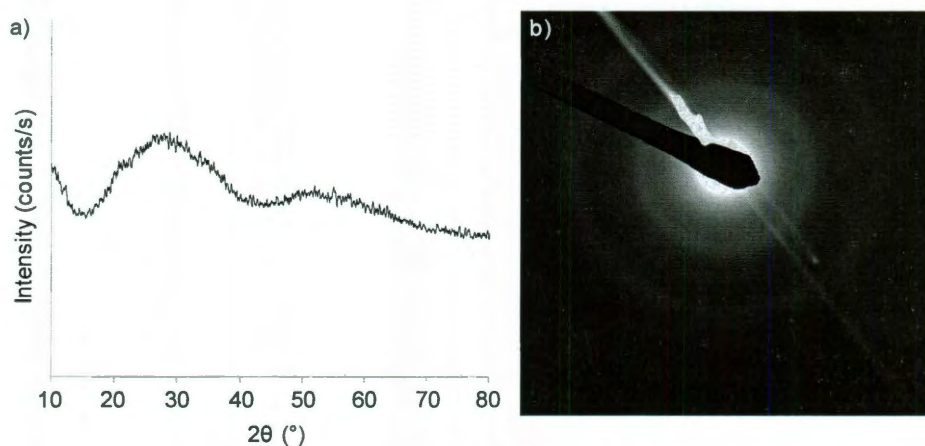


Figure 6.4. a) Powder x-ray diffraction pattern and b) electron diffraction pattern of WO_x NPs

6.6.2 Oxidant co-addition effect

Two major color transitions were observed during the actual synthesis procedure. The first transition occurs at ~ 473 K resulting in a clear blue suspension while the

second occurs at ~ 523 K into a dark brown suspension. The color change corresponds to the reduction and decomposition of the WO_x keggin-core of AMT by NH_3 and/or by oleylamine. The final color changes from light yellow to dark brown indicates the formation of the WO_x NPs. Similar studies by Pope and coworkers concerning heteropoly blues [51-55] and by Ressler and coworkers about ammonium paratungstate (APT) under different reducing atmospheres [56], reported the color change to be associated with a reduction of the oxometallate core.

When the synthesis takes place in the presence of 5 mmol of trimethylamine N-oxide (TANO), the suspension color does not change to blue, but instead remain transparent until changing to yellow at 473 K and finally dark brown at 523 K. The particle size in this case is reduced to 1.0 nm with a standard deviation of 0.40 nm (RSD = 40%) as identified by HAADF STEM and AFM (Figure 6.5). TANO is an oxidation agent [57-59] and therefore prevents the intense reduction that takes place during the synthesis process, resulting in the formation of clusters of 18-24 W atoms. TANO was preferred over bubbling with O_2 to prevent any premature combustion of oleylamine. By doubling the amount of TANO, no particles are made which suggests that nucleation does not occur. WO_x NPs made in the presence of TANO will be referred to as WO_x small (WO_x sNPs).

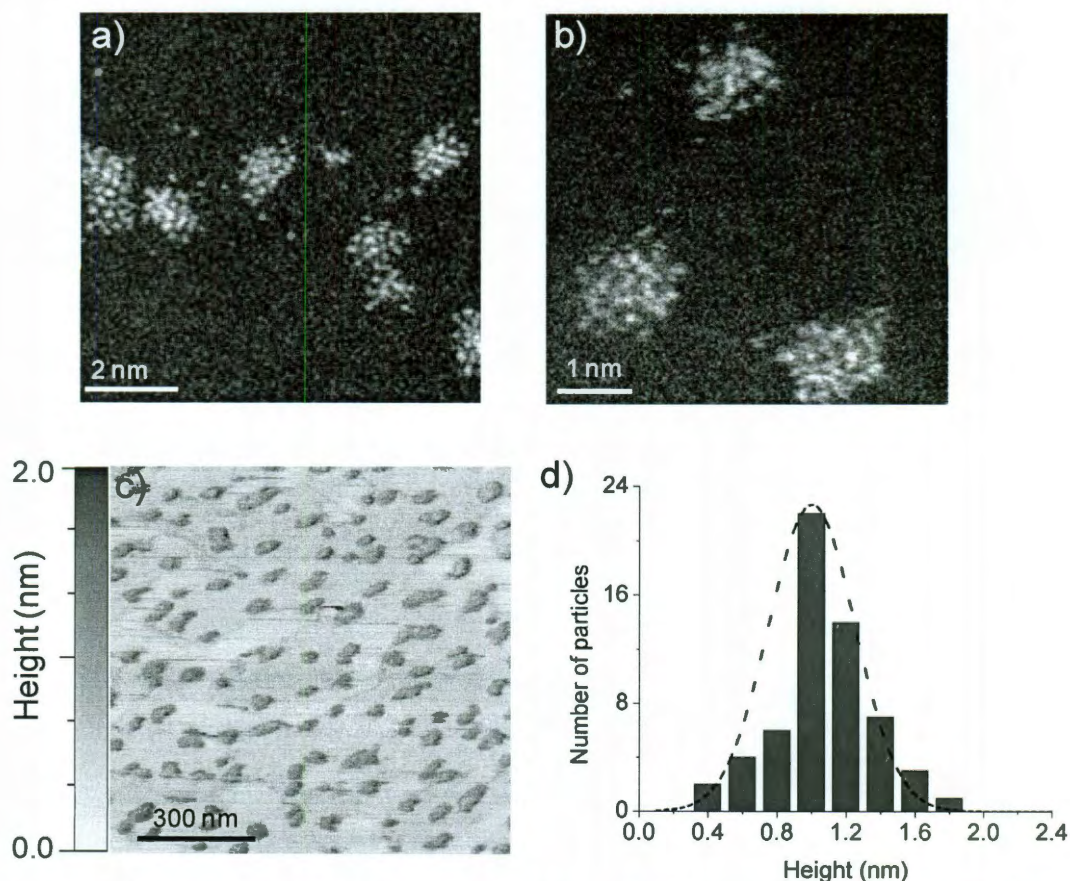


Figure 6.5. a,b) HAADF STEM of WO_x sNPs, c) AFM images of WO_x sNPs, and d) AFM particle height distribution.

6.6.3 Reductant co-addition effect

To test the hypothesis that a reduction mechanism is primarily responsible for the particle growth, 5 mmol of 1, 12-dodecanediol (which is used as a reduction promoter) [59]) was used instead of TANO. In this case, the suspension turned blue at ~ 473 K and remained blue until completion of the reaction. The particles synthesized in this case are WO_x nanorods (NRs) (4 ± 1 nm \times 20 ± 5 nm) (Figure 6.6a and 6.6b) and their structure was identified to be W₁₈O₄₉ [15] with preferred crystal growth along the (010) direction (Figure 6.6c). The absorption of red-infrared light by the WO_x NRs (Figure 6.6d) is not observed for the WO_x NPs and WO_x sNPs. This is due to the presence of oxygen

deficiency sites, which correspond to increased numbers of W^{5+} similar to what has been suggested for WO_3 colloids [60-63] and WO_x NRs [15,18,35,36,64].

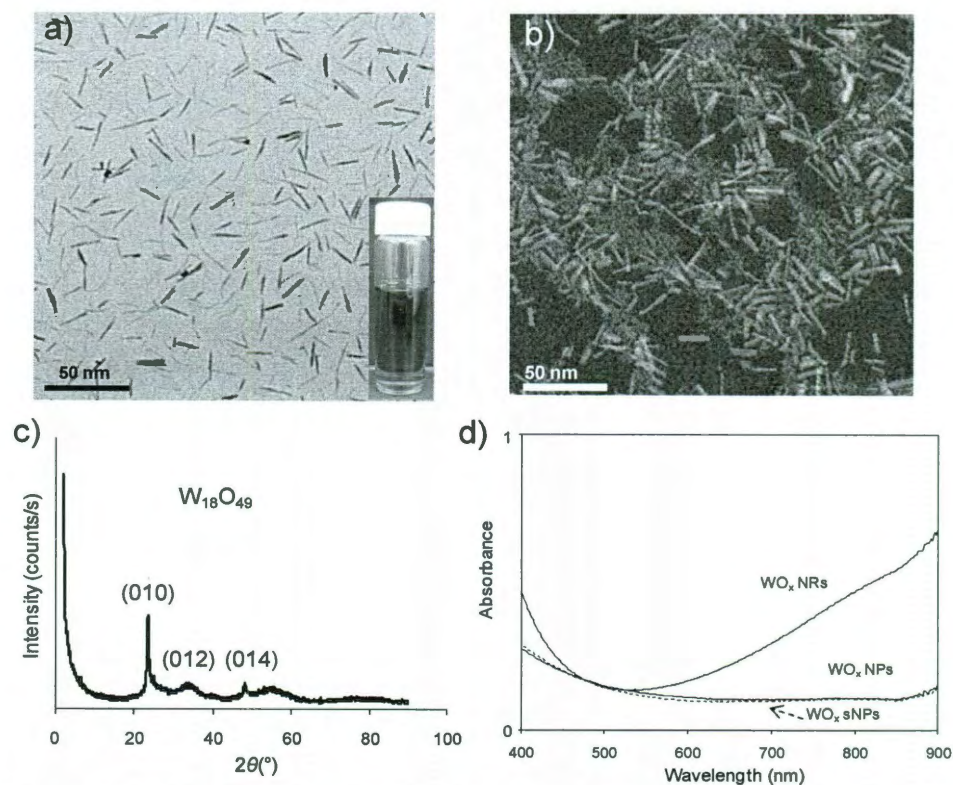


Figure 6.6. a) TEM and b) HAADF STEM of WO_x NRs, c) XRD of WO_x NRs and d) UV-vis absorption spectra of WO_x NRs, NPs, and sNPs normalized to the same NP concentration. Inset: Toluene suspension of WO_x NRs.

6.6.4 Tungsten oxide nanoparticle yield calculation

In Figure 6.7 the TGA data for WO_x NPs, sNPs, NRs, oleylamine, and AMT are presented. AMT appears to lose $\sim 8\%$ of its initial weight due to complete evaporation of H_2O and NH_3 . It is noticed that complete removal of oleylamine was achieved at ~ 773 K, similar to what is noticed for WO_x NPs and sNPs. Organics present in the WO_x NRs sample continued to decompose up to ~ 873 K, possibly due to a stronger interaction between oleylamine and the WO_x core. Each sample was analyzed four times using a constant ramp rate and the average organic content of each sample was determined to be

~48% for NPs, ~65% for the sNPs, and ~27% for the NRs. Based on these results, the remaining 52%, 35%, and 73% of the samples, respectively, corresponds to the inorganic sample content which was used to perform the following yield calculations for 30 different batches (average values shown in Table 6.1). The overall NP yield was found to be $92 \pm 5\%$ (relative standard deviation, $n=30$) for the NPs, $89 \pm 4\%$ (relative standard deviation, $n=15$) for the sNPs and $95 \pm 3\%$ (relative standard deviation, $n=3$) for the NRs. The offset corresponds to minor yield differences in different batches. All TGA plots are qualitatively identical which suggests that neither TANO nor 1, 12-dodecanediol attach to the WO_x surface. An estimation of the ratio of oleylamine-molecules to W atoms is presented for the different particles in Table 6.1. A ratio of 0.1, 0.7, and 0.9 was found for the WO_x NRs, NPs, and sNPs, respectively. This ratio increases as the size of the particles decreases and reaches 0.9 for the sNPs that are expected to have almost all W atoms exposed to the $-\text{NH}_2$ groups of oleylamine.

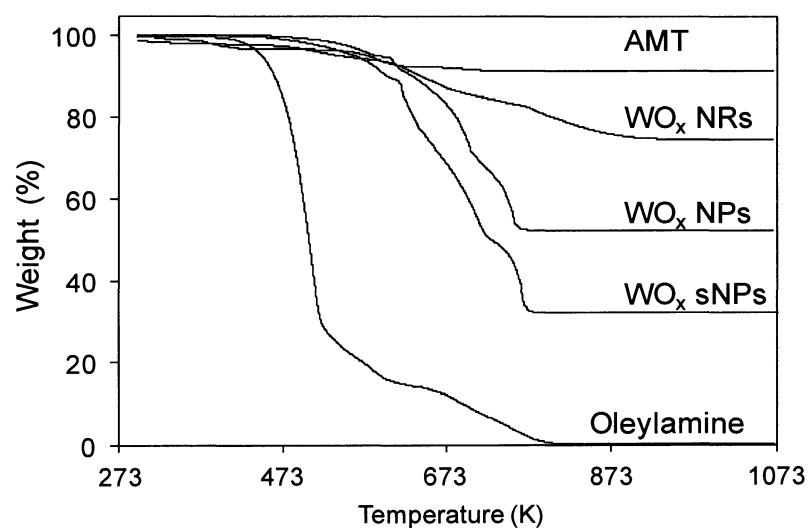


Figure 6.7. TGA of WO_x sNPs, NPs, NRs, oleylamine, and AMT. Ramp rate of 3.0 K/min under flowing air (100cc/min).

Table 6.1. Size, composition and NP yield of WO_x NPs, sNPsc and NRs

	WO _x sNPs	WO _x NPs	WO _x NRs
AFM size (nm)	1.0 ± 0.4	1.6 ± 0.3	-
TEM size (nm)	1.0 ± 0.3	1.6 ± 0.2	4±1 × 20±5
Hydrodynamic diameter (nm)	-	1.3 ± 0.2	-
Organic content (%)	65	48	27
Inorganic content (%)	35	52	73
Nanoparticle yield (%)	89 ± 4	92 ± 5	95 ± 3
Oleylamine molecules per W atom	0.9	0.7	0.1

6.6.5 Pyridine ligand exchange of oleylamine

Pyridine ligand experiments were performed to study the ligand-exchange properties of the WO_x NPs. The color of the suspended particles did not change after performing the experiments and the size of the particles did not change (not shown). The TGA/DSC plots of the pyridine exchanged samples are presented in Figure 6.8. By assuming that the dominant mechanism during this ligand exchange experiment is the ligand replacement and not a ligand addition to the particle, we can estimate the percentage of oleylamine molecules replaced by pyridine after one day and after three days. Based on molecular weight calculations, a complete ligand exchange would decrease the total weight by ~70%. In one day, the organic content decreases by 9% and in three days by 14%. Complete ligand exchange was not achieved in any case because pyridine is a weaker base than oleylamine as indicated by the pKa values (5.2 for pyridine vs. 10.4 for oleylamine).

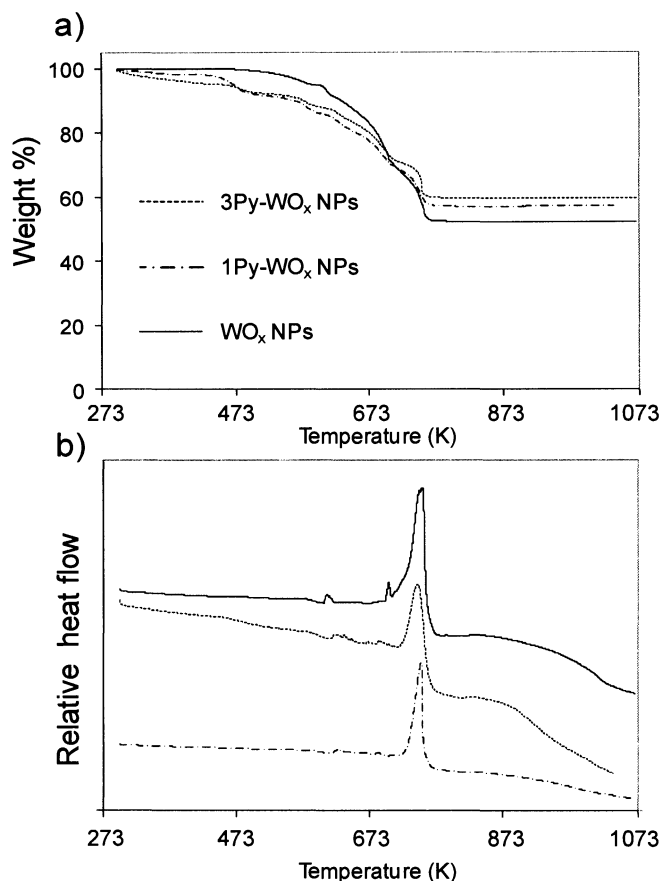


Figure 6.8. TGA/DSC of pyridine exchanged WO_x NPs. Py-1 represents ligand exchange completed in 1-day and Py-3 in 3 days.

6.6.6 Tungsten oxide nanoparticle synthesis mechanism.

The synthesis of the WO_x NPs proceeds via solvothermal decomposition of the water soluble AMT in the presence of oleylamine that operates as capping ligand in the final organometallic complex. The synthesized core-shell structures are soluble in organic solvents like toluene and hexane unlike their ammonium precursors. In our synthesis an excess of oleylamine was used to ensure (1) stabilization and thereby avoid aggregation of the WO_x NPs and (2) good mixing and heat transfer properties within the 4-neck batch reactor. It was also noticed that by using a non-reacting solvent such as 1-

octadecene, rapid growth of the synthesized particles generated larger rod-shaped structures.

In Figure 6.9 the TGA/FTIR decomposition results of AMT and oleylamine under argon atmosphere are presented. The weight loss noticed at ~ 373 - 473 K corresponds to the appearance of two absorption regions (figure 6.9b and 6.9c) assigned to (1) the N-H stretching vibrations ~ 3000 - 3300 cm^{-1} and (2) to the O-H stretching vibrations ~ 3600 - 3700 cm^{-1} due to water and NH_3 respectively, generated upon decomposition of the AMT precursor. The strong band observed at ~ 2350 cm^{-1} and ~ 540 cm^{-1} correspond to the asymmetric stretching and the bending mode of CO_2 , respectively. The band noticed at ~ 900 cm^{-1} appears at ~ 473 K and corresponds to the bending vibration modes of $=\text{C}-\text{H}$. At the same temperature the color of the suspension turned blue and remained unchanged only in the presence of 1, 12-dodecanediol. The detection of the $=\text{C}-\text{H}$ band is a result of incomplete decomposition of oleylamine. It signifies that an activation of oleylamine is required for the decomposition of the AMT core to take place via a reduction mechanism.

Based on this observation, we propose a particle formation model that progresses via the following steps: a) a dehydration of the AMT molecule, b) dissociation of the NH_3^+ groups from the AMT core, c) a reduction of the oxometallate core by oleylamine and NH_3 , d) nucleation of the WO_x NPs, and e) formation of the WO_x NPs via growth and termination by protonated $-\text{NH}_3^+$ groups of oleylamine (proposed reaction scheme presented in Figure 6.10).

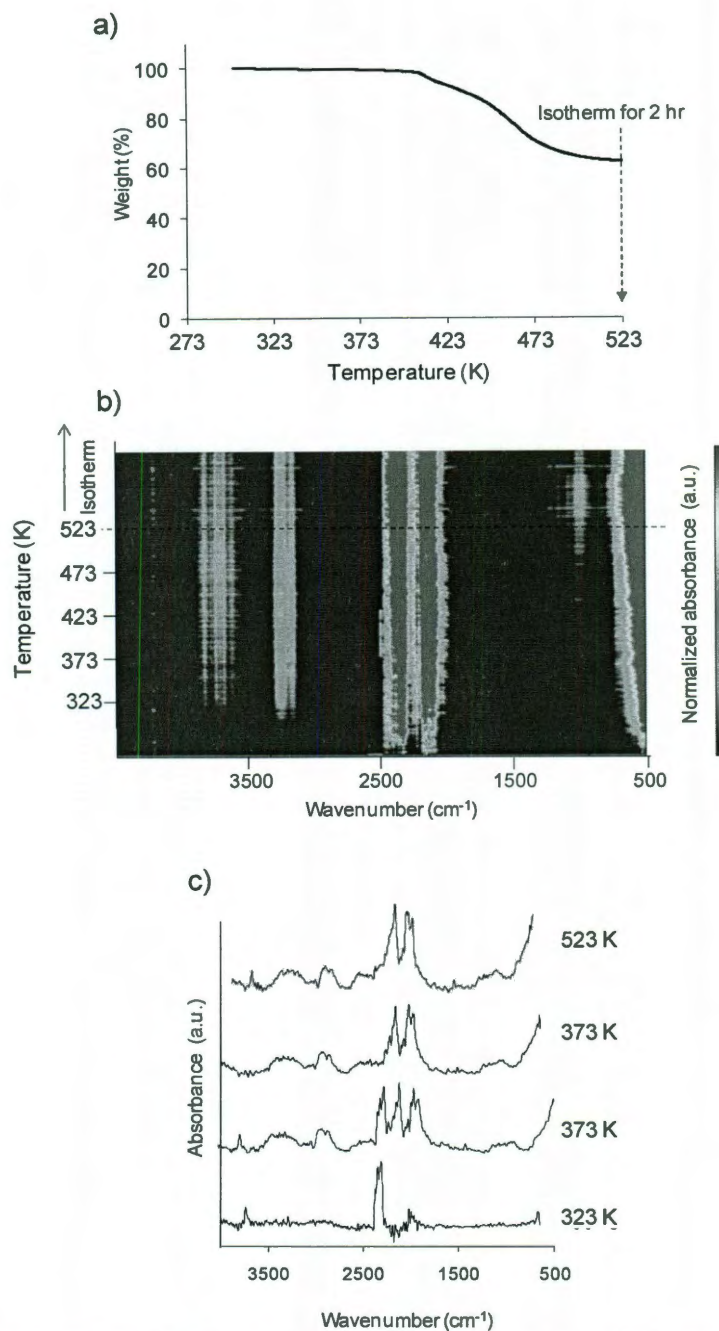


Figure 6.9. TGA/FTIR of AMT and oleylamine. Ramp rate of 2.0 K/min under flowing argon (50cc/min).

The redox mechanism between W^{6+} that act as nucleation sites and W^{5+} [61] that is responsible for the particle growth. W^{5+} atoms are only detected in WO_x NRs due to increased oxygen defected sites at the surface of rod-shaped structures [15,18,35,36,64].

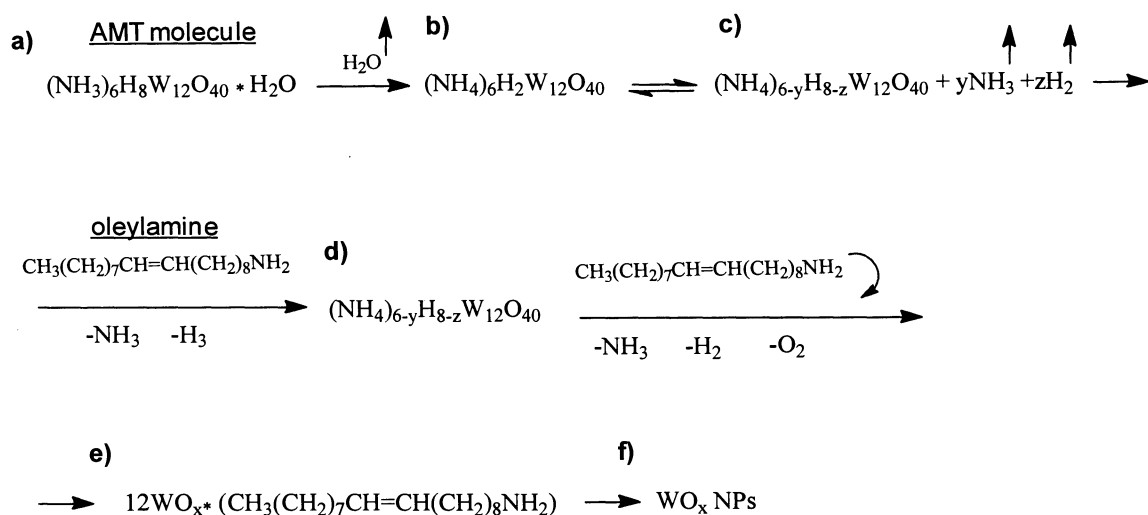


Figure 6.10. Proposed reaction mechanism of the WO_x NPS. The reaction steps are a) dehydration of the AMT core, b) dissociation of amine groups from the AMT core, c) reduction of the AMT core by oleylamine and NH_3 , d) association between oleylamine and decomposed WO_x to initiate nucleation, and e) composition between at least 12 WO_x units for the synthesis of WO_x NPs

6.6.7 Molybdenum and vanadium oxide nanoparticle synthesis

The synthesis of MoO_x and VO_x nanoparticles was successful using the same basic synthesis procedure (no TANO or 1, 12-dodecanediol was used). Similar to WO_x NPs, toluene suspensions of MoO_x NPs were stable and their hydrodynamic radius was found to be 1.2 ± 0.2 nm by DLS and ~ 2.2 nm by SAXS. HAADF images presented in Figure 6.11a and 6.11b show that the MoO_x are of irregular spherical shape, similar to WO_x NPs. AFM (Figure 6.11c) shows that the particles are approximately 1.7 nm with a standard deviation of 0.33 nm (RSD = 20%) (Figure 6.13d).

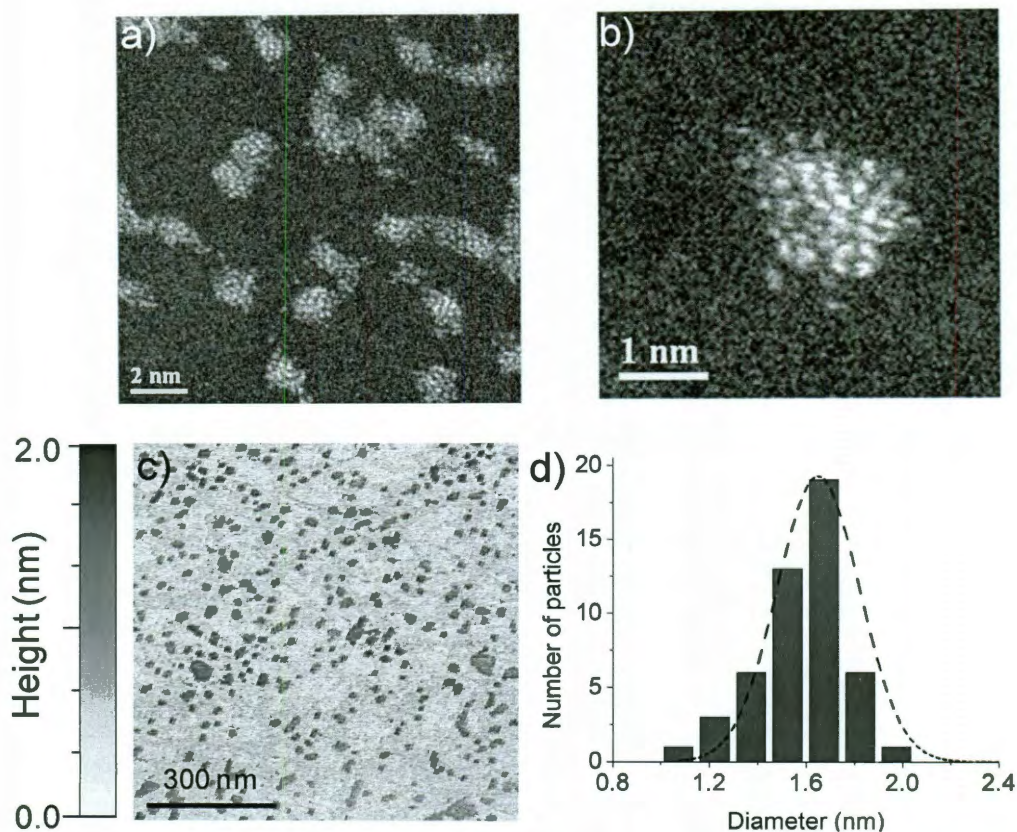


Figure 6.11. a,b) HAADF STEM of MoO_x NPs, c) AFM images of MoO_x sNPs, and d) AFM particle height distribution.

VO_x NPs were less stable; aggregation resulted in complete particle settling within 48 h. Their hydrodynamic radius was estimated by DLS to be 2 ± 0.2 nm and SAXS failed to give any reproducible results. In Figure 6.12a, a single VO_x NP is seen, with the distances between the V atoms being greater as in WO_x and MoO_x NPs. This shows that the assembled particles are very unstable and decompose easily upon the electron beam shower pretreatment. In Figure 6.12b, linear wire-like VO_x patterns are noticed on the carbon film, suggesting that under the basic synthesis procedure presented in this work the synthesis and deposition of VO_x NPs is not possible.

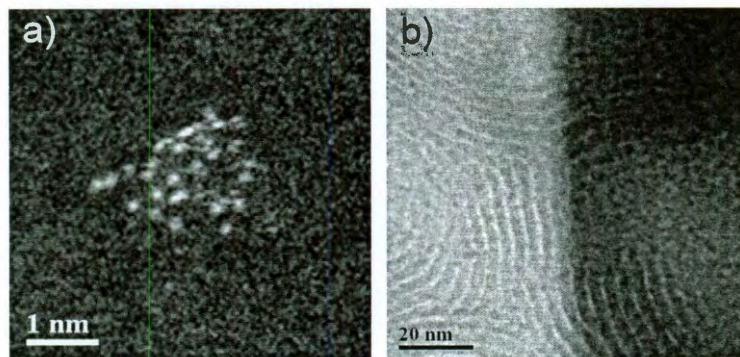


Figure 6.12. a) HAADF STEM of a single VO_x NP and b) self assembly of VO_x NPs

6.7 Summary and conclusions

The synthesis of metal oxide (MO_x) nanoparticles (NPs), such as WO_x , MoO_x , and VO_x , is of great significance in materials chemistry due to their widespread use as catalysts, semiconductors, and gas sensors.. WO_x nanoparticles were efficiently synthesized using a solvothermal reaction between ammonium metatungstate and oleylamine. The size of the particles was modified by controlling the redox/particle growth mechanism. By using an oxidation agent smaller nanoparticles were formed and in the presence of a reduction agent rod-shaped nanoparticles were synthesized.

6.8 References

1. A. S. Arico, P. Bruce, B. Scrosati, J.-M. Tarascon and W. van Schalkwijk, *Nat Mater* 4 (2005) 366-377.
2. X. W. Lou, D. Deng, J. Y. Lee, J. Feng and L. A. Archer, *Advanced Materials* 20 (2008) 258-262.
3. P. Poizot, S. Laruelle, S. Grugeon, L. Dupont and J. M. Tarascon, *Nature* 407 (2000) 496-499.
4. A. C. Dillon, A. H. Mahan, R. Deshpande, P. A. Parilla, K. M. Jones and S. H. Lee, *Thin Solid Films* 516 (2008) 794-797.

5. Y. Wang, Z. Zhang, Y. Zhu, Z. Li, R. Vajtai, L. Ci and P. M. Ajayan, *ACS Nano* 2 (2008) 1492-1496.
6. K. D. Benkstein, B. Raman, C. B. Montgomery, C. J. Martinez and S. Semancik, *Sensors Journal, IEEE* 10 137-144.
7. M. E. Franke, T. J. Koplín and U. Simon, *Small* 2 (2006) 36-50.
8. G. Eranna, B. C. Joshi, D. P. Runthala and R. P. Gupta, *Critical Reviews in Solid State and Materials Sciences* 29 (2004) 111 - 188.
9. X.-L. Li, T.-J. Lou, X.-M. Sun and Y.-D. Li, *Inorganic Chemistry* 43 (2004) 5442-5449.
10. A. Yan, C. Xie, D. Zeng, S. Cai and M. Hu, *Materials Research Bulletin* 45 1541-1547.
11. X. Xie, Y. Li, Z.-Q. Liu, M. Haruta and W. Shen, *Nature* 458 (2009) 746-749.
12. J. V. Ryan, A. D. Berry, M. L. Anderson, J. W. Long, R. M. Stroud, V. M. Cepak, V. M. Browning, D. R. Rolison and C. I. Merzbacher, *Nature* 406 (2000) 169-172.
13. J. A. Rodriguez, S. Ma, P. Liu, J. Hrbek, J. Evans and M. Párez, *Science* 318 (2007) 1757-1760.
14. G. Gu, B. Zheng, W. Q. Han, S. Roth and J. Liu, *Nano Letters* 2 (2002) 849-851.
15. K. Lee, W. S. Seo and J. T. Park, *Journal of the American Chemical Society* 125 (2003) 3408-3409.
16. M. J. Hudson, J. W. Peckett and P. J. F. Harris, *Journal of Materials Chemistry* 13 (2003) 445-446.
17. H. Zhang, M. Feng, F. Liu, L. Liu, H. Chen, H. Gao and J. Li, *Chemical Physics Letters* 389 (2004) 337-341.

18. Jung-wook Seo, Young-wook Jun, S. J. Ko and J. Cheon, *The Journal of Physical Chemistry B* 109 (2005) 5389-5391.
19. A. Phuruangrat, D. J. Ham, S. Thongtem and J. S. Lee, *Electrochemistry Communications* 11 (2009) 1740-1743.
20. M. Zach, K. Ng and R. M. Penner, *Science* 290 (2000) 2120.
21. J. Zhou, N.-S. Xu, S.-Z. Deng, J. Chen, J.-C. She and Z.-L. Wang, *Adv. Mater.* 15 (2003) 1835.
22. K. Du, W. Fu, R. Wei, H. Yang, J. Xu, L. Chang, Q. Yu and G. Zou, *Ultrasonics Sonochemistry* 15 (2008) 233-238.
23. M. Niederberger, F. Krumeich, H. J. Muhr, M. Mueller and R. Nesper, *J. Mater. Chem* 11 (2001) 1941-1945.
24. S. T. Lutta, H. Dong, P. Y. Zavalij and M. S. Whittingham, *Materials Research Bulletin* 40 (2005) 383-393.
25. P. Viswanathamurthi, N. Bhattarai, H. Y. Kim and D. R. Lee, *Scripta Materialia* 49 (2003) 577-581.
26. M. E. Spahr, P. Bitterli, R. Nesper, M. Mueller, K. F. and H. U. Nissen, *Angewandte Chemie International Edition* 37 (1998) 1263-1265.
27. M. E. Spahr, P. Stoschitzki-Bitterli, R. Nesper, O. Haas and P. Novak, *J. Electrochem. Soc.* 146 (1999) 2780-2783.
28. H. J. Muhr, F. Krumeich, U. P. Schönholzer, F. Bieri, M. Niederberger, L. J. Gauckler and R. Nesper, *Advanced Materials* 12 (2000) 231-234.
29. M. Niederberger, H.-J. Muhr, F. Krumeich, F. Bieri, D. Gunther and R. Nesper, *Chemistry of Materials* 12 (2000) 1995-2000.
30. J. Thangala, Z. Chen, A. Chin, C.-Z. Ning and M. K. Sunkara, *Crystal Growth & Design* 9 (2009) 3177-3182.

31. C. S. Blackman and I. P. Parkin, *Chemistry of Materials* 17 (2005) 1583-1590.
32. Y. Koltypin, S. I. Nikitenko and A. Gedanken, *Journal of Materials Chemistry* 12 (2002) 1107-1110.
33. W. Morales, M. Cason, O. Aina, N. R. de Tacconi and K. Rajeshwar, *Journal of the American Chemical Society* 130 (2008) 6318-6319.
34. D. J. Ham, A. Phuruangrat, S. Thongtem and J. S. Lee, *Chemical Engineering Journal* 165 365-369.
35. S. V. Pol, V. G. Pol, V. G. Kessler, G. A. Seisenbaeva, L. A. Solovyov and A. Gedanken, *Inorganic Chemistry* 44 (2005) 9938-9945.
36. J. Wang, E. Khoo, P. S. Lee and J. Ma, *The Journal of Physical Chemistry C* 112 (2008) 14306-14312.
37. X.-L. Li, J.-F. Liu and Y.-D. Li, *Inorganic Chemistry* 42 (2003) 921-924.
38. J. L. Solis, S. Saukko, L. Kish, C. G. Granqvist and V. Lantto, *Thin Solid Films* 391 (2001) 255-260.
39. B. Yang, Y. Zhang, E. Drabarek, P. R. F. Barnes and V. Luca, *Chemistry of Materials* 19 (2007) 5664-5672.
40. C. Santato, M. Ulmann and J. Augustynski, *The Journal of Physical Chemistry B* 105 (2001) 936-940.
41. A. Watcharenwong, W. Chanmanee, N. R. de Tacconi, C. R. Chenthamarakshan, P. Kajitvichyanukul and K. Rajeshwar, *Journal of Electroanalytical Chemistry* 612 (2008) 112-120.
42. E. I. Ross-Medgaarden, W. V. Knowles, T. Kim, M. S. Wong, W. Zhou, C. J. Kiely and I. E. Wachs, *Journal of Catalysis* 256 (2008) 108-125.
43. W. Zhou, E. Ross-Medgaarden, I. E. Wachs and C. J. Kiely, *Microscopy and Microanalysis* 14 (2008) 1350-1351.

44. W. Zhou, E. I. Ross-Medgaarden, W. V. Knowles, M. S. Wong, I. E. Wachs and C. J. Kiely, *Nat Chem* 1 (2009) 722-728.
45. N. Soultanidis, W. Zhou, A. C. Psarras, A. J. Gonzalez, E. F. Iliopoulou, C. J. Kiely, I. E. Wachs and M. S. Wong, *Journal of the American Chemical Society* 132 13462-13471.
46. M. D. Abramoff, P. J. Magalhaes and S. J. Ram, *Biophotonics International* 11 (2004) 36-42.
47. B. D. Cullity and S. R. Stock, *Elements of X-Ray Diffraction* (3rd Edition). Prentice Hall, 2001.
48. I. Horcas, R. Fernandez, J. M. Gomez-Rodriguez, J. Colchero, J. Gomez-Herrero and A. M. Baro, *Rev. Sci. Instrum.* 78 (2007) 013705.
49. V. S. Murthy, J. N. Cha, G. D. Stucky and M. S. Wong, *Journal of the American Chemical Society* 126 (2004) 5292-5299.
50. L. A. Pretzer, Q. X. Nguyen and M. S. Wong, *The Journal of Physical Chemistry C* 114 21226-21233.
51. M. T. Pope, *Heteropoly and Isopoly Oxometalates*. Springer Verlag, New York, 1983.
52. M. T. Pope and G. M. Varga, *Inorganic Chemistry* 5 (1966) 1249-1254.
53. E. Papaconstantinou and M. T. Pope, *Inorganic Chemistry* 9 (1970) 667-669.
54. D. E. Katsoulis and M. T. Pope, *Journal of the American Chemical Society* 106 (1984) 2737-2738.
55. M. T. Pope and A. Müller, *Angewandte Chemie International Edition in English* 30 (1991) 34-48.
56. O. Kirilenko, F. Girgsdies, R. E. Jentoft and T. Ressler, *European Journal of Inorganic Chemistry* 2005 (2005) 2124-2133.

57. J. C. Stichbury, M. J. Mays, P. R. Raithby, M.-A. Rennie and M. R. Fullalove, *Journal of the Chemical Society, Chemical Communications* (1995) 1269-1270.
58. J. A. Soderquist and M. R. Najafi, *The Journal of Organic Chemistry* 51 (1986) 1330-1336.
59. V. M. Rotello, *Nanoparticles: building blocks for nanotechnology*. Kluwer Academic/Plenum Publishers, 2004.
60. I. Bedja, S. Hotchandani and P. V. Kamat, *The Journal of Physical Chemistry* 97 (1993) 11064-11070.
61. P. Gomez-Romero and N. Casan-Pastor, *The Journal of Physical Chemistry* 100 (1996) 12448-12454.
62. T. He, Y. Ma, Y. Cao, X. Hu, H. Liu, G. Zhang, W. Yang and J. Yao, *The Journal of Physical Chemistry B* 106 (2002) 12670-12676.
63. M. T. Nenadovic, T. Rajh, O. I. Micic and A. J. Nozik, *The Journal of Physical Chemistry* 88 (1984) 5827-5830.
64. X. Chang, S. Sun, Z. Li, X. Xu and Y. Qiu, *Applied Surface Science* 257 5726-5730.

Chapter 7

Propene metathesis of silica supported tungsten oxide nanoparticles

7.1. Introduction

7.1.1 Olefin metathesis in industry

Olefin metathesis is an important reaction in the field of (1) synthetic organic chemistry, (2) petrochemicals and (3) polymer industry [1-4]. The three distinct groups of olefin metathesis reactions are (1) exchange metathesis (double bond exchange between two linear olefins), (2) ring-opening metathesis polymerization (opening of the closed ring of a cyclo-olefin followed by polymerization and (3) ring-closing metathesis (opposite to ring-opening metathesis).

For petrochemical applications, exchange metathesis has been utilized in most cases for diversifying the linear olefin products by using one type of olefin (known as productive metathesis) for the production of two different ones (for example propene metathesis for the synthesis of ethane and 2-butene) or for increasing the concentration of a specific olefin by performing the reverse reaction (non-productive metathesis).

The first industrial application of olefin metathesis [2] is the Phillips triolefin process for the production of ethene and 2-butene from propene via productive exchange metathesis (Figure 7.1). The technology was developed by Phillips Petroleum C., USA and achieved near equilibrium conversions and high selectivities using sodium doped WO_x/SiO_2 at 623-698 K. The reverse non-productive reaction for the production of propene was the focus of Lyondell Petrochemical Co., which used ethene and 2-butene (as dimerization products of ethene), via the reverse triolefin process. Other technologies, such as the one developed by Francais du Petrole (IFP) and the Chinese

petroleum corporation, focus on low temperature, high pressure liquid phase reactions that are very efficient but require intense separation and purification post-treatment.

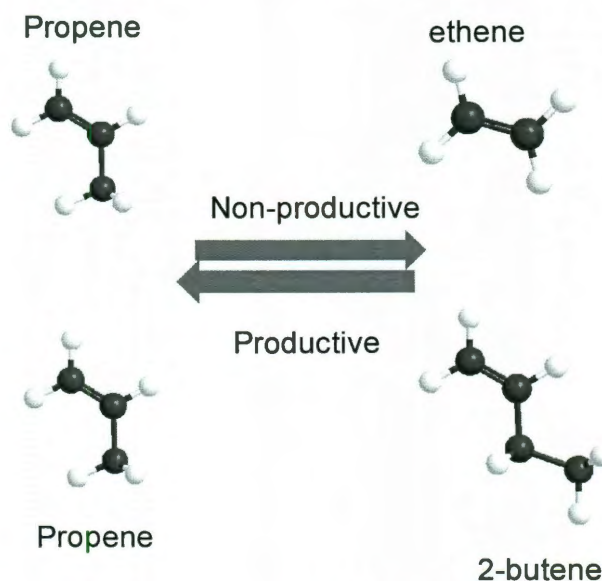


Figure 7.1. Phillips triolefin process, productive (produces two different molecules) metathesis of propene to ethane and 2-butene and non-productive metathesis (reverse reaction)

With increasing market demands for low molecular weight olefins such as propene, ethane and 2-butene, new methods for synthesizing efficient supported catalysts are necessary. Supported metal oxide catalysts (SMOs), such as WO_x/SiO_2 , are excellent candidates for gas phase olefin metathesis reactions such as propene metathesis and they are investigated in this chapter.

The purpose of this chapter is to test the catalytic activity of the supported WO_x NPs synthesized in Chapter 6.

7.1.2 Propene metathesis using WO_x/SiO_2

One of the active metals in all three types of olefin metathesis is supported and unsupported tungsten (W), where W is in various chemical forms (metallic, metal oxide,

organometallic). WO_x/SiO_2 is a SMO that has been extensively investigated [5-19] and used in numerous industrial catalytic units [2] due to its metathesis selectivity, resistance to poisoning [5,14] and easy regeneration [5,14,20]. Higher loadings ($\sim 20\% \text{WO}_3$) are required for achieving maximum activity as opposed to lower loadings ($< 10\% \text{WO}_3$) that are necessary for high selectivity. This indicates a strong structure-activity and selectivity correlation for olefin metathesis using WO_x/SiO_2 .

High concentrations of tetrahedrally coordinated WO_x species, seen in mononuclear species and smaller oligomers [21] (Lewis acid sites [22]), are associated to high metathesis activity [23] and they are highly desired. These very active species are usually found in low concentrations and widely spread on the catalytic surface resulting to localized interphase diffusional limitations [2] that are undesired for industrial applications. Their concentration maximizes at very low WO_x loadings and below monolayer (ML) coverages (0.5 W-atom/nm^2) [24] due to weak interaction between SiO_2 and the WO_x species during calcination. Crystalline WO_3 species (not active for metathesis) are for example detected on SiO_2 support at loadings as low as 10 wt% [2], which suggests that most of the WO_x deposited at higher loadings is not in its most active phase..

A number of experimental methods have been investigated for improving the catalytic activity and selectivity of WO_x/SiO_2 catalysts [2]. In most cases the approach is to dope the catalysts with NH_3 , Na, S, Mg among others to reduce the oxidation state of bulk WO_3 from W^{6+} to W^{5+} and W^{4+} , or to form a mechanical mixture with MgO that promotes the formation of intermediate allyl radicals. To our knowledge, there have been no studies that report a new synthetic approach for improving the catalytic activity and

selectivity of WO_x/SiO_2 . Our focus in this chapter is to explore an alternative synthesis route that promotes the formation of smaller WO_x clusters in the form of monotungstates and smaller polytungstates that would eventually allow achieving higher WO_x loadings without significant aggregation and crystallization to occur.

7.1.3 Metal carbene/metallacycle mechanism

Propene metathesis (Figure 7.1) is an endothermic reaction ($\Delta H = 1.7$ kJ/mol at 298 K) with the equilibrium conversion increasing from $\sim 34\%$ to $\sim 43\%$ with an increase in the reaction temperature from 298 K to 598 K [2]. The reaction mechanism is known as metal carbene/metallacycle mechanism and it was first proposed by Hérisson and Chauvin in 1971 [2].

As seen in Figure 7.2, the reaction is initiated by the formation of transition metal-carbene (compound 1) that coordinates with the incoming propene molecule to form an unstable metallacycle (compound 2). The metallacycle decomposes to give ethene and a new metal-carbene (compound 3) and the cycle is repeated once more for a new metallacyclobutane (compound 4) to be formed that decomposes to generate 2-butene.

Even though this model was established for complicated organometallic complexes used in liquid phase metathesis, it is the prevailing model for SMOs such as WO_x/SiO_2 . There have been no studies that report a mechanism to convert a $\text{M}=\text{O}$ bond to $\text{M}=\text{C}$ for WO_x/SiO_2 . It is generally considered that the metathesis mechanism is promoted on monotungstates and smaller polytungstates as opposed to larger polymeric species that demonstrated strong Brønsted acidity [2].

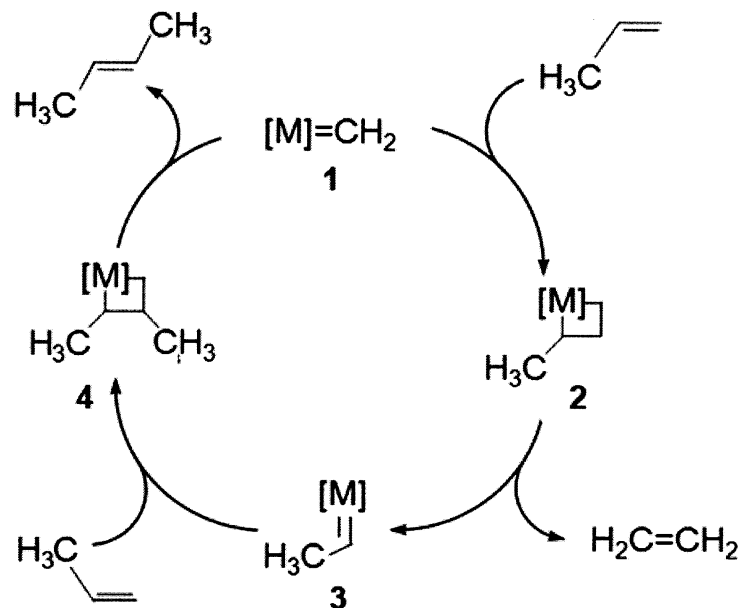


Figure 7.2. Propene metathesis via metal carbene/ metallacycle mechanism, where M is a metal atom. The mechanism precedes via 4 steps (also known as 2+2 reactions), (1,3) the formation of the metal carbene and (2,4) the formation of a metallacycle intermediate.

After successfully synthesizing and characterizing the WO_x NPs in chapter 6, the catalytic activity of supported WO_x NPs is investigated here. Different supports have been used for the preparation of various supported WO_x NPs, preliminary results of which are presented in the final chapter. The focus in this chapter is on the characterization of SiO_2 supported WO_x NPs, on their propene metathesis performance and how that compares to conventional WO_x/SiO_2 catalysts.

7.2. Experimental methods

7.2.1 Chemicals

Ammonium metatungstate hydrate (AMT, $(NH_3)_8W_{12}O_{40} \cdot xH_2O$), oleylamine, acetone, toluene, trimethyl-amine n-oxide, 1,2-dodecanediol were purchased by Sigma-

Aldrich and colloidal SiO₂ (VP Aeroperl ® Pharma) was provided by Degussa. All chemicals were used without further purification.

7.2.2 Synthesis of supported tungsten oxide nanoparticles

The synthesis of WO_x NPs was described previously (Chapter 6, Section 6.4.2). The acquired WO_x NPs were dissolved in toluene to a total volume of 40 ml and were placed in a 200 ml beaker. 1 g of the selected support (ZrO₂, Al₂O₃, SiO₂ or C) was added in the beaker and the slurry was stirred in a vacuum hood at 313 K overnight. The characteristics of all the supports were reported previously (Chapter 5, Section 5.2.1). The resulting gel-like material was further heated overnight at 353 K followed by calcination up to 573 K - 873 K for 3 hours at a rate of 3.0 K/min. The process scheme of the SiO₂ supported WO_x NPs is shown in Figure 7.3.

The following nomenclature is used for the samples prepared in this chapter: For the SiO₂ supported WO_x NPs samples, NP ρ_{surf} WO_x/SiO₂(z,T); for the samples synthesized without an oxidation agent, sNP ρ_{surf} WO_x/SiO₂(z,T); for the samples using an oxidation agent and WO_x NPs, NP ρ_{surf} WO_x/ZrO₂(z,T). ρ_{surf} is the surface density, z is the tungsten weight loading calculated in the form of WO₃ (wt%-WO₃), and T is the calcination temperature (K) similar to previous chapters (Chapter 2, Section 2.2.2). The WO₃ (wt%-WO₃) content for the NP ρ_{surf} WO_x/SiO₂(z,T) was verified by estimating the organic content of each catalyst (Figure 7.4) and by using the calculations presented in chapter 6 section 6.6.4.

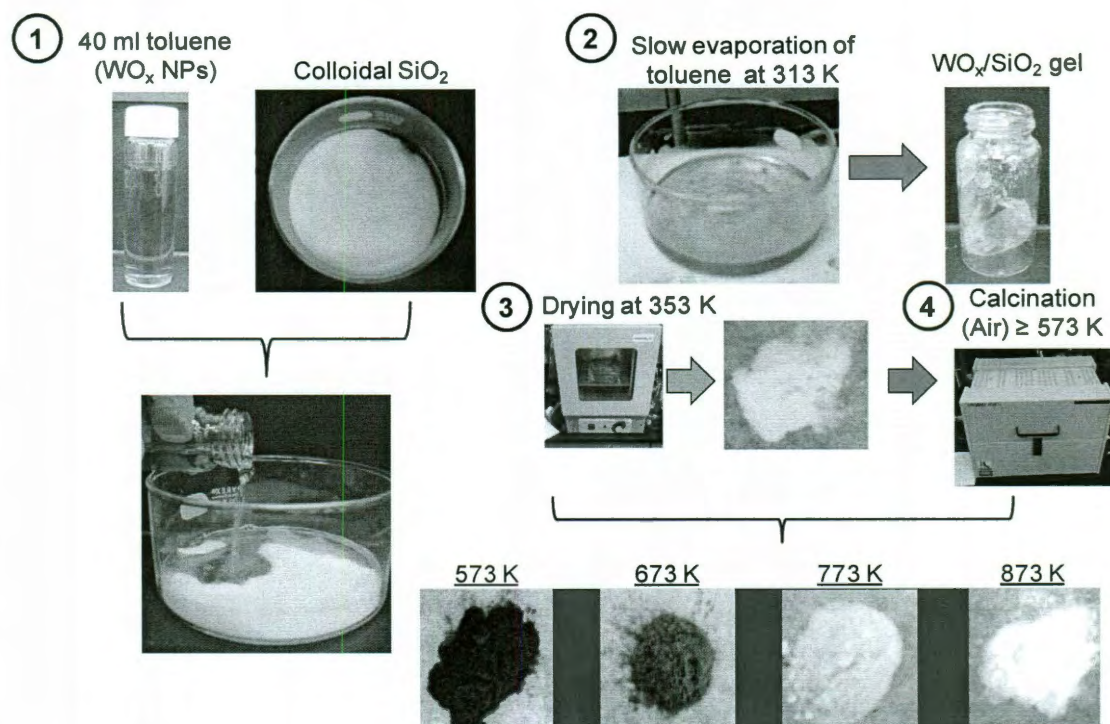


Figure 7.3. Synthesis scheme of SiO₂ supported WO_x NPs. The four steps include (1) mixing of support with toluene suspension of WO_x NPs, (2) slow evaporation of toluene at 313 K, (3) drying of the WO_x/SiO₂ gel at 353 K and (4) calcination at the desired temperature. Residual oleylamine is detected up to 773 K.

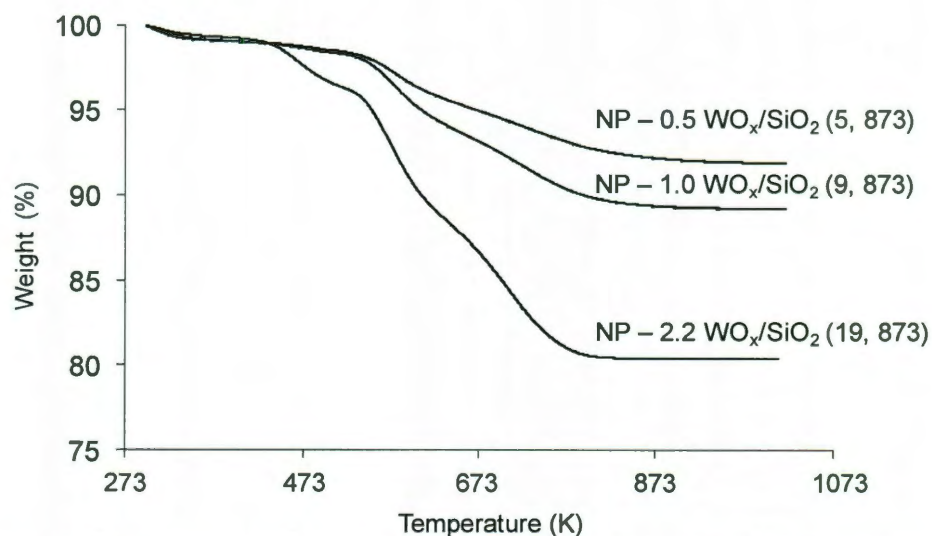


Figure 7.4: TGA plots of NP-WO_x/SiO₂ show the different concentration of organic content for different loadings.

For comparison a series of dry impregnated samples with notation ρ_{surf} $WO_x/SiO_2(z,T)$ were prepared using the protocol presented in previous chapters [25-27] (Chapter 2, Section 2.2.2). Lehigh $WO_x/SiO_2(z,T)$ prepared via a previously published technique by dry impregnation into SiO_2 support, with high dispersion of WO_x amorphous species were provided by Wachs and coworkers [24]. An oleylamine-AMT co-impregnated control sample was also prepared to verify the effect of unreacted oleylamine. This sample is denoted as OA 0.5- $WO_x/SiO_2(5,873)$.

7.3 Characterization

High resolution TEM (HRTEM) imaging and high-angle annular dark field (HAADF) imaging were performed on a 200 kV JEOL 2200FS (S)TEM. Al_2O_3 , ZrO_2 and MgO supported WO_x NP samples have been extensively discussed by Dr. Wu Zhou in his thesis “Nanostructural and Chemical Characterization of Supported Metal Oxide Catalysts by Aberration Corrected Analytical Electron Microscopy” and a brief presentation of these results is included in this chapter. Thermogravimetric analysis, N_2 -physisorption and x-ray diffraction were performed using the same methodology presented earlier. Temperature programmed reduction (TPR) experiments were performed using a blend of 10% H_2 in Ar at a constant flow rate of 50 mL/min and temperature ramp rate of 3.0 K/min using a fully automated catalyst characterization and chemisorption unit (Autochem II 2920, Micromeritics).

Raman spectroscopy studies were also investigated following the previous protocol (Chapter 3, Section 3.3.4) and the following ranges were used for the Raman band assignments [24,28,29]:

1019-1030 cm⁻¹: monotungstates, isolated WO₄/WO₅ species (ν_s of the terminal O=W(-O-Si)₄ bond from surface monotungstates) [24,29].

972-998 cm⁻¹: polytungstates (ν_s at 998 and ν_{as} at 972 dioxo surface of the terminal (O=)₂W(-O-Si)₂ bond from surface polytungstates) [24,29].

715-725, 809-816 cm⁻¹: crystalline WO₃ NPs (ν_{as} of W-O-W) [24,29].

The spectra were normalized using the SiO₂ vibration band at 487 cm⁻¹.

7.4 Catalytic studies

The propene metathesis activity of SiO₂ supported WO_x NPs was tested using an isothermal downflow reactor at 573 K and 1.06 atm. Each catalyst was pretreated with air for 1 hr at 573 K and was purged with ultra high purity (UHP) He to remove any physisorbed O₂ prior to the reaction. A blend of 1% propene and 1% argon (internal standard) in helium was passed through the reactor after establishing constant propene concentration.

The outflow stream was kept at 343 K and the reaction products were analyzed using a flame ionization detector (FID) normalized with the concentration of the internal standard that was detected using a thermal conductivity detector (TCD). No induction period was noticed in this reaction opposite to *n*-pentane isomerization [26]. The propene conversion turnover rate *TOR* (s⁻¹) (propene molecules converted to products per W-atom per unit time) were collected at t = 5 min. The propene metathesis *TOR* (s⁻¹) (propene molecules converted to metathesis products per W-atom per unit time) is defined as (metathesis *TOR*) = ($n_{C_2}^-/n_{C_4}^-$) × *TOR*, where $n_{C_2}^-/n_{C_4}^-$ is defined as the molar ratio ethene (C₂⁻): 2-butene (C₄⁻). The selectivities in this work were calculated on a molar

mass balance (i.e. 2 propene molecules produce 1 molecule of ethene and 1 molecule of 2-butene).

7.5 Results and discussion

7.5.1 Structure of silica supported tungsten oxide nanoparticles

The N₂-physiroption results of the NP-WO_x/SiO₂ samples are summarized in table 7.1. It is noticed that specific surface area (SSA) decreases with ρ_{surf} opposite to trends noticed in WO_x/ZrO₂ [25-27] (Chapter 2, section 2.4.1, table 2.2). Weak interactions between WO_x and SiO₂ lead to the continuous decrease of SSA with increasing ρ_{surf} which is a result of sintering and pore blockage. A comparison between the impregnated WO_x/SiO₂, NP-WO_x/SiO₂ and sNP-WO_x/SiO₂ reveals that the last two have significantly higher SSA at $\rho_{surf} > 1.1$ W/nm². The improved structural stability is an effect of the WO_x (core)-oleylamine (shell) that appears to stabilize the SiO₂ framework and prevents severe sintering. The control sample OA 0.5- WO_x/SiO₂ (5,600) has low SSA, which proves that any oleylamine not attached to WO_x NPs has a negative effect on SSA and does not prevent structural collapse.

Both NP-WO_x/SiO₂ and WO_x/SiO₂ are completely amorphous up to 1 W/nm² (Figure 7.5a and 7.5b). At a surface density of 2.2 W/nm², XRD-detectable WO₃ crystals are present in both catalysts. sNP-WO_x/SiO₂ is similar to NP-WO_x/SiO₂ (not shown here) which suggests that the size of the particles does not have a significant effect on the crystallization of WO_x species to WO₃.

Table 7.1. N₂-physisorption results and tungsten surface density of WO_x/SiO₂ samples calcined at 873 K.

Catalyst Sample	BET S.S.A. (m ² /g)	WO ₃ content (wt% of WO ₃)	ρ_{surf} (W/nm ²)
0.5 WO _x /SiO ₂	262	5	0.5
1.1 WO _x /SiO ₂	220	9	1.1
2.2 WO _x /SiO ₂	167	14	2.2
Lehigh 0.4-WO _x /SiO ₂	332	4	0.4
Lehigh 0.6-WO _x /SiO ₂	310	6	0.6
Lehigh 1.1-WO _x /SiO ₂	267	10	1.1
NP 0.5-WO _x /SiO ₂	265	5	0.5
NP 1.0-WO _x /SiO ₂	241	9	1.0
NP 2.2-WO _x /SiO ₂	234	19	2.2
sNP 0.6-WO _x /SiO ₂	270	5	0.5
sNP 1.1-WO _x /SiO ₂	264	9	1.1
sNP 2.2-WO _x /SiO ₂	240	20	2.2
OA* 0.5- WO _x /SiO ₂	173	5	—

*Oleylamine-treated control sample, 7 wt% of oleylamine was used similar to the weight loss of NP-0.5- WO_x/SiO₂(5,873) after calcination (Figure 7.2).

To study the nature of the WO_x species at both lower and higher loadings, the TPR profiles of NP-WO_x/SiO₂ and WO_x/SiO₂ are presented in Figure 7.6. SiO₂ is not expected to be reduced at the temperature range studied here [13,30,31]. It is noticed at low surface density (0.5 W/nm²), a broad reduction band from 373 K-1373 K is observed for both series. This indicates that the WO_x species is amorphous and in strong coordination with the Si-OH surface groups, resulting in the formation of a W-O-Si species [22,23,32,33] that prevents facile reduction. When NP loadings exceed ML coverages, the TPR profiles show small a H₂-consumption peak at 600-750 K, a distinct H₂-consumption peak at 773-973 K and finally a broad peak at 973 – 1373 K. These transitions correspond to the reduction of WO₃→ WO_{2.9}→ WO₂→ WO [13,30,31] and are shifted to slightly lower temperatures when compared to pure WO₃ due to the interaction with the support.

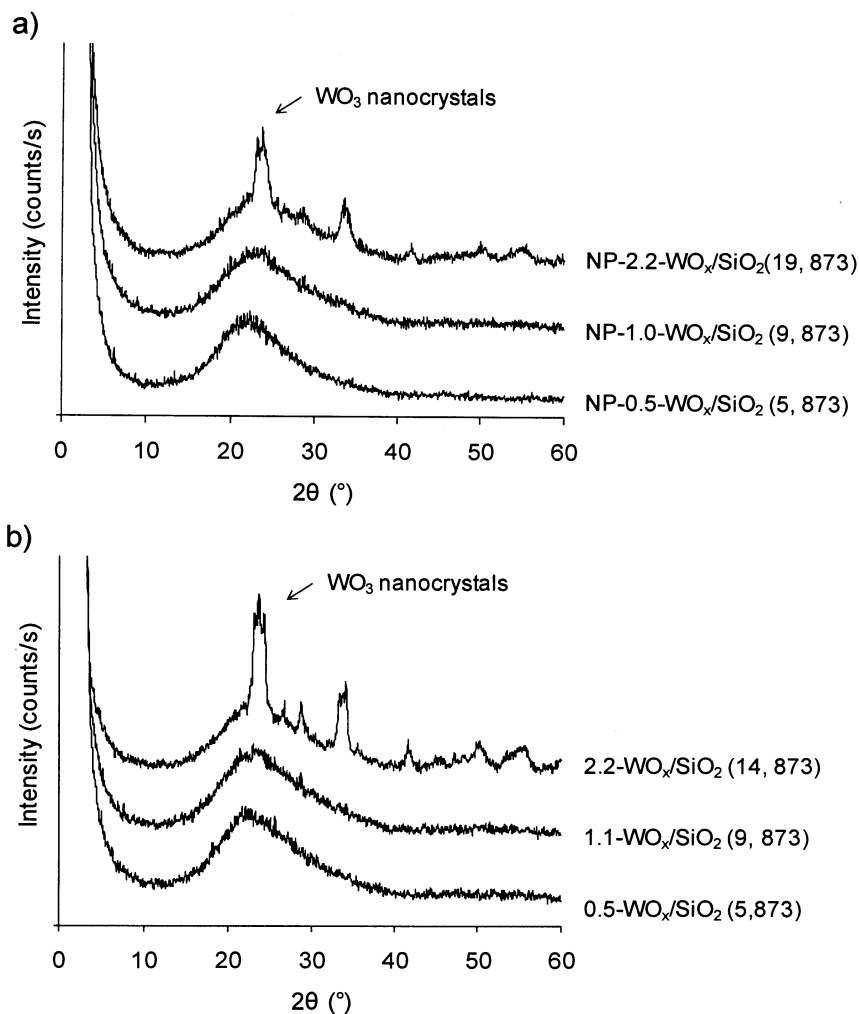


Figure 7.5. Powder XRD patterns of a) NP- WO_x/SiO_2 and b) WO_x/SiO_2 .

It is very interesting to notice that the H_2 -consumption for NP-0.5- WO_x/SiO_2 (5, 873) starts at the beginning of each run at 373 K as opposed to 0.5- WO_x/SiO_2 (5,873) that consumes H_2 only at ≥ 773 K.

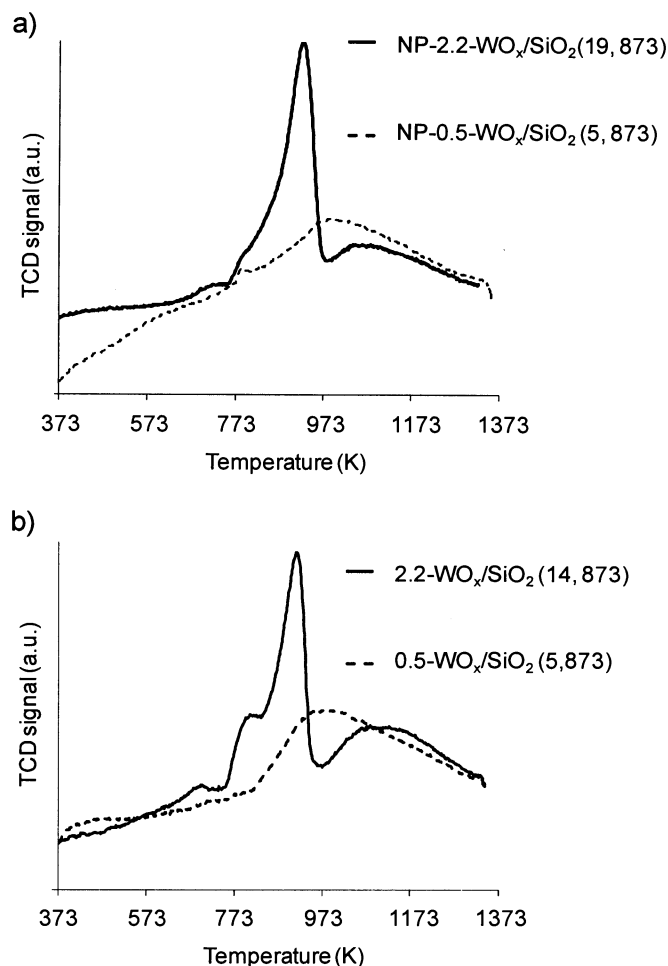


Figure 7.6. Temperature programmed reduction profiles of a) NP-WO_x/SiO₂ and b) WO_x/SiO₂.

7.3.2 *In situ* Raman spectroscopy

The dehydrated Raman spectra of impregnated WO_x/SiO₂ are presented in Figure 7.7. The WO_x/SiO₂ material is similar to Lehigh WO_x/SiO₂ that were characterized by Lee *et al.* [24]. The Wachs group reported that the highest WO_x dispersion achieved without the formation of WO₃ crystals is 6% (0.5 W/nm²). In Figure 7.7a, a weak band at ~ 1000 cm⁻¹ is seen for ρ_{surf} of 0.5 and 1.1 W/nm², that corresponds to the existence of polytungstate species. Weak bands of monotungstates are present as indicated by the

bands at 1030 and 1025 cm^{-1} for 1.1 and 2.2 W/nm^2 respectively. The formation of WO_3 crystals is dominant at $\rho_{surf} \geq 1.1 \text{ W}/\text{nm}^2$.

Two NP WO_x/SiO_2 samples were successfully characterized as shown in Figure 7.7b. At the lowest ρ_{surf} of 0.5 W/nm^2 , intense fluorescence prevented the acquisition of a Raman spectrum.

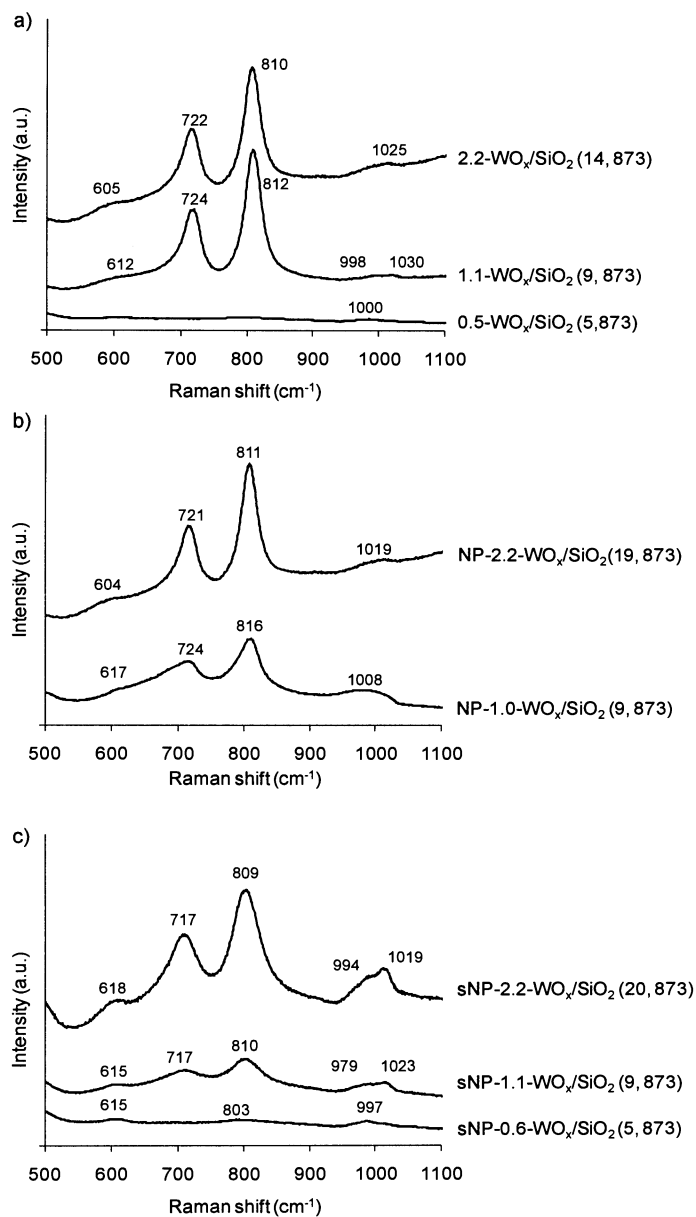


Figure 7.7. Raman spectra of dehydrated a) WO_x/SiO_2 , b) NP WO_x/SiO_2 and c) sNP WO_x/SiO_2 .

Both NP WO_x/SiO_2 samples appear to have high concentrations of monotungstates and polytungstates as indicated by the broad band at 995-1020 cm^{-1} . The shifting of the band to higher wave numbers on increasing ρ_{surf} from 1.0 to 2.2 W/nm^2 indicates an increase in the size of these species.. The intensity of the WO_3 crystal band is clearly weaker for the NP synthesis than the impregnated WO_x/SiO_2 at $\sim 1.0 \text{ W}/\text{nm}^2$, but it is the same at a ρ_{surf} of 2.2 W/nm^2 , which suggests that better dispersion was achieved only at the lower ρ_{surf} .

When smaller NPs are deposited on SiO_2 , the dispersion of the WO_x amorphous species improves as demonstrated by the Raman spectra of sNP WO_x/SiO_2 (Figure 7.7c). Significant concentrations of monotungstates and polytungstates are detected even at the highest ρ_{surf} of 2.2 W/nm^2 , unlike in the previous samples, and crystallization of WO_x to WO_3 is also significantly retarded.

7.3.3 Electron microscopy

All impregnated WO_x/SiO_2 samples consist of various WO_x species similar to what was reported for WO_x/ZrO_2 in chapter 2. The synthesis effect on the species distribution was investigated by electron microscopy for catalysts with $\rho_{surf} \sim 1.0 \text{ W}/\text{nm}^2$. In Figure 7.8a and Figure 7.8b representative HAADF-STEM images of 1.1- WO_x/SiO_2 (9,873) are shown. $> 2 \text{ nm}$ WO_3 crystals are the the dominant species along with monotungstates, polytungstates and distorted WO_x clusters. The distribution profiles shift to smaller species for the NP WO_x/SiO_2 (Figure 7.8c and Figure 7.8d) and even smaller for the sNP WO_x/SiO_2 NP WO_x/SiO_2 (Figure 7.8e and Figure 7.8f).

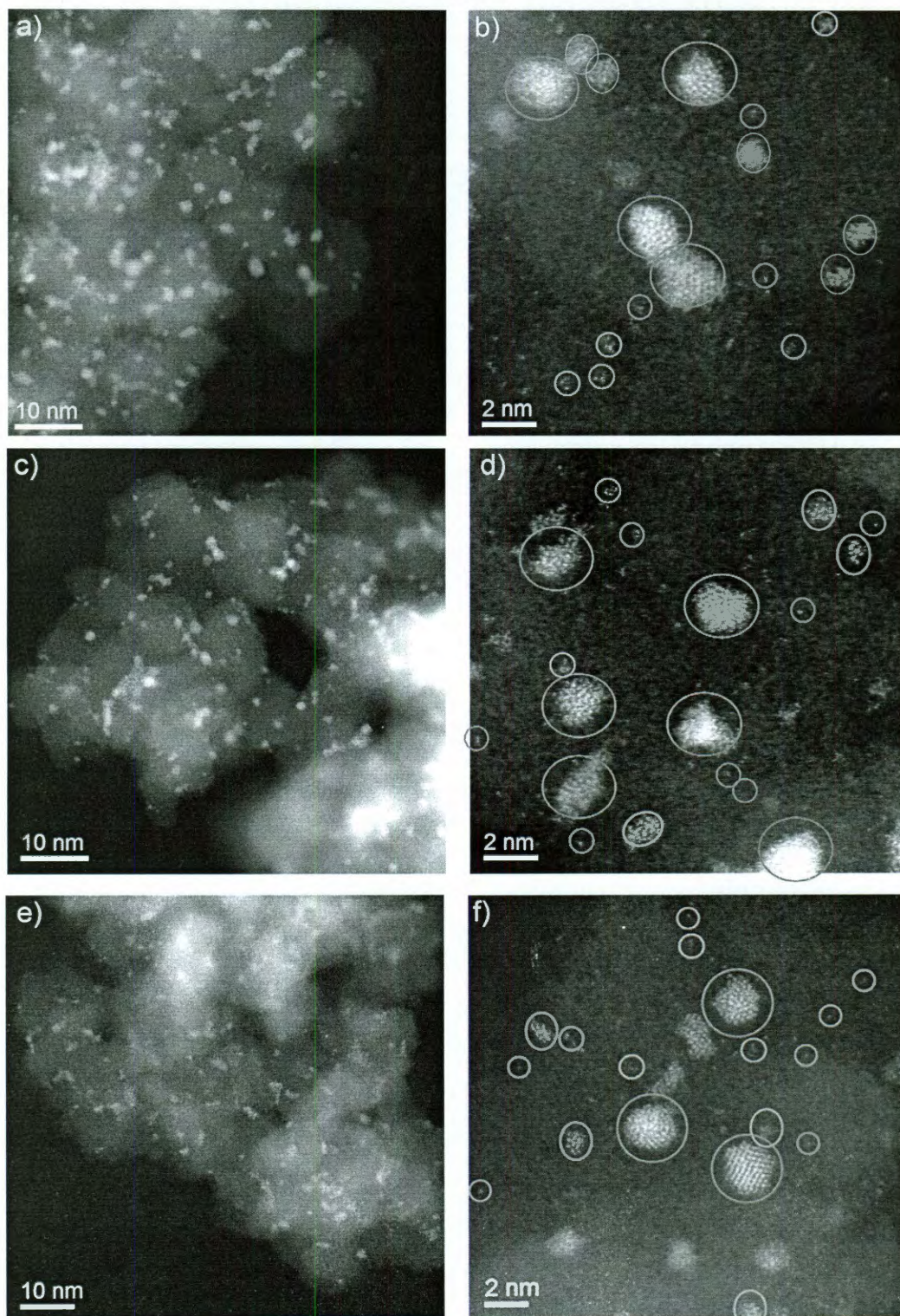


Figure 7.8. Representative HAADF-STEM images of a,b) 1.1-WO_x/SiO₂(9, 873), c,d) NP 1.0-WO_x/SiO₂ (9, 873) and e,f) sNP 1.1-WO_x/SiO₂ (9, 873). Blue (small) circles: surface monotungstate species; Green circles (medium): surface polytungstate species; Yellow circles (large): distorted WO_x clusters; Purple circles (larger): WO₃ crystals.

This observation verifies that there is a higher concentration of smaller WO_x clusters using the proposed synthetic method. Nevertheless, the size of the clusters differs from the synthesized particles as shown in the previous chapter. N_2 -physisorption results show that higher SSAs are achieved after calcinations. We propose that the WO_x NPs decompose upon calcination similar to the impregnated catalysts, but remain significantly confined by the attached oleylamine. As a result an extended aggregation is prevented and the species distribution is shifted towards smaller species such as monotungstates and polytungstates.

7.3.4 Propene metathesis activity

sNP WO_x/SiO_2 is clearly the most active catalyst as noticed in Figure 7.9. At ρ_{surf} of 0.5 W/nm^2 , they are $\sim 100\%$ more active than WO_x/SiO_2 , 75% more active than Lehigh WO_x/SiO_2 and 35% more active than NP WO_x/SiO_2 . In terms of metathesis selectivity (Figure 7.9b), the molar ratio of $n_{\text{C}_2=}/n_{\text{C}_4=}$ appears to be similar (~ 1) for both NP WO_x/SiO_2 and sNP WO_x/SiO_2 at $\rho_{\text{surf}} \sim 0.5 \text{ W/nm}^2$, higher than the 0.85 of WO_x/SiO_2 . Figure 7.9c shows that the metathesis *TOR* of sNP WO_x/SiO_2 is the best in the propene metathesis series; up to 60% better than NP WO_x/SiO_2 and up to 150% better than conventional WO_x/SiO_2 .

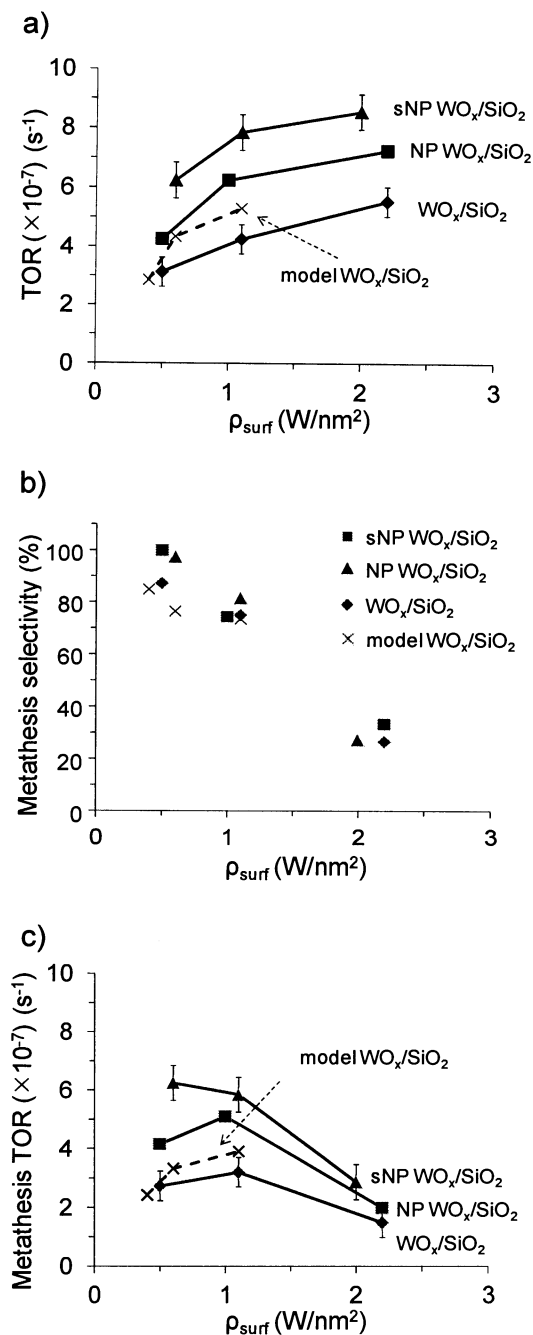


Figure 7.9. a) Steady state propene TOR as function of as a function of tungsten surface density, b) metathesis selectivity expressed as the ratio $\text{C}_2^{\text{=}}:\text{C}_4^{\text{=}}$ and c) steady state metathesis TOR of Lehigh WO_x/SiO_2 , WO_x/SiO_2 (873), NP WO_x/SiO_2 (873) and SNP WO_x/SiO_2 (873).

By Raman spectroscopy and electron microscopy (Section 7.4.2 and 7.4.3) it was noticed that sNP WO_x/SiO_2 have the highest concentration of monotungstates and

polytungstates. Monotungstates are known to be tetrahedrally coordinated (W^{4+}) [10] and smaller polytungstates [21] are expected to have higher concentrations of W^{4+} (weak Lewis sites [22]) that promote the metathesis mechanism. Opposite to *n*-pentane isomerization, lower acidity is required for methathesis reactions and the synthetic procedure presented here generates higher concentrations of these sites. Oleylamine-capped WO_x NPs are constrained during calcination as opposed to WO_x free species in impregnated WO_x/SiO_2 that are very mobile as noticed by their crystallization to bulk WO_3 at low ρ_{surf} . The presence of oleylamine that is attached to the WO_x core retards agglomeration of the most active monomers and small oligomers.

7.4 Summary and conclusions

SiO_2 supported WO_x NPs prepared by using our WO_x NPs formed very active propene metathesis catalysts, up to 3 times more active than conventional impregnated samples. The increased catalytic activity of the SiO_2 supported WO_x NPs correlates to better dispersion of WO_x species in the form of monomers and oligomers on SiO_2 support. The oleylamine-capped WO_x NPs stabilize SiO_2 during calcination resulting in a material with higher SSA than impregnated WO_x/SiO_2 .

7.5 References

1. A. M. Rouhi, Chem. & Eng. News 80 (2002) 29-33.
2. K. J. Ivin and J. C. Moll, Olefin Metathesis and Metathesis Polymerization. Academic Press, London, 1997.
3. L. Delaude and A. F. Noels. 2005. Metathesis. In Kirk-Othmer Encyclopedia of Chemical Technology. John Wiley & Sons, Inc., New York. 1-29.

4. J. C. Mol, *Journal of Molecular Catalysis A: Chemical* 213 (2004) 39-45.
5. C. v. Schalkwyk, A. Spamer, D. J. Moodley, T. Dube, J. Reynhardt and J. M. Botha, *Applied Catalysis A: General* 255 (2003) 121-131.
6. R. Westhoff and J. A. Moulijn, *Journal of Catalysis* 46 (1977) 414-416.
7. A. Andreini and J. C. Mol, *Journal of Colloid and Interface Science* 84 (1981) 57-65.
8. J. C. Mol, J. A. Moulijn, H. P. D.D. Eley and B. W. Paul, *Advances in Catalysis*, Academic Press. 131-171.
9. R. C. Luckner and G. B. Wills, *Journal of Catalysis* 28 (1973) 83-91.
10. Y. Wang, Q. Chen, W. Yang, Z. Xie, W. Xu and D. Huang, *Applied Catalysis A: General* 250 (2003) 25-37.
11. A. Spamer, T. I. Dube, D. J. Moodley, C. van Schalkwyk and J. M. Botha, *Applied Catalysis A: General* 255 (2003) 153-167.
12. I. Rodríguez-Ramos, A. Guerrero-Ruiz, N. Homs, P. R. de la Piscina and J. L. G. Fierro, *Journal of Molecular Catalysis A: Chemical* 95 (1995) 147-154.
13. R. Thomas, J. A. Moulijn, V. H. J. De Beer and J. Medema, *Journal of Molecular Catalysis* 8 (1980) 161-174.
14. D. J. Moodley, C. van Schalkwyk, A. Spamer, J. M. Botha and A. K. Datye, *Applied Catalysis A: General* 318 (2007) 155-159.
15. L. Harmse, C. van Schalkwyk and E. van Steen, *Catalysis Letters* 137 123-131.
16. D. Lokhat, M. Starzak and M. Stelmachowski, *Applied Catalysis A: General* 351 (2008) 137-147.
17. J. Fathikalajahi and G. B. Wills, *Journal of Molecular Catalysis* 8 (1980) 127-134.

18. A. G. Basrur, S. R. Patwardhan and S. N. Was, *Journal of Catalysis* 127 (1991) 86-95.
19. A. Andreini and J. C. Mol, *Journal of the Chemical Society, Faraday Transactions 1: Physical Chemistry in Condensed Phases* 81 (1985) 1705-1714.
20. A. Spamer, T. I. Dube, D. J. Moodley, C. van Schalkwyk and J. M. Botha, *Applied Catalysis A: General* 255 (2003) 133-142.
21. J. A. Horsley, I. E. Wachs, J. M. Brown, G. H. Via and F. D. Hardcastle, *Journal of Physical Chemistry* 91 (1987) 4014-4020.
22. A. J. Van Roosmalen and J. C. Mol, *Journal of Catalysis* 78 (1982) 17-23.
23. F. Verpoort, A. R. Bossuyt and L. Verdonck, *Journal of Molecular Catalysis A: Chemical* 95 (1995) 75-82.
24. E. L. Lee and I. E. Wachs, *The Journal of Physical Chemistry C* 111 (2007) 14410-14425.
25. E. I. Ross-Medgaarden, W. V. Knowles, T. Kim, M. S. Wong, W. Zhou, C. J. Kiely and I. E. Wachs, *Journal of Catalysis* 256 (2008) 108-125.
26. N. Soultanidis, W. Zhou, A. C. Psarras, A. J. Gonzalez, E. F. Iliopoulou, C. J. Kiely, I. E. Wachs and M. S. Wong, *Journal of the American Chemical Society* 132 13462-13471.
27. W. Zhou, E. I. Ross-Medgaarden, W. V. Knowles, M. S. Wong, I. E. Wachs and C. J. Kiely, *Nat Chem* 1 (2009) 722-728.
28. E. L. Lee and I. E. Wachs, *The Journal of Physical Chemistry C* 112 (2008) 6487-6498.
29. D. S. Kim, M. Ostromecki, I. E. Wachs, S. D. Kohler and J. G. Ekerdt, *Catalysis Letters* 33 (1995) 209-215.
30. S. R. Vaudagna, R. A. Comelli and N. S. Figoli, *Applied Catalysis A: General* 164 (1997) 265-280.

31. M. I. Zaki, N. E. Fouad, S. A. A. Mansour and A. I. Muftah, *Thermochimica Acta* 523 90-96.
32. C. Martin, P. Malet, G. Solana and V. Rives, *The Journal of Physical Chemistry B* 102 (1998) 2759-2768.
33. F. Verpoort, A. R. Bossuyt and L. Verdonck, *Journal of Electron Spectroscopy and Related Phenomena* 82 (1996) 151-163.

Chapter 8

Summary and recommendations for future research

8.1 Thesis summary

The discovery of methanol dehydration active Zr-WO_x species on ZrO₂ surface inspired the work presented in this thesis. These super active sub-nm Zr-WO_x clusters were investigated for their intrinsic properties in a more demanding reaction such as *n*-pentane isomerization and structure-activity correlations were presented in chapter 2. High concentrations of Zr-WO_x clusters were shown to correlate to maximum *n*-pentane isomerization activity and selectivity. Due to its high sensitivity to concentration and relative density of the Zr-WO_x clusters, *n*-pentane isomerization is a model probe reaction as opposed to methanol dehydration where even bulk WO₃ is active. Driven by the need to develop a more efficient synthetic strategy that delivers higher concentrations of Zr-WO_x clusters, four types of WO_x/ZrO₂ (impregnated, coprecipitated, sol-gel and surfactant templated WO_x/ZrO₂) were studied in chapter 3. For the first time, the discrimination between two unique Zr-WO_x species, highly and slightly distorted Zr-WO_x, was successful by Raman spectroscopy. Impregnated catalysts were found to consist primarily of slightly distorted Zr-WO_x species and were the only type of WO_x/ZrO₂ catalysts that were active for *n*-pentane isomerization. Calcination temperature was found to play a crucial role in controlling the relative Zr-WO_x cluster density, an important parameter for biomolecular reaction mechanisms.

The bimolecular reaction mechanism was studied in chapter 4 by performing a series of experiments using two olefins (1-pentene and propylene) that were co-fed with *n*-pentane. The olefin type and concentration plays a key role in promoting the *n*-pentane

bimolecular isomerization mechanism. Only 1-pentene increased the catalytic activity and isomerization selectivity, while the presence of propylene promoted the formation of isobutene. This observation suggests that the bimolecular mechanism proceeds via the formation of a C_{10} intermediate that cracks to form isopentane and pentane or other undesired byproducts.

To verify if the proposed mechanism is explicit to WO_x/ZrO_2 , the *n*-pentane isomerization activity of supported phosphotungstic acids (PWA) was investigated in chapter 5. SiO_2 supported PWA were found to be more active than WO_x/ZrO_2 due to the intrinsically strong acidic character of the Keggin PWA. The product distribution profiles suggest that a bimolecular mechanism prevails in strong solid acids. More active, SiO_2 supported PWA catalysts lose their catalytic activity upon regeneration opposite to WO_x/ZrO_2 that remain very active.

The second part of this thesis is focusing on developing a new material synthesis strategy that aims to control the supported metal oxide domain size. A synthesis method that uses oleylamine and ammonium salt and produces ultrasmall metal oxide nanoparticles was established and the results were described in chapter 6. Tungsten oxide (WO_x) nanoparticles (NPs) were successfully characterized and the size and shape of the NPs was controlled after understanding and controlling the particle formation mechanism. The synthesis of WO_x NPs with a diameter less than 2 nm has never been reported before and the results of this work led to a provisional patent application.

Two probe reactions were selected for testing the catalytic properties of the supported WO_x NPs. The propylene metathesis and *n*-pentane isomerization activity of SiO_2 supported and ZrO_2 supported WO_x NPs respectively were discussed in chapter 7.

The interaction between the support and supported phase was found to play a significant role. For ZrO₂ supported WO_x NP, the NP disassembly after calcination resulted in a material that had low *n*-pentane isomerization activity, but a similar effect was beneficial for SiO₂ supported WO_x NPs that formed a very active propylene metathesis material. The presence of oleylamine attached to the WO_x core prevented an extended surface area loss and promoted the formation of smaller WO_x species such as monotungstates and polytungstates after calcination. These catalysts were at least 3 times more active than conventional impregnated WO_x/SiO₂.

8.2 Recommendations for future work

8.2.1 Support/Supported phase interaction

Studying the structure of the supported WO_x NPs is very important to derive structure-activity correlations. The preliminary results presented here show that the nature of the support has a critical effect on the WO_x NP size.

The WO_x species are found to be highly dispersed on the surface of NP-WO_x/MgO (14, 873) presented in Figure 8.1. High concentrations of polytungstates are seen when W cations are absorbed directly onto the Mg atomic column suggesting that there is strong interaction between the support and the WO_x species. This support is known for its basic properties and it cannot be used for acidic reactions since all WO_x acid sites are deactivated.

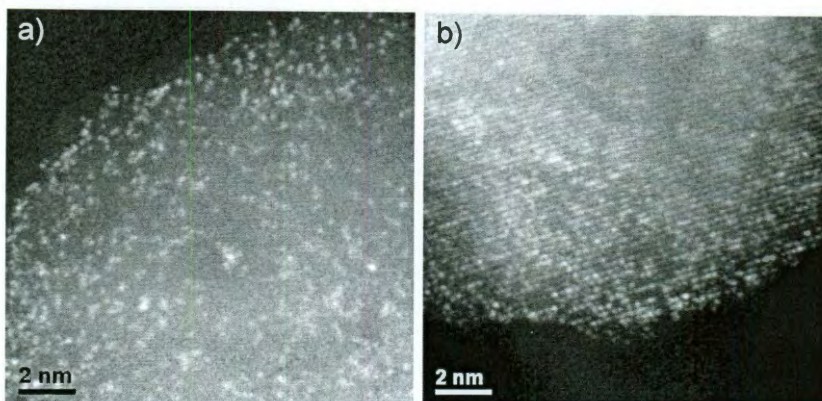


Figure 8.1. STEM-HAADF images of NP-WO_x/MgO (14, 873) shows high dispersion of monotungstates and polytungstates on the MgO surface.

The sub-nm WO_x clusters (Figure 8.2) were smaller than 1 nm containing 5 to 15 W atoms, which suggested that the decomposition of the WO_x NPs did not proceed to the same extent as in NP-WO_x/ZrO₂ (14, 773). Al₂O₃ is a weaker acid than ZrO₂ and the particles formed are larger suggesting a possible relationship between surface acidity WO_x NP decomposition that generates the different WO_x species.

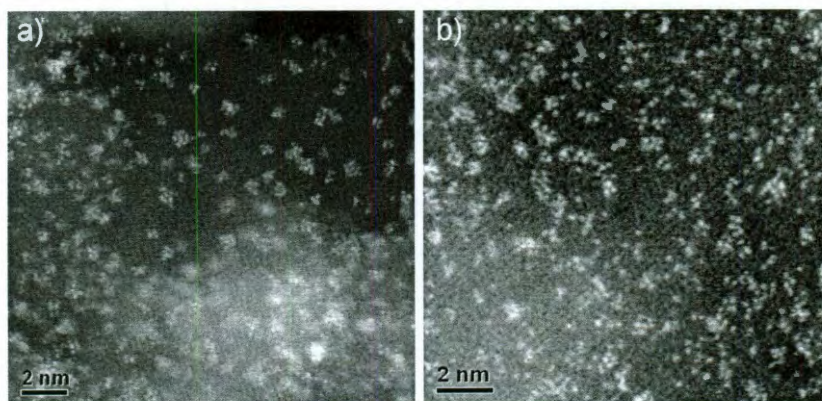


Figure 8.2. STEM-HAADF images of NP-WO_x/Al₂O₃ (14, 873) shows high dispersion of a) sub-nm WO_x clusters and b) monotungstates and polytungstates on the Al₂O₃ surface.

Representative HAADF-STEM images of NP 4.3-WO_x/ZrO₂ (13.5, 773) are presented in Figure 8.3. This sample was calcined at 773 K to compare it with 4.4-WZrOH (21.7, 773) from Chapter 2, section 2.4.1, table 2.2. As reported previously for commercial WZrOH (773), the support of NP 4.3-WO_x/ZrO₂ (13.5, 773) remained mostly amorphous due to the lower calcination temperature. High concentrations of monotungstates and polytungstates are detected, which suggests that the structure of WO_x NPs collapsed upon deposition and during calcination. The WO_x NPs appear to have a strong tendency to wet the ZrO₂ surface and oleylamine cannot prevent the complete decomposition of the WO_x NPs. The sample appeared to contain residual oleylamine (brown color) that was not completely removed by calcination.

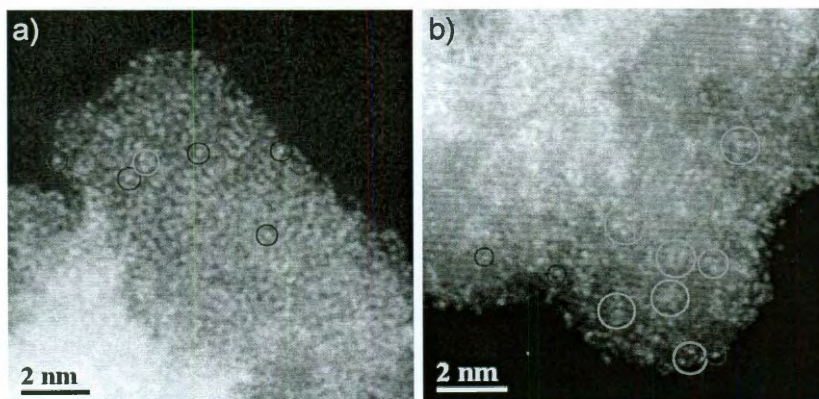


Figure 8.3. Representative STEM-HAADF images of NP-WO_x/ZrO₂ (11.2, 773) shows high dispersion of monotungstates (blue circles) and polytungstates (green circles) on the ZrO₂ surface.

8.2.2 Ligand modification/removal

The synthesis of ultrasmall metal oxide nanoparticles of known or customizable composition offers significant advantages in the field of material synthesis and heterogeneous catalysis. The synthesis of WO_x, VO_x and MoO_x NPs is only the first step

in selectively synthesizing supported metal oxide catalysts with features that can be modified depending on the reaction requirements.

Replacement and/or removal of the oleylamine attached to the WO_x core plays a crucial role for the preparation of heterogeneous catalysts. The following example demonstrates that even a partial replacement of oleylamine by pyridine has a positive effect on the *n*-pentane isomerization activity of NP WO_x/ZrO_2 .

As seen Figure 8.4, NP WO_x/ZrO_2 calcined at 773 and 973 K are less active than the corresponding WZrOH due the structural properties seen in Figure 8.3. It appears that the presence of oleylamine prevents the interaction of WO_x with ZrO_2 that generates the Zr- WO_x clusters responsible for the increased isomerization activity seen in previous chapters. Oleylamine is removed at temperatures ≥ 873 K which means that crystallization of ZrO_2 has occurred before the complete removal of oleylamine, and therefore minimum incorporation of Zr atoms within the WO_x cluster domains is expected. The presence of oleylamine does not only prevent the formation of Zr- WO_x but also retards the agglomeration of the smaller WO_x species to larger 3-D sub-nm clusters that have the desired acidity.

In order to identify if the ligand presence is responsible for the observed lower activity, a ligand-exchange experiment was employed as described earlier (Chapter 6, Section 6.6.5). Py WO_x/ZrO_2 samples differ only in the number of oleylamine molecules exchanged by pyridine, 9% for 1 Py and 14% for 3 Py, respectively. It is noticed that both samples are significantly more active than the corresponding NP 4.4- WO_x/ZrO_2 (11.2, 973) sample.

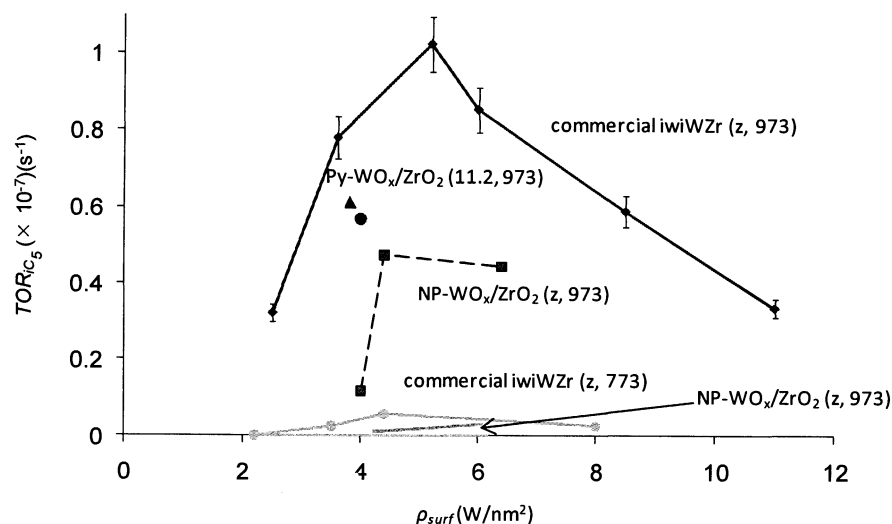


Figure 8.4. Steady state turnover rates (TOR) as a function of tungsten surface density. Sample series include $WZrOH(z,973)$, $WZrO_2(z,773)$, $NP-ZrOH(z,973)$, $NP-ZrOH(z,773)$ and $Py-ZrOH(11.2,973)$. Steady state turnover rates for the $WZrOH$ materials (taken from Chapter 2, Section 2.4.4, Figure 2.9)

$Py\ WO_x/ZrO_2$ (973) samples are more active because pyridine is removed at lower temperatures, allowing easier decomposition of the WO_x NPs. 14% replacement of oleylamine molecules results in a 50% increase in n -pentane isomerization activity, which is still lower than the activity of impregnated WO_x/ZrO_2 . Zr atom addition to the WO_x NPs during synthesis and a controlled removal or replacement of oleylamine could resolve the low activity problem noticed here.

Ligands with different functional groups such as thiols and carboxylic acids failed to synthesize nanoparticles. Nucleation occurred in the presence of 1-dodecanethiol, but severe uncontrolled reduction resulted to the formation of unidentified blue powder that visually had physical characteristics similar to the WO_x NRs (Chapter 6, section 6.6.3). Oleic acid did not initiate any nucleation and WO_x NPs were not formed up to 573 K. Further investigation of different amines could determine a better ligand that can improve the synthesis of more robust and well defined NP structures. A combination of amines

and thiols could possibly generate WO_x NPs with interesting properties before or after partial ligand removal.

Calcination is one way to remove the ligands but it causes severe structural modifications that destroy the WO_x NP structure. Alternative methods that can be used for removing oleylamine is the use of a dilute acid [1], the use of organic solvents such as CH_2Cl_2 [2], or the oxidation using O_3 [2]. These techniques have been successfully applied for coke extraction from spent catalysts.

8.2.3 Metal oxide nanoparticle doping

Modification of the WO_x NP composition by doping with different metal atoms could improve the properties and the structural stability of the nanoparticles. The low activity of ZrO_2 supported WO_x NPs was due to the structural decomposition of the WO_x NPs but also due to the absence of Zr-atoms within the WO_x cluster domain. The acidic enhancement of $\text{H}_3\text{PW}_{12}\text{O}_{40}$ by alteration of the surface structure using Zr atoms is currently studied [3] and simulation results show a significant increase in Brønsted acidity (decrease in the deprotonation energies) by adding surface ZrO_2 species. A similar effect is expected for WO_x clusters, with the addition of Zr-atoms on the outer surface and probably cluster corners to be highly desired (Figure 8.5) for the formation of active Zr- WO_x sites.

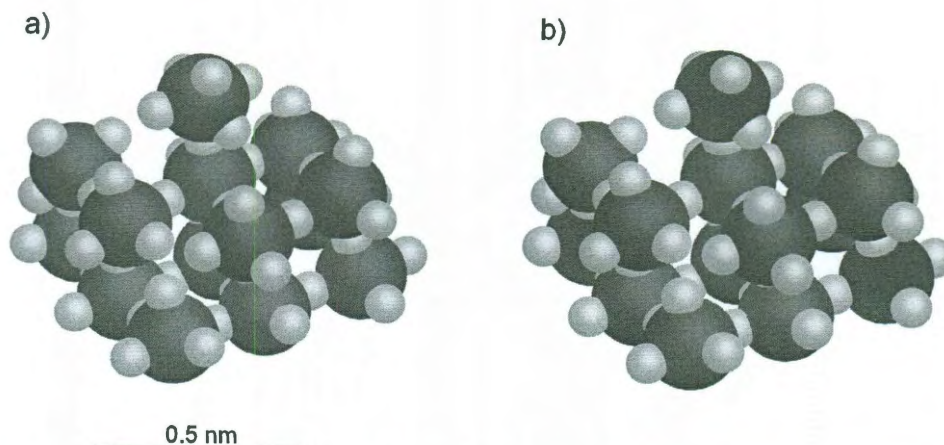


Figure 8.5. Schematic of a) WO_x sub-nm species on ZrO_2 surface that are not expected to be very active acidic sites and b) desired super active sub-nm Zr-WO_x clusters. The addition of Zr -atoms increases the acidic strength of the cluster [3-5]

Zr -atom addition by using an organometallic precursor such as zirconium acetylacetonate (acac) has been tested in this work and preliminary XPS results (not presented) verify the presence of Zr -atoms in the final WO_x NPs. Further investigation of the synthesis conditions (concentration of Zr-acac , hot injection vs. solvothermal decomposition, different Zr -precursors, concentration of oxidation or reduction agents) and extensive characterization is required to extract useful conclusions.

8.2.4 Encapsulation using SiO_2 microcapsules

Encapsulation of the WO_x NPs using SiO_2 microcapsules could improve the thermal and structural stability of these structures. Batch-like concentration gradients that can be adjusted by controlling the porous structure of the nanocapsules, could improve the overall yield and selectivity of reactions such as propylene metathesis. The microcapsules could work like microreactors and in the case of a gas-phase reaction where the product volume is different from the reactant volume; local pressure gradients can increase conversion and selectivity.

The SiO_2 nanoparticle synthesis scheme (published by the Wong and coworkers [6]) is presented in Figure 8.6. Initially using polyallylamine hydrochloride (PAH) and trisodium citrate a polymer-salt aggregate is formed. The addition of SiO_2 NPs results to the formation of a silica/polymer nanoparticle assembled capsule (NAC) that can be transformed into hollow microcapsules after calcination. Considering the non-covalent interactions that drive the formation of the polymer-salt aggregate, a modification of the WO_x NP synthesis method should generate an analogous organometallic aggregate. The major challenge is that this procedure is an aqueous phase synthesis method and the nucleation of the WO_x NPs has only been successful using non-aqueous solvothermal decomposition.

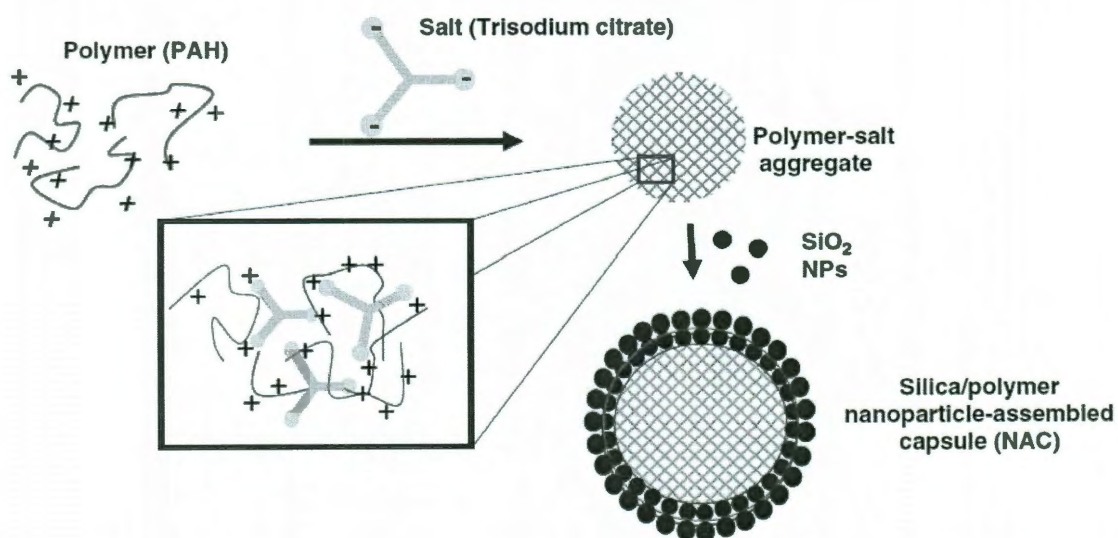


Figure 8.6. Schematic of two NP assembly of silica-polymer microcapsules. Results published by Kadali *et al.* [6].

Using (1) a hydrothermal method under high pressure could possibly form the WO_x NPs or (2) replacing oleylamine with a diamine or another amine that has more than one functional amine groups/molecule, the initial composition of the WO_x NPs could be

modified to meet the requirement in having a hydrophilic surface. By replacing SiO₂ NPs with ZrO₂ NPs, Zr-WO_x NPs can also be synthesized to study their *n*-pentane isomerization activity.

8.2.5 Sulfidation of metal oxide nanoparticles

Preliminary studies indicate that sulfidation of the synthesized WO_x NPs was successful by flowing a mixture of 5% H₂S in argon instead of pure argon. Conventional sulfidation methods require high calcination temperatures > 1273 K under pure H₂S flow and they lack surface structure control since severe aggregation and pore collapse cannot be prevented. Metal sulfides and especially MoS₂ and WS₂ and doped variations of them are very active supported phases for the hydrodesulfurization (HDS) of crude oil. Considering the increasing industrial interest in crude oil purification technologies, this project could contribute significantly in the fundamentals of HDS catalysis.

8.3 References

1. M. R. Gray, Y. Zhao and C. M. McKnight, *Fuel* 79 (2000) 285-294.
2. I. V. Kozhevnikov, S. Holmes and M. R. H. Siddiqui, *Applied Catalysis A: General* 214 (2001) 47-58.
3. H. Xu and M. Neurock, *In preparation* (2011).
4. T. Kim, A. Burrows, C. J. Kiely and I. E. Wachs, *Journal of Catalysis* 246 (2007) 370-381.
5. I. E. Wachs, T. Kim and E. I. Ross, *Catalysis Today* 116 (2006) 162-168.
6. S. Kadali, N. Soultanidis and M. Wong, *Topics in Catalysis* 49 (2008) 251-258.

Appendix A

Selection of catalytic particle size for gas-phase reactions

The procedure followed to select the catalyst pellet size for this study is presented here. Particles with diameters between (A) 600-1200, (B) 300-600 and (C) 150-300 μm (US Standard Series ATM) of one active catalyst, 6.0-WZrOH(21.7,973), were prepared by pelletizing, crushing, and sieving. The catalytic activity, in terms of steady-state $n\text{C}_5$ consumption turnover rate (TOR) values was recorded (Table 1). It was noticed that activity increased with decreasing particle size, specifically by 19% from A to B but only 2% from B to C. Negligible pressure drop was noticed along the catalytic bed for A and B ($\Delta P_A = 0.2$ psi, $\Delta P_B = 0.3$ psi), in contrast to C ($\Delta P_C = 3.7$ psi) where pressure decreased $\sim 25\%$. Assuming a 1st-order reaction and spherical particle morphology, the Weisz-Prater parameters for the three size ranges were estimated using a nonlinear equation solver (Polymath). Particles in range A were not chosen since $C_{WP} > 1$. Particles in ranges B and C had $C_{WP} < 1$ (indicating that internal diffusion was negligible), but the latter was not chosen due to the significant pressure drop. Thus, particle sizes in the 300-600 μm were chosen for all subsequent catalyst experiments.

Table A.1. Selection of particle size range for 6.0-WZrOH (21.7, 973)

Particle size [μm] (label)	TOR ($\times 10^{-7}$) [s^{-1}]	Isopentane selectivity (%)	Thiele modulus ϕ	Internal effectiveness η	Weisz-Prater criterion C_{WP}
600 – 1200 (A)	1.62	45	1.71	0.85	2.48
300 – 600 (B)	1.93	44	0.86	0.96	0.70
150 – 300 (C)	1.97	46	0.43	0.99	0.18

Appendix B

n-pentane isomerization turnover rate calculations

To compare catalysts on the basis of *n*-pentane isomerization performance, the integrated GC peak areas were converted to moles of product *i*. All calculations were performed similar to the methodology presented by Kuba *et al.* [1] (equation B.1)

$$x_i = \frac{(i/5)C_i}{nC_{5in}} \quad (\text{B.1})$$

where *i* =1-6 is the number of carbon atoms of each product from methane to C₆ olefins and hexane, *C_i* is the moles of each product and *nC_{5in}* is the moles of *n*-pentane (*nC₅*) fed to the reactor. After normalizing with respect to the internal standard concentration, the total conversion *X* [(mol *n*-pentane converted)·(mol *n*-pentane fed)⁻¹] was calculated by using equation B.2.

$$X = \frac{\sum_{i=1}^6 (i/5)C_i}{nC_{5in}} \quad (\text{B.2})$$

Selectivity for each product is defined: *S_i* [(conversion of *i* product)·(Total conversion)⁻¹]

$$S_i = \frac{x_i}{X} \quad (\text{B.3})$$

Since the total conversion remained low (≤3%) for all runs, the conditions were considered to be differential and therefore the total conversion rate of *nC₅*, *R_{nC₅}* [(mol *nC₅* converted)·(g-catalyst·s)⁻¹]: could be expressed as:

$$R_{nC_5} = \frac{F_{nC_5} X}{W_{cat}} \quad (\text{B.4})$$

where F_{nC_5} [(mol nC₅)·s⁻¹] is the steady-state molar flow rate of nC₅ and W_{cat} [g] is the amount of catalyst used for each run.

In comparing the activity for the catalyst samples, the nC₅ consumption turnover rate TOR [s⁻¹] and the isomerization turnover rate TOR_{iC_5} [s⁻¹] were used, which respectively represented the number of nC₅ molecules reacted per tungsten atom per second (equation B.5) and the number nC₅ molecules isomerized into isopentane (iC₅) per tungsten atom per second (equation B.6).

$$TOR = \frac{(R_{nC_5})(N_A)}{(N_s)(SSA)(10^{18})} \quad (B.5)$$

$$TOR_{iC_5} = S_{iC_5} TOR \quad (B.6)$$

where N_A is Avogadro's number, SSA is the BET specific surface area, and N_s [sites·nm⁻²] is the active site surface density [2, 3]. N_s was assumed to be numerically equivalent to ρ_{surf} . However, it should be noted that TOR would not represent a true turnover frequency above WO_x monolayer (ML) coverage, *i.e.*, $\rho_{surf} > 4.5 \text{ W} \cdot \text{nm}^{-2}$ [4-7], because the tungsten oxide content would not be 100% accessible for reaction. For the rest of the products, cracking and oligomerization selectivities were calculated using $i=1-4$ and $i>5$, respectively. Steady-state TOR's and selectivities were collected at $t = 10$ hours.

Appendix B. Reference

- [1] S. Kuba, P. Lukinskas, R. Ahmad, F.C. Jentoft, R.K. Grasselli, B.C. Gates, H. Knözinger, *Journal of Catalysis* 219 (2003) 376-388.
- [2] N. Soultanidis, W.V. Knowles, E.I. Ross-Medgaarden, I.E. Wachs, M.S. Wong, in preparation (2009).
- [3] W.V. Knowles, M.O. Nutt, M.S. Wong, *Supported Metal Oxides and Surface Density Metric*. Taylor and Francis: Boca Raton, 2006.
- [4] J. Macht, C.D. Baertsch, M. May-Lozano, S.L. Soled, Y. Wang, E. Iglesia, *Journal of Catalysis* 227 (2004) 479-491.
- [5] J.G. Santiesteban, J.C. Vartuli, S. Han, R.D. Bastian, C.D. Chang, *Journal of Catalysis* 168 (1997) 431-441.
- [6] E.I. Ross-Medgaarden, W.V. Knowles, T. Kim, M.S. Wong, W. Zhou, C.J. Kiely, I.E. Wachs, *Journal of Catalysis* 256 (2008) 108-125.
- [7] D.G. Barton, M. Shtein, R.D. Wilson, S.L. Soled, E. Iglesia, *J. Phys. Chem. B* 103 (1999) 630-640.

Appendix C

Methanol dehydration turnover rate calculations

To compare catalysts on the basis of methanol dehydration performance, the integrated GC peak areas were converted to moles of product i . Gas phase product yield, Y_i [(mol product i formed)·(mol CH₃OH fed)⁻¹], is defined as

$$Y_i = \frac{n_i}{n_{(\text{CH}_3\text{OH})_0}} \quad (\text{C.1})$$

Where n_i is moles of product i and $n_{(\text{CH}_3\text{OH})_0}$ is moles of methanol at t_0 . Catalyst discoloration was not observed, nor was an induction period or deactivation observed for steady state rates, suggesting negligible surface carbon generation (*e.g.*, coke) and supporting its omission from the mass balance. Total methanol conversion, $X_{\text{CH}_3\text{OH}}$ [(mol CH₃OH converted)·(mol CH₃OH fed)⁻¹], is calculated from the sum of the product yields rather than from the change in methanol concentration between t_0 and the steady state value:

$$X_{\text{CH}_3\text{OH}} = \sum Y_i \quad (\text{C.2})$$

Selectivity for product i , S_i [(mol product i formed)·(mol CH₃OH converted)⁻¹], is defined in the traditional manner:

$$S_i = \frac{Y_i}{X_{\text{CH}_3\text{OH}}} \quad (\text{C.3})$$

The activity of each catalyst is expressed as the rate of methanol conversion, $R_{\text{CH}_3\text{OH}}$ [(mol CH₃OH converted)·(g catalyst · s)⁻¹]:

$$R_{\text{CH}_3\text{OH}} = \frac{F_{\text{CH}_3\text{OH}} X_{\text{CH}_3\text{OH}}}{W_{\text{cat}}} \quad (\text{C.4})$$

where F_{CH_3OH} [(mol CH₃OH)·s⁻¹] is the steady state molar flow rate of methanol to the reactor and W_{cat} [g] is the amount of catalyst used for each respective run. Finally, the turnover rate TOR_i [s⁻¹] represents the number of methoxy molecules converted per W-atom per unit time to product i :

$$TOR_i = \frac{(S_i)(R_{CH_3OH})(N_A)}{(N_S)(S_{BET})(10^{18})} \quad (C.5)$$

with Avogadro's number (N_A), the surface active site density (N_S), and the overall composite catalyst BET surface area (S_{BET}). Instead of calculating turnover frequency (TOF_{*i*}) which represents the rate of methoxy turnovers per *exposed* surface site (and requires lengthy measurements), we follow convention for supported metal oxides by calculating TOR assuming 100% exposure of all W-atoms:

$$N_S = \frac{\rho_{surf}}{v_{STOICH}\alpha} \quad (C.6)$$

Here, N_S [sites·nm⁻²] is equivalent to the tungsten surface density (ρ_{surf} [W-atom·nm⁻²]) because α is only a simple unit conversion factor [(1 CH₃O_{ads} molecule)·(1 site)⁻¹] and v_{STOICH} [W-atoms·(1 CH₃O_{ads} molecule)⁻¹] is taken to be 1. Although v_{STOICH} has been shown ~3 for many monolayer-loaded supported metal oxides via due to lateral methoxy interactions in the chemisorbed adsorbate layer, we assign $v_{STOICH} = 1$ because (1) lateral methoxy interactions are assumed weak at sub-monolayer WO_x loadings, (2) the presence of steric methoxy interactions have not yet been experimentally verified on monolayer WO_x/ZrO₂ materials, and (3) the infrared transmittance cell used for quantifying v_{STOICH} was inoperable during data collection for this work.

Appendix D

Mass balance and olefin consumption during *n*-pentane isomerization

Table D.1. Carbon mass balance during 10 hr run for 1% nC₅.

Time (h)	Carbon balance (%)
0.07	98
0.46	97
0.82	98
1.22	97
2.02	96
3.19	97
4.35	98
5.91	97
7.47	96
10.0	97

Table D.2. Carbon mass balance during 10 hr run for 0.01% 1-C₅⁼, 1% nC₅.

Time (h)	Carbon balance (%)
0.75	97
0.45	98
0.83	97
1.24	98
2.02	97
3.17	98
4.36	98
5.89	97
7.48	98
9.95	97

Table D.3. Carbon mass balance during 10 hr run for 0.1% 1-C₅⁼, 1% nC₅.

Time (h)	Carbon balance (%)
0.05	92
0.45	93
0.83	92
1.22	93
2.00	94
3.16	95
4.33	96
5.85	98
7.44	97
9.95	98

Table D.4. Carbon mass balance during 10 hr run for 0.5% 1-C₅⁼, 1% nC₅.

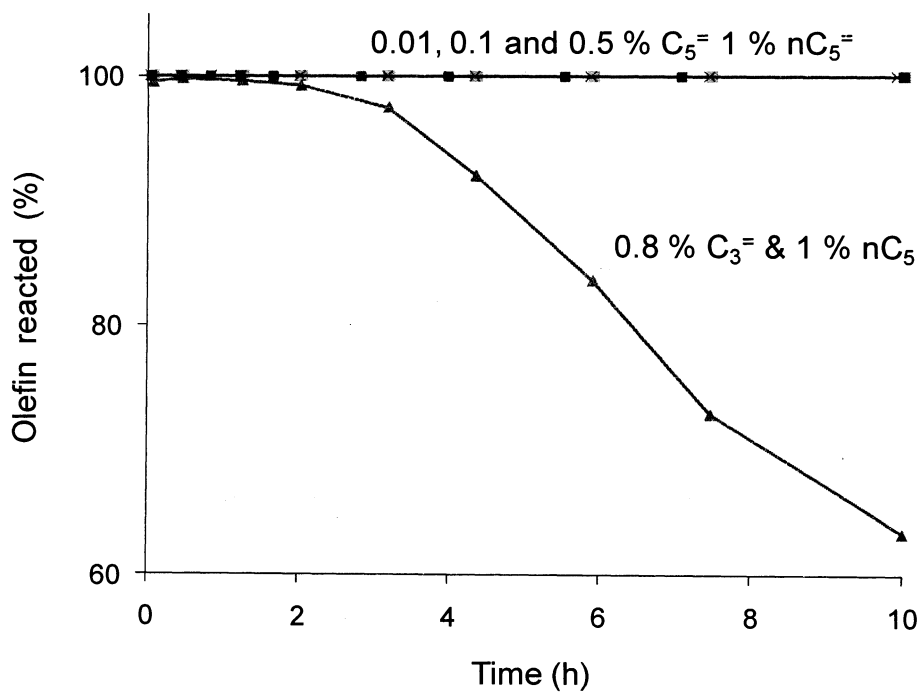
Time (h)	Carbon balance (%)
0.05	90
0.44	93
0.83	95

Table D.4 (continued)

Time (h)	Carbon balance (%)
1.21	97
1.66	98
2.81	97
3.98	97
5.53	97
7.10	99
9.9	97

Table D.5. Carbon mass balance during 10 hr run for 0.8% C₃⁼, 1% nC₅.

Time (h)	Carbon balance (%)
0.07	86
0.45	93
0.82	94
1.25	95
2.02	98
3.20	95
4.38	93
5.92	92
7.47	88
10.0	86

**Figure D.1.** Percentage of olefin reacting as a function of time.